Université Mohamed Khider – Biskra

Faculté des Sciences et de la technologie

Département : Génie Electrique

Ref :………………

جامعة محمد خيضر بسكرة

كلية العلوم و التكنولوجيا

قسم: الهندسة الكهربائية

المرجع:………...

Thèse présentée en vue de l'obtention
Du diplôme de

Doctorat en sciences en : Electronique

Spécialité (Option) : Electronique

Simulation et Analyse des caractéristiques électriques de la diode à barrière de Schottky (SBD) Métal/Carbure de Silicium

Présentée par :
KAMAL ZEGHDAR

Soutenue publiquement le   29/09/2019

Devant le jury composé de :

Pr. Sengouga Noureddine	**Professeur**	**Président**	**Université de Biskra**
Pr. Dehimi Lakhdar	**Professeur**	**Rapporteur**	**Université de Batna 1**
Pr. Lakhdar Nacereddine	**Professeur**	**Examinateur**	**Université d'El Oued**
Dr. Megherbi Mohamed Larbi	**Maitre de Conférences 'A'**	**Examinateur**	**Université de Biskra**

University of Mohamed Khider Biskra

Faculty of Science and Technology

Departement : **Electrical Engineering**

Ref :………………

جامعة محمد خيضر بسكرة
كلية العلوم و التكنولوجيا
قسم:الهندسة الكهربائية
المرجع:…………

Thesis submitted in fulfillment of the requirements
for the degree of
Doctorate in Science in: Electronics

Specialty (Option): Electronics

Simulation and Analysis of the Electrical Characteristics of the Schottky Barrier Diode (SBD) Metal / Silicon Carbide

Presented by:
KAMAL ZEGHDAR

Publicly supported on :   ………………

In front of the jury:

Pr. Sengouga Noureddine	**Professor**	**President**	**University of Biskra**
Pr. Dehimi Lakhdar	**Professor**	Advisor	**University of Batna1**
Pr. Lakhdar Nacereddine	**Professor**	**Examiner**	**University of Eloud**
Dr. Megherbi Mohamed Larbi	**Lecturer 'A'**	**Examiner**	**University of Biskra**

Acknowledgements

In the name of Allah, the Most Merciful, Most Compassionate. All praise belongs to Allah, Lord of the worlds and prayers, and peace be upon Muhammad his servant and messenger.

First and Foremost praise is to Allah, the Almighty, the greatest of all, on whom ultimately we depend for sustenance and guidance. I would like to thank Almighty Allah for giving me opportunity, determination and strength to do my research. His continuous grace and mercy was with me throughout my life and ever more during the tenure of my research.

I would like to express my sincere gratitude to my advisor Prof Lakhdar Dehimi for his incredible patience, and encouragement throughout my study and research. His guidance helped me in all the time of research and writing of this thesis. I could not have imagined having a better advisor and mentor for my Sc.D study.

Besides my advisor, I would like to thank the rest of my thesis committee: Prof. Sengouga Noureddine, Prof. Nacereddine Lakhdar, and Dr. Megherbi Mohamed Larbi for taking time off their busy schedules, and serving on my dissertation committee.

My sincere thanks also go to Pr. Fortunato Pezzimenti , Pr. Francesco G. DellaCorte, and Dr. Sandro Rao of Mediterranea University of Reggio Calabria in Italy for all of their guidance and help.

Last but not the least, I would like to thank my family: my parents, my wife and to my brothers and sister for supporting me spiritually throughout writing this thesis and my life in general.

Abstract

Silicon carbide is a promising semiconductor material for harsh environment sensing applications thanks to its superior material properties compared with silicon and other semiconductor materials. The wide bandgap, high thermal conductivity, and high breakdown field allow SiC based devices to work under extreme conditions.

In this work we are interested in Ti/Al, Mo, W/ 4H-SiC as temperature sensors, so the study of its electrical properties is very important in order to have different effects on the current-voltage characteristics.

The current-voltage *(I-V)* characteristics of Schottky barrier diodes (SBDs) measured at room temperature do not provide detailed information about the nature of the barrier and the charge transport processes at the metal-semiconductor (MS) interface. On the contrary, the temperature dependent *(I-V)* behaviors are useful for giving a better understanding of the conduction mechanisms through the MS interface.

SILVACO-ATLAS simulator allowed us to simulate the current-voltage characteristic *(I-V)*, to see the influence of temperature on the evolution of curves and assess the main parameters that characterize the Schottky diode as the ideality factor, the height of the barrier and the series resistance.

Indeed, the application of the standard method used by most researchers that is based on the extraction of homogeneous parameters (Φ_B, *n*, *Rs*) has some defects such that the decrease in the barrier height (Φ_B) and increase of ideality factor (*n*) with decreasing temperature, the use of inhomogeneous model proposed by Werner on the one hand can interpret abnormalities on electrical parameters extracted and on the other hand approach the value of the Richardson constant which is consistent with that given by the theory (146 A/K^{2}cm^2). The obtained results reveal that the devices in question are well suited for temperature sensing applications.

Keywords :: Schottky diode, Silicon Carbide, Inhomogenity, Silvaco

ملخــــــــــــص

كربيد السيليكون مادة شبه موصلة واعدة لتطبيقات الاستشعار في البيئة القاسية وذلك بفضل خواصها الفائقة مقارنة بالسيليكون ومواد أشباه الموصلات الأخرى. تسمح فجوة الحزمة الواسعة والموصلية الحرارية العالية وحقل الإنهيار العالي للأجهزة التي تعتمد على مادة كربيد السلكون بالعمل في الظروف القاسية.

في هذا المشروع نحن مهتمون بثنائيات حاجز شوتكي Ti/Al, Mo, W/ 4H-SiC كأجهزة استشعار لدرجة الحرارة، وبالتالي فإن دراسة خصائصها الكهربائية جد مهمة بهدف فهم مختلف جوانب الخواص تيار- جهد كهربلئي.

لا توفر خصائص تيار- جهد كهربائي (I-V) لثنائيات حاجز شوتكي المقاسة عند درجة الحرارة المثلى معلومات مفصلة عن طبيعة الحاجز وعمليات نقل الشحنة في واجهة المعدن- شبه الموصل، في حين أن سلوكيات خصائص تيار- جهد كهربلئي التي تعتمد على درجة الحرارة مفيدة في إعطاء فهم لآليات التوصيل عبر واجهة المعدن- شبه الموصل..

أداة المحاكاة سيلفاكو -أطلس سمحت بمعاينة خصائص تيار- جهد كهربلئي لمعرفة تأثير درجة الحرارة على منحنيات التطور،وتقييم المعايير الأساسية التي تمثل ثنائي شوتكي مثل معامل المثالية،حاجز الجهد والمقاومة المتوالية.

في الواقع، استعمال الطريقة القياسية المتبعة من طرف العديد من الباحثين والتي تعتمد على استخراج المعلمات المتجانسة (Φ_B, n, R_S) تبين وجود عدة نقائص كانخفاض حاجز الجهد وارتفاع معامل المثالية بانخفاض الحرارة، إستعمال النموذج غير المثالي المقترح من طرف ورنر يسمح من جهة بتفسير النقائص الملاحظة على المعلمات الكهربائية المستخلصة و تقريب قيمة ثابت ريشاردسون الذي يوافق القيمة النظرية (146 cm² K²/ A). تكشف النتائج التي تم الحصول عليها أن الأجهزة محل الدراسة مناسبة تمامًا لتطبيقات استشعار درجة الحرارة.

كلمات مفتاحية: شوتكي ديود ، كربيد السيليكون ، عدم التجانس ، سيلفاكو.

Résumé

Le carbure de silicium est un matériau semi-conducteur prometteur pour les applications de détection d'environnements difficiles grâce à ses propriétés de matériau supérieures à celles du silicium et d'autres matériaux semi-conducteurs. La large bande interdite, la conductivité thermique élevée et le champ de claquage élevé permettent aux dispositifs à base de SiC de fonctionner dans des conditions extrêmes. Dans ce projet on s'intéresse à Ti/Al, Mo, W/ 4H-SiC comme capteurs de température, donc l'étude de leur propriétés électriques est très important dans le but d'avoir les différents effets sur les caractéristiques courant-tension .

L'analyse des caractéristiques courant-tension (*I-V*) des diodes Schottky à température ambiante ne donnent pas des informations détaillées sur leur processus de conduction ou de la nature de la formation de la barrière à l'interface M/S. La dépendance en température des caractéristiques (*I-V*) nous permet de comprendre les différents aspects des mécanismes de conduction.

Le logiciel SILVACO-ATLAS nous a permis de simuler les caractéristiques courante tension (I-V), de voir l'influence de la température sur l'évolution des courbes, et d'évaluer les principaux paramètres qui caractérisent la diode Schottky tel que le facteur d'idéalité, la hauteur de la barrière, la résistance série...etc.

En effet, l'application de la méthode standard suivie par la plupart des chercheurs qui est basée sur l'extraction des paramètres homogènes (Φ_B, *n, Rs*) présente certaines anomalies telle que la diminution de la hauteur de barrière (Φ_B) et l' augmentation du facteur d'idéalité (*n*) avec la diminution de la température, L'utilisation du modèle inhomogène proposé par Werner permet d'interpréter d'un coté les anomalies observées sur les paramètres électriques extraits et de s'approcher d'un autre coté la valeur de la constante de Richardson qui est en accord avec celle donnée par la théorie (146 A/K^2cm^2). Les résultats obtenus révèlent que les dispositifs en question sont bien adaptés aux applications de détection de température.

Mots clés : Schottky diode, Silicon Carbide, Inhomogenity, Silvaco

Table of Contents

List of Figures

List of Tables

Introduction

Introduction

The considerable industrial interest in Silicon Carbide (SiC) following its promising applications in, hostile-environment electronics and sensors has led to substantial international research effort over the last teen years [1-3].

SiC is a promising semiconductor for sensing applications due to its excellent electrical and physical properties. The wide bandgap energy and low intrinsic carrier concentration allow SiC based semiconductor devices to be functional at much higher temperatures. Moreover, high breakdown field, high-saturated electron velocity, and high thermal conductivity enable SiC devices to work under extreme conditions. The capability of SiC-based devices to operate at high-temperature ensures significant lifetime and reliability benefits in many engineering fields such as aircraft, spacecraft, automotive, and energy production industries [4-6].

In this context, SiC-based Schottky barrier diodes (SBDs) have gained an increasing interest in order to be used as temperature sensors in harsh environments thanks to their high-resolution and chemical inertness [7-11]. The main advantages of diode-based sensors are, in principle, the low manufacturing costs and the full compatibility with the integrated circuits technology [12].

Because of their refractory properties, Titanium (Ti), Molybdenum (Mo) and Tungsten (W) are the materials of choice used for Schottky contacts. However, these devices often show undesirable I–V characteristics that reveal abnormal variations of both the barrier height (BH) and ideality factor with temperature [5,13,14]. The increase of the ideality factor with decreasing temperature is known as the "T_0 effect" and was first described by Padovani and Sumner [15]. Another abnormality was observed in the experimental value of the Richardson constant. The experimental $A*$ was found to be far less than its theoretical value, and in several cases, it is less than the theoretical value by orders of magnitude. Many researchers have tried to find out the cause behind this deviation (abnormal behaviour) and have proposed many different explanations. Some researchers have suggested that the variance of Schottky barrier height (SBH) with temperature should follow the variance of the band gap with temperature [16], but it has generally been found experimentally that this SBH variance is not in agreement with the band-gap variance with temperature [17]. Image Force effects are another possible explanation for the temperature dependence of the barrier height and ideality factor. However, a considerable contribution from other current mechanisms such as quantum mechanical tunnelling and trap assisted tunnelling, to the diode total current, could be a potential reason for all the observed anomalies [18]. Other researchers have proposed that the anomalous behaviour in Φ_B, n, and the Richardson plot can be explained by using Werner and Guttler's model. The model adopted an

analytical potential fluctuation assuming the formation of spatial barrier height inhomogeneities at the MS interface. This proposal has been able to explain most of the abnormal behaviour based on TE theory using a Gaussian distribution function for the barrier heights [19-20]. The single-Gaussian distribution is commonly used because of its simplicity and clear physical meaning. However, the failures of this approach have been recently confirmed by some investigators [21–22], due to the fact that it may not be suitable to characterize more experimental data contains than one Gaussian distribution for most cases and is only used for fitting to a part of distribution rather than all. As a result, the deficiencies in the single-Gaussian approach were removed by a multi-Gaussian consideration with the values of weight, the mean barrier height and the standard deviation for each Gaussian region of the spatial barrier height distribution, introduced by Yu-Long et al [21]. Accordingly, the greatness of the inhomogeneities existing in the barrier is determined by arbitrary distribution functions separately with their own different contribution rations for each distribution region [23].

In order to attain a complete understanding of the Schottky diode characteristics it is, therefore, necessary to model the I-V-T curves by using detailed physical models starting from specific assumptions [24, 25].

In the present thesis, starting from the experimental results on Ti/Al 4H–SiC, Mo/4H–SiC and W/4H–SiC SBDs reported in recent literatures [26-28], a careful simulation study using the ATLAS module of the commercial software (SILVACO-TCAD) is performed over a wide temperatures range in order to explain the abnormal behaviour observed in the experimental I–V characteristics and evaluate the suitability of these devices as temperature sensors.

The temperature dependencies of the current transport parameters are explained based on the assumption of the existence of Gaussian distribution of the Schottky barrier around the Metal/ 4H–SiC interface. Finally, the performance of temperature sensors based on Ti/Al/4H–SiC, Mo/4H–SiC and W/4H–SiC Schottky diodes is investigated. In particular, sensitivity, linearity and root mean square error (RMSE) are accurately analyzed in a wide temperatures range.

This thesis is organised as follows: Chapter one gives a background to silicon carbide and why its material properties give outstanding device performance for power devices and high-temperature applications compared to other semiconductor materials. Chapter two presents an overview of the SBDs devices. Chapter three explains the software used in this and parameters used for simulation for the total forward drop of the devices. Electrical characterization and discussion are found in Chapter four. Finally, this thesis is concluded.

Chapter 1
Material properties
and applications

1.1. Introduction

Silicon carbide (SiC) is a semiconductor material with highly suitable properties for high-power, high-frequency, and high-temperature applications. This almost worn-out opening statement may be found in many papers dealing with SiC. Yet, it cannot be left out because it really brings forward the essence of the material's potential. Silicon carbide is a wide bandgap semiconductor material with high breakdown electric field strength, high saturated drift velocity of electrons, and a high thermal conductivity. In combination with these properties, a native substrate of reasonable size exists, and one may readily grow the material and dope it both n and p-types.

The physical properties of SiC are very important subjects of academic study as well as critical parameters for accurate simulation of devices. This chapter briefly reviews the physical properties of SiC after a brief mention of the history of SiC from its discovery to its use in the electronics industry.

1.2. History

SiC itself is rare in nature, and synthesis of a compound material containing silicon–carbon bonds was first reported by Berzelius in 1824. Later it was Acheson who produced SiC by heating coke and silica together, in a furnace, a method still known as Acheson process. He called the new compound "carborundum" which was to be used for abrasion and cutting due to its hardness.

In the Acheson process, ingots which contain small single crystalline SiC platelets (mainly 6H-SiC) can be obtained as a by-product (Figure (1.1a)). Although these SiC platelets are not pure, they were used for some basic studies on the physical and chemical properties of SiC.

First use of SiC in electronics was the invention of SiC LEDs in 1907. But the use of SiC in electronics was not to last longer because of difficulties in producing high quality SiC crystals due to unavailability of any controlled crystal growth technique [29-30].

In 1955 an important crystal growth technique was invented by J. A. Lely which made controlled crystal growth possible. This resulted in huge research activity on SiC for a short time and first academic event on SiC was held in 1958, a conference at Boston. After this event no considerable technological activity can be seen mainly because no high quality SiC substrates were available at that time [30].

(a)   (b)

Figure 1.1. (a) SiC platelets (mainly 6H-SiC) obtained as a by-product in the Acheson process. (b) 4H-SiC wafers with 100 and 150mm in diameter [29].

It was in 1970s when two Russian scientists Tairov and Tsvetkov discovered a new method for SiC crystal growth known as seeded sublimation growth which made possible, for the first time, the production of SiC wafers (Figure (1.1b)). This was followed by the discovery of yet another technique called 'step controlled epitaxy' in 1987 which made possible epitaxial growth of SiC and resulted in the commercialization of first power electronic devices based on SiC such as the Schottky diodes and MESFETs produced by Cree Inc. and Infineon [29].

1.3. SiC Properties

1.3.1. SiC crystal structure

1.3.1.1. Basic Structure

The basic building block of a silicon carbide crystal is the tetrahedron of four carbon atoms with a silicon atom in the center (Figure (1.2)).
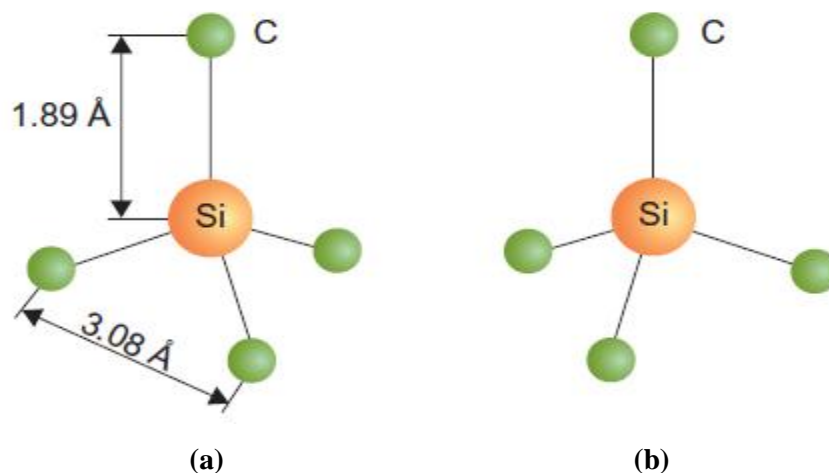
(a)   (b)

Figure 1.2. (a) The basic structural unit in SiC is a tetrahedron of four carbon atoms with a silicon atom in the middle. (b) A second type rotated 180^0 around the stacking direction, with respect to the first type of tetrahedra, can also occur in ther SiC crystals [32].

4

There also exists a second type rotated 180° with respect to the first. The distance between the carbon and silicon atom is 1.89Å and the distance between the carbon atoms is 3.08Å. SiC crystals are constructed with these units joining at the corners [29-32].

1.3.1.2.   Polytypism

Silicon carbide exhibits a two-dimensional polymorphism called polytypism. All polytypes have a hexagonal frame of SiC bilayers. The hexagonal frame should be viewed as sheets of spheres of the same radius and the radii touching, as illustrated in figure (1.3). The sheets are the same for all lattice planes. However, the relative position of the plane directly above or below are shifted somewhat to fit in the "valleys" of the adjacent sheet in a close-packed arrangement. Hence, there are two inequivalent positions for the adjacent sheets. By referencing the possible positions as A, B, and C, we can begin constructing polytypes by arranging the sheets in a specific repetitive order. Thus, the only cubic polytype in SiC is 3C-SiC, which has the stacking sequence ABCABC… The simplest hexagonal structure we can build is 2H, which has a stacking sequence ABAB… The two important polytypes, 6H-SiC and 4H-SiC, have stacking sequences ABCACBABCACB… and ABCBABCB…, respectively. The number in the notation of the resulting crystal structure determines the number of layers before the sequence repeats itself, and the letter determines the resulting structure of the crystal: C for cubic, H for hexagonal, and R for rhomohedral.
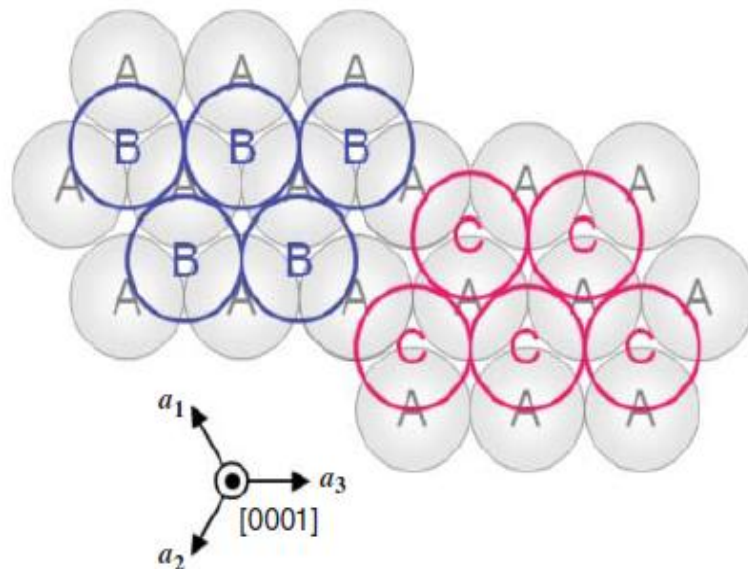
Figure 1.3. Illustration of three close-packed planes of spheres. The first layer is a layer of "A" atoms, followed by a layer of atoms on a "B" position, with a layer of atoms on "C" positions on top of that. The resulting structure in this example is 3C-SiC [29].

All polytypes are SiC of equal proportions of silicon and carbon atoms, but due to the fact that the stacking sequence between the planes differs, the electronic and optical properties differ. The bandgap is, for instance, 2.39 eV for 3C-SiC, 3.023 eV for 6H-SiC, and 3.265 eV for 4H-SiC [30-32].

The unit cell for the different polytypes will naturally vary, as will the number of atoms per unit cell. This will affect the number of electronic bands and the phonon branches for a given polytype.

1.3.1.3.   Impurities in Different Polytypes

A very striking and beautiful feature of polytypism is the behavior of impurity atoms. In figure (1.6), it may be seen that the sites are not equivalent in the hexagonal polytypes 6H-SiC and 4H-SiC. The difference is in the second-nearest neighbors.
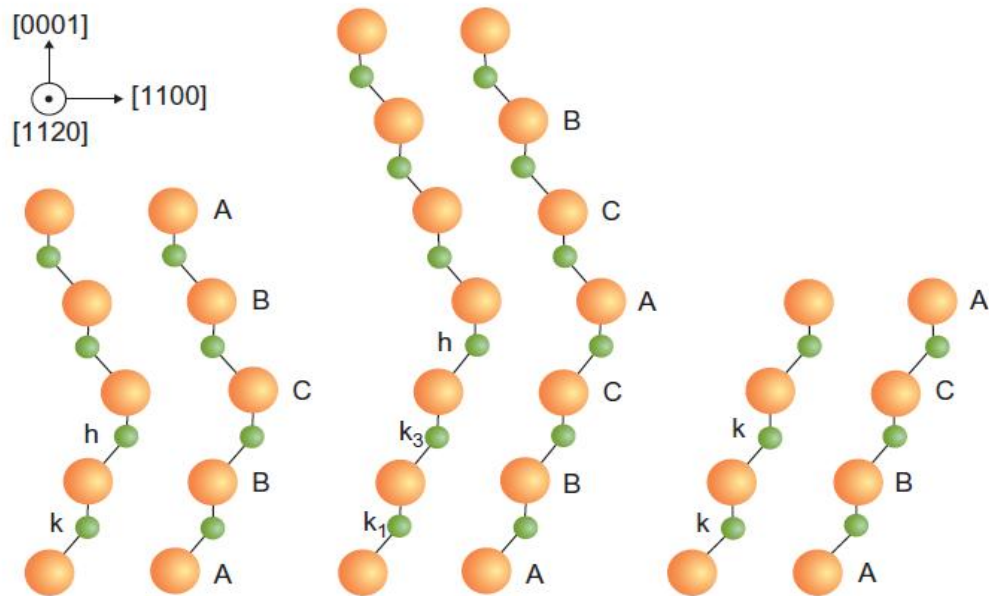
Figure 1.4. The three most common polytypes in SiC viewed in the [1120] plane. From left to right, 4H-SiC, 6H-SiC, and 3C-SiC; k and h denote crystal symmetry points that are cubic and hexagonal, respectively [32].

A nitrogen atom substituting a carbon atom in the lattice can either occupy a "k" site or an "h" site in 4H-SiC. The k site is a lattice site that displays cubic symmetry, whereas the h site has hexagonal symmetry. The immediate vicinity of a nitrogen atom on either site is the same, but the second-nearest neighbors to the sitesare different, which creates a slightly different core binding energy. Thus, 4H-SiC has two binding energies for the nitrogen donor, which has consequences when designing devices. 6H-SiC has three energy levels for nitrogen and 3C-SiC has only one. More complex polytypes such as rhombohedral (15R-SiC) has no less than five binding energies, although only four have been identified [30].

1.3.2. Electrical and Optical Properties

1.3.2.1. Band Structure

Figure (1.5) shows the first Brillouin zones of (a) 3C-SiC and (b) a hexagonal SiC polytype [33, 24]. Note that the height of the Brillouin zone shown in figure (1.5b) is different for different hexagonal polytypes because of their different values of the lattice parameter.

Note that the absolute values of the bandgap are underestimated in this figure, due to a limitation of the theoretical calculation (density functional theory). All the SiC polytypes have an indirect band structure, as is also the case for Si. The top of the valence band is located at the Γ point in the Brillouin zone, whereas the conduction band minima appear at the Brillouin zone boundary. The conduction band minima are located at the X point for 3C-SiC, M point for 4H-SiC, and U point (along the M–L line) for 6H-SiC. Thus, the number of conduction band minima in the first Brillouin zone (Mc) is 3 for 3C-SiC, 3 for 4H-SiC, and 6 for 6H-SiC. Because Si-C covalent bonds are common to all SiC polytypes, the valence band structure is similar amongst the different polytypes, except for the splitting.
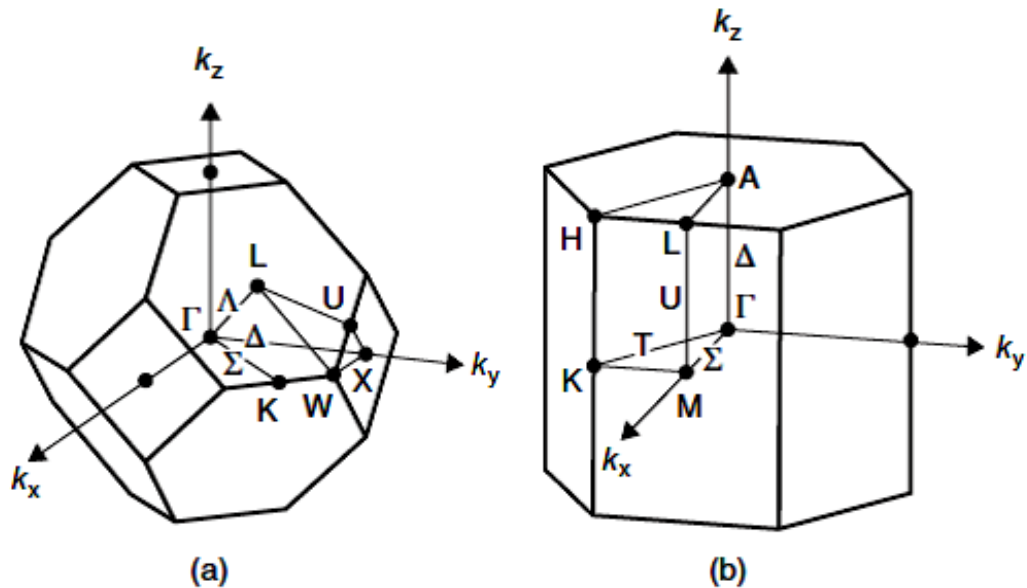
Figure 1.5. Brillouin zones of (a) 3C-SiC and (b) a hexagonal SiC polytype [29,32].

Figure (1.6) depicts the electronic band structures of (a) 3C-SiC, (b) 4H-SiC, and (c) 6H-SiC. The top of the valence band is doubly degenerate in 3C-SiC, as a result of its cubic symmetry, and the next valence band is shifted 10meV from the top by the spin–orbit interaction [35-37]. The crystal field, which exists in all hexagonal polytypes, splits the valence band degeneracy. The magnitudes of the spin–orbit splitting and crystal-field splitting for 4H-SiC are 6.8 and 60meV, respectively [38].

7
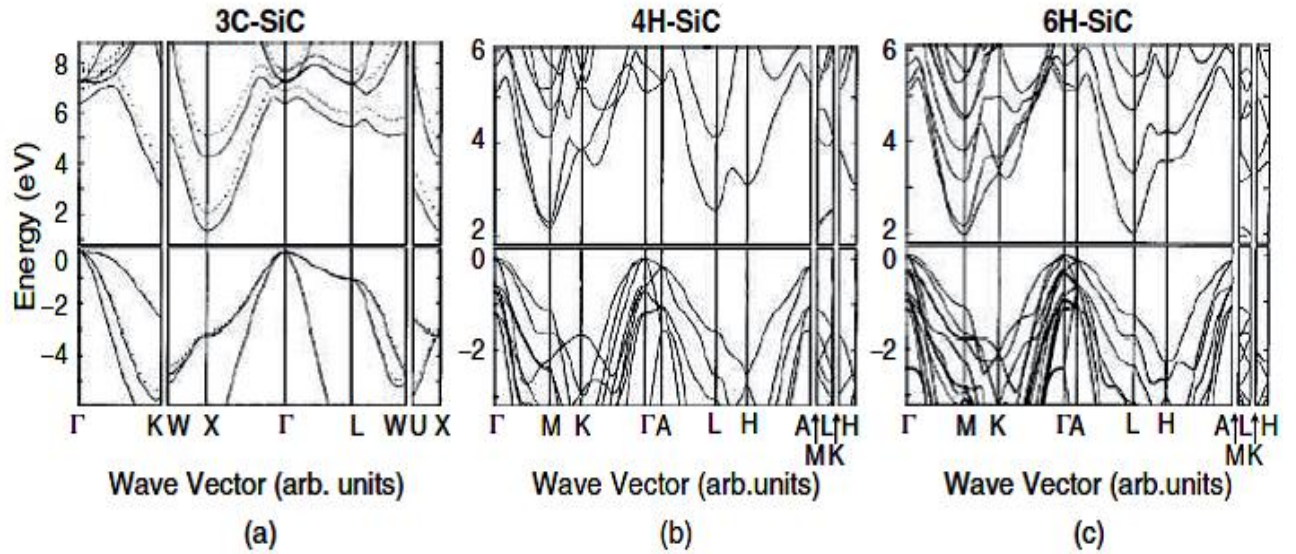
Figure 1.6. Electronic band structures of (a) 3C-SiC, (b) 4H-SiC, and (c) 6H-SiC [29].

Table 1.1 Effective masses of electrons and holes in 3C-, 4H-, and 6H-SiC [39].

Polytype	Effective mass	Experiment (m_0)	Theory (m_0)
	Electron effective mass		
3C-SiC	$m_{/\!/}$	0.667	0.68
	$m\perp$	0.247	0.23
4H-SiC	$m_{ML}(=m_{/\!/})$	0.33	0.31
	$m_{M\Gamma}$	0.58	0.57
	m_{MK}	0.31	0.28
	$m\perp\,(=(m_{M\Gamma}m_{MK})^{1/2})$	0.42	0.40
6H-SiC	$m_{ML}(=m_{/\!/})$	2.0	1.83
	$m_{M\Gamma}$	-	0.75
	m_{MK}	-	0.24
	$m\perp\,(=(m_{M\Gamma}m_{MK})^{1/2})$	0.48	0.42
	Hole effective mass		
3C-SiC	$m_{MT}(=m_{[100]})$	-	0.59
	$m_{MK}(=m_{[110]})$	-	1.32
	$m_{TL}(=m_{[111]})$	-	1.64
4H-SiC	$m_{/\!/}$	1.75	1.62
	$m\perp$	0.66	0.61
6H-SiC	$m_{/\!/}$	1.85	1.65
	$m\perp$	0.66	0.60

Table 1.1 summarizes the effective masses of electrons and holes in 3C-, 4H-, and 6H-SiC [39]. The electron effective mass and its anisotropy depend strongly on the polytype, while the hole effective mass exhibits a weak polytype dependence. The former leads to large variation of electron mobility in different polytypes, and also to anisotropic electron transport.

The exciton gaps of various SiC polytypes at 2K are plotted as a function of "hexagonality" in figure (1.7) [34]. Here, hexagonality means the ratio of the number of hexagonal sites to the total number of Si-C bilayers (hexagonal and cubic sites) in a unit cell (the hexagonality is 1 for 2H-SiC, 0 for 3C-SiC, 1/2 for 4H-SiC, and 1/3 for 6H-SiC).

It is interesting that the bandgap of SiC polytypes increases monotonically with increasing hexagonality. The bandgap at room temperature is 2.36 eV for 3C-SiC, 3.26 eV for 4H-SiC, and 3.02 eV for 6H-SiC.
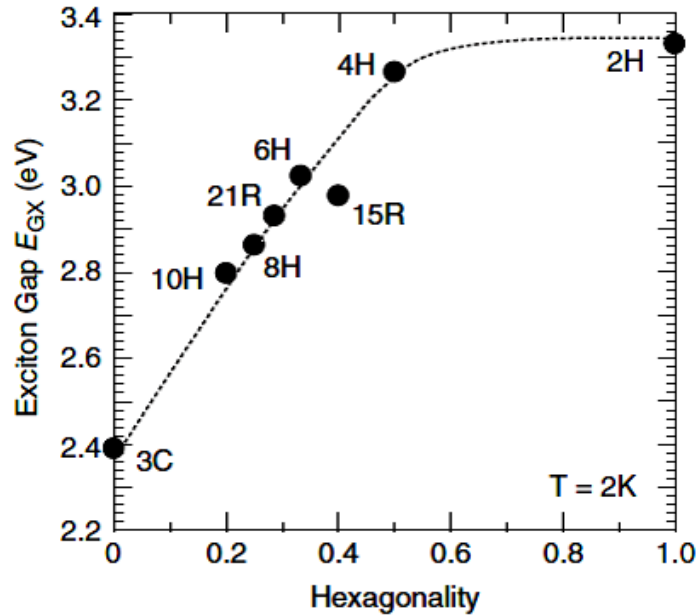
Figure 1.7. Exciton gaps of various SiC polytypes at 2K versus hexagonality [35, 36].

Figure (1.8) shows the temperature dependence of the bandgap for several SiC polytypes [41]. The bandgap (Eg) decreases with increasing temperature because of thermal expansion, and its temperature dependence can be semi-empirically expressed as [42]:

$$E_g(T) = E_{g0} - \frac{\alpha \times T^2}{\beta + T} \tag{1.1}$$

where E_{g0} is the bandgap at 0 K, T the absolute temperature, and α and β are fitting parameters ($\alpha = 8.2 \times 10^{-4}$ eV K^{-1}, $\beta = 1.8 \times 10^3$ K).

Note that the bandgap also depends on the doping density; very high impurity doping, above 10^{19} cm^{-3}, causes the bandgap to shrink because of the formation of pronounced tail states near the band edges [43].
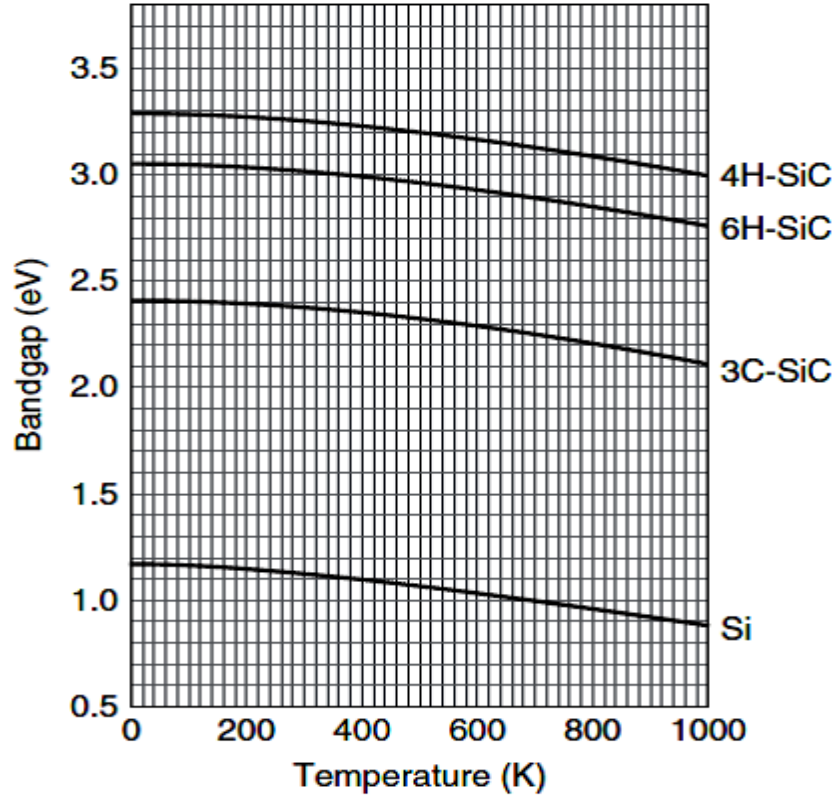
Figure 1.8. Temperature dependence of bandgap for several SiC polytypes [41].

1.3.2.2.   Optical Absorption Coefficient and Refractive Index

Figure (1.9) shows the optical absorption coefficients versus photon energy for the major SiC polytypes [44]. Because of the indirect band structure of SiC, the absorption coefficient (α_{opt}) slowly increases, even when the photon energy exceeds the bandgap.

Taking account of phonon absorption and emission, the absorption coefficient can be approximated as [45]:

$$\alpha_{opt} = \frac{A_{ab}}{hv}\left\{\frac{\left(hv - E_g + \hbar\omega\right)^2}{exp(hv/kT) - 1} + \frac{\left(hv - E_g + \hbar\omega\right)^2}{1 - exp(-hv/kT)}\right\} \qquad (1.2)$$

Here hv is the photon energy, $\hbar\omega$ the energy of a phonon involved, k the Boltzmann constant, and Aab the parameter. When several different phonons are involved, the sum of those contributions must be calculated.

10

The absorption coefficient of 4H-SiC at room temperature is 69 cm^{-1} at 365 nm (3.397 eV, Hg lamp), 210 cm^{-1} at 355 nm (3.493 eV, 3HG Nd-YAG laser), 1350 cm^{-1} at 325 nm (3.815 eV, He-Cd laser), and 14 200 cm^{-1} at 244 nm (5.082 eV, 2HG Ar ion laser). These values should be kept in mind when SiC materials are characterized by any optical technique, or when SiC-based photodetectors are fabricated.

For example, the penetration depth, as defined by $1/\alpha_{opt}$, is 145 μm at 365 nm, 7.4 μm at 325 nm, and 0.7 μm at 244 nm for 4H-SiC at room temperature.
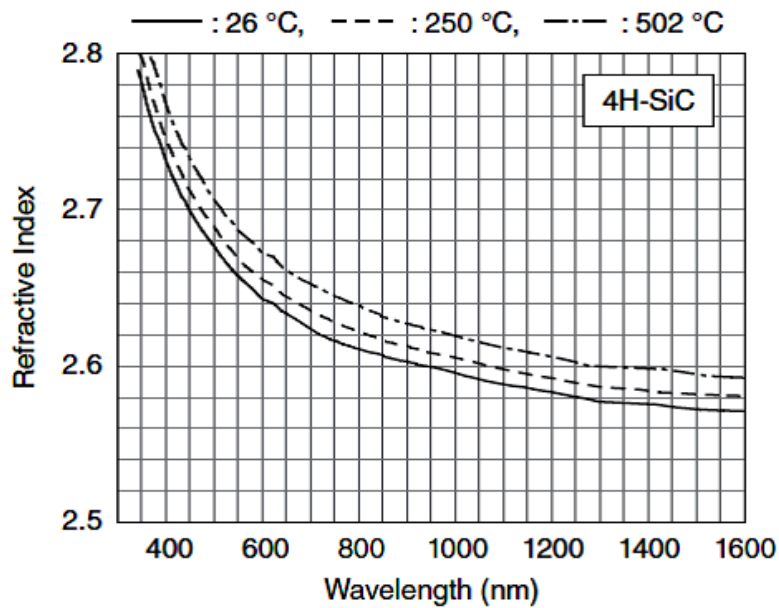
Figure 1.9. Refractive index of 4H-SiC versus wavelength across a wide range from ultraviolet to infrared at various temperatures[44 ,46].

Figure (1.9) shows the refractive index of 4H-SiC versus wavelength across a wide range, from ultraviolet to infrared, at various temperatures [46]. This dispersion of the refractive index $n(\lambda)$ is described by a simple *Sellmeier equation* given by [47]:

$$n(\lambda) = A + \frac{B \times \lambda^2}{\lambda^2 - C^2}$$ (1.3)

where *A, B,* and *C* are parameters. The refractive index at a wavelength of 600 nm is 2.64 for 4H-SiC. The thermo-optic coefficient, defined by dn/dT, is $(4.4–5.0) \times 10^{-4}$ K^{-1} in the visible–infrared region and increases to $(7–8) \times 10^{-4}$ K^{-1} near the ultraviolet region, due to the shrinkage of the bandgap at elevated temperature [46]. The relative dielectric constant has also been reported for several SiC polytypes [42, 48]. The relative dielectric constants in the high-frequency (100 kHz to 1 MHz) region for 4H-SiC (6H-SiC) at room temperature are 9.76 (9.66) perpendicular to the *c*-axis and 10.32 (10.03) parallel to the *c*-axis [48]. The dielectric constant of 3C-SiC is isotropic, 9.72.

1.3.2.3.   **Impurity Doping and Carrier Density**

SiC is an exceptional wide bandgap semiconductor, in the sense that control of both n- and p-type doping over a wide range is relatively easy. Nitrogen or phosphorus are employed for n-type doping and aluminum for p-type doping. Although boron was also previously employed as an acceptor, it is currently not preferred because of its large ionization energy (~350 meV) [49], generation of a boron-related deep level (D center) [49, 50], and its abnormal diffusion [50, 51]. Gallium and arsenic work as acceptor and donor, respectively, in SiC. Their ionization energies are, however, relatively large, and their solubility limits are low. Nitrogen substitutes at the C sub-lattice site, while phosphorus, aluminum, and boron substitute at the Si sub-lattice site.

Table 1.2 Nonpolar covalent radii of Si, C, and major dopants for SiC [52].

Atom	Si	C	N	P	B	Al
Radius (Å)	1.17	0.77	0.74	1.10	0.82	1.26

Table 1.3 Ionization energies and the solubility limits of nitrogen, phosphorus, aluminum, and boron in major SiC polytypes.

	Nitrogen	Phosphorus	Aluminum	Boron (shallow)
Ionization energy (meV)				
3C-SiC	55	–	250	350
4H-SiC (hexagonal/cubic)	61/126	60/120	198/201	280
6H-SiC (hexagonal/cubic)	85/140	80/130	240	350
Solubility limit (cm^{-3})	2×10^{20}	($\sim 1 \times 10^{21}$)	1×10^{21}	2×10^{19}

Table 1.2 shows the non polar covalent radii of Si, C, and major dopants for SiC [52]. The *ionization energies* and the *solubility limits* of nitrogen, phosphorus, and aluminum in major SiC polytypes are summarized in Table 1.3 [53]. In SiC, the ionization energies of dopants depend on the lattice site, in particular, whether the site is hexagonal or cubic (site effect). In the case of nitrogen or phosphorus doping, the ionization energy of the donors is relatively small, and the ionization ratio of donors at room temperature is reasonably high, ranging from 50 to nearly 100%, depending on polytype and doping density.

Conversely, the ionization energy of aluminum is large (200 – 250 meV), and *incomplete ionization* (5 – 30%) of acceptors is observed at room temperature. Note that the ionization energy decreases when the doping density is increased, as a result of bandgap

shrinkage and formation of an impurity band. The dependence of dopant ionization energy, ΔE_{dopant}, on the dopant density is described by Efros *et al.* [54]:

$$\Delta E_{dopant,0} \, \Delta E_{dopant} = -\alpha_d (N_{dopant})^{1/3} \tag{1.4}$$

Here $\Delta E_{dopant,0}$ is the ionization energy in lightly-doped materials, N_{dopant} the dopant density, and a α_d parameter ($\alpha_d = (2–4) \times 10^{-8}$ eV cm). When the dopant density exceeds 10^{19} cm^{-3}, the ionization energy decreases sharply.

As a result, near-perfect ionization is observed in heavily aluminum-doped SiC ($>5 \times 10^{20}$ cm^{-3}), in spite of the relatively large ionization energy of aluminum [55]. Because the band structure (bandgap, effective mass) is known, one can calculate the effective densities of states in the conduction band N_c and valence band N_v as well as the intrinsic carrier density n_i as follows [56]:

$$N_c(T) = 2M_C \times \left(\frac{2\pi kT m_{de}^*}{h^2}\right)^{\frac{3}{2}} \tag{1.5}$$

$$N_v(T) = 2 \times \left(\frac{2\pi kT m_{dh}^*}{h^2}\right)^{\frac{3}{2}} \tag{1.6}$$

$$n_i(T) = \sqrt{N_c N_v} \times e^{\left(-\frac{E_g(T)}{2kT}\right)} \tag{1.7}$$

Here, MC is the number of conduction band minima, $m_{de}*$ ($m_{dh}*$) the density-of-state effective mass of electrons (holes), and h the Planck constant.

By using the density-of-state effective mass of electrons (holes) and the number of conduction band minima, the NC and NV values for 4H-SiC at room temperature are calculated as 1.8×10^{19} and 2.1×10^{19} cm^{-3}, respectively. These values are important as they allow us to estimate whether the material will be degenerate when heavy impurity doping is performed.

Figure (1.10) plots the temperature dependence of (a) the effective densities of states in the bands and (b) the intrinsic carrier density for major SiC polytypes, together with that of Si. Here, the temperature dependence of band gaps is taken into account.

The intrinsic carrier density at room temperature is extremely low in SiC, because of the wide band gap, about 0.13 cm^{-3} for 3C-SiC, 5×10^{-9} cm^{-3} for 4H-SiC, and 1×10^{-6} cm^{-3} for

6H-SiC. This is the main reason why SiC electronic devices can operate at high temperatures with low leakage current.
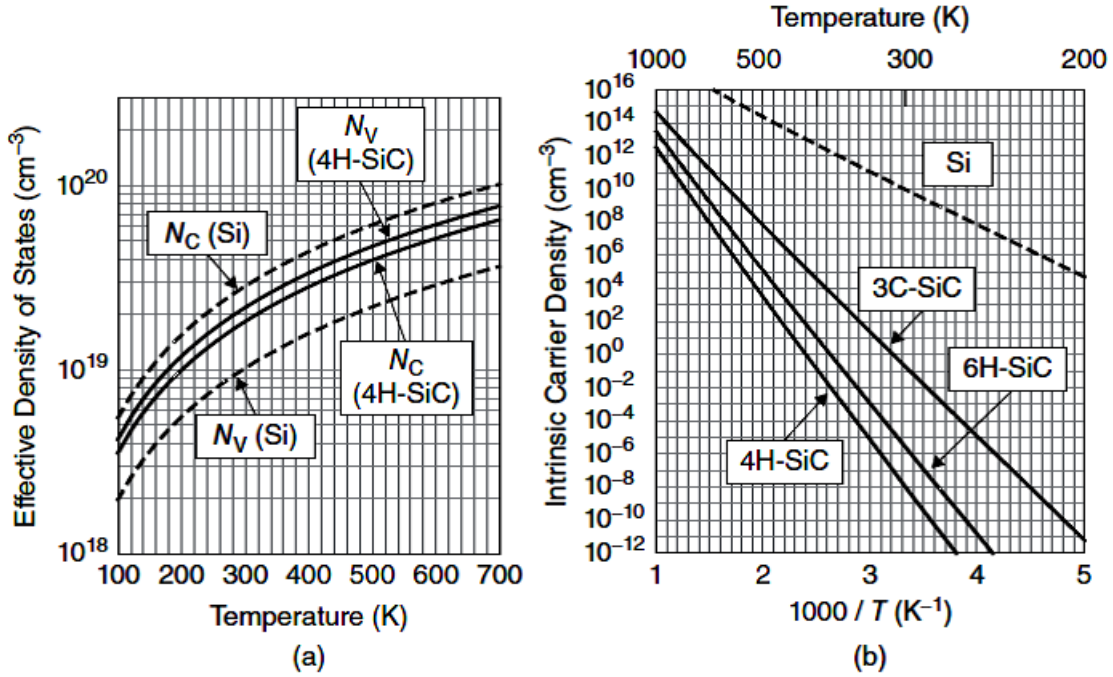
Figure 1.10. Temperature dependence of (a) the effective densities of states in the bands and (b) the intrinsic carrier density for major SiC polytypes, together with that of Si [29].

Based on the Boltzmann approximation for a nondegenerate semiconductor, the neutrality equations in a semiconductor containing one type of donor or acceptor are given by [57]:

$$n + N_{comp,A} = \frac{N_D}{1 + \left(\frac{g_D n}{N_C}\right) exp\left(\frac{\Delta E_D}{kT}\right)} \tag{1.8}$$

$$p + N_{comp,D} = \frac{N_A}{1 + \left(\frac{g_A p}{N_V}\right) exp\left(\frac{\Delta E_A}{kT}\right)} \tag{1.9}$$

Here $n(p)$ is the free electron (hole) density, $N_{comp,A}$ ($N_{comp,D}$) the density of compensating acceptor (donor) levels, N_D (N_A) the donor (acceptor) density, ΔE_D (ΔE_A) the ionization energy of the donor (acceptor), and g_D (g_A) are the degeneracy factors for donors (acceptors), respectively.

When multiple donor (or acceptor) levels exist, the sum for corresponding dopants must be considered in the right-hand term of the equation. This is the case for hexagonal SiC polytypes, because the donor (and acceptor) impurities at inequivalent lattice sites (e.g., $i = k, h$ for 4H-SiC) exhibit different energy levels.

14
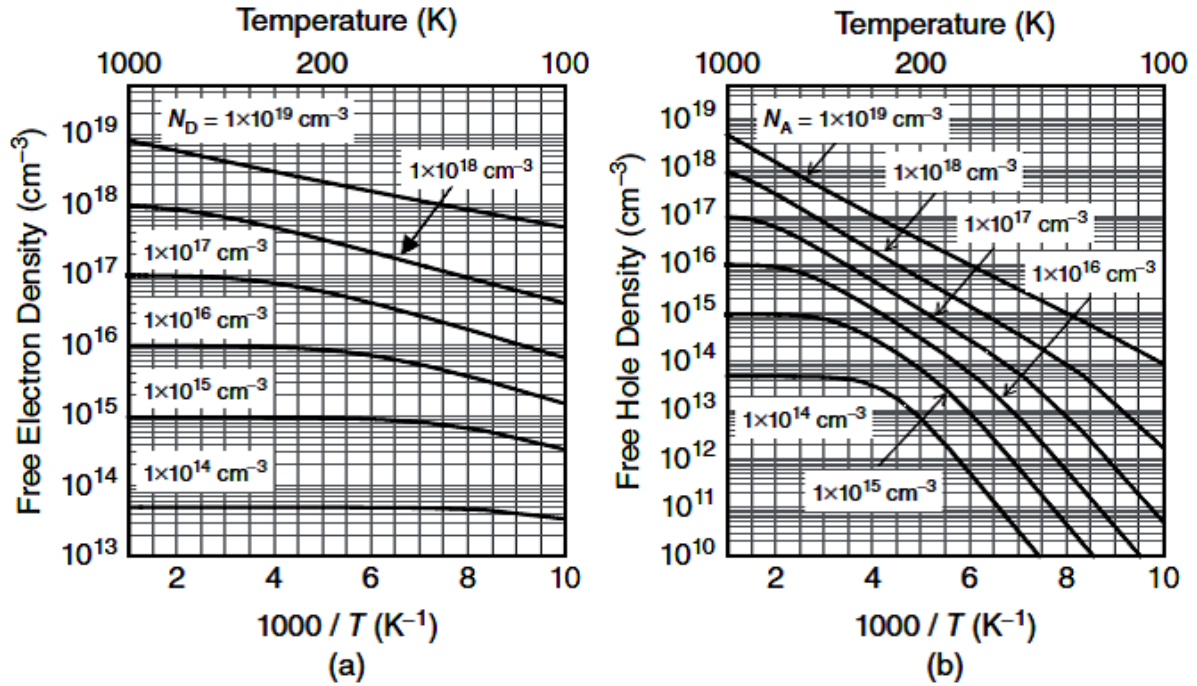
Figure 1.11. Arrhenius plots of the free carrier density in (a) nitrogen-doped and (b) aluminum-doped 4H-SiC. Here, the temperature dependence of the bandgap and the doping-density dependence of the ionization energies are taken into account. A compensating-level density of 5×1013 cm^{-3} is assumed[29].

The Arrhenius plots of the free carrier density in (a) nitrogen-doped and (b) aluminum-doped 4H-SiC are shown in figure (1.11). Here, the temperature dependence of the bandgap and the doping-density dependence of the ionization energies are taken into account. A compensating-level density of 5×10^{13} cm−3 is assumed. As shown in figure (1.11), incomplete ionization is significant for p-type SiC.

The position of the Fermi level EF in nondegenerate semiconductors is calculated by [56]:

$$E_F = E_C - kTln\frac{N_C}{n} \qquad (1.10)$$

$$E_F = E_V + kTln\frac{N_V}{p} \qquad (1.11)$$

Here E_C (E_V) is the energy of the conduction (valence) band edge. Figure (1.12) shows the Fermi level for nitrogen- or aluminum-doped 4H-SiC as a function of temperature and impurity concentration, taking into account the temperature dependence of the bandgap and the incomplete ionization of dopants at low temperature. Because of the wide bandgap, the Fermi level does not approach the midgap (intrinsic level) even at a fairly high temperature of 700 − 800 K.
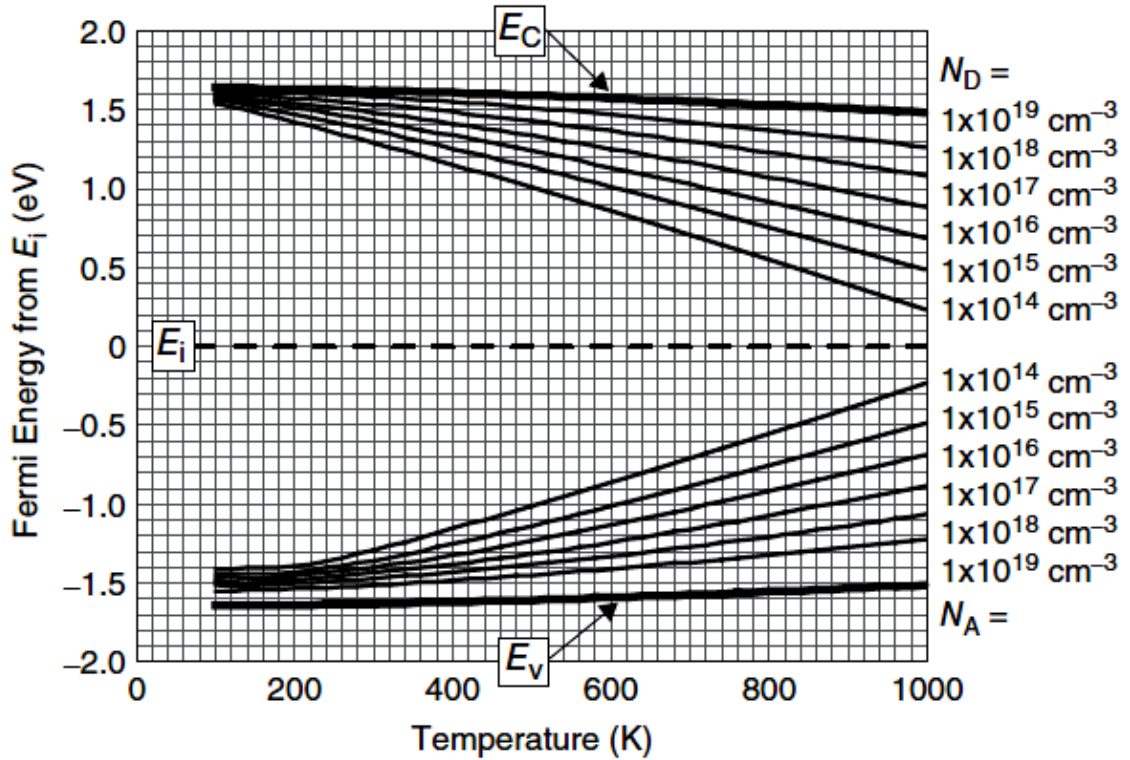
Figure 1.12. Fermi level for nitrogen- or aluminum-doped 4H-SiC as a function of temperature and impurity concentration, taking into account the temperature dependence of the bandgap and the incomplete ionization of dopants at low temperature [29].

1.3.2.4.   Mobility

Figure (1.13) shows (a) the low-field electron mobility versus donor density and (b) the hole mobility versus acceptor density for 4H-SiC and 6H-SiC at room temperature. The electron mobility of 4H-SiC is almost double that of 6H-SiC at a given dopant density, and 4H-SiC exhibits a slightly higher hole mobility than 6H-SiC. The low-field electron and hole mobilities can be expressed by Caughey – Thomas equations as follows [55, 58]:

$$\mu_h(4H - SiC) = \frac{118}{1 + \left(\frac{N_D + N_A}{2.2 \times 10^{18}}\right)^{0.7}} \ (cm^2 V^{-1} s^{-1}) \tag{1.12}$$

$$\mu_h(6H - SiC) = \frac{98}{1 + \left(\frac{N_D + N_A}{2.4 \times 10^{18}}\right)^{0.7}} \ (cm^2 V^{-1} s^{-1}) \tag{1.13}$$

Here N_D and N_A are given in units of cm^{-3}. The slight differences in the doping-dependence param- eters between 4H- and 6H-SiC originate from the differences in ionization energies of the dopants. It should be noted that hexagonal (and rhombohedral) SiC polytypes exhibit strong anisotropy in electron mobility [58, 59].
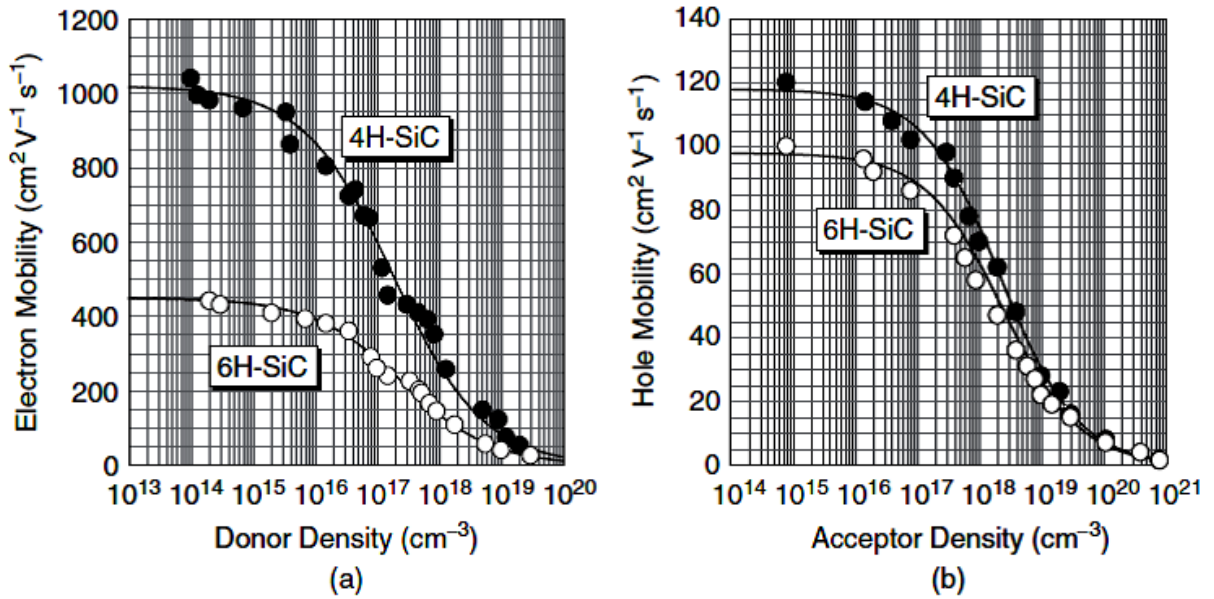
Figure 1.13. (a) Low-field electron mobility versus donor density and (b) hole mobility versus acceptor density for 4H-SiC and 6H-SiC at room temperature.

The data shown in figure (1.13) are mobilities perpendicular to the c-axis. The anisotropy is particularly notable in 6H-SiC, where the electron mobility along the c-axis direction is only $20 - 25\%$ of that perpendicular to the c-axis (the maximum electron mobility along the c-axis is about $100\ \mathrm{cm^2V^{-1}s^{-1}}$ in 6H-SiC at room temperature) [58].

The mobility anisotropy is relatively small in 4H-SiC, where the electron mobility along the c-axis direction is approximately $1200\ \mathrm{cm^2V^{-1}s^{-1}}$ at room temperature, which is 20% higher than that perpendicular to the c-axis. This is one of the major reasons why 4H-SiC is the most attractive polytype for vertical power devices fabricated on SiC{0001} wafers. The bulk mobility in 3C-SiC is isotropic. The electron mobility in lightly doped 3C-SiC is $750\ \mathrm{cm^2V^{-1}s^{-1}}$ in experiments [60] and is predicted to be $1000\ \mathrm{cm^2V^{-1}s^{-1}}$ in high-quality material [41].

In nondegen- erate semiconductors, the diffusion coefficients of carriers (D) can be obtained by using the Einstein relation [56]:

$$D = \frac{kT}{q}\mu \tag{1.14}$$

Here q is the elementary charge. If the carrier lifetime τ is given, the diffusion length is given by $L = (D\tau)^{1/2}$.

Figure 1.14 (a) Low-field electron mobility versus donor density and (b) hole mobility versus acceptor density for 4H-SiC at different temperatures.
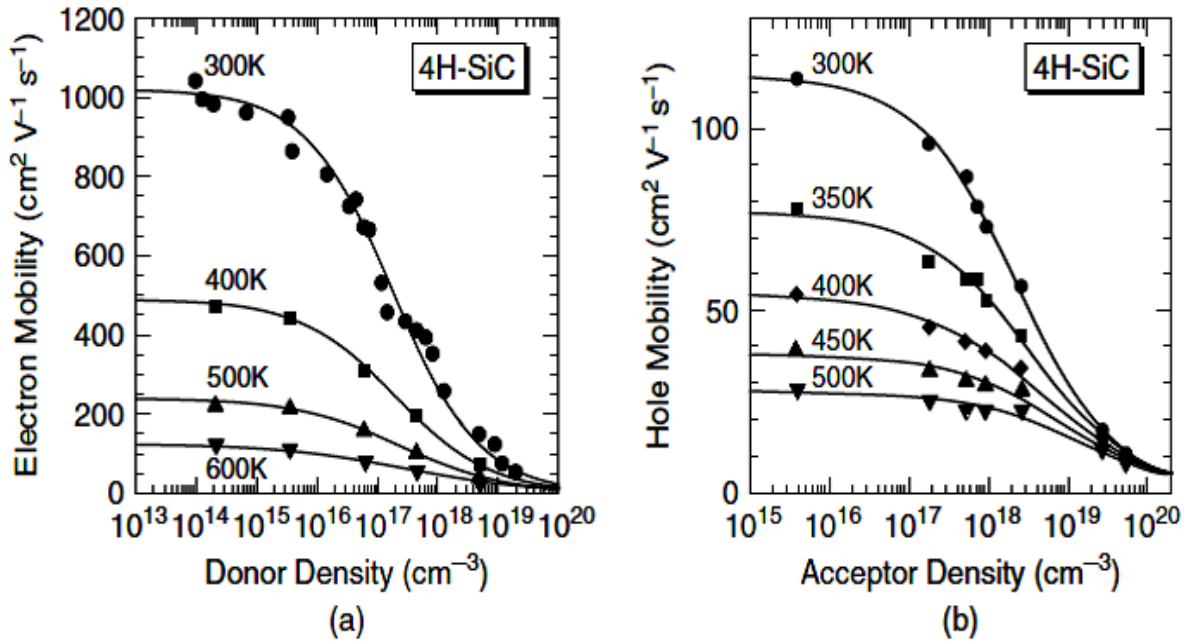
Figure 1.14. (a) Low-field electron mobility versus donor density and (b) hole mobility versus acceptor density for 4H-SiC at different temperatures [29].

Figure (1.14) shows (a) the low-field electron mobility versus donor density and (b) the hole mobility versus acceptor density for 4H-SiC at different temperature.

At high temperature, the doping dependence of mobility becomes small, because the influence of impurity scattering decreases. In general, the temperature dependence of mobility is discussed by using a relationship of $\mu \sim T^{-n}$, where μ is the mobility and T the absolute temperature.

As seen from figure (1.14), the value n depends strongly on the doping density, since the dominant scattering mechanism varies for SiC with different doping density. For example, the n value is 2.6 for lightly-doped and 1.5 for highly-doped n-type 4H-SiC.

Figure (1.15) shows the resistivity versus doping density at 300 K for nitrogen- or aluminum-doped 4H-SiC [55]. In very heavily doped materials, the resistivity decreases to 0.003 Ω cm for n-type and 0.018 Ω cm for p-type.

Note that the data shown in figure (1.15) are obtained in high-quality epitaxial layers. In ion-implanted SiC, where a high density of point and extended defects is created, the resistivity is significantly higher than that shown in the figure for any given doping density. Substrates grown by sublimation (or other techniques) also show higher resistivities than those shown in figure (1.15) because of a higher density of unwanted impurities and point defects.
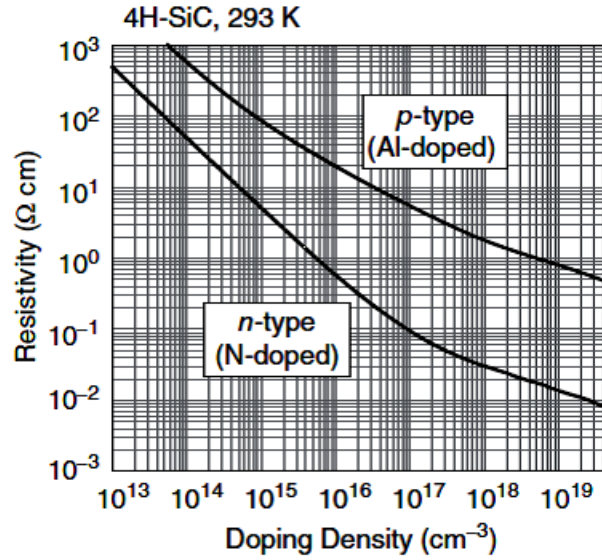
Figure 1.15. Resistivity versus doping density at 293 K for nitrogen- or aluminum-doped 4H-SiC [29].

The temperature dependence of electron mobility in nitrogen-doped 4H-SiC is shown in figure (1.16), for donor densities of (a) 3.5×10^{15} cm^{-3} and (b) 7.5×10^{17} cm^{-3}[29]. Carrier scattering processes include acoustic-phonon scattering (ac), polar-optical-phonon scattering (pop), nonpolar-optical-phonon scattering (n_{po}), intervalley scattering by phonons (i$_{ph}$), ionized-impurity scattering (ii), and neutral-impurity scattering (n_i). In the figures, electron mobility determined by each scattering process is indicated, and the total mobility (μ) is approximately expressed according to Matthiessen's rule [62]:

$$\frac{1}{\mu} \cong \sum_i \frac{1}{\mu_i} \tag{1.15}$$
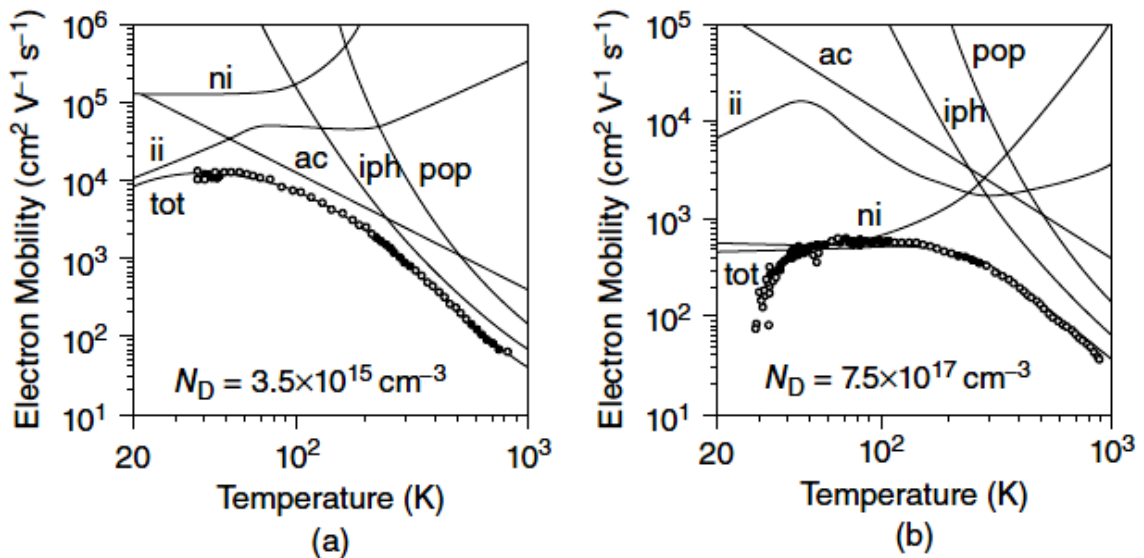
Figure 1.16. Temperature dependence of electron mobility in nitrogen-doped 4H-SiC for donor densi- ties of (a) 3.5×10^{15} cm^{-3} and (b) 7.5×10^{17} cm^{-3}[29].

In lightly-doped n-type SiC, the electron mobility is mainly determined by acoustic phonon scattering at low temperature (70 – 200 K) and by intervalley scattering at temperatures higher than 300 K, which is similar to the case of Si. In heavily-doped n-type SiC, the major scattering process is neutral impurity scattering at low temperature and intervalley scattering at high temperature.

Figure (1.17) shows the temperature dependence of hole mobility in aluminum-doped 4H-SiC with acceptor densities of (a) 1.8×10^{17} cm^{-3} and (b) 2.7×10^{19} cm^{-3} [29]. Mobilities determined by several scattering processes are also plotted. In moderately-doped p-type SiC, the hole mobility is mainly determined by acoustic phonon scattering at or below room temperature, and by nonpolar optical phonon scattering at high temperature (>400 K). In heavily-doped p-type SiC, the major scattering process is neutral impurity scattering over a wide temperature range, since most Al acceptors remain neutral because of their large ionization energy.
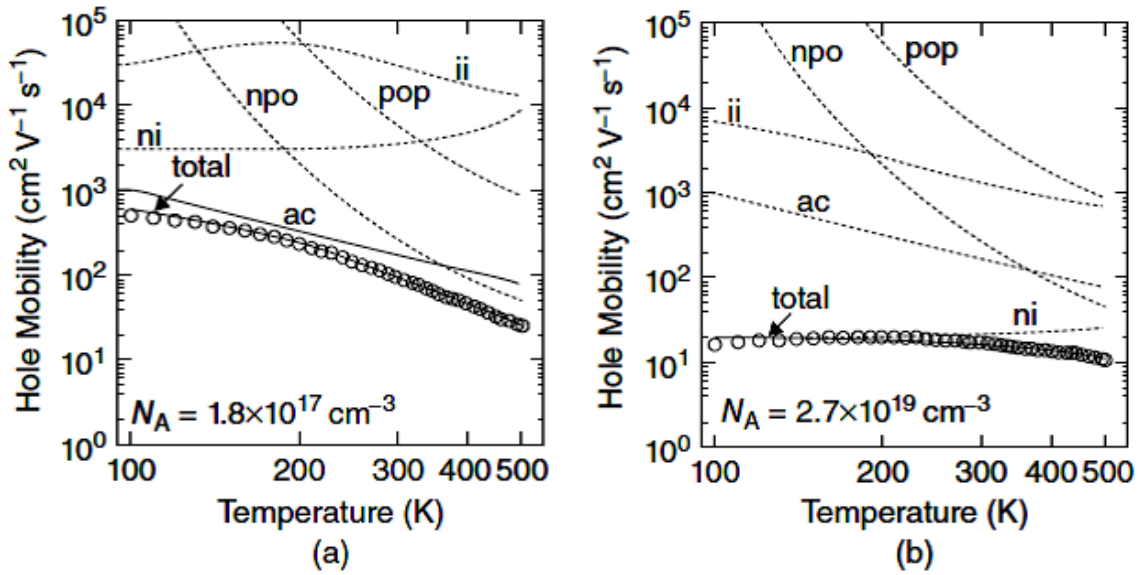
Figure 1.17. Temperature dependence of hole mobility in aluminum-doped 4H-SiC with acceptor densities of (a) 1.8×10^{17} cm^{-3} and (b) 2.7×10^{19} cm^{-3}[29].

1.3.2.5.   Drift Velocity

At low electric fields, the drift velocity of carriers (vd) is proportional to the electric field strength (E), $v_d = \mu E$. When the electric field is high, the accelerated carriers transfer more energy to the lattice by emitting more phonons, leading to nonlinear field dependence of drift velocity. The electric field dependence of the drift velocity is expressed by [62]:

$$v_d = \frac{\mu E}{\left\{1 + \left(\frac{\mu E}{v_s}\right)^\gamma\right\}^{1/\gamma}} \qquad (1.16)$$

where v_s is the sound velocity in a semiconductor and γ the parameter. At sufficiently high electric fields, carriers start to interact with optical phonons, and finally the drift velocity becomes saturated. The saturated drift velocity (v_{sat}) is approximately given by [56, 62]:

$$v_{sat} = \sqrt{\frac{8\hbar\omega}{3\pi m^*}}$$

(1.17)

where $\hbar\omega$ is the energy of the optical phonon (LO (longitudinal optical) phonon) emitted. Figure (1.18) shows the measured drift velocity of electrons versus applied electric field for n-type (a) 4H-SiC and (b) 6H-SiC [63]. The measurements were conducted in a structure carefully designed to minimize inaccuracy in potential distribution. For 4H-SiC, a low-field mobility of 450 $cm^2V^{-1}s^{-1}$ was determined from the slope at low electric fields (<104 V cm^{-1}) at room temperature; this agrees with the data shown in figure (1.13) for the donor density (2×10^{17} cm^{-3}) of this particular sample. The saturated drift velocity is determined as 2.2×10^7 cm s^{-1} at room temperature. This value is also in good agreement with that estimated from Equation 1.17. As indicated in figure (1.18), the saturated drift velocity decreases with increasing temperature. Note that a so-called transferred-electron effect (Gunn effect) is not observed in SiC because of its indirect band structure. The saturated drift velocity of electrons in 6H-SiC is experimentally estimated as 1.9×10^7 cm s^{-1} [63]. Although the saturated drift velocity of holes in SiC has not been experimentally studied, it can be estimated at 1.3×10^7 cm s^{-1} for 4H-SiC from Equation 1.17.
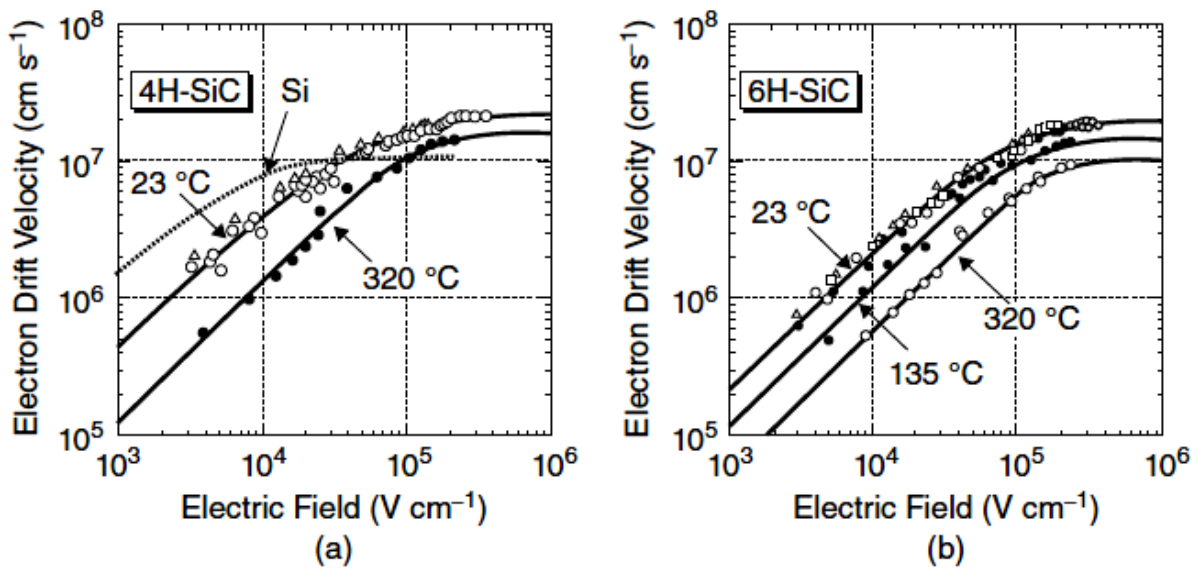
Figure 1.18. Drift velocity of electrons versus applied electric field for n-type (a) 4H-SiC and (b) 6H-SiC [63].

1.3.2.6. Breakdown Electric Field Strength

When a very high electric field is applied to a pn junction or Schottky barrier in the reverse-bias direction, the leakage current increases as a result of generation of electron – hole pairs, and the junction eventu- ally breaks down. The breakdown mechanisms can be classified into (I) avalanche breakdown and (II) Zener (tunneling) breakdown [56, 65]. For junctions with a lightly-doped region, avalanche breakdown is dominant; this is the case for most power devices. In avalanche breakdown, the carriers can gain enough energy under very high electric fields to excite electron – hole pairs by impact ionization. The generation of electron – hole pairs is multiplied inside the space-charge region of a junction, eventually leading to breakdown.

Avalanche breakdown is well described by using the impact ionization coefficients of electrons and holes. Breakdown can be defined as when the multiplication factor of the current approaches infinity, which has been shown to be equivalent to the following relationship [56, 65]:

$$\int_0^w \alpha_h \, exp\left\{-\int_0^x (\alpha_h - \alpha_e)dx^{'}\right\}dx \tag{1.18}$$

Here, α_e and α_h are the impact ionization coefficients for electrons and holes, respectively. Integration is performed in the space charge region extending from x = 0 to x = W. The integral term of the equation is called the ionization integral. Because the impact ionization coefficients depend strongly on the electric field strength, and the field strength is not uniform inside the space-charge region, numerical calculation is required to obtain the ionization integral given by Equation 1.18. Conversely, the impact ionization coefficients can be determined by measuring the multiplication factor as a function of electric field in properly designed pn junction diodes. In the measurements, light illumination is employed to increase the current at low reverse-bias voltages, and thereby to minimize the influence of nonideal leakage current. This is important for accurate determination of the multiplication factors. In general, the impact ionization coefficients are approximately expressed by the Chynoweth equation [66]:

$$\alpha_i = a_i \, exp\left(-\frac{b_i}{E}\right), (i: e \; or \; h) \tag{1.19}$$

where a_i and b_i are the parameters and E the electric field strength.

Figure (1.19) shows the impact ionization coefficients for electrons and holes in 4H-SiC versus the inverse of electric field strength [67].
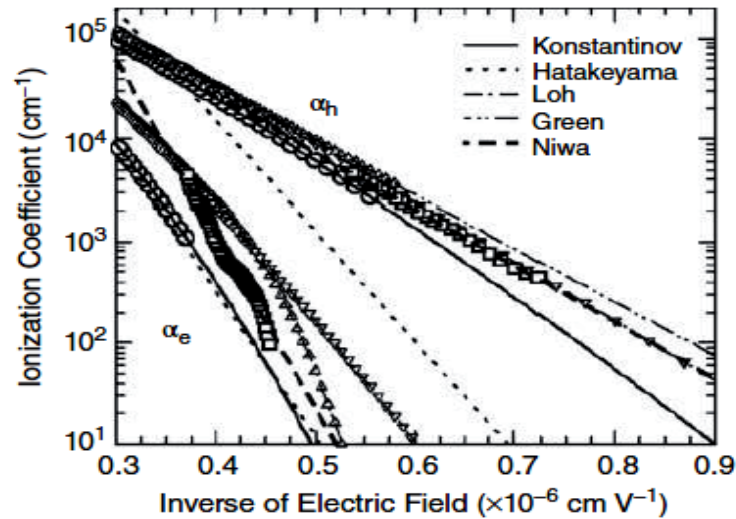
Figure 1.19. Impact ionization coefficients for electrons and holes in 4H-SiC versus the inverse of elec- tric field strength [67 , 68].

Different groups have reported similar but slightly different impact ionization coefficients. The ionization coefficients for 4H-SiC are considerably lower than those for Si owing to the wide bandgap of SiC. Another striking feature of figure (1.19) is that the ionization coefficient for holes is much larger than that for electrons ($\alpha h > \alpha e$) in SiC, which is completely opposite to the case of Si ($\alpha e > \alpha h$). In 4H-SiC, the energy range of the conduction band is rather small because of the folding effect in the $E - k$ relationship, and the highest energy of hot electrons is limited by the upper edge of the conduction band [68, 69]. This may be the reason why the ionization coefficient for electrons is unusually low in 4H-SiC (and in 6H-SiC). Note that the data shown in figure (1.19) are extrapolated from several experimental data sets. In particular, the ionization coefficients at relatively low electric fields need more careful investigation. The temperature dependence of the coefficients has been recently reported. It should also be noted that all data in figure (1.19) are valid along the <0001> direction because they were obtained from 4H-SiC pn diodes on off-axis {0001} substrates. Since the carrier acceleration and scattering are strongly influenced by the energy band structure, the impact ionization coefficients depend on the crystallographic orientation. In particular, hexagonal SiC polytypes exhibit strong anisotropy in impact ionization and breakdown characteristics [68, 69].

A semiconductor junction breaks down when the maximum electric field strength reaches a critical value which is inherent to the material. This critical value is called the critical electric field strength or breakdown electric field strength. The critical electric field strength EB can be determined by calculation of the ionization integral using the impact ionization coefficients described above. Alternatively, it can be obtained experimentally from the breakdown characteristics of devices in which electric field crowding is perfectly suppressed. In n-type

Schottky barrier diodes or a one-sided p+n junction, the breakdown voltage VB is given by [56, 57]:

$$V_B = \frac{\varepsilon_s E_B{}^2}{2qN_D}$$

(1. 20)

Here a non-punch through structure is considered. εs is the dielectric constant of a semiconductor.

Figure (1.20) shows the critical electric field strength versus doping density for 4H-SiC <0001>, 6H-SiC <0001>, and 3C-SiC <111> [66, 67, 70, 71]. The data for Si are also shown for comparison. 4H- and 6H-SiC exhibit approximately eight times higher critical electric field strengths than Si at a given doping density, while the field strength of 3C-SiC is only three or four times higher because this polytype has a relatively small bandgap (similar to GaP).

The high critical field strength of hexagonal SiC polytypes is the main reason why SiC is very attractive for power device applications [71]. One must be aware of the fact that the critical field strength is strongly dependent on the doping density, as shown in figure (1.20). When the doping density is increased, the width of the space-charge region becomes small and the distance for carriers to be accelerated becomes short. Furthermore, the mobility is reduced in highly-doped materials because of enhanced impurity scattering. These are the reasons why the critical electric field strength apparently increases with increasing doping. As shown in figure (1.20), the critical electric field of 6H-SiC <0001> is slightly higher than that of 4H-SiC <0001>, in spite of its smaller bandgap (Eg = 3.02 eV for 6H-SiC and 3.26 eV for 4H-SiC). As described in Section 1.3.2.4, 6H-SiC exhibits strong anisotropy in carrier transport, and the electron mobility along the <0001> direction is unusually low, about 100 $\mathrm{cm}^2\mathrm{V}^{-1}\mathrm{s}^{-1}$ even in a high-purity material.

The narrow width of the conduction band in 6H-SiC also helps to increase the critical electric field strength of 6H-SiC <0001>. Conversely, it is known that the critical field strength of 6H-SiC <1120> is only half that of 6H-SiC <0001> [68]. The anisotropy in critical field strength of 4H-SiC is smaller, and the field strength of 4H-SiC <1120> is only 20 − 25% lower than that of 4H-SiC <0001> [69].

The critical field strength is a convenient physical property when the ideal breakdown voltage is estimated. However, it should be noted that the critical field strength is valid only for junctions with non-punchthrough structures. When punchthrough structures are considered, the critical field strength shown in figure (1.20) does not give the correct breakdown voltage. In this case, simulation of leakage current or calculation of the ionization integral using a device simulator is required to determine the ideal breakdown voltage.
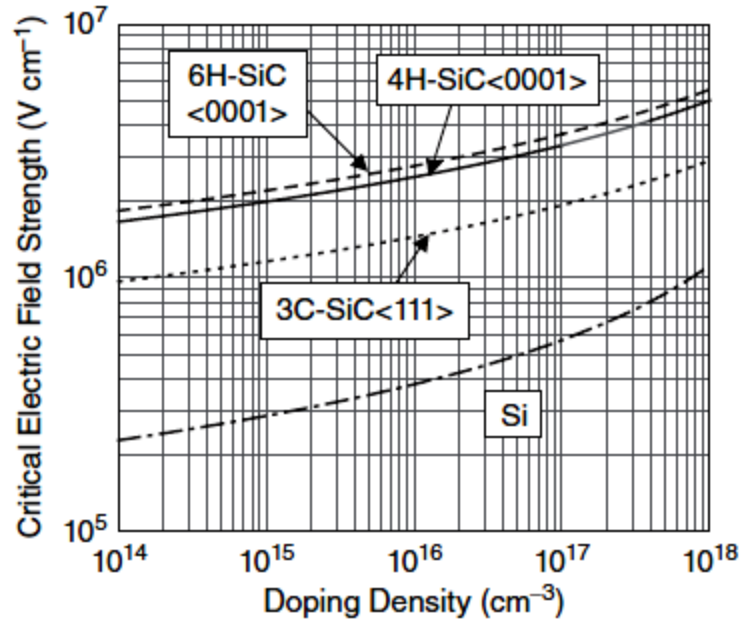
Figure 1.20. Critical electric field strength versus doping density for 4H-SiC <0001>, 6H-SiC <0001>, and 3C-SiC <111> [66, 67, 70, 71].

1.3.3.   Thermal and Mechanical Properties

1.3.3.1.   Thermal Conductivity
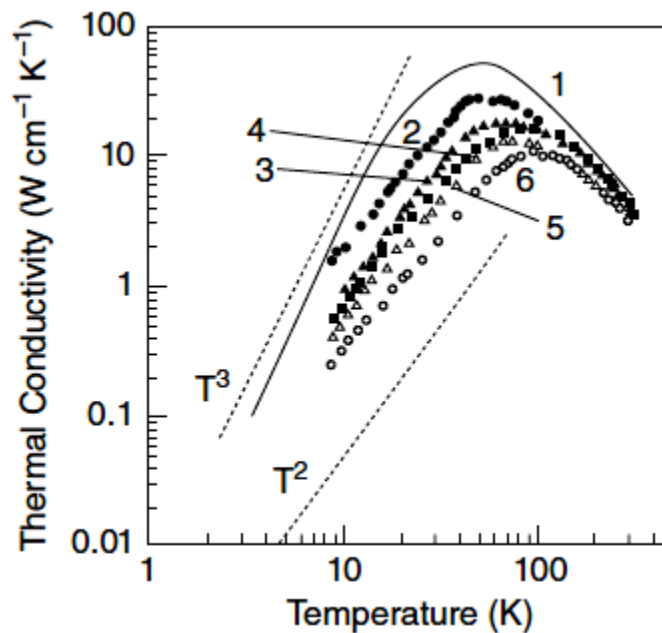
Figure 1.21. Temperature dependence of thermal conductivity for SiC and Si [72].

Figure (1.21) shows the temperature dependence of thermal conductivity for SiC and Si [72]. SiC, with its significant contribution from phonons, has a much higher thermal conductivity (4.9W cm^{-1} K^{-1} for high-purity SiC at room temperature) than Si. It has been reported that the thermal conductivity is not sensitive to the SiC polytype, but depends on the doping density and

25

the crystal direction. In heavily-nitrogen-doped 4H-SiC substrates, which are usually employed as n+-substrates for vertical power devices, the thermal conductivity along <0001> is 3.3W cm^{-1} K^{-1} at room temperature [73].

1.3.3.2.   **Phonons**

Figure (1.22) shows the phonon dispersion relationships for (a) 3C-SiC and (b) 4H-SiC [74, 75]. The basic branches consist of TA (transverse acoustic), LA (longitudinal acoustic), TO (transverse optical), and LO phonons, as in other semiconductors. Due to the large energy of Si-C bonds, the phonon frequencies in SiC are high. The unit cell length of the nH polytype (n = 2, 4, 6 …) along the c-axis is n times larger than the unit length (Si-C bilayer). Thus, the Brillouin zone in the direction of Γ− L is reduced to 1/n of the basic Brillouin zone. The dispersion curves of the phonons propagating along the <0001> direction in such polytypes can be approximated by folding the basic dispersion curve.This zone folding provides new phonon modes at the Γ point, which are called "folded modes." The number of atoms in the unit cell is 2 for 3C-SiC, 8 for 4H-SiC, and 12 for 6H-SiC. Therefore, the number of phonon branches is 6 for 3C-SiC, 24 for 4H-SiC, and 36 for 6H-SiC, neglecting the degeneracy.
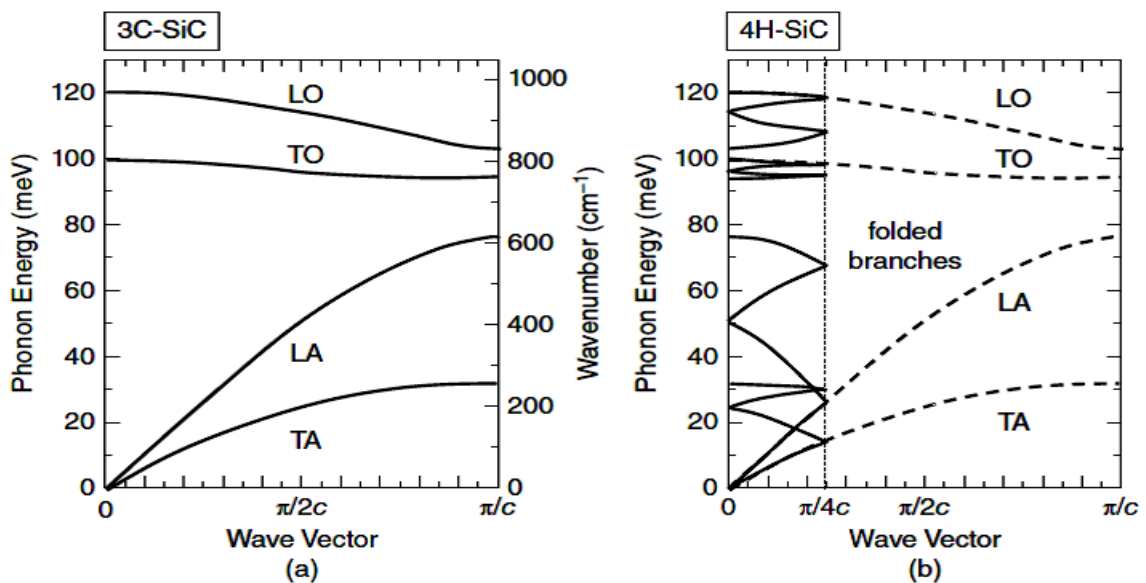
Figure 1.22. Phonon dispersion relationships for (a) 3C-SiC and (b) 4H-SiC [29].

The major phonon energies (or wave number) can be directly observed by Raman scattering spectroscopy. Different phonon frequencies in different SiC polytypes enable identification of individual polytypes by Raman scattering measurements [77].

It is known that the observed frequency of LO phonons increases with increasing carrier density because of a carrier − LO phonon coupling effect. Phonon energies are also important in

luminescence measurements. In particular, photoluminescence (PL) at low temperature is a powerful tool to characterize the purity and quality of SiC crystals [40, 76]. Because SiC has an indirect band structure, phonons are intensively involved in carrier recombination processes.

As a result, strong multiple phonon replicas of a zero-phonon emission line are often observed in PL spectra of SiC. For example, the energies of major phonons which create phonon replicas in PL from 4H-SiC{0001} are 36 (TA), 46, 51, 77 (LA), 95, 96 (TO), 104, and 107 meV (LO).

1.3.3.3.   Hardness and Mechanical Properties

The mechanical properties of SiC are also unique; SiC is one of the hardest known materials. Table 1.4 shows the major mechanical properties of SiC and Si [24, 42], where the polytype dependence is small. The hardness and Young's modulus (380 – 700 GPa [77]) of SiC are much higher than those of Si, while the Poisson's ratio (0.21) of SiC is very similar to that of other semiconductors. SiC retains its high hardness and elasticity, even at very high temperatures. The yield (fracture) strength of SiC is as high as 21 GPa at room temperature and is estimated to be 0.3 GPa at 1000 °C, while the yield strength of Si falls to 0.05 GPa at 500 °C [78].

Table 1.4 Major mechanical and thermal properties of SiC and Si at room temperature [24, 42].

Properties	4H- or 6H-SiC	Si
Density (g cm−3)	3.21	2.33
Young's modulus (GPa)	390 – 690	160
Fracture strength (GPa)	21	7
Poisson's ratio	0.21	0.22
Elastic constant (GPa)		
c11	501	166
c12	111	64
c13	52	–
c33	553	–
c44	163	80
Specific heat (J g^{-1} K^{-1})	0.69	0.7
Thermal conductivity (W cm^{-1} K^{-1})	3.3 – 4.9	1.4 – 1.5

1.4.   SiC Device Applications

SiC is a very hard material. This has resulted in a wide variety of applications already at the polycrystalline era. To make it a physicist's dream, SiC is also chemically inert and extremely radiation hard. It may thus be used in the most hostile environments, for example, near nuclear reactors and in outer space. Some of the properties of silicon carbide compared to some other semiconductors are listed in Table 1.5. It may be noticed that silicon is inferior to SiC in many respects. Diamond would be the ultimate semiconductor for power electronics, but problems related to its use appear to be even larger than in the case of SiC. There are also some other potential wide-bandgap semiconductors that compete with SiC, for example, gallium and aluminum nitride.

Table 1.5 Properties of silicon carbide compared to other some semiconductor materials.

Properties	Si	GaAs	Diamond	GaN	4H-SiC
Band gap, E_g (eV)	1.12	1.43	5.45	3.45	3.26
Dielectric Constant	11.9	13.1	5.5	9	9.76
Breakdown Electric Field (MV cm^{-1})	0.3	0.4	10	2.0	3
Electron Mobility (cm^2 V^{-1} s^{-1})	1350	8500	2200	1250	1020
Hole Mobility (cm^2 V^{-1} s^{-1})	480	400	850	850	120
Saturation Velocity (cm s^{-1})	1	1	2.7	2.2	2.7
Electron Affinity (eV)	4.05	4.07	depending on surfaces	4.1	3.3
Thermal conductivity (W cm^{-1} K^{-1})	1.5	0.46	22	1.3	4.9

Electronic devices based on SiC are suitable for high power and high frequency operations and due to better performance in power conversion and high switching speeds find applications in military, avionics, modern hybrid automobile power systems, uninterruptible power supplies, microwave and so on. Some of the major applications are discussed below.

1.4.1. Power Conversion

Major applications of SiC based electronic devices can be found in power conversion from DC-DC or from DC-AC. For switched mode DC-DC conversion, Schottky diodes are combined with inductors or capacitors in a circuit to either step up the input power or to step it down. Inductor transfers its stored energy through Schottky diodes during power conversion. DC-DC conversion finds widespread applications in industrial and consumer electronics. DC-AC conversion, on the other hand, uses multiple diodes coupled with inductors which transfer their stored energy through these diodes. DC-AC power conversion finds applications mostly in uninterruptible power supplies and motor speed control [30].

1.4.2. SiC Devices As Gas Sensors

Schottky barrier diodes (SBD) and FETs based on SiC can detect some important gases such as oxygen, hydrogen, carbon monoxide and hydrocarbons. When thin metal film of SiC Schottky contact is exposed to gases e.g. hydrogen the current-voltage characteristics of the SBD are affected within a few milliseconds of the exposure. This occurs due to the fact that the Schottky barrier height of the SBD changes when the device comes in contact with some of the gases to which the SiC SBDs are sensitive. SiC gas sensors find applications in automobiles and aircrafts for detecting the fuel leakage and for detecting fires [30].

1.4.3. UV Detection

Silicon carbide Schottky barrier diodes (SBD) are able to detect ultra-violet radiation (UV) in a better way than Si based UV detectors because of SiCs wide bandgap. Because of wide bandgap SiC based SBDs are insensitive to radiation with frequencies below UV and can detect exclusively ultraviolet light even in the presence of visible and infrared light. Silicon based gas sensors however, are sensitive to visible and infrared light too and show poor performance in their presence unless additional radiation filtering is provided [79].

1.4.4. Microwave Applications

Superior material properties of silicon carbide are also exploited for microwave applications. Due to better RF and dc performance SiC based electronic devices are preferred over devices based on conventional semiconductors such as silicon or gallium-arsenide. Devices based on SiC exhibit much better microwave power at room temperature than their Si and GaAs counterparts [80]. Use of 4H-SiC in microwave technology can result in low cost, high power and smaller sized devices with greater bandwidth control. For these reasons SiC MESFETs are

being designed for continuous wave applications through X band and SiC static induction transistors (SIT), for high power pulsed transmitter technology, through L band operation [81].

Chapter 2
Metal semiconductor contacts to SiC: Physics and Applications

2.1.Introduction

The physics and technology of metal/semiconductor interfaces are key-points in the development of silicon carbide (SiC) based devices. Although in the last decade, the metal to 4H-SiC contacts, either Ohmic or Schottky type, have been extensively investigated with important achievements, these remain even now an intriguing topic since metal contacts are fundamental bricks of all electronic devices. Hence, their comprehension is at the base of the improvement of the performances of simple devices and complex systems. In this context, this chapter aims to highlight some relevant aspects related to metal/semiconductor contacts to SiC, with an emphasis on the role of the barrier and on the carrier transport mechanisms at the interfaces. Selected examples of 4H-SiC schottky diode applications are also briefly discussed.

2.2. Homogeneous Schottky barrier formation models

2.2.1. Mott-Schottky model

The model proposes that the SBH between a metal and a semiconductor depend only on the work function of the metal $q\phi_M$ and the electron affinity of the semiconductor $q\chi$ [56,82]. as shown in figure (2.1).
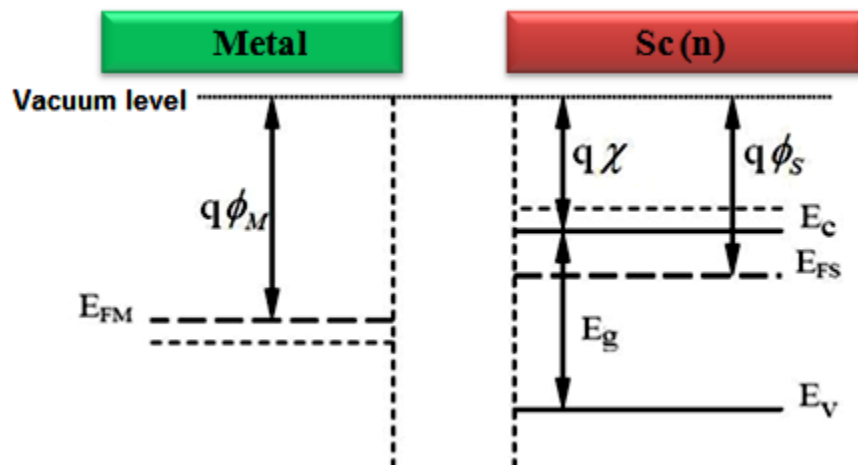
Figure 2.1. Energy band diagram of a metal adjacent to n-type semiconductor under thermal non equilibrium condition [82].

The work function of a material is defined as the minimal energy required to extract an electron from it. In term of energy levels, it is the difference between the Fermi level and vacuum level, and it is noted $q\phi_M$ for metals and $q\phi s$ for semiconductors. The work function of selected metals as measured in vacuum can be found in figure (2.2) [83].

$$q\emptyset_M = E_{vacuum} - E_{FM} \tag{2.1}$$

Because the Fermi level is in the forbidden gap in insulators and semiconductors; and which depends mainly on the semiconductor doping density, it is not worth to talk about the work function of a semiconductor. In this case, we must use another definition instead of the work function, which is the electronic affinity. It is the difference between the vacuum level and the minimum of the conduction band, and it is noted $q\chi$ where:

$$q\chi = E_{vacuum} - E_C \tag{2.2}$$
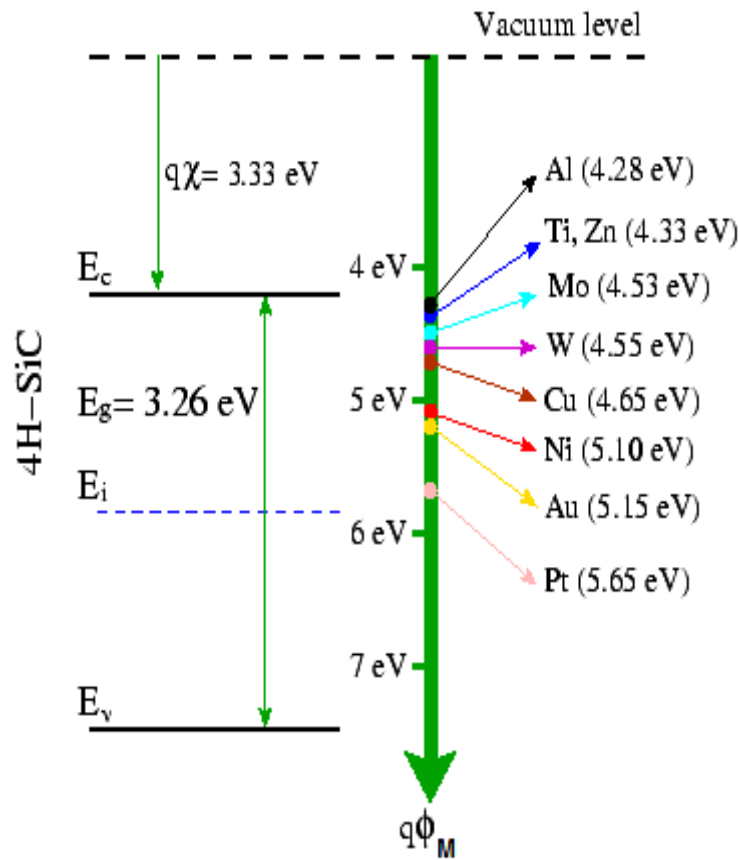
Figure 2.2. Energy band diagram of the selected metals and 4H-SiC [83].

2.2.1.1. Schottky barrier formation

A Metal-Semiconductor contact is formed when a metal and a semiconductor are brought into intimate contact with each other [82-84].

Figure (2.1) shows the energy band-diagram for an n-type semiconductor and metal, which are electrically neutral and isolated to each other, with the assumption that the work function of semiconductor ($q\phi_s$) is less than that of the metal work function ($q\phi_M$).
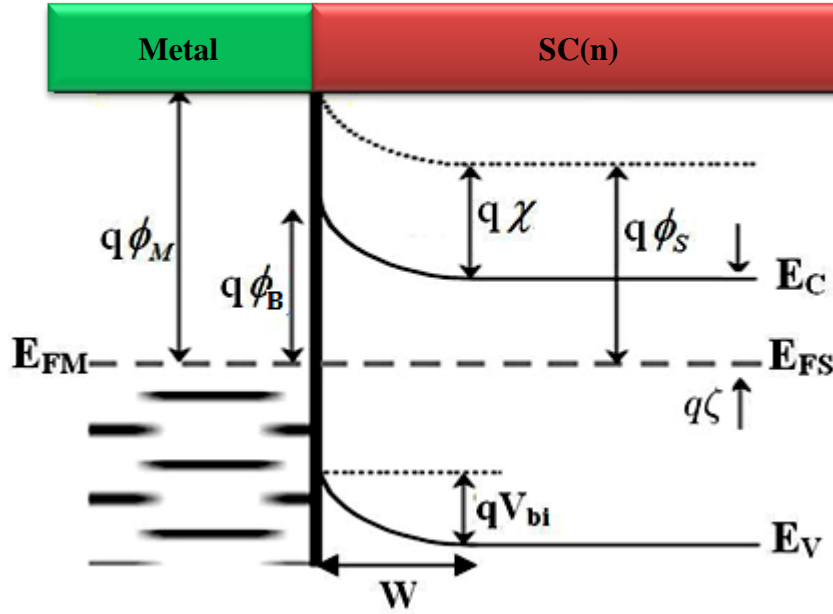
Figure 2.3. Energy band diagram of a metal semiconductor contact in thermal equilibrium [82]

When a metal is making intimate contact with 4H-SiC material, the Fermi levels in the two materials must be coincident at thermal equilibrium and the vacuum level must be continuous across the interface. In addition, the metal work function is different from that of the semiconductor. These two requirements determine a unique energy band diagram for an ideal metal-semiconductor contact where surface states are absent, as shown in figure (2.3) [82]. For this ideal case, the potential barrier, known as Schottky Barrier Height (SBH), at the metal-semiconductor interface is simply the difference between the metal work function $q\phi_M$ and the electron affinity of the semiconductor:

$$q\emptyset_B = q\emptyset_M - q\chi \qquad (2.3)$$

This equation is known as the Schottky-Mott Limit [56], and gives the limiting value for the barrier height in ideal metal-semiconductor contacts and is based on following assumptions:

a) The surface dipole contributions to ϕ_M and χ do not change when the metal and semiconductor are brought in contact with each other.

b) There are no localized states present on the surface of the semiconductor.

c) There is perfect contact between the metal and the semiconductor; i.e., there is no interfacial layer present between metal and semiconductor.

2.2.1.2. Space charge region

To determine the deserted area in n-type Schottky junction, first we consider that the charge density "ρ" in this area is equal to doping concentration "$(N_A^- - N_D^+)$" and equal to zero outside it [56,84]. Now we can determine the potential by using the one dimensional Poisson's equation:

$$\frac{d^2\rho(x)}{dx^2} = -\frac{\rho}{\varepsilon_s} \tag{2.4}$$

Where ε_s is the static dielectric constant of the Semiconductor.

By taking into account as a boundary conditions that the charge density "ρ" in the space-charge region is given by the doping density:

$$\rho(x) = q(N_D - N_A) \quad 0 \leq x \leq w \tag{2.5}$$

The electric field is then obtained by integrating the equation (2.4):

$$E(x) = -\frac{dV(x)}{dx} = \left(\frac{qN_D}{\varepsilon_0\varepsilon_s}\right)x + C_1 \tag{2.6}$$

The constants $C1$ can be determined using the following boundary conditions:

$$E(x) = 0 \quad x \geq w \tag{2.7}$$

By substituting $C1$ into equation (2.6), one obtains the spatial distributions of the electric field inside the depletion region, which is given by:

$$E(x) = \left(\frac{qN_D}{\varepsilon_0\varepsilon_s}\right)(x - w) \tag{2.8}$$

The potential distribution can be obtained by integrating equation (2.8) taking the interface as the potentials origin, which yields:

$$V(x) = -\left(\frac{qN_D}{\varepsilon_0\varepsilon_s}\right)\left(\frac{x^2}{2} - wx\right) \tag{2.9}$$

The depletion layer width w can be expressed in terms of N_D, V_{bi} (built-in voltage), and V_a (applied voltage) across the barrier. From equation (2.9) one obtains the potential at $x = w$ as:

$$V(x = w) = V_{bi} - V_a = \frac{qN_Dw^2}{\varepsilon_0\varepsilon_s} \tag{2.10}$$

From equation (2.10), the depletion layer width w is given by:

$$W = \sqrt{\frac{2\varepsilon_0\varepsilon_s(V_{bi} - V_a)}{qN_D}} \tag{2.11}$$

It is seen from equation (2.11) that the depletion layer width is directly proportional to the square root of the applied voltage (Va), and is inversely proportional to the square root of the dopant density of the semiconductor. Furthermore, equation (2.11) shows that the depletion layer width decreases with the square root of the forward-bias voltage (i.e., for Va $\geq$ 0), and increases with the square root of the reverse-bias voltage (i.e., for Va < 0) [56, 84].

The previous approximation is valid for $V_{bi}kT/q \gg 1$. Therefore, equation (2.11) is corrected to:

$$W = \sqrt{\frac{2\varepsilon_0\varepsilon_s\left(V_{bi} - V_a - \frac{kT}{q}\right)}{qN_D}} \tag{2.12}$$

2.2.1.3. Capacitance

To calculate the capacitance the charge density stored in the space charge region which is mainly due to ionized dopant atoms must be defined first. So, the charge density per unit surface at the thermodynamic equilibrium is given by:

$$Q = qN_DW = \sqrt{2qN_D\varepsilon_0\varepsilon_s\left(V_{bi} - V_a - \frac{kT}{q}\right)} \tag{2.13}$$

To take into account the charges resulting from the traps in the depletion region, N_D must be replaced by N_{SCR} (ionized impurity in the space charge region). $N_{SCR} = N_D^+ \pm (n, p)_T^{-,+}$, where n_T^- are deep-level or shallow-level acceptors occupied by electrons, and P_T^+ are deep-level or shallow-level donors occupied by holes [56].

The depletion layer capacitance (junction capacitance) per unit area can be obtained by differentiating equation (2.13) with respect to the applied voltage ($C=|dQ/dV|$), which yields

$$C_d = \frac{dQ}{dV_a} = \sqrt{\frac{qN_{SCR}\varepsilon_0\varepsilon_s}{2\left(V_{bi} - V_a - \frac{kT}{q}\right)}} \tag{2.14}$$

Equation (2.14) can also be written as:

$$\frac{1}{{C_d}^2} = \frac{2\left(V_{bi} - V_a - \frac{kT}{q}\right)}{q\, N_{\text{SCR}}\, \varepsilon_0 \varepsilon_s} \tag{2.15}$$

By plotting $1/{C_d}^2$ as a function of applied voltage we can find the doping concentration and built-in voltage V_{bi}. If the doping concentration is homogeneous the plot should be linear. $V_{bi} = V' + (kT/q)$, where V' is the extrapolation to the voltage axis such that $1/C_d = 0$. The doping concentration can be determined from the slop via [56].

$$N_{SCR} = \frac{2}{q\varepsilon_0 \varepsilon_s} \left[\frac{1}{d{C_d}^2 \big/ dV} \right] \tag{2.16}$$

2.2.2. Bardeen model

The Schottky-Mott theory suggests that the barrier height is a function of the metal work function and the electron affinity of the semiconductor. However, it is practically found that the barrier height is a less sensitive function of the metal work function and in some situation is almost independent of ϕ_M [82, 84]. A possible cause of this discrepancy was given by Bardeen in 1947, who suggested that the discrepancy may be due to the effect of surface states [85]. Figure (2.4) illustrates a Schottky contact with the presence of a thin interfacial and there is a continuous distribution of surface states present at the surface of semiconductor and characterized by a neutral level ϕ_0.

The occupancy of the surface states is determined by the Fermi level which is constant throughout the barrier region in the absence of applied bias. If the neutral level ϕ_0 is above the Fermi level E_F, the surface states contain a net positive charge. On the other hand, if ϕ_0 is below E_F, then the surface states have a net negative charge. The surface states behave like a negative feedback loop, the error signal of which is the deviation of ϕ_0 from E_F. If the density of surface states becomes very large, the error signal will be very small and $\phi_0 \approx E_F$. As a result, the barrier height is determined by the property of the semiconductor surface and not the metal work function. When this state is reached, the barrier height is said to be "pinned" by the high density of the surface states.

This is called the Bardeen Limit and when it is reached, the surface states screen the semiconductor from the electric field in the insulating layer so that the amount of charge in the

depletion region and the barrier height is independent of the metal work function ϕ_M. The Bardeen Limit is given by:

$$\emptyset_B = \frac{E_g}{q} - \emptyset_0 \tag{2.17}$$

The Schottky-Mott Limit and the Bardeen Limit are the two limiting cases for the barrier height $\emptyset_B$, for M/S contacts. Usually, the actual Schottky Barrier Height falls somewhere between the Schottky-Mott Limit and the Bardeen Limit [82, 84]..
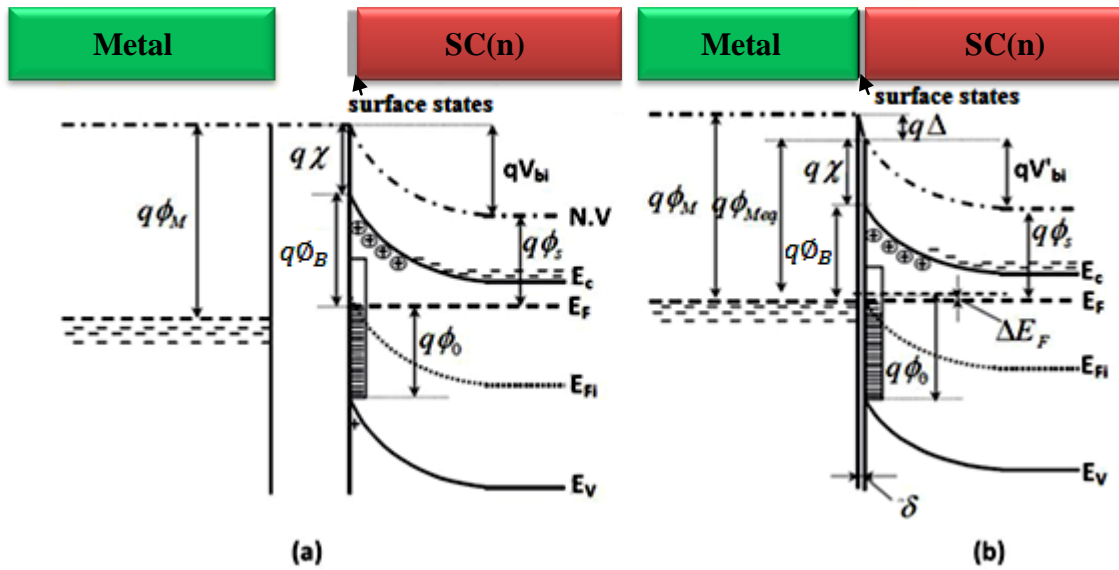
Figure 2.4. Band diagram of a metal and n-type semiconductor with surface states (a) before the contact and (b) after the contact with an interfacial layer of width δ. The interface states are assumed to have a charge neutrality level Φ_0 [84].

2.2.3. Cowley et Sze model

A.M.Cowley et S.M.Sze [86], developed a more realistic model, which take into account the effect of both surface states, the metal work function on the SBH and the interface dipole.

Cowley and Sze was derived based on the following assumptions: (1) the contact between the metal and the semiconductor has an interfacial layer of the order of atomic dimensions; it is further assumed that this layer is transparent to electrons with energy greater than the potential barrier but can with stand potential across it. (2) The surface state density (per unit area per electron volt) at the interface is a property only of the semiconductor surface and is independent of the metal. The schematic shown in figure (2.5) is the energy band diagram illustrating model [82,84].

Where $\emptyset_M$ is the work function of metal, $\emptyset_B$ is the barrier height without image force lowering, $\emptyset_0$ is the neutral level of interface states, Δ is the potential across interfacial layer, χ is the electron affinity of semiconductor, V_{bi} is the built-in potential, δ is the interfacial layer thickness, Q_{sc} space charge density in semiconductor, Q_{ss} interface trap charge, Q_M surface charge density on metal, D_{it} interface trap density and ε_i is the interface layer permittivity.
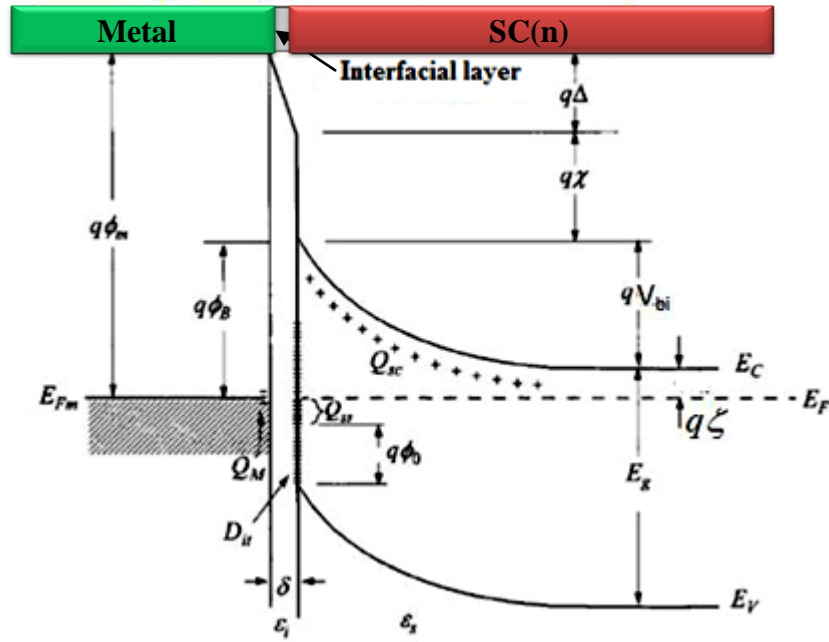
Figure 2.5. Energy band diagram of Metal-n-type semiconductor based on Cowley and Sze model [82,84].

With the above assumptions, the barrier height for n-type semiconductor-metal contacts is found to be a linear combination of the metal work function Φ_M and a quantity Φ_0, which is defined as the energy below which the surface states must be filled for charge neutrality at the semiconductor surface. For constant surface state density the theoretical expression obtained is [84]:

$$\emptyset_B = \gamma(\emptyset_M - x_{sc}) + (1 - \gamma)\left(\frac{E_g}{q} - \emptyset_0\right) \tag{2.18}$$

Where γ is equivalent to the interface behavior parameter $S = \dfrac{\partial \emptyset_B}{\partial \emptyset_M}$

$$\gamma = \frac{\partial \emptyset_{Bn}}{\partial \emptyset_M} = \frac{\varepsilon_i}{\varepsilon_i + q\delta D_{it}} \tag{2.19}$$

For a high density of states ($\gamma \ll 1$), the second term on the right hand side of equation (2.18) dominates and the Fermi-level will pinned by interface states close to the level Φ_0. In the

case where interface states are neglected, ($\gamma \simeq 1$) and SBH equation is identical to Mott-Schottky equation (ideal diode).

2.2.4. Metal induced gap states model

Metal induced gap states (MIGS) is the first interactive model developed by V. Heine in 1965 [87], he started from assumption that vacuum cleaved surface cannot contain a high density interface states which can pin the Fermi level. The interaction between the metal and semiconductor was expressed by the overlap of wave function at a MS interface, this overlap of wave function alter the electronic structure and the charge distribution in the ISR and induce electronic states in the band gap of the semiconductor. This theory does not take into account the atomic structure and bonding at the interface [84].
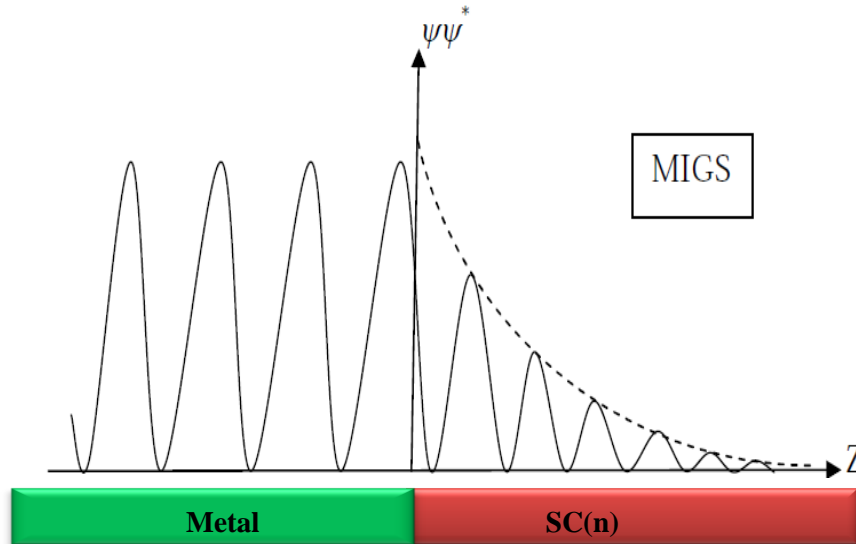
Figure 2.6. Schematic representation of the wave function at metal-semiconductor interface illustrating MIGS concept [88].

2.2.5. Unified defect model (UDM)

Spicer and co-workers [89] proposed that defects are generated near the semiconductor surface when the contact metal is deposited on that surface. These defects in turn lead to pinning of the Fermi-level. This is called the unified defect model (UDM).

Hughes [90] suggested that the pinning is caused by extrinsic defects in the semiconductor resulting from the incorporation of impurities or the deposited metal atoms into the semiconductor lattice. "Dangling bonds" at incoherent or semi-coherent metal-semiconductor interfaces were also suggested to be responsible for the Fermi-level pinning [91].

2.2.6. Image force barrier lowering of the Schottky barrier

The presence of a free porter (electron) in the semiconductor near the metal contacts leads to the creation of an attractive force by electrostatic effect and thus an electric field. This field induces a potential difference and therefore a change in the energy diagram. Because the created force is attractive, the potential difference created is negative, thus corresponds to a lowering of the existing barrier. This lowering is known as the image-force lowering or the Schottky effect [84].

Consider a metal-vacuum system first. The minimum energy necessary for an electron to escape into vacuum from an initial energy at the Fermi level is the work function Φ_m as shown in figure (2.7). When an electron is at a distance x from the metal, a positive charge will be induced on the surface of metal. The force of attraction between the electron and induced positive charge is equivalent to the force that would exist between electron and an equal positive charge located at position –x, which is referred to as image charge. The force of attraction between electron and its image charge can be expressed as [56, 82, 84]:

$$F(x) = \frac{q^2}{4\pi\varepsilon_0(2x)^2} \tag{2. 20}$$

where ε_0 is the permittivity of free space. The work done to an electron in the course of its transfer from infinity to the point x is given by

$$E(x) = -\frac{q^2}{16\pi\varepsilon_d x} \tag{2.21}$$

This energy corresponds to the potential energy of an electron placed at a distance x from the metal surface, shown in figure (2.7), and is measured downwards from the *x*-axis. When an external field ξ is applied (in this example in the -*x* direction), the total potential energy *PE* as a function of distance is given by the sum

$$PE(x) = -\frac{q^2}{16\pi\varepsilon_0 x} - q|\xi|x \tag{2.22}$$

This equation has a maximum value. The image-force lowering $\Delta\Phi$ and the location of the lowering *x*, (as shown in figure (2.7)), are given by the condition *d(PE) /dx* = 0, or

$$x_m = \sqrt{\frac{q}{16\pi\varepsilon_0|\xi|}} \tag{2.23}$$

$$\Delta\emptyset = \sqrt{\frac{q|\xi|}{4\pi\varepsilon_0}} = 2|\xi| \tag{2.24}$$

These results can be applied to metal-semiconductor systems. However, the field should be replaced by the appropriate field at the interface, and the free-space permittivity ε_0 should be replaced by an appropriate permittivity ε_s characterizing the semiconductor medium [84], that is, so,

$$\Delta\emptyset = \sqrt{\frac{q\xi_m}{4\pi\varepsilon_s}} = \left[\frac{q^3 N_D}{8\pi^2 \varepsilon_s^3}\left(\emptyset_B - V - \zeta - \frac{kT}{q}\right)\right]^{1/4} \tag{2.25}$$
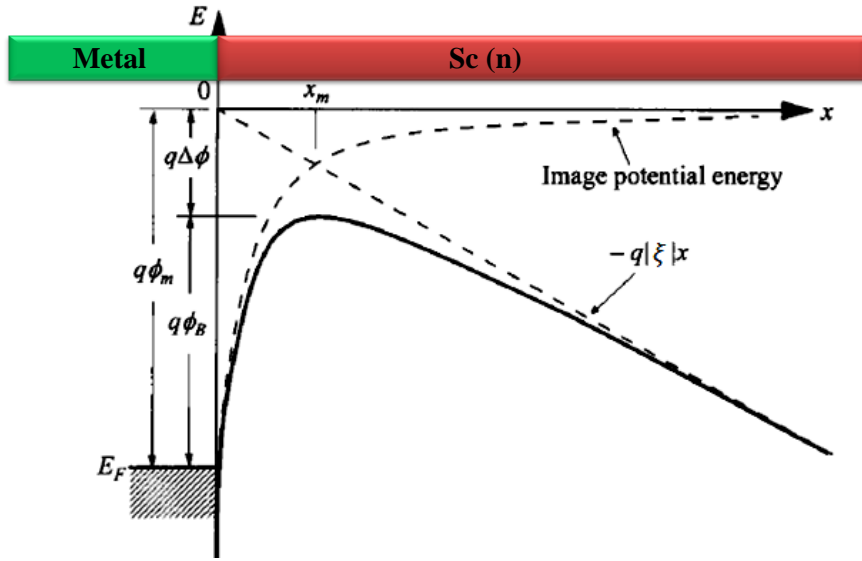
Figure 2.7. Image force barrier lowering in Schottky barrier diodes [82,84].

The effect of the image force is that the barrier which an electron has to surmount in passing from the metal into the semiconductor is lowered by an amount $\Delta\emptyset$ The image-force lowering differs from the other contributions to $\emptyset_B$ in that it arises from the field produced by the particular electron under consideration and is absent if there is no electron in the conduction band near the top of the barrier. On the other hand, contributions to $\emptyset_B$ from the work-function difference, surface state charge, and so on, are present whether or not there is an electron near the top of the barrier. We shall use $\emptyset_B$ to denote the barrier height arising from the latter causes, and will denote the image-force lowering explicitly by the quantity $\Delta\emptyset$.

Measurements of the barrier height which depend on the movement of conduction electrons from metal to semiconductor or vice versa yield the quantity $\emptyset_B - \Delta\emptyset$, whereas measurements which depend on the space charge in the depletion region (e.g. capacitance measurements) give without the effect of the image force [84].

2.2.7. Current conduction mechanism

The transport through a Schottky junction is dominated by the majority charge carriers, I.e. electrons (holes) in the case of n-type (p-type) semiconductors, respectively. Figure (2.8) shows the basic transport mechanisms that can contribute to the total current [56, 82, 84]:

(a) Emission of electrons over the barrier,

(b) Tunneling through the barrier

(c) Recombination in the depletion region

(d) Hole injection from metal.
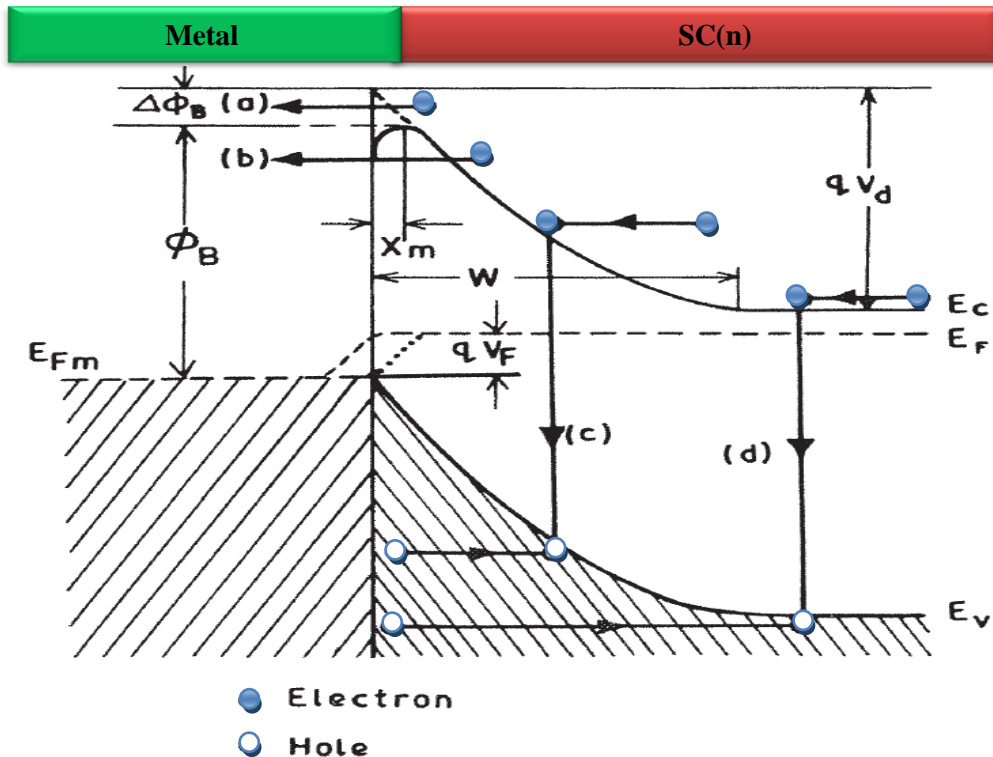
Figure 2.8. Current transport mechanisms in a forward-biased Schottky Barrier [84].

2.2.7.1. Emission of electrons over the barrier

The transport of electrons above the barrier is the dominant process for ideal Schottky with moderately doped semiconductors operated at moderate or high temperatures. This process was described by three theory, diffusion of Schottky, thermionic emission (TE) of Bethe and thermionic emission diffusion (TED) of Sze and Crowell. The current density expressions of the diffusion and thermionic-emission theories are basically very similar, while TED theory is a combination of the two theories. Here we will discuss thermionic emission theory since it is the most widely used in the interpretation of the experimental I-V characteristics Schottky barrier diodes [56, 82, 84].

a)   Thermionic emission theory

The thermionic emission theory is derived by using the assumptions that the barrier height is much larger than kT, so that the Maxwell-Boltzmann approximation applies and that thermal equilibrium is not affected by this process. The current density from the semiconductor to the metal $J_{s\to m}$ is then given by the concentration of electrons with energies sufficient to overcome the potential barrier [56].

$$J_{s\to m} = \int_{E_F + q\emptyset_B}^{\infty} q v_x \, dn \tag{2.26}$$

Where $E_F + q\emptyset_b$, is the minimum energy required for thermionic emission into the metal, and v_x is the carrier velocity in the direction of transport. The electron density in an incremental energy range is given by

$$dn = N(E)F(E)dE \tag{2.27}$$

Where *N(E)* and *F(E)* are the density of states and the distribution function, respectively.

$$dn \approx \frac{4\pi(2m^*)^{3/2}}{h^3}\sqrt{E - E_C}\exp\left(-\frac{E - E_C + q\emptyset_B}{kT}\right)dE \tag{2.28}$$

For a given energy E, the carrier velocity v is determined by:

$$E = E_c + \frac{1}{2}m^*v^2 \tag{2.29}$$

Thus, we obtain

$$\sqrt{E - E_c} = v\sqrt{\frac{m^*}{2}} \tag{2.30}$$

And

$$dE = m^*v\,dv \tag{2.31}$$

Therefore, we write equation (2.31)

$$dn \approx 2\left(\frac{m^*}{h}\right)^3 exp\left(-\frac{q\emptyset_B}{kT}\right)exp\left(-\frac{m^*v^2}{2kT}\right)(4\pi v^2 dv) \tag{2.32}$$

Then the one-dimensional integral over $4\pi v^2 dv$ is converted into a three-fold integral over. Integration over all velocities in y and z directions yields a factor $2\pi\, kT\,/m^*$. The integration over v_x runs from the minimum velocity v_{0x} necessary to pass the barrier

$$\int_{v_{0x}}^{\infty} exp\left(-\frac{m^*v_x^2}{2kT}\right) v_x dv_x = \frac{kT}{m^*} exp\left(-\frac{m^*v_{0x}^2}{2kT}\right) \tag{2.33}$$

With the minimum velocity determined by

$$\frac{1}{2}m^*v_{ox}^2 = q(V_{bi} - V) \tag{2.34}$$

Substituting (2.34) into (2.33) yields

$$J_{s\rightarrow m} = \left(\frac{4\pi m^* k^2}{h^3}\right) T^2 exp\left(-\frac{q\emptyset_B}{kT}\right) exp\left(\frac{qV}{KT}\right) \tag{2.35}$$

Where $4\pi qm^*k^2/h^3$ called Richardson constant (A^*).

Since the barrier height for electrons moving from the metal into the semiconductor remains the same under bias, the current flowing into the semiconductor I thus unaffected by the applied voltage. It must therefore be equal to the current flowing from the semiconductor into the metal when thermal equilibrium prevails (i.e., when V = 0). This corresponding current density is obtained from Equation (2.35) by setting V = 0,

$$J_{m\rightarrow s} = -A^*T^2 exp\left(-\frac{q\emptyset_B}{kT}\right) \tag{2.36}$$

The total current density is given by the sum of Eqs. 2.35 and 2.36.

$$J_{TE} = \left[A^*T^2 exp\left(-\frac{q\emptyset_B}{kT}\right)\right]\left[exp\left(\frac{qV}{KT}\right) - 1\right] \tag{2.37}$$

b)   Diffusion theory

According to the diffusion theory, the electron concentration at semiconductor side of MS interface is given by [56]:

$$n = N_c exp[-q(E_c - E_F)/kT] \tag{2.38}$$

Where Nc is the effective density of states in the conduction band, E_c is the energy of the bottom of conduction band. And E_F is the quasi-Fermi level for electrons. The current density is given by:

$$J_D = qn\mu\xi + qD_n\frac{dn}{dx} \tag{2.39}$$

Where ξ is the electric field in the barrier, D_n the diffusion coefficient, and µ the electron mobility.

Making use of Einstein's relationship, $\mu/D_n = q/kT$ equation (3.39) can be rewritten as

$$J_D = qn\mu \frac{dE_F}{dx} \tag{2.40}$$

The final current density-voltage relationship is given by

$$J_D = J_0(e^{\frac{qV}{kT}} - 1) \tag{2.41}$$

Where

$$J_0 = qN_C\mu \, \xi_{max} \, e^{-\frac{q\emptyset_b}{kT}} \tag{2.42}$$

The maximum field strength is given by $\xi_{max} = q \, N_d \, w/\mathcal{E}_s$, where w is the depletion width and $\mathcal{E}_s$ the permittivity of the semiconductor.

c)   Thermionic emission - Diffusion theory

The combined thermionic emission-diffusion theory was first introduced by crowll and Sze [92]. In this theory, one defines an effective recombination velocity v_r the potential maximum. The current density due to electrons emitted over the barrier is given by:

$$J_{TED} = q(n_m - n_0)v_r \tag{2.43}$$

Where n_m is the electron density at x_m when the current is flowing and is given by

$$n_m = N_c exp[-q(\emptyset_B - E_F(x_m))/kT] \tag{2.44}$$

Where $E_F(x_m)$ is the quasi-Fermi level at x_m under bias *V*, and n_0 is the electron density level at x_m under quasi-equilibrium condition and is given by

$$n_0 = N_c exp[-q\emptyset_B/kT] \tag{2.45}$$

Letting the diffusion current be equal to the emission current. Crowell and Sze obtained the final expression for electron current density

$$J_{TED} = \frac{qN_c v_r}{1 + \frac{v_r}{v_d}} e^{-\frac{q\emptyset_B}{kT}} (e^{-\frac{qV}{kT}} - 1) \tag{2.46}$$

Where

$$v_d = \left\{ \int_{x_m}^{w} \frac{q}{\mu kT} e^{-q(\emptyset_b - E_c)/kT} dx \right\}^{-1} \tag{2.47}$$

For a maxwellian distribution of electrons and an ideal thermal emitter, the effective recombination velocity is given by

$$v_r = \frac{A^* T^2}{q N_c} \tag{2.48}$$

If $v_d \gg v_r$, the pre-exponential term in equation (2.46) is dominated by v_r and the thermionic theory most nearly applies. If, however, $v_d \ll v_r$, the diffusion process is dominant.

2.2.7.2. Tunneling

Tunneling of electrons thought the barrier potential is an important phenomenon which can dominate the transport process in certain conditions. In contrary of classical physics, the particles in quantum physics can escape the barrier potential even if its energy is below the maximum of this potential. There are two physical models describing the tunneling phenomenon (Figure (2.9)), thermionic field emission (TFE) and field emission (FE) [56,82,84].
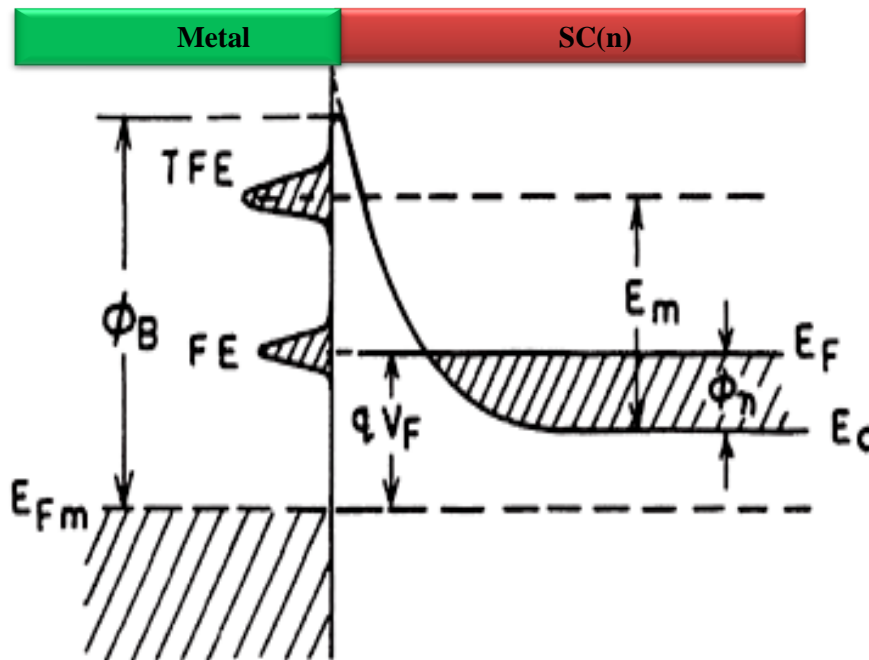
Figure 2.9. Field and thermionic-field emission under forward bias [84].

Field emissions is a pure tunneling process and occur in the case of a degenerate semiconductor at low temperature, where the donor density is so high, and the potential barrier so thin, the current arises from electrons with energies close to the Fermi energy. While thermionic field-emission is tunneling of thermally excited carrier and occur at higher temperature, electrons are excited to higher energies, and the tunneling probability increases very rapidly because the electrons 'see' a thinner and lower barrier. On the other hand, the number of electrons having a particular energy decreases very rapidly with increasing energy, and there will be a maximum contribution to the current from electrons which have energy above the bottom of

the conduction band [93]. According to Padovani and Stratton [94] FE and TEF current density can be expressed as

$$J = J_0 exp\left(\frac{E}{E_{00}}\right) \tag{2.49}$$

Where J_0 is the saturation current density given by:

$$J_{0(FE)} = \frac{2\pi A^* E_{00} \exp\left(-\frac{\emptyset_B}{E_{00}}\right)}{kT\left[log\left\{2\left(\frac{\emptyset_B - E}{\emptyset_n}\right)\right\}\right] sin\left[\frac{\pi kT}{2E_{00}} log\left\{2\left(\frac{\emptyset_B - E}{\emptyset_n}\right)\right\}\right]} \tag{2.50}$$

$$J_{0(TFE)} = \frac{A^* (\pi E_{00}(\emptyset_B - E + \emptyset_n)^{1/2}}{KT cosh(E_{00/kT})} \, exp\left[\frac{\emptyset_n}{kT} - \frac{\emptyset_B - \emptyset_n}{E_0}\right] \tag{2.51}$$

Where Φ_B is the potential energy of the top of the barrier with respect to the Fermi level of the metal, E is the potential energy associated with an applied bias V, Φ_n is the energy of the Fermi level of the semiconductor measured with respect to the bottom of the conduction band, A^* is the effective Richardson constant of the semiconductor and the metal in the case of forward bias and reverse bias respectively, E_0 and E_{00} are the energy given by:

$$E_0 = E_{00} cosh\left(\frac{E_{00}}{kT}\right) \tag{2.52}$$

$$E_{00} = \frac{qh}{4\pi} \sqrt{\left(\frac{N_D}{m^* \varepsilon_s}\right)} \tag{2.53}$$

where m^* is the electron effective mass and h is Planck's constant.

By comparing the thermal energy kT to E_{00} (characteristic tunneling energy that is related to the tunnel effect transmission probability) one can predict the dominant transport process [94]. When $kT \gg E_{00}$ TE dominates, when $kT \ll E_{00}$ FE dominates and when $kT \approx E_{00}$ TFE is the main mechanism which is a combination of TE and TFE.

2.2.7.3.   Electron-hole recombination in the space-charge region

The recombination in the depletion region usually takes place due to the presence localized states in the semiconductor. The localized states are often referred to as "traps" since they act as trapping centre for the minority carriers. The localized states are formed due to defects, surface states, dangling bonds and impurities. These traps have an energy level which is usually located in the forbidden energy gap.

The most effective trap centers are those with energies lying near the center of the forbidden gap [84]. The theory of current due to such recombination centers is similar to that for p-n junctions, and is predicted by the S-H-R (Shockley, Hall and Read) model.

The Recombination current is a common cause of departure from ideal behavior in Schottky diodes. A recombination center in a semiconductor is most effective when its energy level is near the center of the band gap. For recombination through these mid-gap deep traps, the current density J_r caused by the carrier recombination in the depletion region is given by [56]:

$$J_r = J_{ro} \, exp\left(\frac{qV}{2kT}\right)\left\{1 - exp\left(-\frac{qV}{kT}\right)\right\}$$ (2.54)

where $J_{ro} = qn_i w/2\tau_r$ Here n_i is the intrinsic electron concentration, w is the thickness of the depletion region, and is τ_r the lifetime within the depletion region. This current density (J_r) is added to the thermionic emission current density and in some cases may be responsible for a value of n > 1.

2.2.7.4.   Hole Injection in the neutral region of semiconductor

When the height of the Schottky barrier on n-type material is higher than half of the energy band gap, the semiconductor region at and near the surface becomes p-type and contains a high-density of holes. These holes diffuse into the neutral region of the semiconductor under the influence of forward bias and thus giving rise to the injection of the holes.

 If hole concentration exceeds that of the electrons, the surface is inverted and forms a p-n junction with the bulk. This effect is only noticeable in large barrier heights with weakly doped semiconductors [56]. Since SiC has a large bandgap and has a very low intrinsic carrier concentration so, the hole injection is negligible in SiC devices [95].

2.2.8. Forward characteristics

The current/voltage relationship predicted by the thermionic-emission theory [Equation (3.37)] is of the form of the ideal rectifier characteristic $J=J_0\{exp(qv/kt)-1\}$, with $J_0=A^* \, T^2 exp(-q\Phi_B/kT)$, provided the barrier height is independent of bias. However, there are several reasons why the barrier height may depend on the electric field in the depletion region and hence on the applied bias [82, 84].

Let us now consider the case of a Schottky barrier junction made on an n-type semiconductor. For the sake of simplicity we assume that the bias dependence of the barrier height Φ_B can be expressed by the relation

$$\emptyset_B = \emptyset_e + \beta qV \qquad (2.55)$$

Obviously β is positive since $\emptyset_B$ increases with increasing forward bias. $\emptyset_e$ is called the apparent barrier height or the zero-bias barrier height [84]. The current density now becomes

$$J = A^*T^2 exp\left(-\frac{q(\emptyset_e + \beta qV)}{kT}\right)\left[exp\left(\frac{qV}{KT}\right) - 1\right] = J_0 exp\left(-\frac{\beta qV)}{kT}\right)\left[exp\left(\frac{qV}{KT}\right) - 1\right] \quad (2.56)$$

where

$$J_0 = A^*T^2 exp\left(-\frac{q\emptyset_e}{kT}\right) \qquad (2.57)$$

We can write equation (2.56) in the form

$$J = J_0 exp\left(\frac{qV}{nkT}\right)\left[1 - exp\left(-\frac{qV}{KT}\right)\right] \qquad (2.58)$$

where

$$\frac{1}{n} = 1 - \beta = 1 - \left(\frac{\partial \emptyset_B}{\partial V}\right) \qquad (2.59)$$

n is often called the 'ideality factor'. If $\partial \emptyset_B / \partial V$ is constant, n is also constant.

For values of V greater than $3kT/q$, Equation (2.58) can be written in the simpler form

$$J = J_0 exp\left(\frac{qV}{nkT}\right) \qquad (2.60)$$

More usually $\partial \emptyset_B / \partial V$ is not constant and the plot of $ln[J_0\{1 - exp(- qV/kT)]$ against V is not linear. The ideality factor can be obtained from the experimental J-V characteristic through the relationship

$$\frac{1}{n} = \frac{kT}{q}\frac{d}{dV}ln\left[J/\left\{1 - exp\left(-\frac{qV}{KT}\right)\right\}\right] \qquad (2.61)$$

or, for $V > 3kT/q$,

$$\frac{1}{n} = \frac{kT}{q}\frac{d(lnJ)}{dV} \qquad (2.62)$$

The apparent barrier height (Φe)values are determined from equation (2.57)

$$\emptyset_e = -\frac{kT}{q}ln\left(\frac{J_0}{A^*T^2}\right) \qquad (2.63)$$

Furthermore, the apparent barrier height Φe may be determined in another way such as the Richardson plot (lnJ_o/T^2 versus $1/T$). The slope of this plot yields the value of a mean apparent barrier height$\overline{\Phi e}$, independent of temperature [31, 84]. Thus, Equation (2.57) can be rewritten as

$$ln\left(\frac{J_0}{T^2}\right) = lnA^* - \frac{q\overline{\emptyset}_e}{kT} \tag{2.64}$$

When the interface states are in equilibrium with semiconductor, the n ideality factor is expressed by Rhoderick and Card [96] as,

$$n(V) = 1 + \frac{\delta}{\varepsilon_i}\left[\frac{\varepsilon_s}{w} + qN_{ss}\right] \tag{2.65}$$

where w is the width of depletion layer of semiconductor, N_{ss} is the density of the interface states which is in equilibrium with the semiconductor, ε_i and ε_s are the dielectric constants of the interface oxide layer and semiconductor, respectively. ε_s for 4H-SiC is given as 9.7 [97,98]. As a result, N_{ss} may be written from equation (2.65) as,

$$N_{ss}(V) = \frac{1}{q}\left[\frac{\varepsilon_i}{\delta}(n(V) - 1) - \frac{\varepsilon_s}{w}\right] \tag{2.66}$$

Also, for an n-type 4H-SiC semiconductor, E_{sc} - E_{ss} which is the energy of the interface states with respect to the bottom of the conduction band at surface of the semiconductor is expressed by,

$$E_{sc} - E_{ss} = q\emptyset_e - qV \tag{2.67}$$

The image force lowering effect is one of the factors which cause the I–V and C–V barrier height differences and Schottky barrier inhomogeneities. The ΔΦb barrier reduction in the junction due to the image-force lowering effect is calculated from Equation (2.25). And the diode ideality factor can be calculated by using the following expression [84]:

$$\frac{1}{n} = 1 - \frac{1}{4}\left(\frac{q^3N}{8\pi^2\varepsilon_s^3}\right)^{\frac{1}{4}}\left[\emptyset_B - V - \zeta - \frac{kT}{q}\right]^{-\frac{3}{4}}. \tag{2.68}$$

On the other hand, Padovani and Stratton [94] reported that the tunneling through barrier is responsible for current transportation mechanism of forward bias J–V curves, except for very low values of forward bias and as a result, E_{00} characteristic tunneling energy is calculated from equation (2.53), Furthermore, the n ideality factor is related to E_{00} characteristic tunneling parameter in Equation (2.53) through the equation given below:

$$n = \frac{qE_{00}}{kT} coth\left(\frac{qE_{00}}{kT}\right) \tag{2.69}$$

As different from equation (2.69), Horvath [99] demonstrates that the n ideality factor is presented by an equation expressed as,

$$n = \frac{qE_{00}}{(1-\beta)kT} coth\left(\frac{qE_{00}}{kT}\right) \tag{2.70}$$

where β is the bias dependence of barrier height for I–V curves which dominate of the thermionic-field emission.

If the departure of n from unity arises from image-force lowering or from interface effects, n, should be independent of temperature, but if it is due to thermionic-field emission or to the effect of recombination in the depletion region, n will be temperature dependent. The majority of Schottky diodes exhibit n values which depend on temperature and in some cases this temperature dependence can be expressed by the relation [31, 82, 84,]:

$$nT = n_0 T + T_0 \tag{2.71}$$

The temperature dependence of the BH and ideality factor in Schottky diodes is called the "T_0 effect" Such a phenomenon has been observed from all types of SBDs. If a diode displays the T_0 effect, its current expression may be given by

$$J = J_0 exp\left(\frac{qV}{nkT}\right) = J_0 exp\left(\frac{qV}{(n_0 + \frac{T_0}{T})kT}\right) \tag{2.72}$$

If J is measured as a function of V at a number of temperatures and nT is plotted as a function of T, different current transport mechanisms can be identified as shown in Fig. 2.10 [82,100].

Fig 2.10 showing the five basic categories of the temperature dependence of the ideality factor.

Curve I is an ideal SB that follows the prediction of thermionic emission theory.

Curve II shows a temperature independent, greater-than-unity ideality factor, usually between 1 and 1,1. Sze et al [92] showed that such a value of n can approximately be accounted for when the image forces are taken into account.

Curve III displays the T_0 effect where T_0, is a constant >0 and it is independent of temperature.

Curve IV represent the behaviors when conduction is dominated by TFE, in this case T_0 is not

constant with respect to temperature. It increases at lower temperatures. **Curve V** represents the behaviors when conduction is dominated by FE.
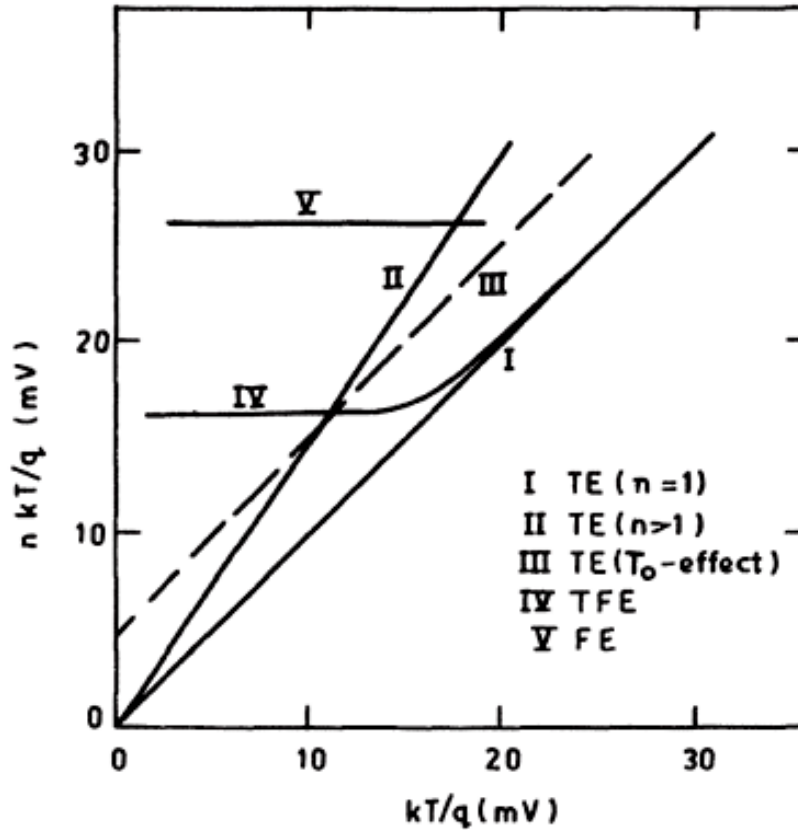
Figure 2.10. Plots of *nkT/q* as a function of *kT / q* for identifying t he different current transport mechanisms (after Saxena [100]).

2.3. Barrier inhomogeneities

Schottky barrier height inhomogeneities can be defined as the lateral variation of the barrier height, this lateral variation was attributed to interface propriety and the fabrication process [101]. Evidence for the presence of inhomogeneity in the SBH's was recognized and reported only sporadically before the 1990 [102], the inhomogeneities was described by two parallel diodes with different barrier height and the junction current is a sum of the contribution from the two diodes. These models is in signification error when the SBH varies spatially on a scale less than, or comparable to the width of the space-charge region.

The development of the ballistic electron emission microscopy (BEEM) technique [103-105], provided the spatial resolution needed to examine the distribution of local SBH underneath ultrathin metal layers.

There are several reasons for such potential Inhomogeneities at the interface of metal-semiconductor contacts [106].

1.   The dopant atoms are randomly distributed within the semiconductor.

2.   Atomic steps and lattice defects at the interface modulated the barrier height even at single crystal epitaxial contacts.

3.   The dependence of the Schottky barrier on the relative orientation of semiconductor and metal atoms results in barrier height fluctuations over the area of polycrystalline Schottky contacts.

4.   At polycrystalline contacts, grain boundaries in the metal may modify the Schottky barrier.

5.   Interface roughness results in spatially varying effective Schottky barriers by local barrier lowering due to field emission even for nominally homogeneous contacts.

6.   In the particular case of reactive contacts, e.g., silicide/Si, different phase of metal yield different barrier heights.

7.   The metal atoms can diffuse into the semiconductor and there will be a redistribution of dopant atoms in the vicinity of the interface.

8.   Contact edges are often sites of charges which locally modify the Schottky barrier height. The contact appears therefore also inhomogeneous.

After 1990 more sophisticated models were developed. Werner and Guttler model [19] and Tung model [20].

2.3.1. Werner and Guttler model

The model considered a large area device which contains potential fluctuation or barrier inhomogeneities at the MS interface [101]. Figure (2.11) on length a scale, and this potential fluctuation is smaller than the width of the space-charge region, i.e., < 1 μm.

More in detail, the spatial barrier inhomogeneities in SBDs are described by assuming a Gaussian distribution $\rho(\emptyset_B)$ of the SBH with a standard deviation (σ_0) around a mean value ($\bar{\emptyset}_{B0}$):

$$\rho(\emptyset_B) = \frac{1}{\sigma\sqrt{2\pi}} e^{-\frac{(\emptyset_B - \bar{\emptyset}_{B0})^2}{2\sigma^2}} \tag{2.73}$$
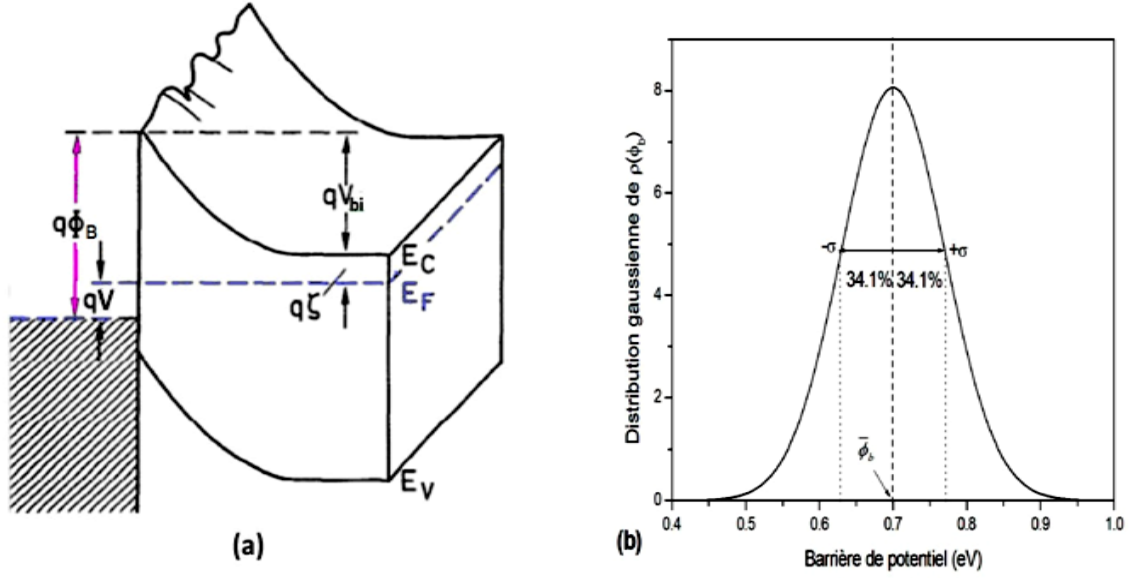
Figure 2.11. a)Two-dimensional band diagram of an inhomogeneous Schottky contact b) Gaussian distribution of barrier height fluctuations according to the Werner model.

The pre-exponential term is a normalization constant. The total forward current across the Schottky barrier diode is given by:

$$I = \int i(V,\emptyset_B)\rho(\emptyset_B)d\emptyset_B \tag{2.74}$$

where $i(\mathrm{V},\emptyset_B)$ is the current based on the TE model equation (2.58). It is assumed that $\overline{\emptyset}_B$ and σ are linearly bias-dependent on Gaussian parameters as follows:

$$\overline{\emptyset}_B = \overline{\emptyset}_{B0} + \rho_2 V, \tag{2.75}$$

$$\sigma^2 = \sigma_0{}^2 + \rho_3 V \tag{2.76}$$

where $\overline{\emptyset}_{B0}$ and σ_0 are the zero-bias reference parameters, and ρ_2 and ρ_3 are temperature-independent voltage coefficients which model the voltage deformation of the barrier distribution.

By introducing $i(\mathrm{V},\emptyset_B)$ and $\rho(\emptyset_B)$ from Eqs.(2.58) and (2.73) into (2.74), and performing the integration we can write:

$$I = AA^*T^2\left[-\frac{q}{kT}\left(\overline{\emptyset}_{B0} - \frac{q\sigma_0^2}{2kT}\right)\right]exp\left(\frac{qV}{n_{ap}\,kT}\right)\left[1 - exp\left(-\frac{qV}{kT}\right)\right], \tag{2.77}$$

$$I_0 = AA^*T^2exp\left(-\frac{q\emptyset_{Bap}}{kT}\right) \tag{2.78}$$

where $\emptyset_{Bap}$ and n_{ap} are the apparent SBH and ideality factor, respectively, in the form of

$$\emptyset_{Bap} = \overline{\emptyset}_{B0} - \frac{q\sigma_0^2}{2kT}, \tag{2.79}$$

$$\frac{1}{n_{ap}} - 1 = -\rho_2 + \frac{q\rho_3}{2kT}. \tag{2.80}$$

2.3.2. Tung model

A cording to Tung [20], the barrier inhomogeneities is a result of the presence of small regions with a low SBH ($\emptyset_B^0 - \Delta$) embedded in an interface with an otherwise uniform high SBH ($\emptyset_B^0$). Two geometries were considered for the low-SBH region, a small circular patches and narrow semi-infinite strips [20].
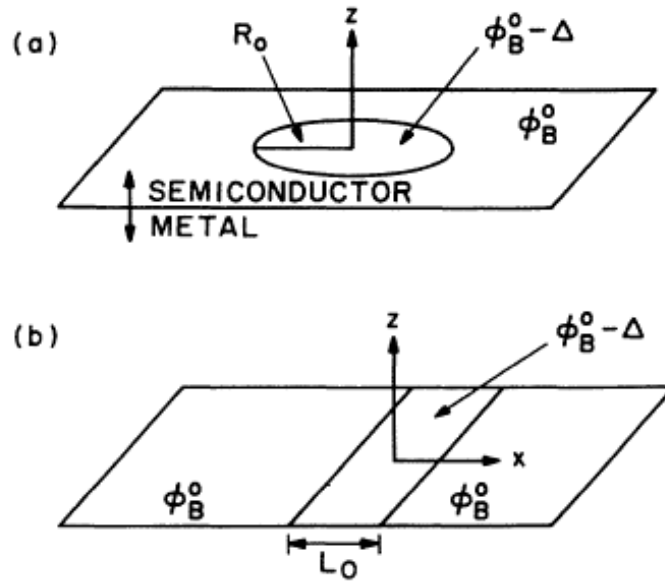
Figure 2.12. Geometries and coordinates of examples of the inhomogeneities in Tung model. (a) Circular patch, (b) narrow strip [20].

As seen in figure (2.12), the small regions with low SBH are characterized by two important parameters, the value of the barrier which is lower than the uniform barrier by a value Δ (eV), and the second parameter is the radius R_0 or the length L_0 (for the circular patches and semi-infinite strips respectively) which represent the surface of the small regions with low SBH.

The potential around the circular patch and the narrow strip are given by next equations:

$$V(\rho, z) = V_{BB}\left(1 - \frac{z}{W}\right)^2 + V_n + V_a - \frac{V_{bb}\Gamma^3 zW^2}{(z^2 + \rho^2)^{3/2}} \tag{2.81}$$

$$V(x, y, z) = V_{BB} \left(1 - \frac{z}{W}\right)^2 + V_n + V_a - \frac{2V_{bb}\Omega^2 WZ}{x^2 + z^2} \tag{2.82}$$

Where V_{bb} is the band bending corresponding to a MS junction with a uniform ($V_{bb}=V_{bi}-V_a$), W is the depletion width, V_n is the difference between the Fermi-level (FL) and the conduction band maximum (CBM), ρ is the radial coordinate, Γ and Ω are a dimensionless quantity that measures the strength of the patch and the strip respectively.

$$\Gamma^3 = \frac{\Delta R_0^2}{2V_{bb}W^2} = \frac{\Delta R_0^2}{4\eta V_{bb}{}^2} \tag{2.83}$$

$$\Omega^2 = \frac{\Delta L_0}{2\pi V_{bb}W} \tag{2.84}$$

Where $\eta = \mathcal{E}_s/qN_D$.

In contrary of the previous model, Tung model take in to account the length scale of the inhomogeneities by introducing the radius R_0 and the length L_0 of the patch and the strip in the potential equation. In addition, it takes in to account the interaction between the small low barriers regions by phenomenon called pinch-off.

A small low barrier region is said to be pinched-off if the carrier need to go over a potential of a neighbor region that has a higher potential. For a large Δ, or small R_0, the potential in front of the patch is obviously pinched-off.

Figure (2.13) illustrates the pinch-off effect by plotting the potential close to a low-SBH patch as a function of the radius R_0, the patch has a $\Delta=0.2$ (eV) and the uniform barrier of the diode $\emptyset_B^0=0.8$ (eV), which mean that the barrier of the patch equal to 0.6 (eV) ($\emptyset_B^0-\Delta$).

When the patch's radius has a large value (0.07 um) the potential in close to the patch is equal to the barrier of the patch (0.6 eV), when the patch's radius be smaller the potential in close to the patch reaches a value close to the uniform barrier value (0.8 eV) [20,101].
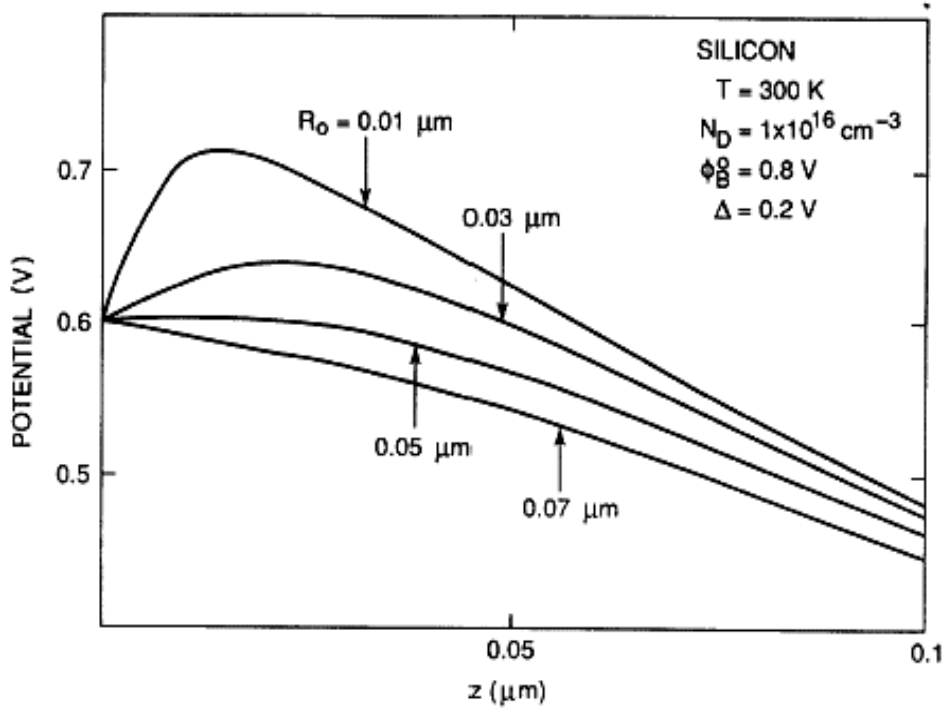
Figure 2.13. CBM potentials along the z axis in close to a low-SBH patch, illustrating the influence of the radius of a low-SBH patch on potential pinch-off [20].

The condition for pinch-off is obtained from equation (2.81) and equation (2.82) for the patch and the strip respectively

$$\frac{\Delta}{V_{bb}} > \frac{2R_0}{W} \tag{2.85}$$

$$\frac{\Delta}{V_{bb}} > \frac{\pi L_0}{2W} \tag{2.86}$$

Effectively the total current of inhomogeneous diode is given by two formulas depending on the density distribution type of the patches as a function of the parameter γ. Where γ is a constant related to the patch characteristics (a true parameter of the MS interface inhomogeneity) and is given by:

$$\gamma = 3\left(\frac{\Delta R_0^2}{4}\right)^{\frac{1}{3}} (cm^{\frac{2}{3}}V^{\frac{1}{3}}) \tag{2.87}$$

The most used expression in the interpretation of experimental results [20] is based on one-half of a Gaussian distribution. The density of patches with their parameter γ lying between γ and $\gamma + d\gamma$ is $N(\gamma)\,d\gamma$:

57

$$N(\gamma) = \begin{cases} \dfrac{\sqrt{2}C_1}{\sqrt{\pi}\sigma_1} exp\left(-\dfrac{\gamma^2}{2\sigma_1^2}\right), & \gamma > 0 \\ 0, & \gamma > 0 \end{cases} \tag{2.88}$$

Where σ_1 ($cm^{2/3}$ $V^{2/3}$) is the standard deviation and C_1 (cm^{-2}) is the total density of patches. The strip also has a parameter ω and $N(\omega)$ similar to the parameter γ and $N(\gamma)$ of the patch respectively. The total current at any given bias is approximately given by

$$I_{total} = A^* A T^2 exp(-\beta\emptyset_{B0})[exp(\beta V_a) - 1]\left[1 + f(V_{bb})exp\left(\beta^2 k\, V_{bb}^{\xi}\right)\right] \tag{2.89}$$

Where $\beta = \frac{q}{kT}$, the constants ξ and k and the slowly varying function f are defined in Table 2.1.

Table 2.1 Parameters for electron transport at an inhomogeneous SB with one-half of a Gaussian distribution [20].

Parameter	Patch	Si
ξ	2/3	1/2
k	$\dfrac{\sigma_1^2}{2\eta^{2/3}}$	$\dfrac{\sigma_2^2}{2\eta^{1/2}}$
$f(\beta, V_{bb})$	$\dfrac{8c_1\sigma_1^2\pi\eta^{1/3}}{9V_{bb}^{1/3}}$	$\dfrac{c_2\pi\sigma_2^{3/2}\sqrt{\beta}\eta^{1/8}L_{strip}}{1.46V_{bb}^{1/8}}$

The current in equation (2.89) is made up of two components: one being the current over the entire diode, which has a uniform SBH of $\emptyset_B^0$ and represented by 1 in the last term of equation (2.89), this current dominates at high temperatures and displays near unity ideality factor. The other term represents an additional current due to the presence of the low-SBH patches or strips, at low temperatures this term becomes much larger than 1, and the low-SBH patches dominate at small bias and the ideality factor is larger than 1. In addition, the effect of patches on the I-V characteristic of the diode can be seen clearly, in the reverse bias the current never saturates, while in the forward bias at small values the I-V characteristic shows a curvature or double diode behaviour. One can remark that the parameter γ does not appear in the total current equation, but is present indirectly by σ_1 which have the same unit.

The combined effect of all the low-SBH regions is as if there were a big low-SBH region in the diode with an effective area (A_{eff}) and an effective SBH ($\emptyset_{eff}$). Even though the effective SBH of each individual patch is roughly temperature independent, but together they may be represented by a temperature dependent effective SBH. That is, at each temperature the current

flow through some patches with identical γ. A_{eff} and $\emptyset_{eff}$ of the patches are given by the following relations [20].

$$\emptyset_{eff} = \emptyset_B^0 - \frac{\sigma_1^2}{2kT}\left(\frac{V_{bb}}{\eta}\right)^{2/3} \tag{2.90}$$

$$A_{eff} = AC_1 A_P \tag{2.91}$$

Where A_P is the effective area of one patch and is given by:

$$A_p = \frac{8\pi\sigma_1^2}{9}\left(\frac{\eta}{V_{bb}}\right)^{1/3} \tag{2.92}$$

From equation (2.90) and equation (2.92) A_P can be rewritten as:

$$A_p = \frac{8\pi(2kT)}{9}\left(\frac{\eta}{V_{bb}}\right)\left(\emptyset_{B0} - \emptyset_{eff}\right) \tag{2.93}$$

2.4. Examples of SiC schottky diodes applications

2.4.1. Applications in power electronics

Power conversion systems are present in everyone's day by day life. Hence, the reduction of the global energy consumption is strictly related to the development of new energy efficient power devices. In this context. SiC is today the most promising material to satisfy such challenging request [5].

The diode is widely used as a companion of the transistor in almost all the conversion systems and the addressed market is huge. As can be seen in the power versus voltage chart depicted in figure (2.14), the most common applications in the present market (e.g., in consumer electronics, renewable energies, industrial and automotive sectors, etc.) require devices able to sustain off-state voltages in the range 650 V — l.7 kV [5,107]. For all of these applications, the possible solution based on Silicon rectifiers is the bipolar diode which is characterized by very high switching losses. In figure (2.15) a typical reverse recovery waveform of a 4H-SiC SBD is compared with different commercial Si bipolar diodes, each with a recovery time determined by a different carrier lifetime enhancement technique. Independent of the bipolar Si technology, the unipolar 4H-SiC SBD has the minimum recovery loss due to its absence of minority carriers. It is the fundamental characteristics of SiC, its high critical electric field. That permits a SiC unipolar diode to be rated at the same voltage as the Si bipolar device, without suffering great conduction losses [5].
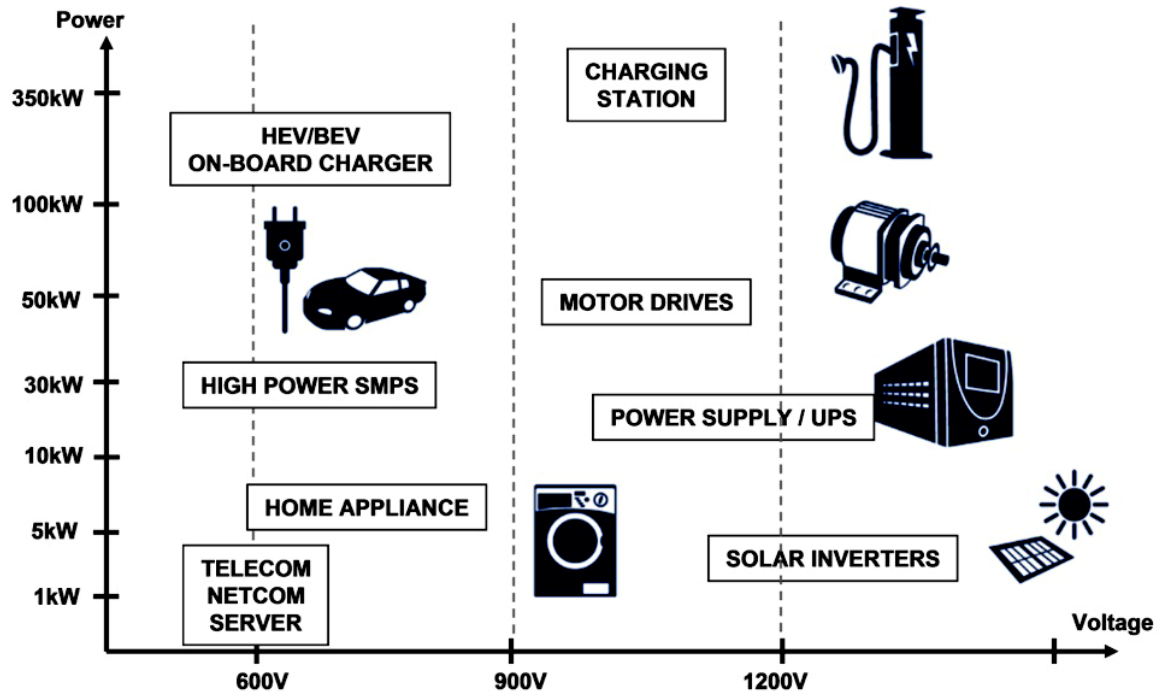
Figure 2.14. Power versus blocking voltage chart of the most common applications of power devices in the range 650-1700 V [5].
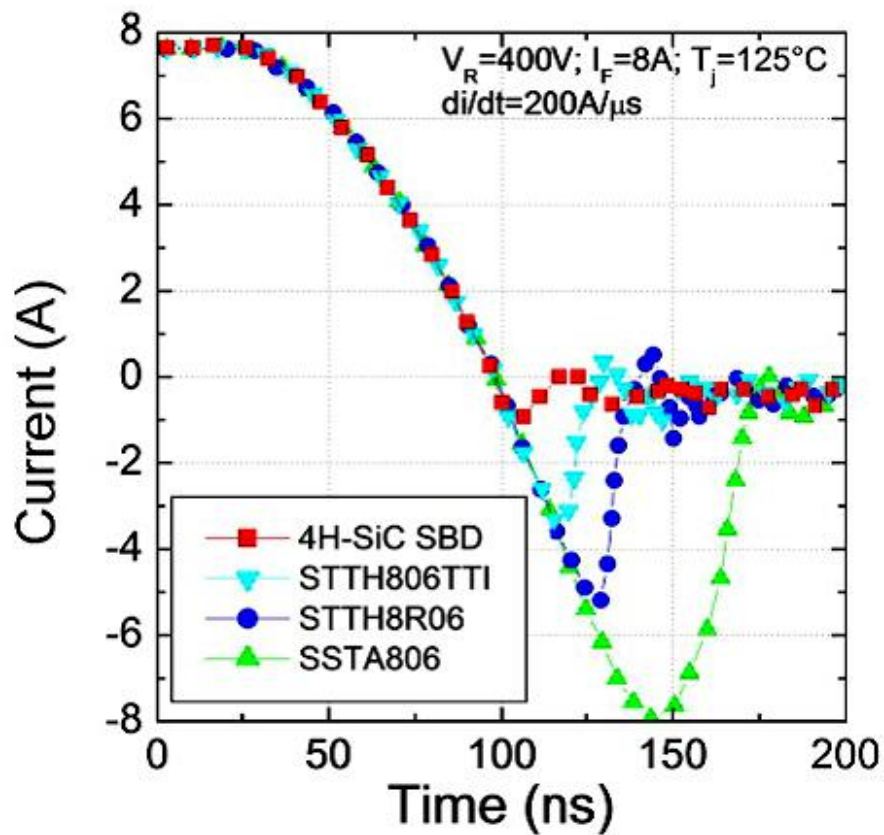
Figure 2.15. Reverse recovery waveforms of a 4H-SiC Schottky diode (600 V/8 A) at 125[0] Compared with different ultra -fast commercial Si bipolar diodes [5].

2.4.2. Temperature sensors

4H-SiC Schottky barrier diodes can be used also as a high-temperature sensor, suitable in harsh environments - high shock or intense vibration, high radiation, erosive and corrosive conditions. In particular, temperature probes based on 4H-SiC SBD, capable of operating under those extreme conditions, can have significant applications in several fields, e.g., automotive and aircraft engines, geothermal systems, industrial furnaces, oil and gas detection, etc. [5,107].

For temperature monitoring sensor applications, the SiC SBDs are forward biased as a constant current. The I_F-V_F; characteristics of the devices exhibit an excellent linearity of the $ln(I_F)$ versus V_F plot over many orders of magnitude, up to high temperatures. Therefore, for low current density where R_S can be neglected, the voltage dependence on temperature can be obtained from Eq.2.60 yielding [8,11].

$$V_F = R_s I_F + n\emptyset_B + \frac{kTn}{q} ln\left(\frac{I_F}{AA^* T^2}\right) \tag{2.61}$$

The detection sensitivity of the sensor, S, is defined by:

$$S = \frac{dV_F}{dT} \tag{2.62}$$

Clearly, both Φ_{Bo} and n should ideally be temperature-independent, in order to ensure a stable and reproducible detection sensitivity. Moreover, high SBH metals are preferred to operate at high temperatures.

The advantage of SBD temperature sensors, if compared with other sensors that can be on-chip integrated, e.g., thermistors, are the compatibility with IC technology, the low manufacturing costs, the quasi-linear output characteristic, preserving at the same time a high sensitivity. To date, the diodes are realized for applications at temperatures of about 300 °C, i.e., oil and gas exploration, nuclear environments and similar [5].

2.4.3. UV-detectors

An important application field of SiC Schottky diodes is the Ultra-Violet (UV) radiation detection. The operating principle of this device is the detection of the photocurrent generated in the depletion region of a reverse biased SBD under UV-light exposure.

Traditionally, Silicon photomultipliers have been used for the detection of UV light. However, the main problem of using Si for UV-radiation detection lies in its narrow band gap (1.12 eV), leading to the need for supplementary filters to eliminate the visible and infrared components of the light, which do not need to be detected. In addition, their low quantum

efficiency in the UV range, large size, high cost, and high operation voltage limit their practical use in several cases.

4H-SiC due to its large band gap (3.2 eV) means that this material will only respond to the radiation with wavelength below approximately 400 nm. The longer wavelengths from the visible and infra-red spectrum cannot be absorbed and, hence, the detectors based on SiC are insensitive to this portion of the spectrum. This characteristic is extremely advantageous since it allows SiC detectors to be used even in the presence of visible and infrared background, as occurs in many applications. In addition, owing to the low intrinsic carrier concentration of the material, 4H-SiC Schottky diodes have an extremely low leakage current, thus increasing the sensitivity of the devices [5].

Chapter 3
Models and parameters of
4H-SiC for device simulation

3.1. Introduction

Numerical device modeling and simulation are essential for analyzing and developing semiconductor devices. They help a design engineer, not only gain an increased understanding of the device operation, but also provide the ability to predict electrical characteristics, behavior, and parameter-effects influence of the device. With this knowledge and abilities the designer can design a better structure, estimate device performance, perform worst case analysis, and optimize device parameters to yield an optimize device performance.

It is the aim of this chapter to analyze the applicability of 4H-SiC material parameters from the literature and to implement them into the two-dimensional ATLAS SILVACO as a way to calibrate the simulation process with the real device characteristics.

3.2. Application of Device Simulation

The goal of the device simulation procedure is to use the output of the simulation process for predictive analysis of the properties and behavior of the simulated device structure with a unique insight into the internal process and structure operation, along with the possibility of further optimization and development. Two- and three-dimensional modeling and the simulation process contribute to a better understanding of the properties and behavior of the new devices by identifying the inevitable parasitic devices attributing to standard malfunction behaviors and degraded performances. Based on the interpretation of experimentally obtained data along with the result of device simulation, new structures and devices with modified layouts and concentration profiles can be designed and verified [108].

3.3. SILVACO'S ATLAS DEVICE SIMULATOR

ATLAS is Silvaco International's primary TCAD device simulator and has the ability to model devices of many different materials and physical characteristics [109].

The primary method of interfacing with the ATLAS simulator is using Silvaco's Deckbuild operating environment. Devices can either be completely constructed in Deckbuild to be run by ATLAS or they can be built using Silvaco's ATHENA device frame work simulator. Figure (3.1) shows a flow chart that describes how the different programs of Silvaco's TCAD suite interact with the ATLAS device simulator.

ATLAS simulations use two input files. The first input file is a text file that contains commands for ATLAS to execute. The second input file is a structure file that defines the structure to be simulated. ATLAS produces three types of output files. The first type of output file

is the run-time output, which gives the progress and error with warning messages as the simulation proceeds. The second type of output file is the log file, which stores all terminal voltages and currents from the device analysis. The third type of output file is the solution file, which stores 2D and 3D data relating to the values of solution variables within the device at a given bias point. The log files and the solution files are visualized using TONYPLOT [109].
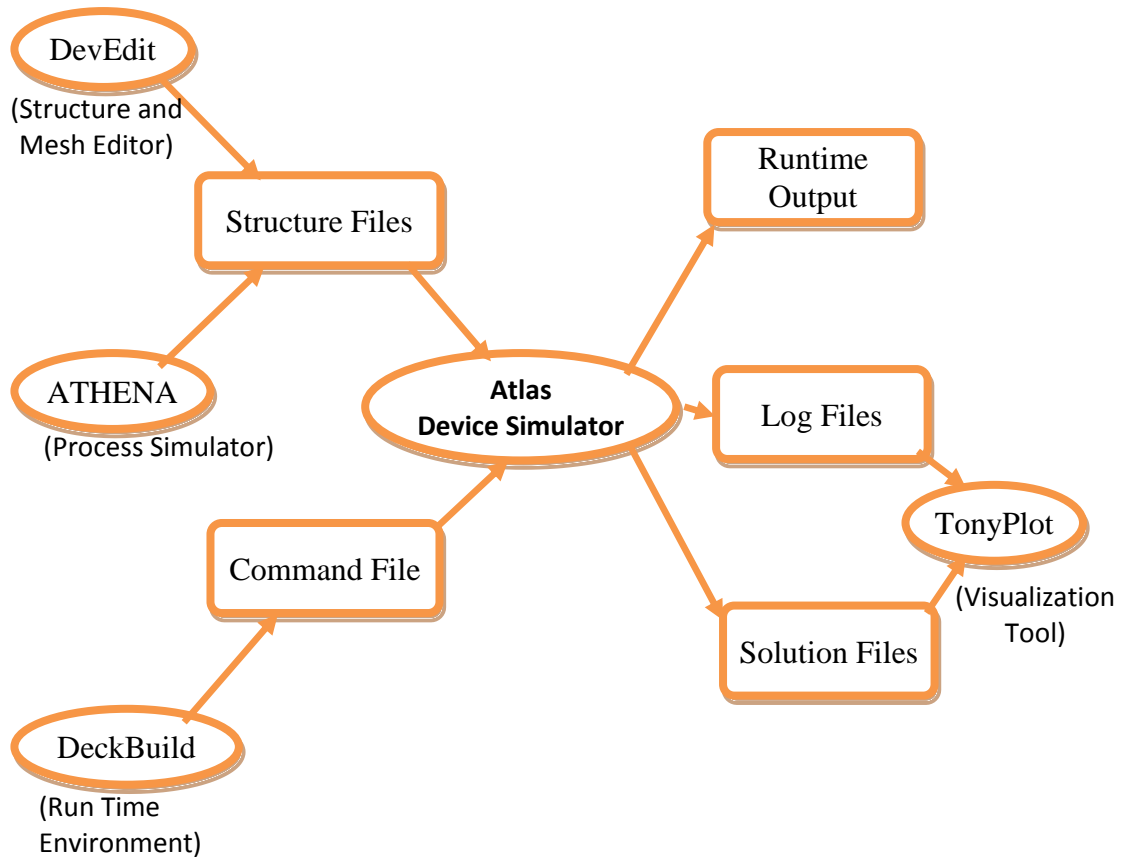
Figure 3.1. ATLAS inputs and outputs [109].

3.3.1. Deckbuild

Deckbuild is a powerful interactive run-time environment tool that allows user to transparently go from process simulation to device simulation to spice model extraction. It is easy to use run time environment for core simulators such as ATLAS. Deckbuild helps in creating the input files to ATLAS. Multiple windows provide menu-based or text-based input decks for the information entered. The deck can be modified any time. Multiple decks are also created if there is any information that is being repeated. Multiple simulators can be called from the input deck, and transfer of information is transparent to the user. It offers complete control of run, kill, pause, and stop-at, restart, and single-step and history initialization operation to back-track a previous point in the deck and run it from that instance. Other simulator tools, such as TONYPLOT, DEVEDIT and MASKVIEW can also be invoked from Deckbuild.

3.3.2. ATHENA

ATHENA is a physically based process simulator module which predicts the structures that result from specified process sequences. This is done by solving systems of equations that describe the physics and chemistry of semiconductor processes. It provides a platform for simulating diffusion, deposition, etching, ion implantation, oxidation, lithography of semiconductor materials. Costly wafer experiments can be replaced with simulations using ATHENA.

3.3.3. Devedit

Devedit is an interactive tool for defining and altering structures. It uses SILVACO's Master structure file format to communicate with process and device simulators. Analytic functions in Devedit are helpful in defining and altering the doping profiles. It is used for defining structures and later invoked by Deckbuild to perform ATLAS simulation of the device structure. This tool is valuable as a pre- processor for 2D device simulators. A new mode of DEVEDIT supports the definition and meshing of 3D structures.

3.3.4. Tonyplot

This is the common visualization tool in Silvaco TCAD products. It provides comprehensive potential for viewing and analyzing simulator output. The data can be plotted as desired by the user either in 1D x-y data, 2D contour data, Smith charts or polar charts. Measured data can also be imported and plotted.

The overlays feature helps in comparing the multiple simulation runs. It annotates plots to create meaningful figures for reports and presentations. It can plot to files, postscript printers, and other printer formats in sharp colors. It allows I-V (current-voltage) data or 1D plots to be over-laid to examine how process conditions affect electrical results. It supports plotting of user defined equations with the variables being either electrical data or physical parameters.

3.4. ATLAS approach in designing the SiC Schottky Diodes

Silicon Carbide is a compound semiconductor and can be simulated using ATLAS simulator. To provide input to ATLAS, there are five groups in each input file which contain the information as shown in table 3.1.

The order of statements in which they occur are important otherwise it would lead to incorrect operation of the program [108].

Table. 3.1 ATLAS Command Groups with man statements in each group [108].

Group	Statement
Structure Specification	1. MESH 2. ELECTRODE 3. REGION 4. DOPING
Material Model Specification	1.MATERIAL 2. MODELS 3. CONTACT 4. INTERFACE
Numerical Method	1. METHOD
Solution Specification	1. LOG 2. SOLVE

3.4.1. Structure Specifications

Structure specification includes generation of mesh, defining regions and electrodes, and doping for the device [109].

3.4.1.1.   Mesh Generation

The first statement in structure declaration is the mesh statement. Mesh statement allows the user to specify many structure types, rectangular, circular and cylindrical each of these structure types can be defined in 2 or 3 dimension. Here will see how to define a 2D cylindrical structure [109].

MESH CYLINDRICAL

This is followed by a series of X.MESH and Y.MESH statements.

X.MESH LOCATION=<VALUE> SPACING=<VALUE>

Y.MESH LOCATION=<VALUE> SPACING=<VALUE>

The X.MESH and Y.MESH statements are used to specify the locations in microns of vertical and horizontal lines, respectively, together with the vertical or horizontal spacing associated with that line. The X.MESH and Y.MESH statements must be listed in the order of increasing x and y. Both negative and positive values of x and y are allowed.

Atlas sets some limits on the maximum number of grid nodes that can be used. In the default version, 2D Atlas simulations have a maximum node limit of 100,000 [109]. In cylindrical coordination Atlas operates with x=0 as the axis of symmetry around which the cylindrical geometry is placed. The calculated current is in Amps rather than the usual Amps per micron. The CYLINDRICAL parameter setting isn't stored in mesh files. Therefore, this

parameter must be specified each time a mesh file, which contains cylindrical symmetry, is loaded

MESH INF=NAME.STR CYLINDRICAL

Specifying a good grid is a crucial issue in device simulation but there is a trade-off between the requirements of accuracy and numerical efficiency. Accuracy requires a fine grid that resolves the structure in solutions. Numerical efficiency is greater when fewer grid points are used. The critical areas to resolve are difficult to generalize because they depend on the technology and the transport phenomena. For Schottky barrier diode the critical area is in the interface between metal and semiconductor. The CPU time required to obtain a solution is typically proportional to N^α, where N is the number of nodes and α varies from 2 to 3 depending on the complexity of the problem. Thus, the most efficient way is to allocate a fine grid only in critical areas and a coarser grid elsewhere.

The three most important factors to look for in any grid are [109]:

    ☐ Ensure adequate mesh density in high field areas.

    ☐ Avoid abrupt discontinuities in mesh density.

    ☐ Avoid abrupt discontinuities in mesh density.
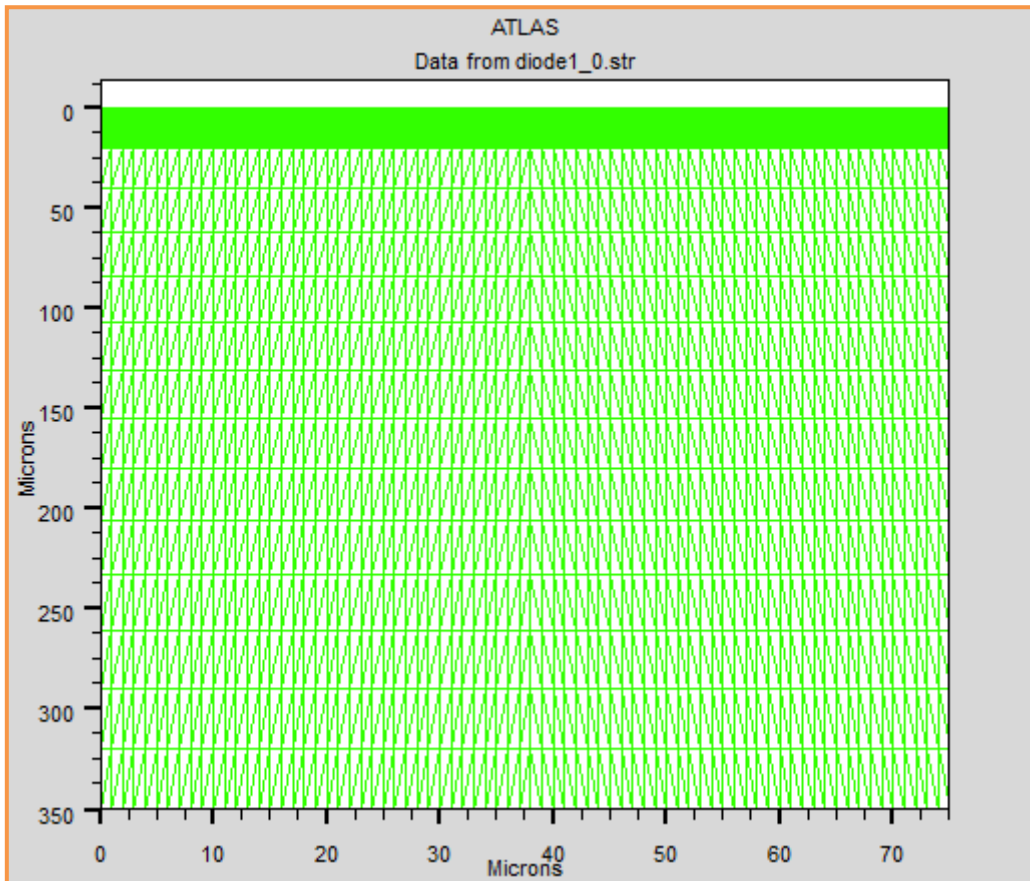
Figure 3.2. Typical mesh in Atlas

3.4.1.2. Region

After defining the mesh, it is necessary to define the regions. In defining a region, all locations of the mesh are divided into numbered areas, where each is associated with a specific material from the ATLASTM library. Regions are created with the following statements:

REGION NUMBER=<INTEGER> MATERIAL= <CHARACTER> <POSITION PARAMETERS>

The position parameters are specified in microns using the X.MIN, X.MAX, Y.MIN, and Y.MAX parameters.
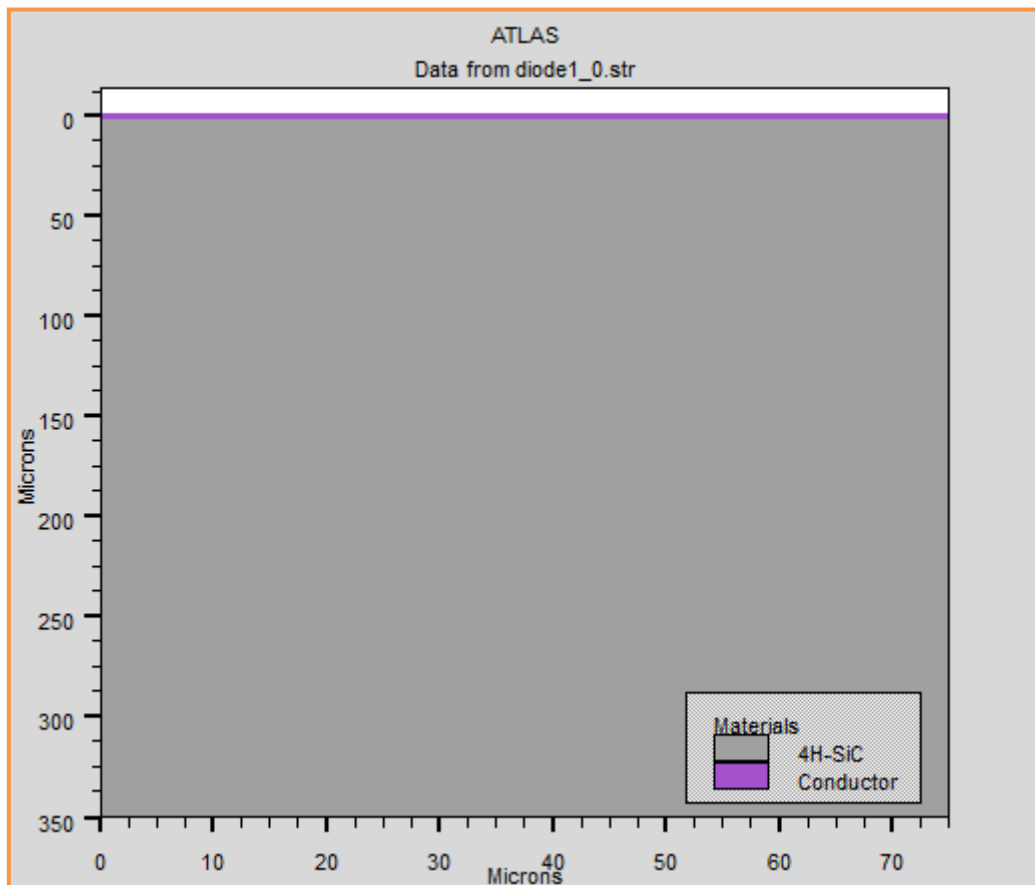
Figure 3.3. ATLAS region boundaries and region statements

3.4.1.3. Electrode

The next structure specification corresponds to electrodes. Typically, in this simulation the only electrodes defined are the anode and the cathode. However, Silvaco Atlas has a limit of 50 electrodes that can be defined. The format to define electrodes is as follows:

ELECTRODE NAME=<ELECTRODE NAME> <POSITION_PARAMETERS>

BOTTOM and TOP statements specify that the electrode is positioned along the bottom or the top of the device, respectively. Otherwise, minimum and maximum position boundaries must be specified, using X.MIN, X.MAX, Y.MIN, and Y.MAX statements. From figure (3.4), the electrode statements are defined for the anode and the cathode.
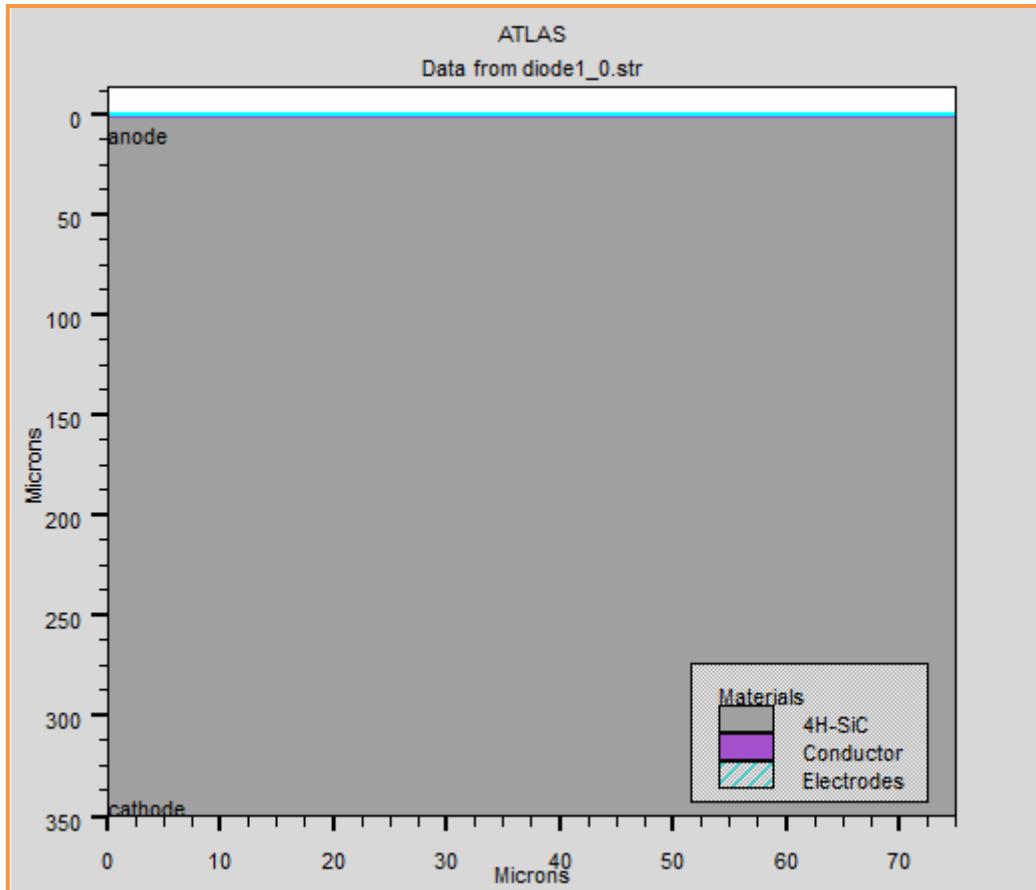
Figure 3.4: Electrodes deposition

3.4.1.4. Doping

The doping profiles can be specifies either analytically or from an input file. The doping statement must contain the distribution type of doping, the doping concentration, the dopant type and the position parameters.

The position parameters can be defined by x.min, x.max, y.min and y.max or by material type or by region number. For example can be specify as flows

DOPING N.TYPE CONC=1.2E16 UNIFORM MATERIAL=4H-SIC

From figure (3.5), the doping types and the doping levels are defined. Doping can be n-type or p-type. The distribution type can be uniform or Gaussian.
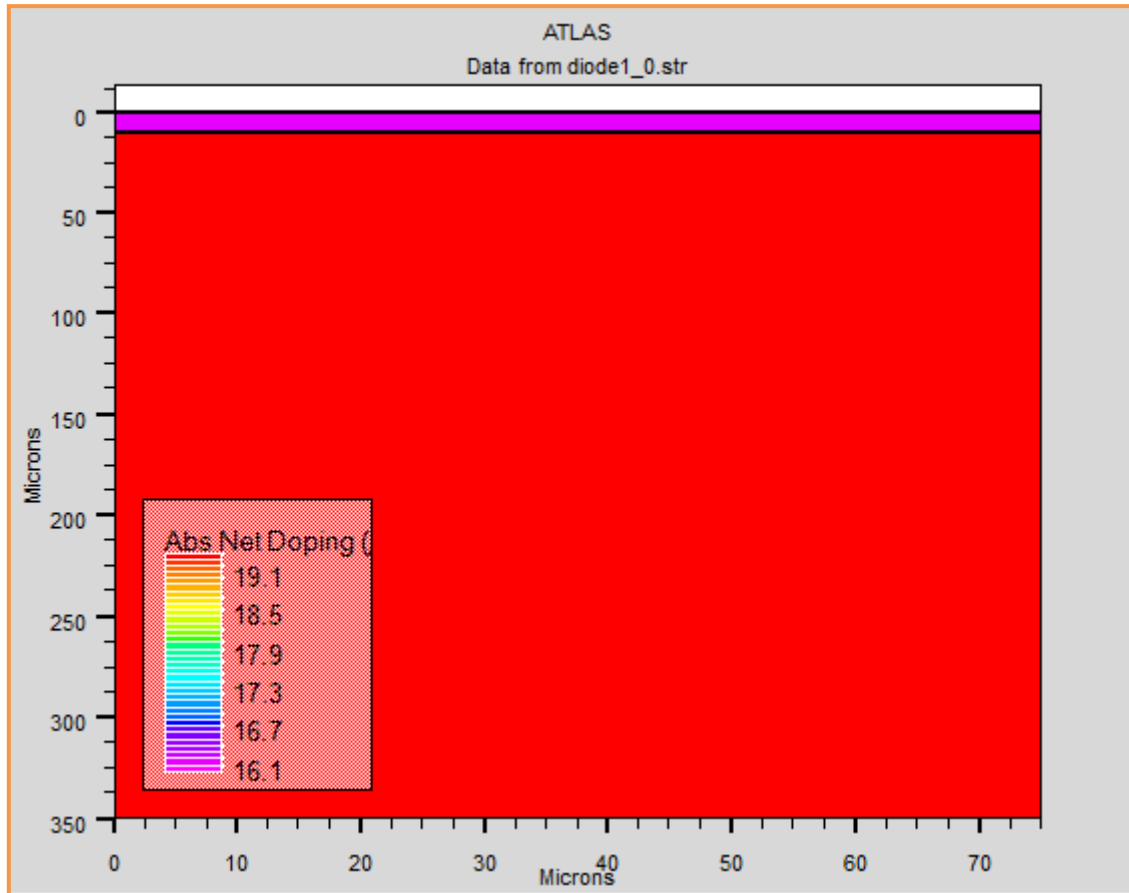
Figure 3.5. ATLAS doping

3.4.2. Material and model specification

After the definition of the structure the material parameters, physical model, the contact and interface specification must be given in this sequence to Atlas used during the device simulation.

3.4.2.1. Specifying material properties

All materials are split into three classes: semiconductors, insulators and conductors. Each class requires a different set of parameters to be specified. For semiconductors, these properties include a lot of parameters such as electron affinity, band gap, density of states, etc. There are default parameters for material properties used in device simulation for many materials but is better to define the parameters manually. If a material does not exist then it must defined with the name of existing material using its own parameters values instead the values of the existing material. The syntax of material statement is written as

MATERIAL <LOCALIZATION> <MATERIAL_DEFINITION>

70

The localization can be defined by region if for example the same material constitutes several but with different parameters such as semiconductor with different alloy composition, or it can be done with material statement, for example

MATERIAL MATERIAL=4H-SiC AFFINITY=3.3

Various other parameters can be defined as the material statement. Examples of these parameters are the band gap at room temperature (EG300), electron mobility (MUN), electron (TAUN0) and hole (TAUP0) recombination lifetimes, conduction band density at room temperature (NC300), among others.

3.4.2.2.   Specifying Physical Models

Physical models are specified using the MODELS statement except impact ionization models which are specified using IMPACT statements. The parameters for these models appear on many statements including: MODELS, IMPACT, MOBILITY, and MATERIAL. The physical models can be grouped into five classes: mobility, recombination, carrier statistics, impact ionization, and tunneling. Some physical model Atlas activate them by default such as low filed mobility model and density of states temperature dependence with default material parameters, when the material parameters are defined in the MATERIAL statement Atlas use these parameters to calculates this physical models. Other physical models are activated when their material parameters are defined in the MAERIAL, CONTACT, or INTERFACE statements such as image force lowering and thermionic emission current. The MODEL statement used in this work is given as:

  MODEL TEMPERATURE=303 SRH AUGER INCOMPLETE BGN ANALYTIC PRINT

TEMPERATURE: defined the lattice temperature where the parameters and the electrical characteristics will be calculated.

SRH : activates Schokcley-Read-Hall recombination.

 AUGER: activates Auger recombination.

INCOMPLET: activates incomplete ionization of impurity.

BGN: Specifies bandgap narrowing model.

 ANALYTIC: Specifies an analytic concentration dependent mobility model for silicon which includes temperature dependence.

PRINT: lists to the run time output the models and parameters, which will be used during the simulation. This allows the verification of models and material parameters.

3.4.2.3.   Specifying Contact Characteristics

An electrode in contact with semiconductor material is assumed by default to be ohmic. If a work function is defined in the CONTACT statement, the electrode is treated as a Schottky contact. The NAME parameter is used to identify which electrode will have its properties modified. The NUMBER parameter is used to define the electrode number in case there is several electrodes have the same name. Here will see the CONTACT statement parameters used in this work. The WORKFUNCTION parameter sets the workfunction of the electrode. For example, the statement:

CONTACT NAME= anode WORKFUNCTION=4.53 BARRIER

•   WORKFUNCTION: used to define the metal work function that used as Schottky contact.

•   BARRIER: Turns on the barrier lowering for Schottky contact.

3.4.2.4.   Specifying Interface Properties

The INTERFACE statement is used to define the interface charge density, surface recombination velocity at interfaces between semiconductors and insulators. The interface statement can be written as

INTERFACE <LOCALIZATION> <PARAMETER>

3.4.3. Numerical method selection

ATLAS allows several different methods for calculating the solution for semiconductor device problems [108,109]. For each model type there are three types of solution techniques: (a) decoupled (GUMMEL), (b) fully coupled (NEWTON) and (c) BLOCK. The GUMMEL method will solve for each unknown in turn keeping the other variables constant, repeating the process until a stable solution is achieved. The NEWTON method solves the total system of unknowns together. The BLOCK methods will solve some equations fully coupled while others are decoupled.

Generally, the GUMMEL method is useful where the system of equations is weakly coupled but has only linear convergence. The NEWTON method is useful when the system of equations is strongly coupled and has quadratic convergence. The NEWTON method may,

however, spend extra time solving for quantities, which are essentially constant or weakly coupled. NEWTON also requires a more accurate initial guess to the problem to obtain convergence. Thus, a BLOCK method can provide for faster simulations times in these cases over NEWTON. GUMMEL can often provide better initial guesses to problems. It can be useful to start a solution with a few GUMMEL iterations to generate a better guess. Then, switch to NEWTON to complete the solution. Specification of the solution method is carried out as follows:

<p align="center">METHOD NEWTON MAXTRAP=10</p>

MAXTRAP parameters Specifies the number of times the trap procedure will be repeated in case of divergence. The value of MAXTRAPS may range from 1 to 10.

3.4.4. Solution specification

Atlas can calculate DC, AC small signal, and transient solutions. Obtaining solutions is similar to setting up parametric test equipment for device tests. The user defines the voltages on each of the electrodes in the device. Atlas then calculates the current through each electrode. Atlas also calculates internal quantities, such as carrier concentrations and electric fields throughout the device. This is information that is difficult or impossible to measure.

 The solution is obtained by specifying the statement SOLVE INIT which gives an initial guess for potential and carrier concentrations from the doping profile which help to obtain convergence for the equation used.

The terminal characteristics calculated by Atlas is stored in log file by the next statement:

<p align="center">LOG OUTFILE=NAME.LOG</p>

The bias sweep to calculate the DC and AC small signal can be done by the next statements respectively

<p align="center">SOLVE VANODE= 0.0 VSTEP= 0.1 VFINAL= 1.0 NAME= ANODE</p>

The model used in ATLAS consists of a set of fundamental equations, which link together the electrostatic potential and the carrier densities, within some simulation domain. These equations, which are solved inside any general purpose device simulator, have been derived from Maxwell's laws and consist of Poisson's equation, the carrier continuity equations and the transport equations.The current density equations, or charge transport models, are usually obtained by applying approximations and simplifications to the Boltzmann Transport Equation. These assumptions can result in a number of different transport models.

The simplest model of charge transport that is useful is the drift–diffusion model. This model is adequate for nearly all devices that were technologically feasible [109]. This model is based on the two first equations cited above.

The Poisson's equation which is expressed by:

$$\varepsilon \frac{d^2\psi}{dx^2} = -\rho(x), \tag{3.1}$$

Where ψ is the electrostatic potential, ε is the local permittivity, and ρ is the local space charge density.

The continuity equations are given by:

$$0 = \frac{1}{q}\frac{dJ_n}{dx} + G_n - R_n, \tag{3.2}$$

$$0 = -\frac{1}{q}\frac{dJ_p}{dx} + G_p - R_p, \tag{3.3}$$

where n and p are the electron and hole concentration, $\vec{J_n}$ and $\vec{J_p}$ are the electron and hole current densities, G_n and G_p are the generation rates for electrons and holes, R_n and R_p are the recombination rates for electrons and holes, and q is the electron charge.

The classic drift-diffusion equations for electrons and holes are expressed as:

$$\vec{J_n} = -q\mu_n n \frac{d\phi_n}{dx}, \tag{3.4}$$

$$\vec{J_p} = -q\mu_p p \frac{d\phi_p}{dx}, \tag{3.5}$$

Where μ_n and μ_p are the electron and hole mobilities, respectively. The quasi-Fermi levels are linked to the carrier concentrations and the potential through the two Boltzmann approximations:

$$n = n_i \exp\left(\frac{\psi - \phi_n}{k_B T}\right), \tag{3.6}$$

$$p = n_i \exp\left(-\frac{\psi - \phi_p}{k_B T}\right), \tag{3.7}$$

Where T is the lattice temperature and n_i is the effective intrinsic concentration.

The set of equations (3.l)-(3.7) can be solved for the primary variables ϕ_n, ϕ_p and ψ satisfied the boundary conditions of the derivative variables J_n, and J_p at the metal-semiconductor contact.

The user can enable the thermionic emission model by specifying any of the following parameters of the CONTACT statement: SURF.REC or BARRIERL. In this case, the quasi-Fermi levels, ϕ_n and ϕ_p, are no longer equal to $V_{applied}$. Instead, these parameters are defined by current boundary conditions at the surface [92]:

$$J_n = q(n_m - n_0)v_{Rn},\qquad\qquad(3.8)$$

$$J_p = q(p_m - n_0)v_{Rp},\qquad\qquad(3.9)$$

Where n_m, is the surface electron concentration and p_m is the surface hole concentrations. The terms, n_0 and p_0, are the equilibrium electron and hole concentrations assuming infinite surface recombination velocity. v_{Rn} and v_{Rp} and are the recombination velocities of electrons and holes in the semiconductor their values will be calculated using:

$$v_{Rn} = \frac{A_n^* T^2}{q N_c},\qquad\qquad(3.10)$$

$$v_{Rp} = \frac{A_p^* T^2}{q N_v},\qquad\qquad(3.11)$$

Here, A_n^* and A_p^* are the effective Richardson constants for electrons and holes, taking account of quantum mechanical reflections and tunneling, N_C and N_V are the conduction and valence band density of states.

The Schottky thermionic emission model also accounts for field-dependent barrier lowering mechanisms. These mechanisms are caused by image forces and possible static dipole layers at the metal-semiconductor interface [56].With barrier lowering; the amount of energy by which barrier heights are lowered is defined by:

$$\Delta\emptyset = \sqrt{\left(\frac{q E_m}{4\pi \varepsilon_s}\right)},\qquad\qquad(3.12)$$

Here, E_m is the magnitude of the electric field at the interface and ε_s the semiconductor permittivity.

3.4.5. Results Analysis

3.4.5.1. Tony plot

TonyPlot is a graphical post processing tool for use with all Silvaco simulators and is an integral part of the VWF Interactive Tools. Tony Plot can operate stand-alone or along with other VWF Interactive Tools, such as DECKBUILD, VWF, or SPDB.

To plot a log file or several log file with tony plot the statement are respectively

TONYPLOT file1.LOG

TONYPLOT - OVERLAY file1.LOG file2.LOG

3.4.5.2.   Extract

The EXTRACT command provides within the DeckBuild environment allows extracting device parameters. EXTRACT operates on the previous solved curve or structure file. By default, EXTRACT uses the currently open log file. To override this default, supply the name of a file to be used by EXTRACT before the extraction routine. For example:

EXTRACT INIT INFILE="NAME.LOG"

3.5. Calibration of device simulator

To calibrate a device simulator (ATLAS), the experimental I-V characteristics of the device obtained are set to best match the output of the DECKBUILD ATLAS program based on the same device dimension and structure. In order to obtain a match between the electrical characteristics of a real fabricated device and that with a simulated one, different advanced mobility models taking care of different scattering along with different doping profiles and different carrier transport models are analyzed iteratively, as shown in figure (3.6) [108].
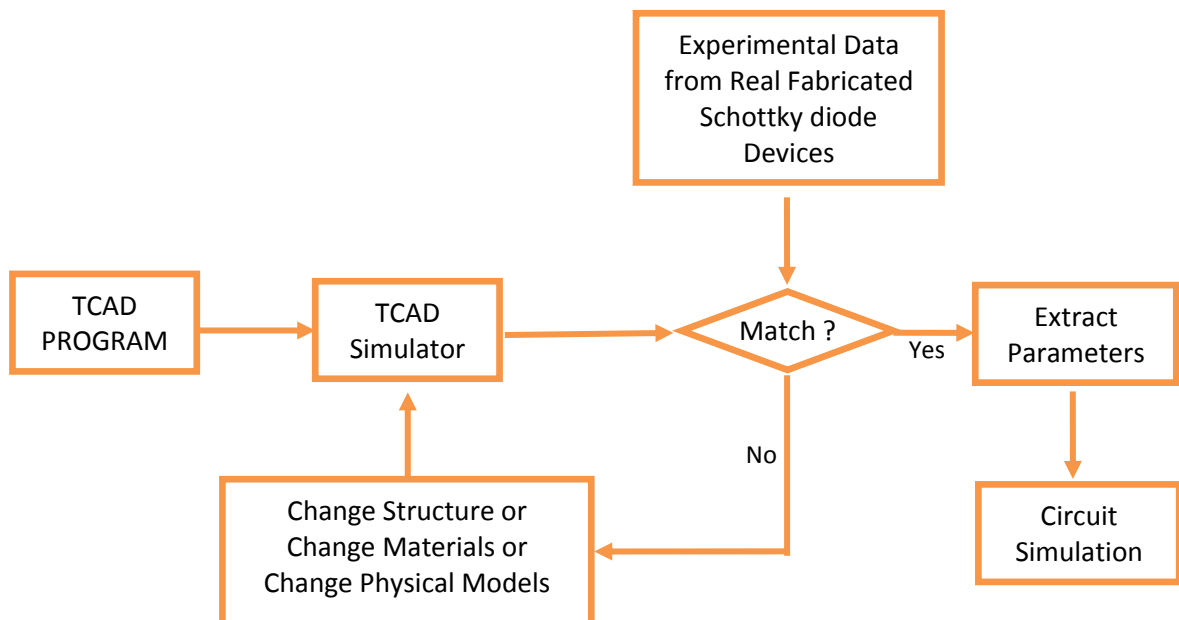
Figure 3.6: Method for calibration [108].

3.6.4H-SiC physical models and parameters

The choice of appropriate physical models is fundamental for any comparative study that involves numerical simulation. In order to fit the experimental curves, we carefully taken into account fundamental 4H-SiC physical models such as the Shockley–Read–Hall (SRH) and Auger recombination processes, the band-gap temperature dependence and apparent band-gap narrowing (BGN), the concentration and temperature dependent carrier mobility, the incomplete ionization of dopants, and the Schottky thermionic emission model involving the field-dependent barrier lowering effect.

The temperature dependence of the 4H-SiC band-gap is assumed in the form of [110]:

$$E_g(T) = E_{g0} - \alpha(T - 300) \tag{3.13}$$

where α= 3.3 x 10^{-4} eV/K is a specific material parameters, and E_{g0}= 3.26 eVis the band-gap energy at 300K.

An apparent band-gap narrowing effect as a function of the activated doping in the n-type and p-type regions, i.e. ΔE_{gn} and ΔE_{gp}, respectively, is accounted for according to the Lindefelt's model of the band edge displacements [111]:

$$\Delta E_{gn,p} = A_{n,p} \left(\frac{N_{D,A}^{+\,-}}{10^{18}}\right)^{1/2} + B_{n,p} \left(\frac{N_{D,A}^{+\,-}}{10^{18}}\right)^{1/3} + C_{n,p} \left(\frac{N_{D,A}^{+\,-}}{10^{18}}\right)^{1/4} \tag{3.14}$$

where $A_{n,p}$, $B_{n,p}$ and $C_{n,p}$, are appropriate 4H-SiC constants listed in Table 3.3 [112].

Table 3.2 Apparent band-gap narrowing parameters

	n	p
A	1.17×10⁻²	1.54×10⁻³
B	1.50×10⁻²	1.30×10⁻²
C	1.90×10⁻²	1.57×10⁻²

For the doping and temperature dependent low-field carrier mobility, the Caughey and Thomas mobility model is used [113].

$$\mu_{n,p} = \mu_{0n.p}^{min} \left(\frac{T}{300}\right)^{\alpha_{np}} + \frac{\mu_{0n.p}^{max} \left(\frac{T}{300}\right)^{\beta_{n.p}} - \mu_{0n\,p}^{min} \left(\frac{T}{300}\right)^{\alpha_{n.p}}}{1+\left(\frac{T}{300}\right)^{\gamma_{n.p}} \left(\frac{N}{N_{n.p}^{crit}}\right)^{\delta_{n.p}}} \tag{3.15}$$

Where N is the local concentration of the ionized impurities. The model parameters μ_0^{min}, μ_0^{max}, N^{crit}, α, β, γ and δ, are taken from [110,113] and summarized in Table 3.4.

<div align="center">

Table 3.3 4H-SiC carrier mobility parameters

</div>

	n	p
μ_0^{min} (cm²/Vs)	40	15.9
μ_0^{max} (cm²/Vs)	950	125
N^{crit} (cm^{-3})	2×10^{17}	1.76×10^{19}
α	0.50	0.50
β	2.40	2.15
γ	0.76	0.34
δ	0.76	0.34

Assuming the Fermi-Dirac statistics, the incomplete ionization of impurities can be expressed by means of [112, 114]

$$N_{A,D}^{-+} = N_{A,D}\left(\frac{-1+\sqrt{1+4g_{V,C}\frac{N_{A,D}}{N_{V,C}^{(T)}}e^{\frac{\Delta E_{A,D}}{kT}}}}{2g_{V,C}\frac{N_{A,D}}{N_{V,C}^{(T)}}e^{\frac{\Delta E_{A,D}}{kT}}}\right) \tag{3.16}$$

where, N_D and N_A are the n-type and p-type doping concentrations, ΔE_D and ΔE_A are the donor and acceptor energy levels, and $g_C = 2$ and $g_V = 4$ are the appropriate degeneracy factors of the conduction and valence band, respectively. N_C and N_V are the electron and hole density of states varying with temperature as given by [37]:

$$N_{C,V}(T) = N_{C,V\,300}\left(\frac{T}{300}\right)^{3/2} \tag{3.17}$$

Here, $N_{C300} = 1.66\times10^{19}$ cm^{-3} and $N_{V\,300} = 3.29\times10^{19}$ cm^{-3} are the electron and hole density of states at room temperature.

The Auger and SRH recombination rates are modeled using the standard expressions [115]:

$$R_{Auger} = (C_n n + C_p p)(np - n_i^2) \tag{3.18}$$

$$R_{SRH} = \frac{np - n_i^2}{\tau_n \left(p + n_i \exp\left(-\frac{E_{trap}}{kT}\right) \right) + \tau_p \left(n + n_i \exp\left(\frac{E_{trap}}{kT}\right) \right)} \tag{3.19}$$

where $C_n = 5 \times 10^{-31}$ cm^{6}s^{-1} and $C_p = 2 \times 10^{-31}$ cm^{6}s^{-1} are the Auger coefficients [116], E_{trap} is the difference between the trap energy level and the intrinsic Fermi level, and τ_n and τ_p are the carrier lifetimes modeled through the semi-empirical formula proposed in [117] considering a temperature dependence described by a power law [118]:

$$\tau_{n,p} = \frac{\tau_{0n,p} \left(\frac{T}{300}\right)^{\theta_{n,p}}}{1 + \left(\frac{N}{N_{n,p}^{SRH}}\right)} \tag{3.20}$$

Here, N is the local doping concentration, $\tau_{0n} = 500$ ns and $\tau_{0p} = 100$ ns are process-dependent parameters, and $N_{n,p}^{SRH} = 5 \times 10^{16}$ cm^{-3} is a reference constant [119].

Finally, the barrier height $(\emptyset_B)$ is modelled with the standard expression [109]

$$\emptyset_B = \left(\theta_M - \chi_S \right) \tag{3.21}$$

where the metal work function θ_M was fixed to 4.33 eV, 4.53 eV and 4..55eV for Al/Ti, Mo and W respectively [26-28], and the electron affinity χ_S was used as fitting parameter as in [120,121].

It must be noted that the assumed simulation setup has also been used in other recent manuscripts addressed to the study of SiC-based devices [122-125] and it is supported by experimental results on both Schottky and p-i-n diodes [1,10,126].

Chapter 4:
Results and discussion

4.1. Introduction

Starting from the experimental results on Ti/Al 4H–SiC, Mo/4H–SiC and W/4H–SiC Schottky barrier diodes (SBDs) reported in recent literatures [26-28]. In this chapter, the forward *I-V* characteristics of these devices are investigated by means of a combined numerical and analytical simulation study in wide temperatures range in order to explain the abnormal behavior observed in the experimental I–V characteristics and evaluate the suitability of these devices as temperature sensors. The temperature dependencies of the current transport parameters are explained based on the assumption of the existence of Gaussian distribution (GD) of the Schottky barrier around the Metal/ 4H–SiC interface. Finally, the performance of temperature sensors based on Ti/Al 4H–SiC, Mo/4H–SiC and W/4H–SiC Schottky diodes are investigated. In particular, sensitivity, linearity and root mean square error (RMSE) are accurately analyzed in a wide temperatures range.

4.2. Simulation and analysis of the current–voltage–temperature (*I-V-T*) characteristics of Ti/Al 4H-SiC Schottky diode for high performance temperature sensor

In this section, simulation and measurements of the current–voltage–temperature characteristics of Ti/Al 4H–SiC diode are compared. Since the analysis of the diode is focused on the performance as temperature sensor, only the forward curves are modeled through ATLAS Silvaco numerical simulator.

In order to fit the experimental curves, we carefully taken into account fundamental physical models such as the Shockley–Read–Hall (*SRH*) and Auger recombination processes, the band-gap temperature dependence and apparent band-gap narrowing (*BGN*), the concentration and temperature dependent carrier mobility, the incomplete ionization of dopants, and the Schottky thermionic emission model involving the field-dependent barrier lowering effect. The 4H-SiC physical parameters are set as in chapter 3.

The forward *I–V-T* characteristics for Schottky diodes are usually used in order to identify the different conduction mechanisms in current transport. At first, we consider a pure thermionic emission (*TE*) theory in our simulation that we will later modify to account for the T_0 effect.

4.2.1. Device structure

A schematic cross sectional view of the 4H-SiC Schottky diodes considered in this work is shown in figure (4.1) (plot not in scale).
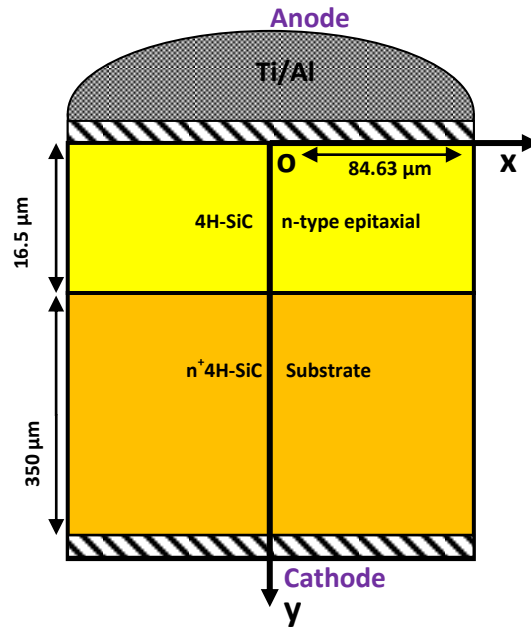
Figure. 4.1. Ti/Al 4H-SiC Schottky barrier diode schematic cross section.

The experimental devices were fabricated and provided by the CNR-Institute for Microelectronics and Microsystems (IMM), unit of Bologna (Italy). They are based on a commercial available <0001> 7°62' off-axis n/n⁺4H-SiC epitaxial wafer with a resistivity of 0.021 Ω·cm. The epi-layer is 16.5 μm-thick and has a net doping density of 3×10^{15} cm⁻³.

The fabrication processes involve standard technological steps ensuring good reproducibility of the samples. Photolithography and wet chemical etching were used to define the Ti/Al Schottky contact with an area of about 2.25×10^4 μm². Finally, a 200 nm-thick nickel (Ni) film was deposited on the n⁺ back surface of the wafer to form the cathode contact, and an annealing treatment was performed in vacuum at 1000 °C for 2 min.

A Micromanipulator probe station and a HP4156B parameter analyzer were used to obtain the *I-V* characteristics of the diodes. Further details about the diode fabrication process are provided in [26] and references therein.

4.2.2. Study of the *I-V* characteristics of Ti/Al 4H-SiC Schottky diode using numerical simulation analysis

The measured and simulated forward *I-V-T* curves of the considered Ti/Al 4H-SiC SBDs obtained by using Atals-Silvaco for ten different temperatures from 85 K to 445 K are shown in figure (4.2).
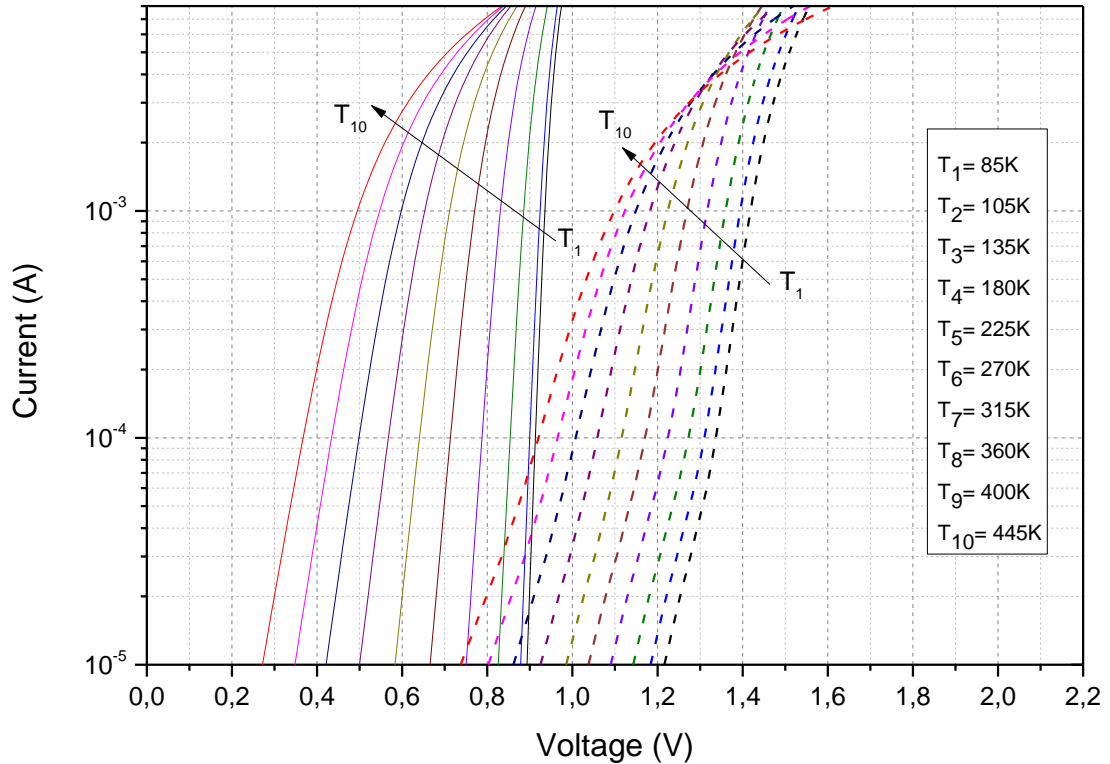
Figure.4.2.Experimental (dashed lines) and simulated (solid lines) current–voltage characteristics of the Al/Ti/4H–SiC Schottky diode at different temperatures.

As shown in figure (4.2), the simulated characteristics obtained by considering a pure thermionic emission (*TE*) theory with homogeneous Schootky barrier height do not fit the experimental ones. The simulated current is found to be greater than the experimental current by several orders of magnitude in temperature range of 85-445 K. Thus, for the same forward current, the Schottky diode will have about 0.4V less voltage drop than the experimental results.

As evident from figure (4.2), the interesting observation is that the experimental *ln(I)–V* curves intersect, unlike the curves generated by using Atlas Silvaco. The intersecting behaviour of current–voltage characteristics of Schottky diodes have been investigated by Subhash Chand [127]. The results showed that the crossing of *ln(I)–V* curves is an inherent property even of homogeneous Schottky diodes of constant BH and is normally hidden due to saturation in current caused by series resistance. While the intersection of the *ln (I) -V* curves is observable in the normal range due to the apparent temperature-dependent BH in inhomogeneous Schottky diodes.

A correspondence between the results obtained by Subhash [127] and those shown in figure (4.3) can be observed when we increase the current bias value above 10 uA.
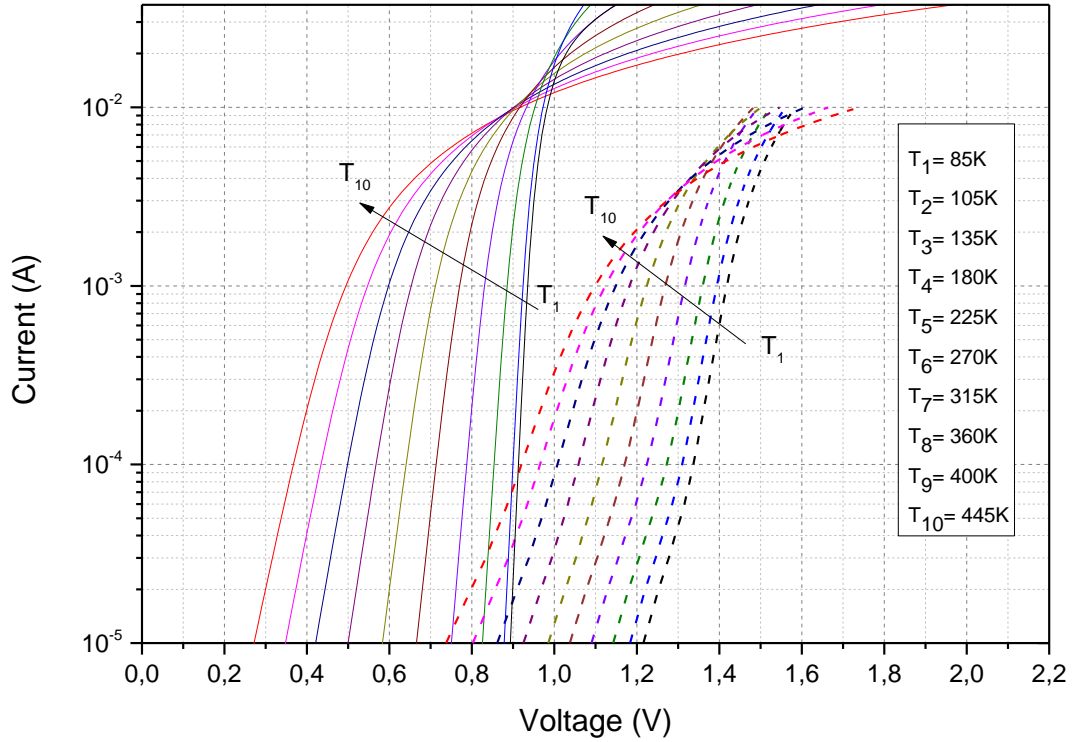
Figure.4.3.Experimental (dashed lines) and simulated (solid lines) current–voltage characteristics of the Al/Ti/4H–SiC Schottky diode at different temperatures.

By assuming the TE theory in the current range for each temperature, the current-voltage conduction model can be considered in the form of [84, 128]

$$I = I_0 \left[exp \left(\frac{qV - R_s I}{nkT} \right) - 1 \right] \qquad (4.1)$$

where, n is the ideality factor, V is the diode bias voltage, Rs is the series resistance, q is the electronic charge , k is the Boltzmann constant, and I_0 is saturation current given by:

$$I_0 = AA^* T^2 exp \left(-\frac{q\emptyset_B}{kT} \right) \qquad (4.2)$$

where $\emptyset_B$ is the zero-bias barrier height, A is the area of the diode, and A^* is the Richardson constant that takes into account the quantum mechanical reflections and tunneling phenomena. Its value is theoretically in the order of $A^* =146$ Acm^{-2}K^{-2}for n-type 4H-SiC [129].

Hence, when forward-biased, the diode voltage drop can be written as follows:

$$V = R_s I + n\emptyset_B + \frac{kTn}{q} ln \left(\frac{I}{AA^* T^2} \right) \qquad (4.3)$$

From the experimental and simulated I–V-T curves in figure (4.2) we extracted the fundamental diode parameters I_0 ,$\emptyset_B$, n and Rs similarly to[130].

In particular, at each temperature, the saturation current I_0 was determined from the intercept of the plot $ln(I)$ vs V for $V = 0$. Afterwards, the barrier height $\emptyset_B$ was calculated from equation (4.2) resulting $\emptyset_B = (kT/q)ln(AA^*T^2/I_0)$.

The obtained values of the SBH, the ideality factor, the saturation current and the series resistance as a function of temperature are shown in Table (4.1).

Table 4.1: The simulated and experimental parameters obtained from *I–V* characteristics.

T (K)	Simulated parameters				Experimental parameters			
	$\emptyset_B$ (eV)	n	I_0(A)	$R_s(\Omega)$	$\emptyset_B$ (eV)	n	I_0(A)	$R_s(\Omega)$
445	1,024	1,0791	$1,45 \times 10^{-08}$	36,23	1,312	1,445	$7,56 \times 10^{-12}$	57,12
400	1,0176	1,0741	$9,15 \times 10^{-10}$	30,43	1,273	1,463	$5,62 \times 10^{-13}$	46,94
360	1,0121	1,0695	$3,45 \times 10^{-11}$	25,24	1,230	1,473	$3,13 \times 10^{-14}$	39,09
315	1,009	1,061	$3,64 \times 10^{-13}$	20,11	1,189	1,484	$5,08 \times 10^{-16}$	30,08
270	1,0085	1,0502	$5,45 \times 10^{-16}$	15,22	1,080	1,639	$2,53 \times 10^{-17}$	20,72
225	1,0151	1,0319	$4,02 \times 10^{-20}$	10,93	0,983	1,782	$2,04 \times 10^{-19}$	15,06
180	1,0208	1,018	$1,45 \times 10^{-26}$	7,184	0,822	2,142	$5,90 \times 10^{-21}$	11,25
135	1,0221	1,0144	$3,86 \times 10^{-36}$	6,631	0,655	2,699	$1,95 \times 10^{-22}$	10,98
105	1,0237	1,0124	$1,15 \times 10^{-47}$	6,056	0,525	3,371	$1,44 \times 10^{-23}$	10,86
85	1,0283	1,0048	$3,81 \times 10^{-59}$	5,035	0,407	4,394	$2,28 \times 10^{-22}$	10,37

As we can see, n and $\emptyset_B$ extracted from simulated *I-V* characteristics do not show temperature dependence behavior, the saturation current values are found to be less than the experimental current by several orders of magnitude in temperature range of 85–180 K.

The increase of experimental saturation current values Compared to simulated ones could be related either to a decrease of the Schottky barrier or to the presence of deep levels in the band gap. However, it has been already reported that no deep level has been evidenced by deep-level transient spectroscopy (DLTS) measurements in the diode annealed at high-temperature [129, 131]. Thus, the significant changes occurring in the forward characteristics after high-temperature annealing (1000 °C in our case) can be associated to a modification of the Schottky barrier. In this case, other phenomena should be considered to fit the experimental curves.

4.2.3. Study of the *I-V* characteristics of Ti/Al 4H-SiC Schottky diode by means of a combined numerical and analytical simulation

In order to precisely fit the experimental *I-V* characteristics of Schottky diodes, where a variation of *n* with temperature is observed, Padovani and Sumner [15] have suggested replacing *T* by (T_0+n_0T) in the thermionic-emission model. Therefore, equation (4.1) becomes:

$$I = I_0 \left[exp\left(\frac{qV - R_sI}{k(n_0T + T_0)} \right) - 1 \right]$$

(4.4)

Where n_0 and T_0 are constants, T_0 is independent of temperature and voltage over a wide range of temperatures. This is equivalent to writing $n=n_0+(T_0/T)$.

When thermionic-field emission (TFE) and field emission (FE) are assumed to be the dominant mechanisms in the *I-V* behavior of the Schottky barrier diode, then in this case T_0 is not constant with respect to temperature. It increases at lower temperatures [100]. All the mechanisms which have been invoked to explain the form of the *I-V* characteristic (i.e. *n* values greater than unity) also affect the zero-bias barrier height [84].

when forward-biased, equation (4.3) can be written as follows:

$$V = R_sI + n_0\emptyset_B + \frac{kTn_0}{q} ln\left(\frac{I}{AA^*T^2} \right) + \emptyset_B \frac{T_0}{T} + \frac{kT_0}{q} ln\left(\frac{I}{AA^*T^2} \right) = V_1 + V_2$$

(4.5)

With

$$V_1 = R_sI + n_0\emptyset_B + \frac{kTn_0}{q} ln\left(\frac{I}{AA^*T^2} \right)$$

(4.6)

$$V_2 = \emptyset_B \frac{T_0}{T} + \frac{kT_0}{q} ln\left(\frac{I}{AA^*T^2} \right)$$

(4.7)

To simulate experimental results, we use Atlas-Silvaco to get the term V_1 of equation (4.5), after calibrating the barrier height as such mentioned in [120] and [121]. Then, we vary the value of T_0 until good agreement was reached between the two sets of data as shown in figure (4.4).

A shunt resistance of $Rsh = 1.3 \times 10^5 \Omega$ was also added to account for the side-wall leakage and other leakage paths and to reproduce the low voltage.
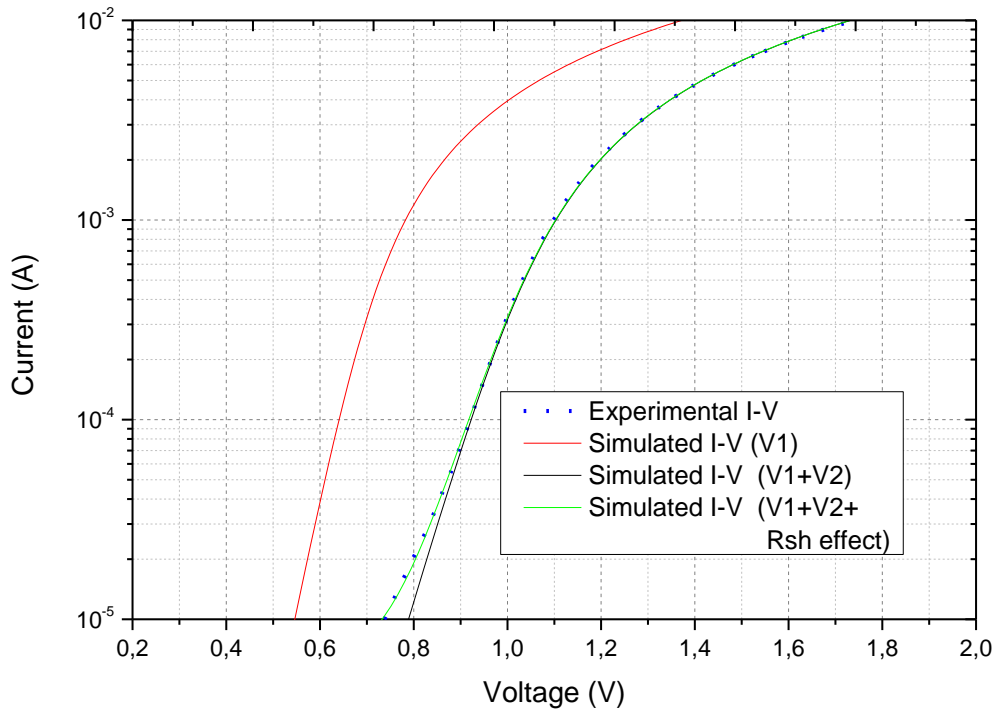
Figure.4.4.Experimental (dotted lines) and simulated (solid lines) current–voltage characteristics of the Al/Ti/4H–SiC Schottky diode at 445K.

The measured and simulated forward *I-V-T* curves of the considered Ti/Al 4H-SiC SBDs for ten different temperatures from 85 K to 445 K are shown in figure (4.5). The diodes were current biased in the range 10 µA ≤ *I* ≤ 10 mA with a current resolution of 10 nA. It is worth noting that the results obtained by means of a combined numerical and analytical simulation are in good agreement with the experimental data.
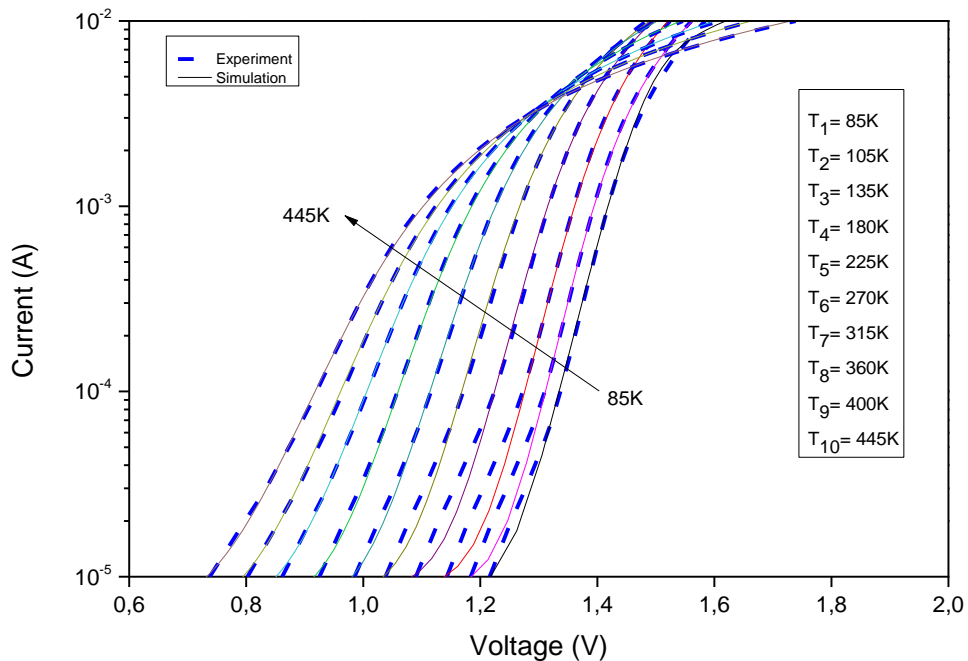
Figure.4.5.Experimental (dashed lines) and simulated (solid lines) current–voltage characteristics of the Al/Ti/4H–SiC Schottky diode at different temperatures.

86

The values of the zero-bias barrier height $\emptyset_B$ and the ideality factor n of the diode at de different temperatures are calculated from the *I–V* characteristics of figure (4.5) and given in figure (4.6) and table (4.2).
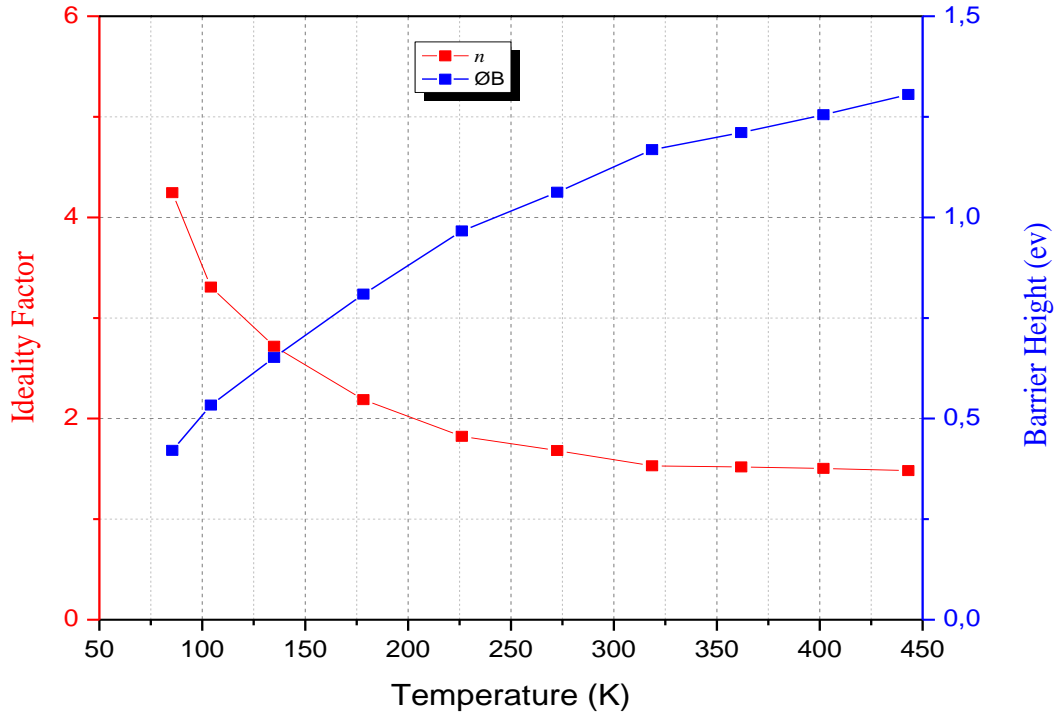
Figure. **4.6**. Ideality factor and barrier height behaviors
as a function of temperature for the device in Figure.4. 2.

Table 4.2: Summary of the temperature dependent values of the Schottky barrier height ($\emptyset_B$), ideality factor (*n*), series resistance (*Rs*) and reverse current (*I₀*) obtained from the Simulated *I-V* characteristics.

T (K)	Simulated parameters			
	$\emptyset_B$ *(eV)*	*n*	*$I_0(A)$*	*$R_s(\Omega)$*
445	1,3054	1,4827	$9,13 \times 10^{-12}$	55,39
400	1,2552	1,5038	$9,58 \times 10^{-13}$	46,14
360	1,2106	1,5184	$5,94 \times 10^{-14}$	37,81
315	1,1684	1,5301	$1,10 \times 10^{-15}$	28,91
270	1,0624	1,6821	$5,48 \times 10^{-17}$	20,6
225	0,9662	1,8236	$4,95 \times 10^{-19}$	15,55
180	0,8091	2,1871	$1,40 \times 10^{-20}$	11,47
135	0,6518	2,7187	$2,65 \times 10^{-22}$	9,748
105	0,5334	3,3063	$5,81 \times 10^{-24}$	11,07
85	0,421	4,2449	$3,48 \times 10^{-23}$	12,83

As can be seen in figure (4.6), both parameters exhibit strong temperature dependence; that is, the ideality factor decreases while the barrier height increases with increasing temperature.

As shown in figure (4.5), the forward bias *I-V* characteristics are linear on a semilogarithmic at low forward bias voltages, but deviate from linearity due to the effect of series resistance *Rs*. Figure (4.7) shows the plot of series resistance values obtained against temperature. The series resistance increase with increasing temperature as could be expected for semiconductors in the temperature region where there is no carrier freezing out, which is non-negligible only below ~100 K [56]. Similar temperature dependence was obtained theoretically by Osvald and Horvath [132] and experimentally for the epitaxial-layer of a Ti/4H-SiC, Mo/4H-SiC and W/4H-SiC diodes [26-28].
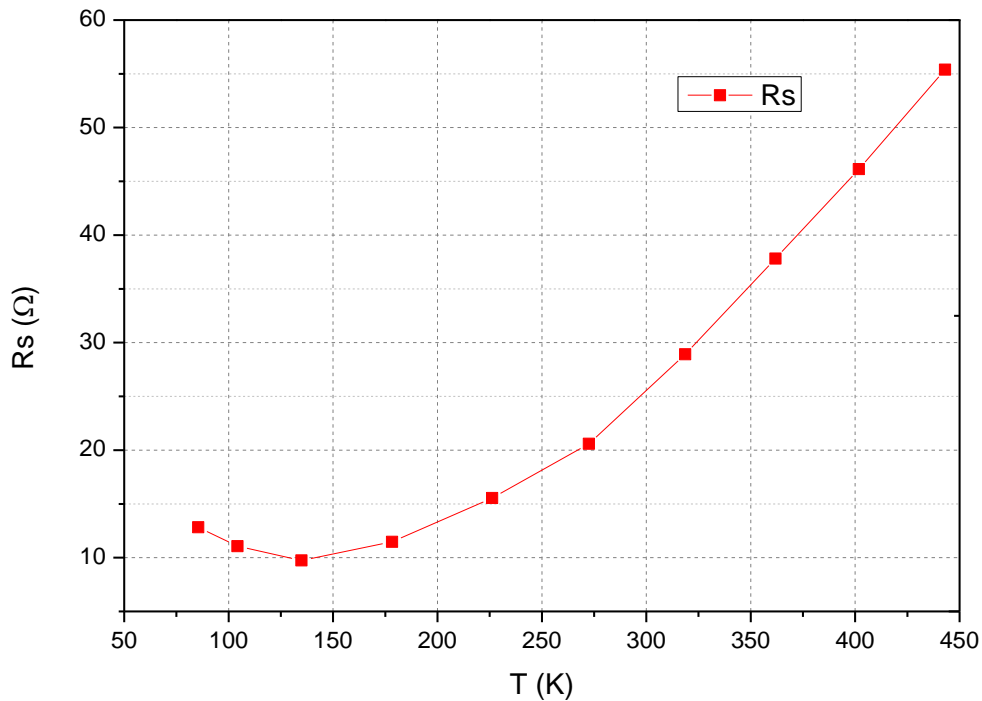
Figure.4.7. The temperature dependence of the series resistance.

By considering equation (4.2) in the form of $ln(I_0/T^2) = ln(AA^*) - (q/kT)\emptyset_B$, the Arrhenius plot of term $ln(I_0/T^2)$against 1000/*T* is shown in figure (4.8).

The Arrhenius plot shows a significant deviation of the term $ln(I_0/T^2)$ from linearity at low temperatures and the data fit asymptotically to a straight line only at higher temperatures (*T*> 270 K). From the slope of this straight line, an activation energy of 0.82 eV was obtained. At the same time, from the line intercept with the ordinate axis, the Richardson constant *A** is 4.64×10^{-4} Acm^{-2}K^{-2}, namely a much lower value than the theoretical one expected for n-type 4H-SiC.
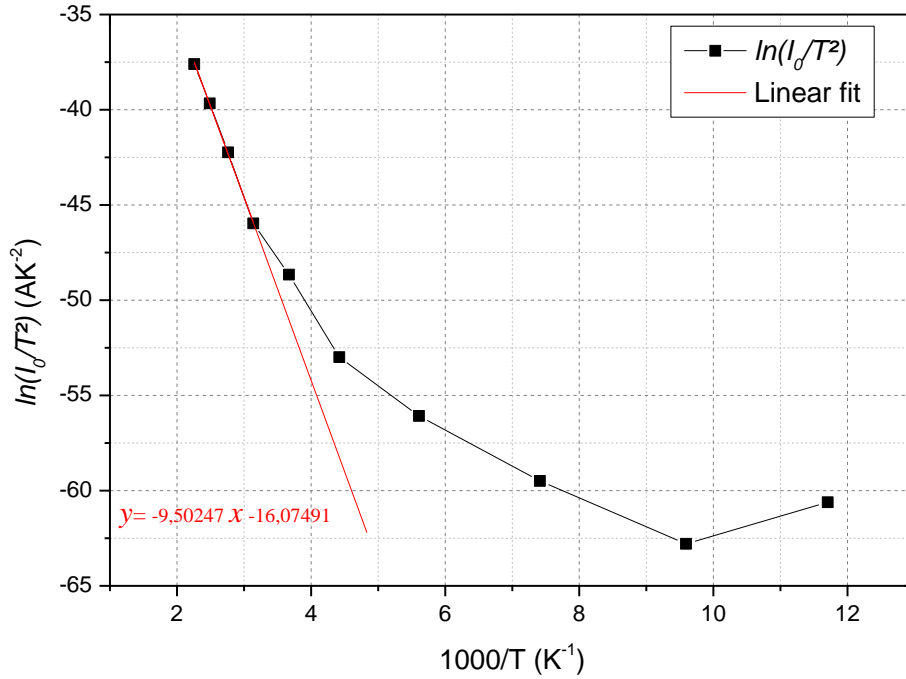
Figure.4. 8.Arrhenius plot of $ln(I_0/T^2)$vs.$1000/T$.

The strong temperature-dependence of the barrier height and ideality factor can be attributed to several reasons. The most common explanation is the deviation from the pure TE theory due to the contribution of other current mechanisms, mainly thermionic field emission (TFE), and field emission (tunnelling, FE) through the barrier, and also recombination current in the depletion region [18, 133]. Barrier lowering due to image force effects can also contribute to the abnormal reduction in barrier height with temperature. Another possible explanation of the temperature-dependent barrier height and ideality factor is attributed to the theory of barrier inhomogeneity, which assumes a formation of a laterally nonuniform Schottky contact with different barrier heights of Gaussian distribution (GD) [19, 20,134].

In the next sections, the temperature dependency effect of $\emptyset_B$ and n of the Ti/Al 4H-SiC based Schottky diodes will be discussed taking into consideration different possible explanations.

4.2.4. The image force effect

In order to understand the factors influencing the barrier height (BH) lowering and the ideality factor increase with decreasing temperature, the image-force effect was considered at first. In particular, the BH lowering due to the image-force mechanism was modeled in the form of [84].

$$\Delta\emptyset = \left\{\left(\frac{q^3 N_D}{8\pi^2 \varepsilon_s^3}\right)\left[\emptyset_B - V - \zeta - \frac{kT}{q}\right]\right\}^{1/4} \tag{4.8}$$

where V is the applied bias voltage, $\varepsilon_s = 9.66\varepsilon_0$ is the material permittivity, N_D is the ionized impurity concentration, and $\zeta = (kT/q)ln(N_c/N_D)$. The value of N_D varies from 4.85×10^{15} cm^{-3} at 85K to 3×10^{15} cm^{-3} at 445K, respectively.

The calculated $\Delta\emptyset$ varies from 7.332 meV to 17.059 meV in the $85 - 445$ K temperature range for the barrier height $\emptyset_B$ ranging from 0.421 eV to 1.305 eV as in figure (4.6). These results point out that the influence of the barrier lowering due to the image-force on $\emptyset_B$ is nearly constant and the image-force effect alone cannot determine the observed device characteristics.

At the same time, the diode ideality factor can be calculated by using the following expression [84]:

$$\frac{1}{n} = 1 - \frac{1}{4}\left(\frac{q^3 N_D}{8\pi^2 \varepsilon_s^3}\right)^{\frac{1}{4}}\left[\emptyset_B - V - \zeta - \frac{kT}{q}\right]^{-\frac{3}{4}} \tag{4.9}$$

It varies from 1.006 to 1.012 showing a negligible effect of the image-force lowering on the device forward current behavior. In addition, the n value is very close to 1 predicting an almost unrealistic homogeneous barrier at the diode interface.

4.2.5. Flat-band barrier height and modified Richardson plots

The barrier height, which decreases with decreasing temperature, obtained from equation (4.2) is called apparent or zero –bias barrier height. The barrier height obtained under flat-band condition is called flat-band barrier height and considered to be real fundamental quantity. Unlike the case of zero-bias barrier height, the electric field in the semiconductor is zero under the flat-band condition [135-138].

$\emptyset_B$ is the zero-bias barrier height

N_c is the effective density of states in the conduction band

 N_D the ionized donor density of the 4H-SiC.

To find the value of $\emptyset_{Bf}$, the following expression is used [139]

$$\emptyset_{Bf} = n\emptyset_B - (n-1)\left(\frac{kT}{q}\right) ln\left(\frac{N_c}{N_D}\right) \tag{4.10}$$

Where N_c is the effective density of states in the conduction band and N_D ($=4.85\text{x}10^{15}$ cm^{-3} and $3\text{x}10^{15}$ cm^{-3} for T = 85 K and 445 K, respectively) the ionized donor density of the 4H-SiC.

Figure (4.9) shows the variation of $\emptyset_{Bf}$ as a function of temperature. It can be seen that the flat-band BH is larger than the zero-bias BH at low temperature. The flat-band BH of the Ti/Al 4H-SiC Schottky contacts is calculated from the zero-bias BHs and the corresponding ideality factor at various temperatures. The temperature dependence of the flat-band BH can be described by

$$\emptyset_{Bf}(T) = \emptyset_{Bf}(T = 0) + \alpha T \tag{4.11}$$

where $\emptyset_{Bf}(T = 0)$ is the flat band barrier height extrapolated to $T = 0$ K and α is its temperature coefficient.

The value of N_c as function of temperature can calculate by $2(2\pi m^* kT/^2)^{3/2}$ with m^* being the majority carrier effective mass, $m^* = 0.02\ m_e$ for 4H-SiC [129].

The effective density of states N_c will change with temperature according to the relation

$$N_C(T) = N_{C\ 300}\left(\frac{T}{300}\right)^{3/2} \tag{4.12}$$

Here, $N_{C\ 300} = 1.66\times10^{19}$ cm^{-3} is the electron density of states at room temperature.

The value of N_c varies from $2.52\text{x}10^{18}$ cm^{-3} at 85K to $2.98\text{x}10^{19}$ cm^{-3} at 445K, respectively.
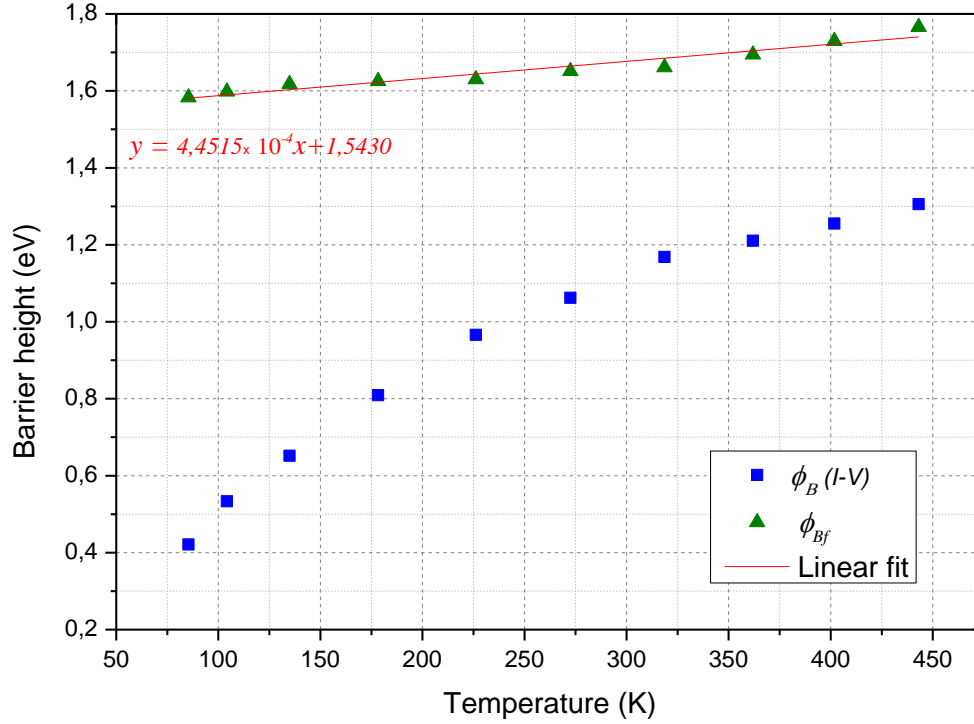
Figure.4. 9. Temperature dependence of the zero-bias BH $\emptyset_B$ and flat-band BH $\emptyset_{Bf}$ for the Al/Ti/4H–SiC Schottky barrier diode in the temperature range of 85–445 K.

In figure (4.9), the fitting of $\emptyset_{Bf}(T)$ data in equation (4.11) provides $\emptyset_{Bf}(T = 0)= 1.54$ eV and α=4.54 x 10^{-4} eV K^{-1}, which is probably due to extremely high values of the ideality factor, due to its increase with decreasing temperature. In contrast, in the case of zero-bias BHs, the electric field in the semiconductor is zero under the flat-band condition and thus the energy bands are flat, which eliminates the effect of tunneling and image force lowering that would affect the *I-V* characteristics and removes the influence of lateral inhomogeneity [135-138].

Flat-band saturation current density I_{0f} can be written similar to the equation (4.2) as [136]

$$I_{0f} = AA^*T^2 exp\left(-\frac{q\emptyset_{Bf}}{nkT}\right)$$ (4.13)

So, the relation between I_{0f} and zero-bias saturation current density I_0 is given by

$$I_{0f} = I_0 exp\left(\left(\frac{n-1}{n}\right) ln\left(\frac{N_c}{N_D}\right)\right)$$ (4.14)

When considering the ideality factor varies with temperature, the plot of $ln(J_{0f}/T^2)$ versus *1000/nT* according to equation (4.13) should be a straight line with the slope and the intercept at the ordinate, directly yielding $\emptyset_{Bf}$ and *A**, respectively. The $ln(J_{0f}/T^2)$ versus *1000/ nT* plot is also shown in the figure (4.10). The linear portion of this plot gives 0.142 eV and 0.343 A cm^{-2}K^{-2} for $\emptyset_{Bf} = (T = 0)$. These results show that the value of the Richardson constant is different

from the known theoretical value of 146 $AK^{-2}cm^{-2}$ for electrons in the n-type 4H-SiC [129]. The presented results seem to predict current transport mechanisms not following the pure TE theory and the existence of barrier inhomogeneities need to be evaluated.
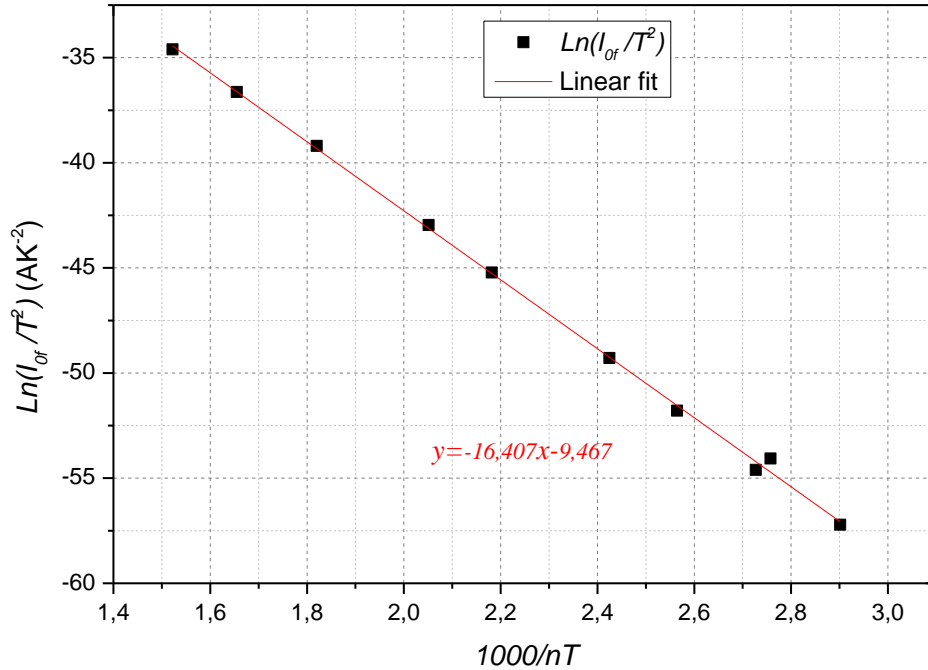
Figure.4. 10. Richardson plots of $ln(I_{0f}/T^2)$ vs. $1000/nT$
and their linear fits for the Al/Ti/4H–SiC Schottky diode.

4.2.6. Inhomogeneous barrier analysis

The ideality factor is simply a manifestation of the barrier uniformity [136]. A significant increase in the ideality factor and decrease in the SBH at low temperature are possibly originated by structural defects in the semiconductor, inhomogeneous doping, interface roughness, interfacial reactions, diffusion/interdiffusion of the contaminations of applied materials on semiconductor surface, inhomogeneities of thickness and composition of the layer, and non-uniformity of interfacial charges or the presence of a thin insulating layer between the metal and the semiconductor [19,134,136]. Since current transport across the MS interface is a temperature-activated process, the current will be controlled by the current through the patches having low BH at the low temperatures.

In this section, the $\emptyset_B$ and n anomalous behaviors reported above are explained by assuming spatially inhomogeneous barrier heights and potential fluctuations at the Schottky interface that consist of low and high barrier areas as suggested by Werner and Guttler in [19]. More in detail, the spatial barrier inhomogeneities in SBDs are described by assuming a Gaussian distribution $A(\emptyset_B)$ of the SBH with a standard deviation (σ) around a mean value ($\overline{\emptyset_B}$):

$$A(\emptyset_B) = \frac{1}{\sigma\sqrt{2\pi}} e^{-\frac{(\emptyset_B - \overline{\emptyset}_B)^2}{2\sigma^2}} \tag{4.15}$$

The pre-exponential term is a normalization constant. The total forward current across the Schottky barrier diode is given by:

$$I = \int i(V, \emptyset_B) A(\emptyset_B) d\emptyset_B \tag{4.16}$$

where $i(V, \emptyset_B)$ is the current based on the TE model (Equation4.1). It is assumed that $\overline{\emptyset}_B$ and σ are linearly bias-dependent on Gaussian parameters as follows:

$$\overline{\emptyset}_B = \overline{\emptyset}_{B0} + \rho_2 V \tag{4.17}$$

$$\sigma^2 = \sigma_0^2 + \rho_3 V \tag{4.18}$$

where $\overline{\emptyset}_{B0}$ and σ_0 are the zero-bias reference parameters, and ρ_2 and ρ_3 are temperature-independent voltage coefficients which model the voltage deformation of the barrier distribution.

By introducing $i(V, \emptyset_B)$ and $A(\emptyset_B)$ from (4.1) and (4.15) into (4.16), and performing the integration we can write:

$$I = I_0 \left[exp\left(\frac{qV - R_s I}{n_{ap} kT} \right) - 1 \right] \tag{4.19}$$

$$I_0 = AA^* T^2 exp\left(-\frac{q\emptyset_{Bap}}{kT} \right) \tag{4.20}$$

where $\emptyset_{Bap}$ and n_{ap} are the apparent SBH and ideality factor, respectively, in the form of

$$\emptyset_{Bap} = \overline{\emptyset}_{B0} - \frac{q\sigma_0^2}{2kT} \tag{4.21}$$

$$\frac{1}{n_{ap}} - 1 = -\rho_2 + \frac{q\rho_3}{2kT} \tag{4.22}$$

However, unlike single-Gaussian distribution model, it is supposed that the barrier anomalies consist of infinite number of Gaussian distributions with different mean barrier heights and standard deviations and as a result, using an arbitrary distribution function rather than any pre-assumed distribution is to be more attractive to depict inhomogeneities [23, 140]. Thus, according to multi-Gaussian approach, the arbitrary distribution function, $A(\emptyset_B)$, may be written as,

$$A(\emptyset_B) = \sum_{i=1}^{n} \frac{A_i}{\sigma_i \sqrt{2\pi}} \, exp\left(-\frac{(\emptyset_B - \overline{\emptyset}_{Bi})^2}{2\sigma_i^2}\right) \tag{4.23}$$

In equation (4.23), A_i, σ_i and $\overline{\emptyset}_{Bi}$ are the weight, the standard deviation and the mean barrier height of each Gaussian distribution, respectively. In addition, total of the A_i arbitrary distribution values from the normalization condition may be written as [23],

$$A_1 + A_2 + A_3 + \cdots + A_n = 1 \tag{4.24}$$

And the total arbitrary distribution function is expressed as,

$$A(\emptyset_B) = A_1(\emptyset_B) + A_2(\emptyset_B) + A_3(\emptyset_B) + \cdots + A_n(\emptyset_B) \tag{4.25}$$

According to the multi-Gaussian distribution approach, the temperature dependence of the barrier height can be commented by the terms of inhomogeneous Schottky contact. Thus, the relationship with the temperature of the barrier height is given by [23]

$$\emptyset_{Bap} = -\frac{kT}{q} \, ln \sum_{i=1}^{n} A_i \, exp\left(-\frac{q\overline{\emptyset}_{B0i}}{kT} + \frac{q^2\sigma_{0i}^2}{2k^2T^2}\right) \tag{4.26}$$

For example, in case of $n = 1$, equation (4.26) can be simplified to well-known formula as

$$\emptyset_{Bap} = \overline{\emptyset}_{B01} - \frac{q\sigma_{01}^2}{2kT} \tag{4.27}$$

Equation (4.27) is an equation used frequently in case of a single-Gaussian distribution of the spatial barrier height values and it yields the values of standard deviation σ_{0i} and mean barrier height $\overline{\emptyset}_{B0i}$ of each distribution region for a multi-Gaussian distribution condition.

The plot of the barrier height and ideality factor as a function of $q/2kT$ aids to characterize the behavior of the inhomogeneous potential barrier as shown in figure (4.11) and figure (4.13), respectively.

From figure (4.11), $\overline{\emptyset}_{B0i}$ is the intercept and σ_{0i} is the slope of the straight line of the best linear fit calculated considering three different temperature ranges, namely 85 $\leq \Delta T_1 \leq$ 135 K, 180 $\leq \Delta T_2 \leq$ 270 K, and 315 $\leq \Delta T_3 \leq$ 445 K. In particular, the $\overline{\emptyset}_{B0}$ and σ_0 values are 1.05 eV and 0.096 in the range ΔT_1, 1.543 eV and 0.15 in the range ΔT_2, and 1.643 eV and 0.169 in the range ΔT_3, respectively.
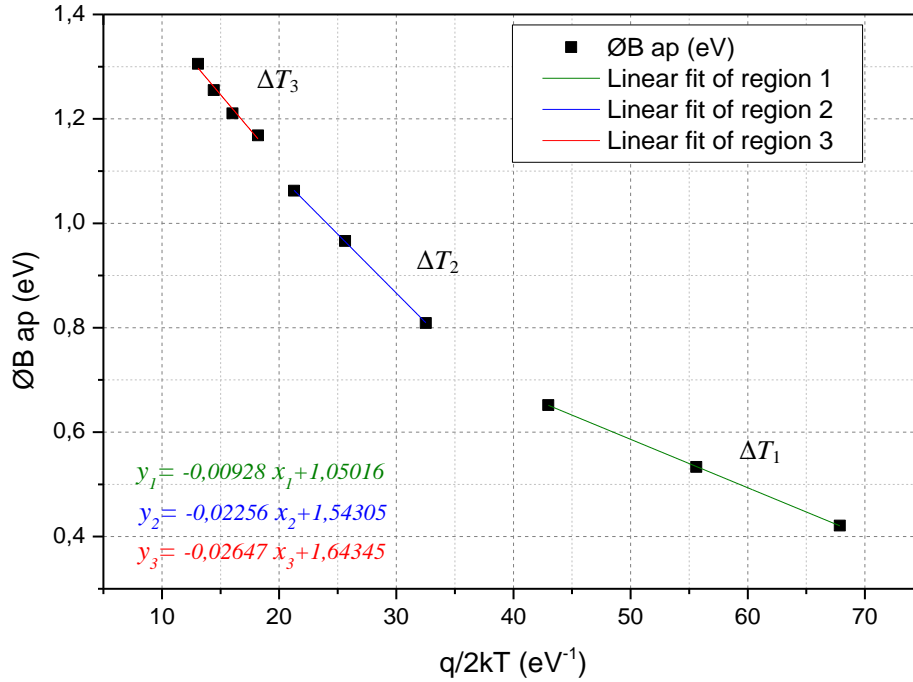
Figure.4. 11.$\emptyset_{B\text{ap}}$ vs.$q/2kT$ according to a Gaussian distribution of the SBH.

Figure (4.12) demonstrates $A_1(\emptyset_B)$, $A_2(\emptyset_B)$, $A_3(\emptyset_B)$ and total $A(\emptyset_B)$, distribution functions calculated using Eqs. (4.23) and (4.25). As shown in figure (4.12), the $A_3(\emptyset_B)$ distribution function represents the barrier distribution at high temperatures, while the $A_1(\emptyset_B)$ and $A_2(\emptyset_B)$ depicts the distribution at low temperatures.

In addition, from figure (4.12), it may be noted that the contribution of the $A_1(\emptyset_B)$ and $A_2(\emptyset_B)$ distribution are far lower than that of the $A_3(\emptyset_B)$ distribution. Compared to that of these distribution functions, it describes that dominant patches along Schottky diode area have a 1.05 eV mean barrier height with 40% density at high temperatures. The same diode area has 1.643 eV and 1.543 eV with mean barrier height of 30% for low temperatures.

This result expresses clearly that the contribution of the mean barrier observed at low temperatures is far lower than the contribution of the other mean barrier height.
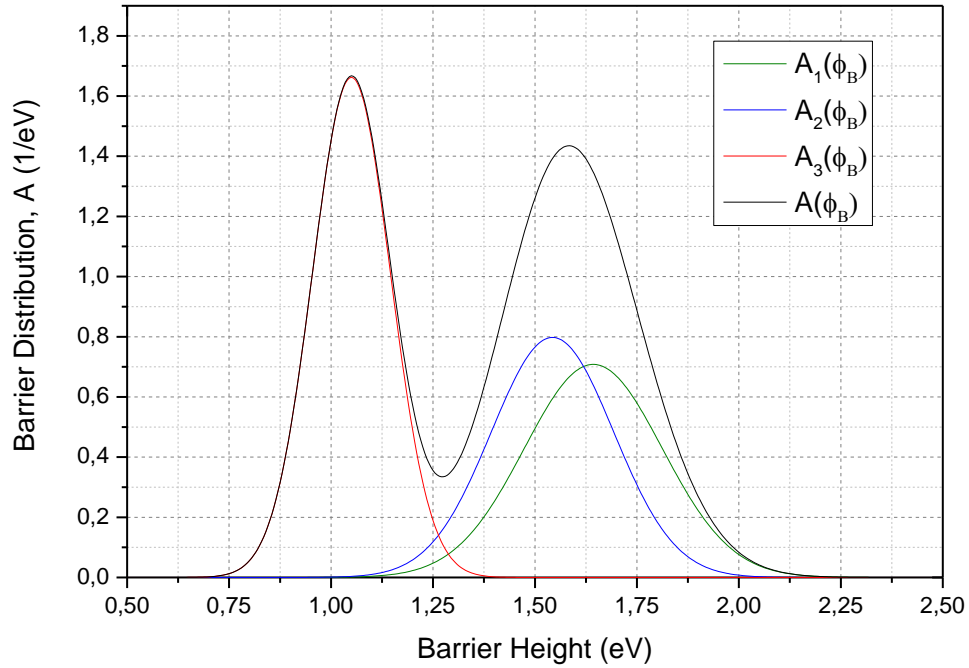
Figure.4. 12. Triple-Gaussian distribution function for Al/Ti/4H–SiC junction.

Similarly, from the plot of the term $(n_{ap}^{-1} - 1)$ vs. $q/2kT$ in Figure (4.13), we calculated the coefficients ρ_2 as the intercept and ρ_3 as the slope of the straight line which fits the diode data for each temperature range.

It results ρ_2= 0.403 V and ρ_3= -0.005 V in the range ΔT_1, ρ_2= 0.141 V and ρ_3= -0.012 V in the range ΔT_2, and, ρ_2= 0.276 V and ρ_3= -0.004 V in the range ΔT_3, respectively.

This analysis, predicting three different Gaussian distributions of the barrier height at the Ti/Al 4H–SiC interface.
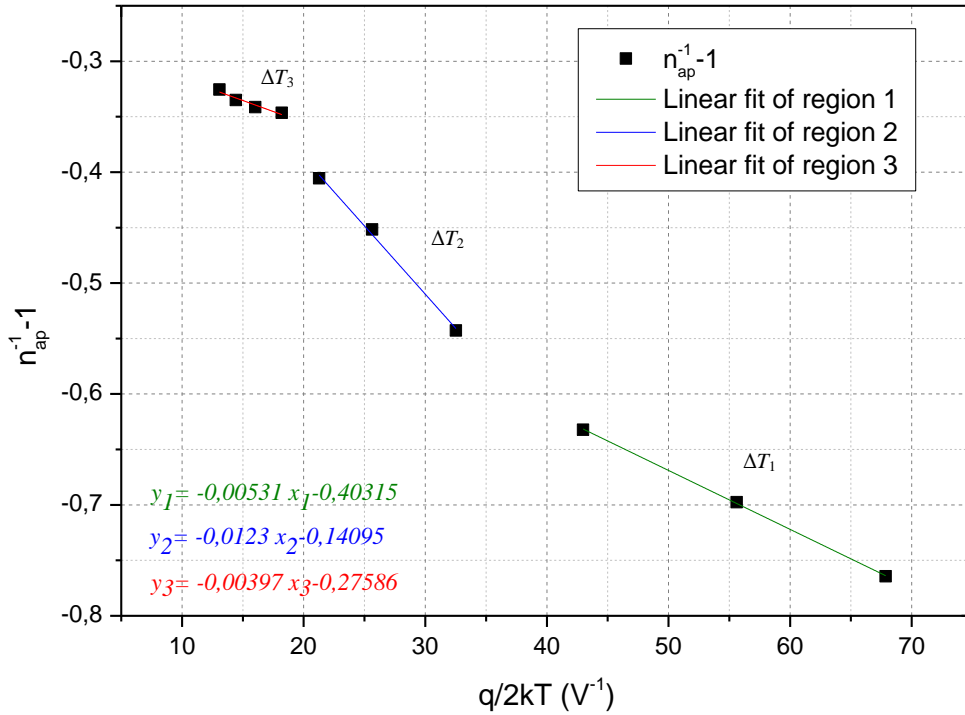
Figure. 4.13. $(n_{ap}^{-1} - 1)$ vs. $q/2kT$ according to a Gaussian distribution of the SBH.

Schmitsdorf et al [141] used Tung's theoretical approach that there is a linear relation between the apparent zero bias barrier height and ideality factors. The variation of the apparent barrier height versus the ideality factor is shown in figure (4.14).
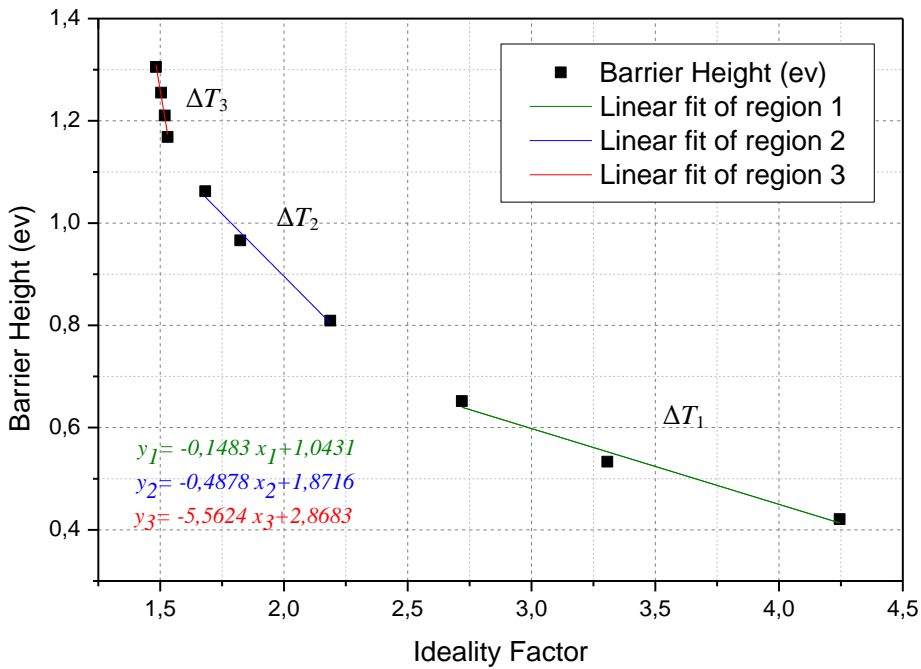
Figure. 4.14. Schmistsdorf's plot showing zero-bias barrier height versus ideality factor.

According to Tung's theory [20]; there should be a linear correlation between the $\emptyset_B$ and n for various temperatures. As shown in the figure (4.14), there are three different linear regions. The extrapolation of the apparent barrier height versus the ideality factor plot to $n = 1$ has given a homogeneous Schootky barrier height of approximately, 0.894eV, 1.383eV and 2.694eV in the range ΔT_1, ΔT_2 and ΔT_3, respectively. These results indicate that the current transport is controlled by different mechanisms in different temperature ranges.

The large values of ideality factor indicate deviation from TE theory for current transport mechanism. The ideality factor is found to vary with temperature as shown in figure (4.6). In addition, an information required about the current transportation mechanism of a Schottky diode is may be obtained through a plot of n versus T.

The phenomenon which explains this behavior is generally known as T_0 effect. The ideality factor of the diode varies with temperature as [23],

$$n(T) = n_0 + \frac{T_0}{T} \qquad (4.27)$$

As shown in figure (4.15), plots of n_0 versus 1000/T also present three straight lines, and the values of n_0 and T_0 are obtained as 0.023 and 355K in the range ΔT_1, 0.689 and 264K in the range ΔT_2, and 1.369 and 52K in the range ΔT_3, respectively. Explanations of the possible origin of such cases have been proposed taking into account the generation recombination current in the depletion region or the TFE [138].
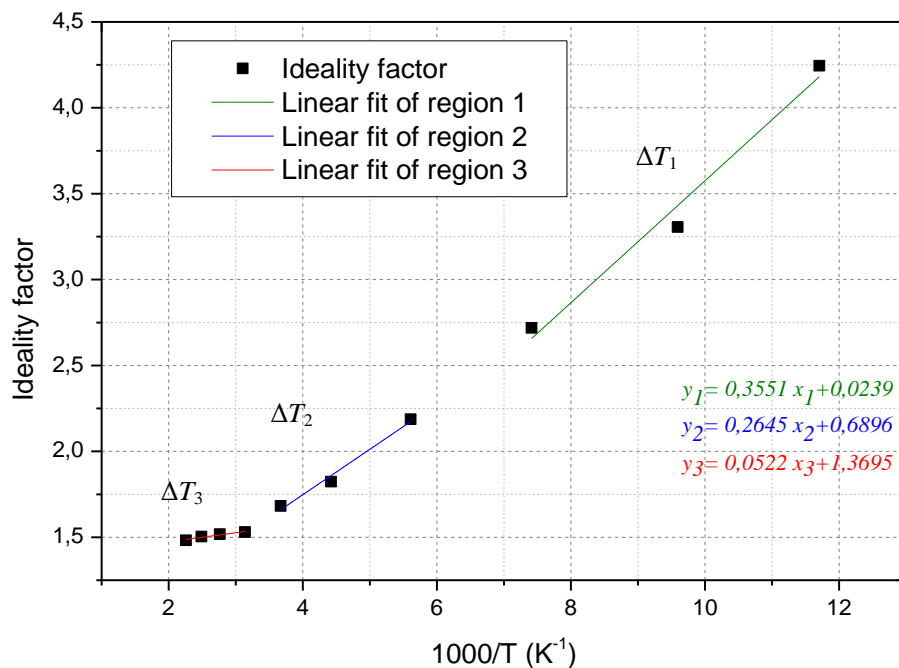
Figure. 4.15. Plots of the n vs. 1000/T for Al/Ti/4H–SiC SBD.

Figure (4.16) shows a plot of *nkT/q* vs. *kT/q* reporting the temperature dependence of the *n*, in which the straight line reported as a reference represents the ideal behavior of Schottky contact (i.e. with *n = 1*). In this behavior, the straight line fitted to the obtained data for the T_0 effect should be parallel to that of the ideal Schottky contact behavior [143].

As can be seen from figure (4.16) the straight line fitted to the obtained data is not parallel to that of the ideal Schottky contact behavior. This is explainable in terms of SBH inhomogeneity.
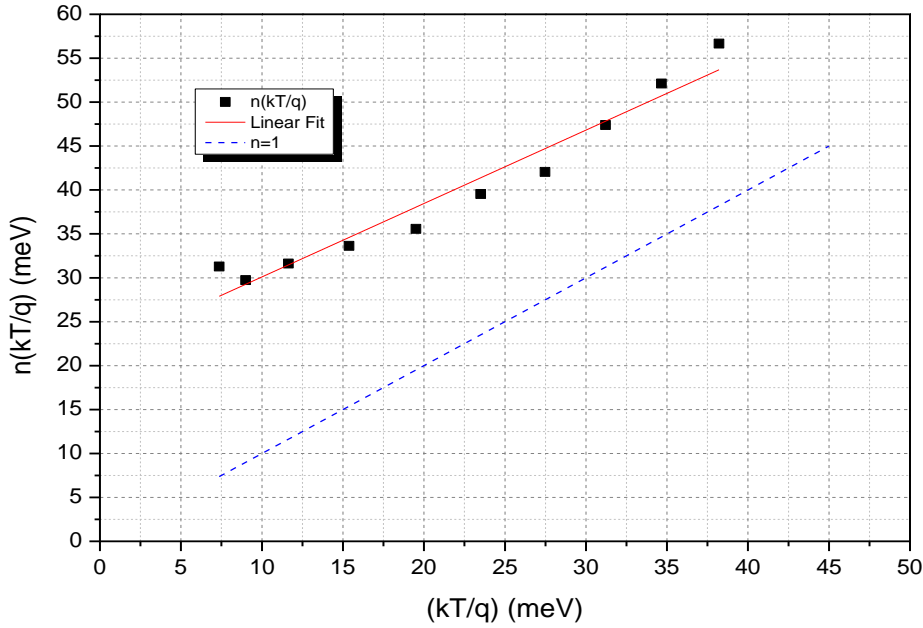
Figure. 4.16. Plot of *nkT* versus *kT* showing the T_0 effect.
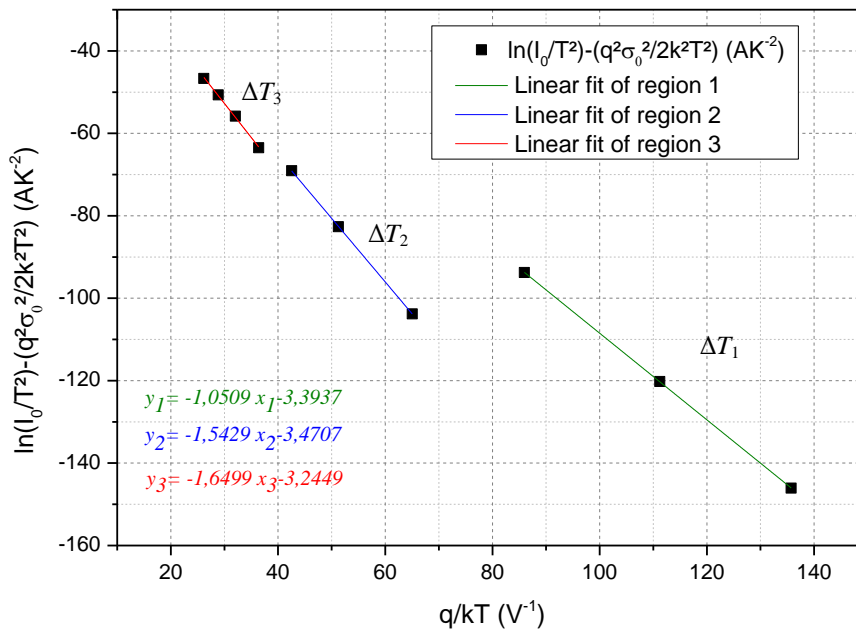
Figure.4.17.$ln(I_0/T^2) - (q^2\sigma_0^2/2k^2T^2)$vs.$q/kT$ according to a Gaussian distribution of the SBH.

Finally, by combining (4.20) and (4.26), we obtain

$$ln\left(\frac{I_0}{T^2}\right) - \left(\frac{q^2\sigma_{0i}^2}{2k^2T^2}\right) = ln(AA^*) - \left(\frac{q\overline{\emptyset}_{B0i}}{kT}\right) \tag{4.28}$$

The slope and intercept of the linear fitting of the plot $ln(I_0/T^2) - (q^2\sigma_{0i}^2/2k^2T^2)$ vs. q/kT (see figure. 4.17) allow to determine $\overline{\emptyset}_{B0}$ and A^* as follows: 1.05 eV and 149.26 A cm^{-2} K^{-2} for the first region, 1.543 eV and 138.19 A cm^{-2} K^{-2} for the second region, and 1.649 eV and 173.21 A cm^{-2} K^{-2} for the third region, respectively.

It is worth noting that $\overline{\emptyset}_{B0}$ is in good agreement with the results in figure (4.11). At the same time, the modified Richardson constants are close around the expected theoretical value (146 AK^{-2}cm^{-2} for electrons in the n-type 4H-SiC [129]).

4.2.7. Thermionic field emission transport

If the current transport is controlled by the thermionic field emission theory, the relationship between the diode current and voltage can be expressed by using [84]

$$I = I_0 \, exp^{\left(\frac{qV}{E_0}\right)} \tag{4.29}$$

where the term E_0 is related to the tunnel phenomena that increase for increasing temperatures and it is defined by means of the characteristic tunneling energy E_{00} as follows:

$$E_0 = E_{00}\coth\left(\frac{E_{00}}{kT}\right) \tag{4.30}$$

$$E_{00} = \frac{h}{4\pi}\left(\frac{N_D}{m^*\varepsilon_s}\right)^{1/2} \tag{4.31}$$

Here, h is the Planck constant and $m^* = 0.2 \, m_e$ is the effective electron mass [129].

Depending on the diode temperature, if E_0 tends to kT, namely $kT \gg E_{00}$, the current transport corresponds to the ideal thermionic emission. On the other hand, for temperatures such that $kT \sim E_{00}$ the thermionic field emission should be considered and the ideality factor of the I-V curve is calculated from (4.29) and (4.30) as

$$n = \frac{E_{00}}{kT}\coth\left(\frac{E_{00}}{kT}\right) \tag{4.32}$$

By considering the current mechanisms through the junction dominated by the TFE effect, the ideality factor behavior as a function of the temperature for different values of E_{00} is shown in figure (4.18). Here, the n values extracted from the I-V curves in figure (4.5) are also reported for comparison. It is observed that the dependence of n from temperature is in good agreement with the theoretical curve for $E_{00} = 31.5$ meV up to T is in the limit of about 230 K.
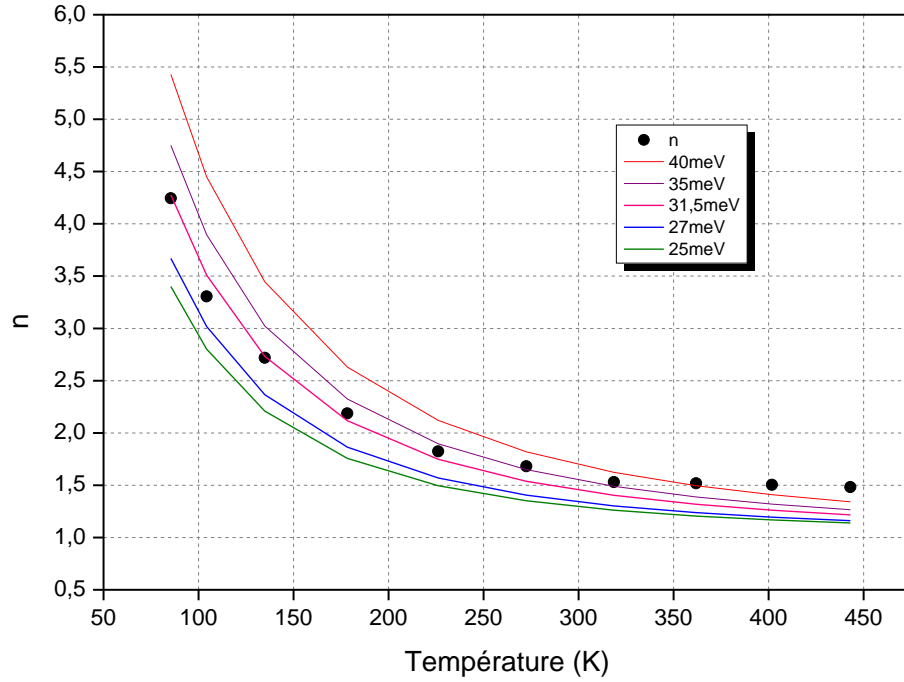
Figure. 4.18.(Solid lines) Ideality factor as a function of the temperature for different values of E_{00}. (Dots) n values extracted from the *I-V* curves in figure. 4.5.

In accordance with the analysis developed in [144], we can assume that the energy E_{00} determines the real BH profile. From equation (4.31) its value is mainly related to the carrier concentration and dielectric constant as well as the density of states at the semiconductor surface through the effective electron mass. In other words, depending on the diode operation conditions (i.e. bias voltage and temperature) a local enhancement of the electric field can determine a local reduction of the barrier height and therefore an enhanced tunneling probability.

4.2.8. State of Ti/Al 4H-SiC interface

Although the analysis of the *I–V–T* data provide an indirect evidence of barrier inhomogeneities at the Ti/Al SiC interface, the method does not directly give information on the many issues that might contribute to the degradation of the quality of the interface. The interface quality could be degraded due to the existence of a thin oxide layer, non-optimized surface preparation and cleaning prior to Ti/Al deposition, process-induced contamination as well as vacuum conditions during evaporation [28]. These are usually the critical factors for achieving a good epitaxy and common reasons for deviations from the ideal behaviour of Schottky contacts in SiC. The reaction kinetics and the phase equilibria according to thermodynamic consideration lead to different possibilities of interface reactions. So what happens at the Ti/Al SiC interface determines the electrical properties of the device [145].

The distribution of Ti, C, and Si is determined from the energy dispersive x-ray analysis (*EDX*) on the interface between SiC and the Ti Schottky metal. Previous research has shown that thermal treatment allows the SiC and Ti to react to form TiC and Si. Then, TiSix is generated from the subsequent reaction of TiC and Si at the TiC interface [146, 147].

S. Kyoung et al [145] conducted an experiment to apply various annealing conditions so as to improve the low Schottky barrier height (LSBH) and inhomogeneity of Ti /Al 4H-SiC SBDs. The experimental results showed that the condition of 873 K/30 min annealing produced a stable SBH and a low Rs value, which improved inhomogeneity. EDX and Transmission Electron Microscopy (*TEM*) analysis showed that the cause of the improved SBH at this condition is attributable to the generation of TiSix, which has a higher SBH than that of Ti. On the other hand, the improved Rs value at this condition is attributable to a change in the γ-phase Ti_3Al (which has a lower resistance), caused by diffused Al resulting from proper annealing. However, when more heat is applied, Rs increased and SBH decreased. EDX and TEM analyses showed that the LSBH was caused by Al spiking, which created an Al Schottky junction with a lower SBH than that of a Ti Schottky junction. The higher Rs value resulted from the change to α-TiAl phase at the Al–Ti interface layer because of excessive diffusion of Ti and Al, which is due to the greater amount of applied heat.

To sum up, these studies show that the final phases formed in Ti/Al SiC interface depend on the method of metal deposition as well as the temperature of annealing.

On the basis of the results presented in our study, we believe that the reaction mechanism in Al/Ti 4H-SiC Schottky contact which formed by depositing Al/Ti on the SiC substrate and annealed at 1000 ^{0}C as described in Section (4.2.1) lead to a formation of Al spiking.

The inhomogeneity observed in this work can be explained by formation of Al spiking, which create an Al Schottky junction with a lower SBH than that of a Ti Schottky junction and yield a high T_0 value. The higher *Rs* value results from the change to α-TiAl phase at the Al–Ti interface layer because of excessive diffusion of Ti and Al, which is due to the greater amount of heat used in the annealing treatment.

4.2.9. Ti/Al 4H-SiC SBD Sensor Performances

As a temperature sensor, the SBD is forward biased at a constant current. In this case, the relationship between the forward voltage and the current of the SBD considering the series resistance can be expressed as [84]:

$$V = R_s I + n\emptyset_B + \frac{kTn}{q} ln\left(\frac{I}{AA^*T^2}\right) \qquad (4.33)$$

The forward voltage (V) as a function of temperature for applied current values in the range from 10µA to 1.2 mA for the whole temperature range of 85 K up to 445 K are shown in figure (4.19).

The sensor sensitivity (S) is defined as the temperature derivative of equation (4.33) and, therefore, it can be obtained from the slope of the V–T characteristics. The calculated sensitivity varies from 1.87 mV/K to 1.22 mV/K in the 85-445 K temperature range.
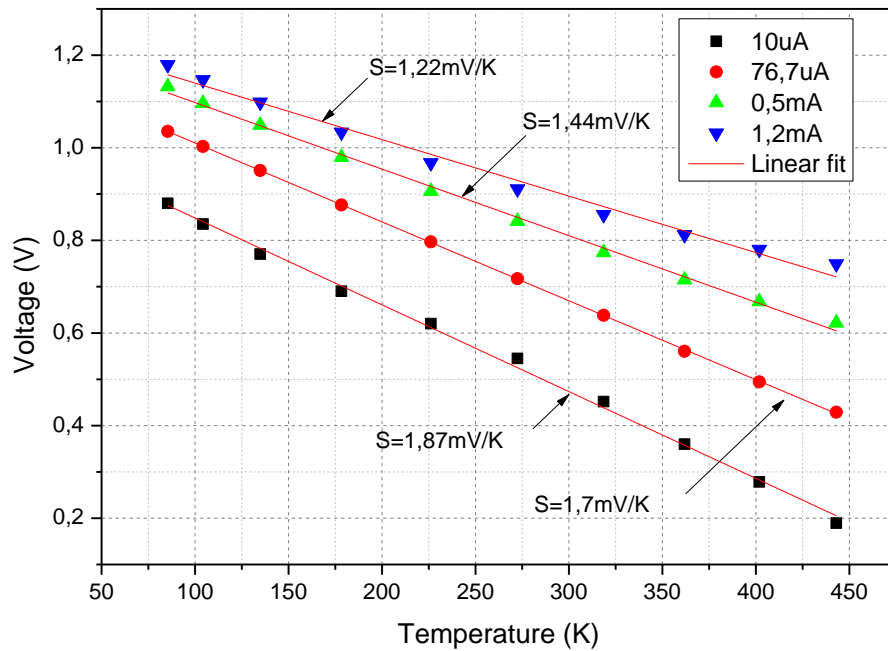
Figure.4. 19. Forward voltages versus temperature at four
currents I (10µA, 76.7µA, 0.5 mA, and 1.2 mA). V-T data are fitted
with the best-calculated linear model.

Moreover, in order to evaluate the agreement between the V-T data and the corresponding linear best-fit the coefficient of determination (R^2) and the temperature error (e_T) had been calculated.

In figure (4.20 (a)) is shown the calculated value of S and R^2 for different bias currents. The V-T characteristics show a good degree of linearity. As reported, when I is 1.2 mA the sensitivity is 1.22mV/K and monotonically increases up to 1.87 mV/K for I =10µA.
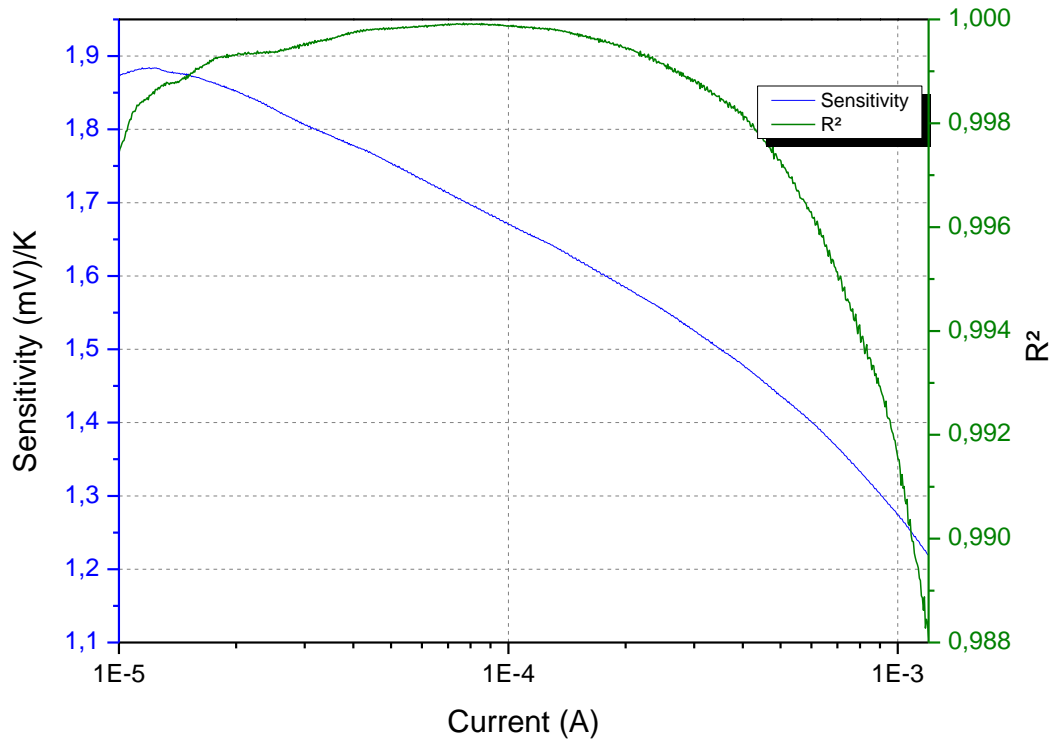
(a)
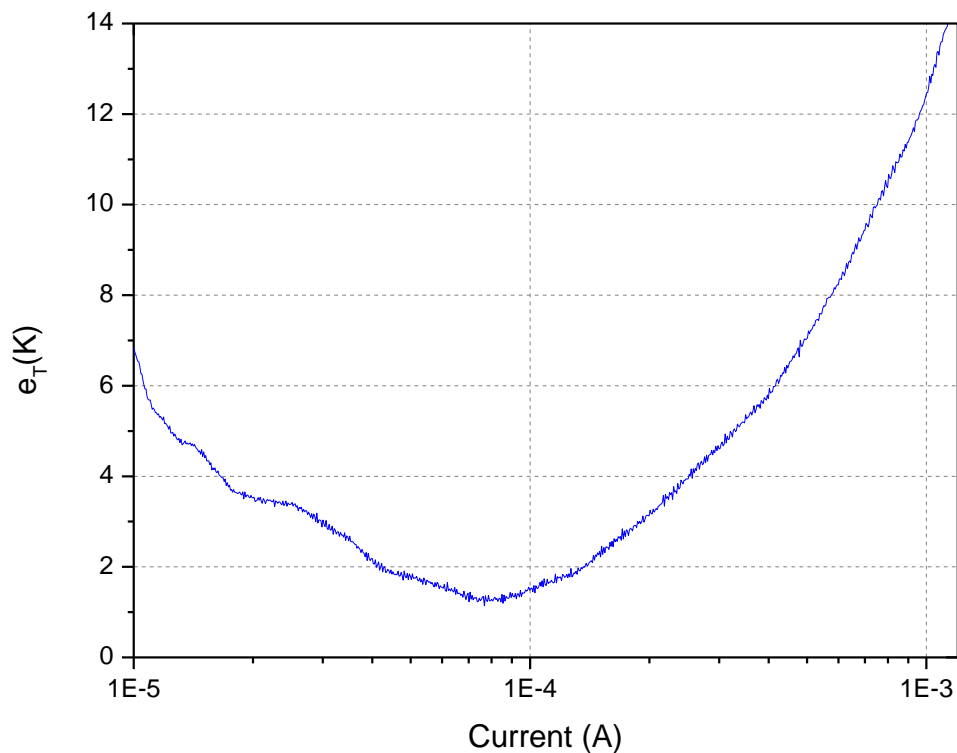
(b)

Figure. 4.20. (a) Coefficient of determination and sensitivity calculated for
802 values of the bias currents between I= 10 µA and 1.2 mA.
(b) Corresponding RMSE in the temperature range T = 85–445 K.

The maximum of R^2=0.9999 has been calculated for I =76.7 µA corresponding to a sensitivity S=1.7 mV/K. The decrease of R^2 for bias currents higher than 7.23 mA can be due to the influence of the series resistance, and for low currents (‹ 86.9 nA) due to non-exponential behaviour of diodes at low voltages (side-wall leakage and other leakage paths).

The temperature error (e_T) between the *V-T* data and the corresponding linear best-fit, evaluated as [26]:

$$e_T = S^{-1}e_{RMS,V} = S^{-1}\sqrt{n^{-1}\sum_{i=1}^{n}(V_i - f_{L,i})^2} \qquad (4.34)$$

where $e_{RMS,V}$ is the root-mean-square error of the diode voltage drop and S is the sensor sensitivity obtained from the slope of linear best-fit ($f_{L,i}$) and n is the number of temperature set points.

The calculated plot, e_T versus I, for the considered temperature range is reported in figure 4.20(b). e_T is always lower than 14 K for applied current values in the range from 10 µA to 1.2 mA while the minimum e_T = 1.14 K is obtained for I= 76.7 µA.

The increase of e_T for bias currents higher than 7.23 mA and for low currents (‹ 86.9 nA) is believed to be due to factors responsible for decrease of R^2.

These results show that Ti/Al 4H-SiC Schottky diodes are good candidates for high temperature sensing applications in a wide range of biasing currents.

4.3. Simulation and analysis of the current–voltage–temperature (*I-V-T*) characteristics of Mo/4H-SiC Schottky diode for high performance temperature sensor

In this section, a 4H-SiC schottky diode fabricated and reported by L. Boussouar et al. [27] was simulated in the cylindrical coordinate system by using the thermionic emission model in a commercial device simulator Atals-Silvaco [109]. All the physical models described in chapter three were used. Resultant *I-V-T* curves were compared with measured data.

4.3.1. Device structure

A schematic cross sectional view of the 4H-SiC Schottky diodes considered in this work is shown in figure (4.21) (plot not in scale).

The substrate material used for the experimental devices was n-type 4H–SiC <0001> from Cree Inc. The epi-layer is 10 μm thick and has a net doping density of about 1.3×10^{16} cm^{-3}. The Schottky diodes had a circular geometry with a diameter of 150 μm.

The Schottky contacts were formed by depositing, through e-beam evaporation, molybdenum on the SiC substrate at a pressure of approximately 1×10^{-5} Pa followed by annealing in an open furnace at 500 °C under a N$_2$ flow of about 1000 sccm. More details about the diode fabrication process are provided in [27].
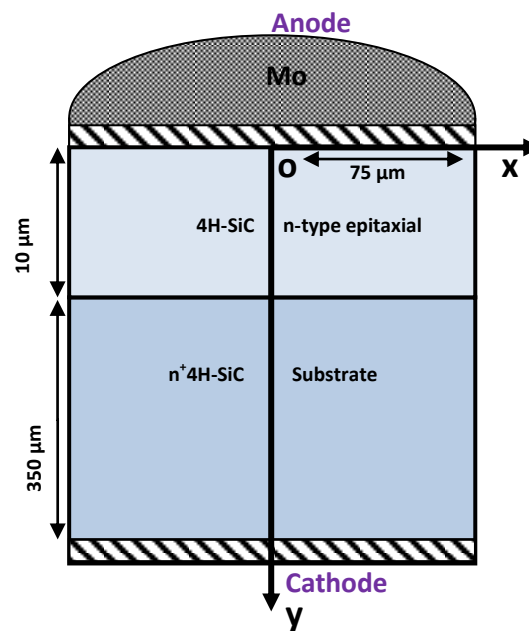
Figure. 4.21. Mo/4H-SiC Schottky barrier diode schematic cross section.

4.3.2. *I-V -T* characteristics

The measured (as reported in [27]) and simulated forward *I-V-T* curves of the considered Mo/4H-SiC SBDs for nine different temperatures from 303 K to 498 K are shown in figure (4.22).

It is worth noting that the numerical simulation results are in good agreement with the experimental data.
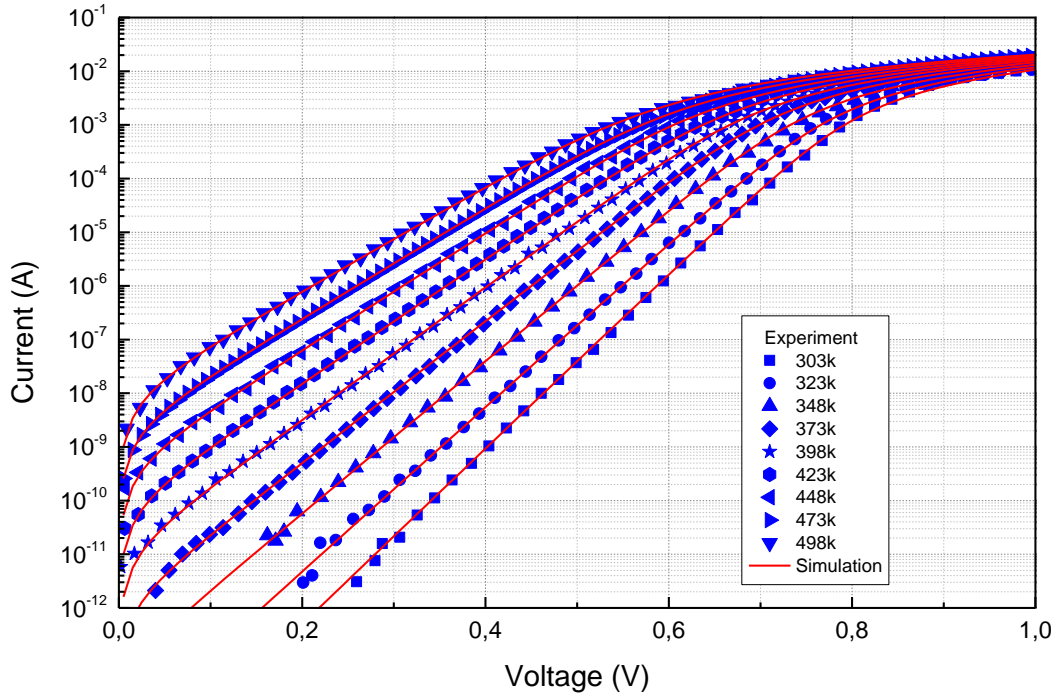
Figure4.22. Measured (symbols) and simulated (solid lines) current–voltage
characteristics of the Mo/4H-SiC Schottky diode at different temperatures.

From the simulation *I-V-T* curves in figure (4.22) we extracted the fundamental diode
parameters I_0, $\emptyset_B$, and n similarly to [130]. The values of the ideality factor and barrier height of
the diode at different temperature are plotted as function of temperature in figure (4.23).
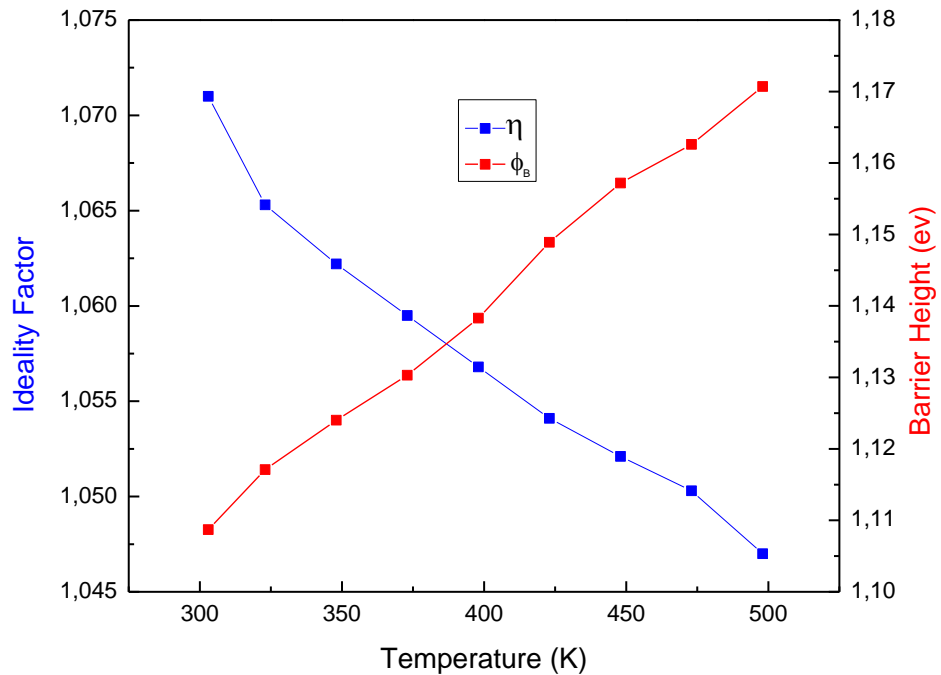
Figure. 4.23. Ideality factor and barrier height behaviors
as a function of temperature for the device in figure (4.22).

The barrier height and ideality factor are found to be strong dependence, the plot shows that the ideality factor decrease while the barrier height increase with increasing temperature.

The variation of series resistance values of Mo/4H-SiC versus temperature extracted from our curves is shown in figure. (4.24).
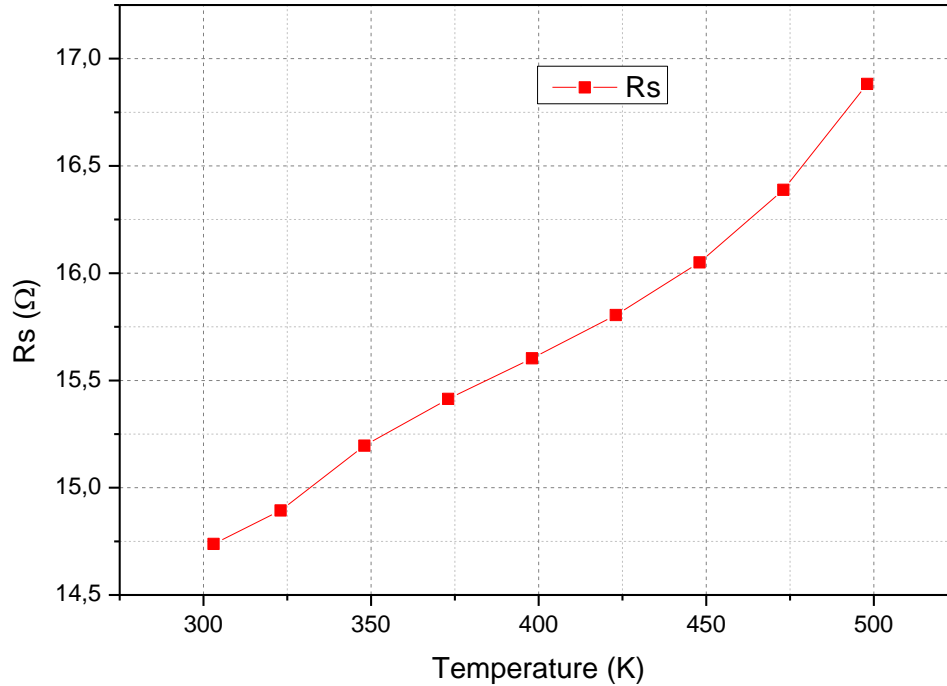
Figure.4.24. Temperature dependence of the series resistance.

As seen in figure (4.24), the values of *Rs* increase with increasing temperature. The variation with temperature of the series resistance can be explained as follows: when temperature increases, more impurities are ionized and the mobility limited by the phonon scattering becomes dominant mechanism, which causes the conductivity of 4H-SiC to decrease and consequently leads the series resistance to increase [148].

By considering equation (4.2) in the form of $ln(I_0/T^2) = ln(AA^*) - (q/kT)\emptyset_B$, the Arrhenius plot of term $ln(I_0/T^2)$ against $1000/T$ is shown in figure (4.25).

The value of A* obtained from the intercept of the linear portion of the ordinate is $3.67\,A \cdot cm^{-2} \cdot K^2$ that is much lower than the theoretically calculated value, which is $\approx 146\,A \cdot cm^{-2} \cdot K^2$ for n-type 4H-SiC [129]. A barrier height value of $1.013\,eV$ is obtained from the slope of the straight line.

The presented results seem to predict current transport mechanisms not following the pure TE theory and the barrier height and ideality factor are found to be strong dependence.
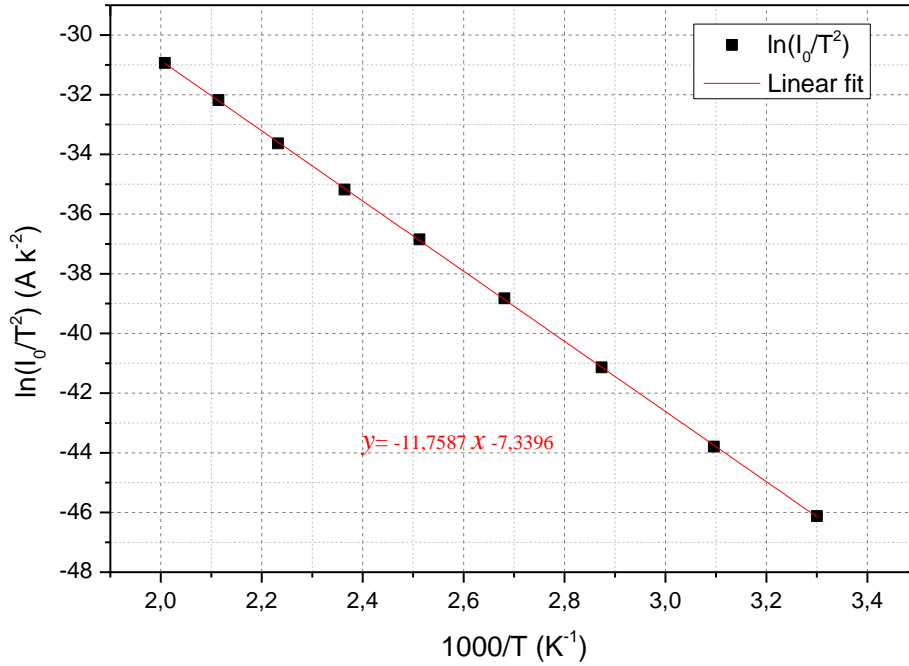
Figure. 4.25.Arrhenius plot of $ln(I_0/T^2)$vs.$1000/T$.

4.3.3. Effect of image-force lowering

Barrier height lowering and the increase in ideality factor with decreasing temperature can be considered to be due to the image-force lowering. The values of $\Delta\emptyset$ found by using equation (4.8) varies from 23.41 meV to 24.30meV in the 303 – 498 K temperature range for the barrier height $\emptyset_B$ ranging from 1.108 eV to 1.17 eV as in figure (4.23), the value of N_D varies from 1.27×10^{16} cm^{-3} at 303K to 1.3×10^{16} cm^{-3} at 498K, respectively and a typical forward bias voltage of 0.2 V in the present work. The variation in barrier lowering with temperatures is too low and it is almost constant for each doping level compared to the reduction in the values of the barrier height for the same temperature range. Therefore, the image-force lowering alone cannot account for the lowering of the barrier height.

The ideality factors found by using equation (4.9) are 1.009 and 1.010 at 303 and 498 K, respectively. These values also show that the observed variation in the ideality factor cannot be explained by the image-force lowering. In this case, the other current transport mechanisms such as Thermionic Field Emission (TFE) or recombination generation should be accounted as the reason of the increase in the ideality factor with decreasing measurement temperature [136].

4.3.4. Flat-band barrier height and modified Richardson plots

The barrier height obtained under flat-band condition is called flat-band barrier height $\emptyset_{Bf}$ and is considered to be real essential quantity. Unlike the case of zero-bias barrier height, the

electrical field in the semiconductor is zero under the flat-band condition and semiconductor bands are flat, which eliminates the effect of tunneling and image force lowering that would affect the *I–V* characteristics and removes the influence of lateral inhomogeneity [129-138].

The flat-band barrier height ϕ_{Bf} can be calculated from equation (4.10). Figure (4.26) shows the variation ϕ_{Bf} as a function of temperature. It can be seen that ϕ_{Bf} is always larger than zero-bias barrier height ϕ_B. The flat-band barrier height ϕ_{Bf} increases with decreasing temperature. Furthermore, the temperature dependence of the flat-band barrier height is described as $\phi_{bf}(T) = \phi_{bf}(T = 0) + \alpha T$, where $\phi_{Bf}(T = 0K)$ is the zero-temperature flat-band barrier height and is the temperature coefficient of ϕ_{Bf}. The linear fitting of the $\phi_{Bf}(T)$ data in equation (4.11) shown in figure (4.26) yields $\phi_{Bf}(T = 0K) = 1.114$ eV and $\alpha = 1.91 \times 10^{-4}$ eV/K.
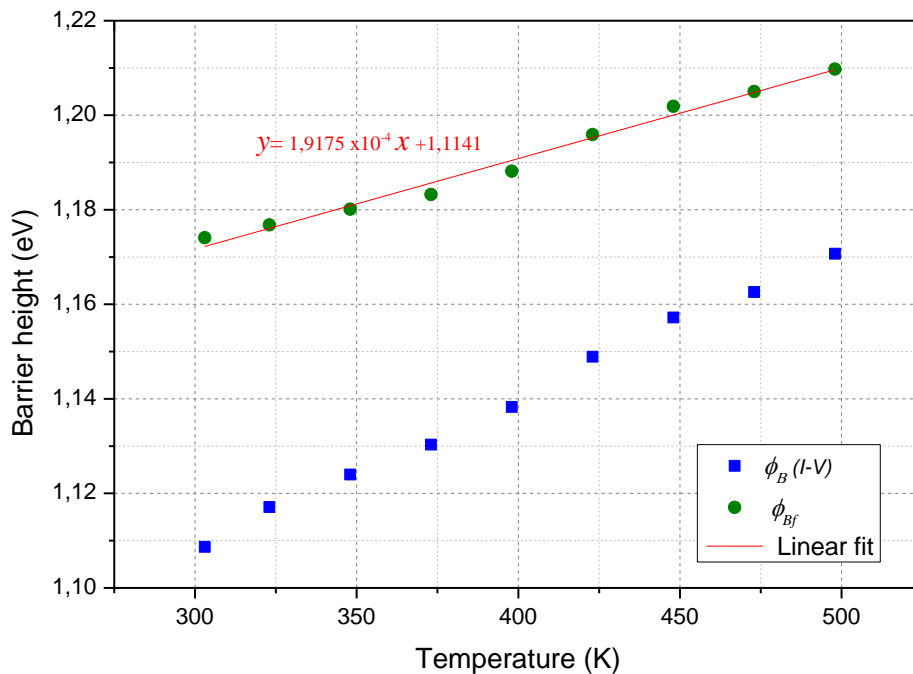
Figure.4. 26. Temperature dependence of the zero-bias BH ϕ_B and flat-band BH ϕ_{Bf} for the Mo/4H–SiC Schottky barrier diode in the temperature range of 303–498 K.

Considering the temperature dependence of the ideality factor *n*, the plot of $ln(I_{0f}/T^2)$ versus *1/nT* according to equation (4.14) should be a straight line with the slope directly yielding $\phi_{Bf}(T = 0K)$ and the intercept at the ordinate determining A* for a given diode area A [136]. Figure (4.27) shows the $ln(I_{0f}/T^2)$ versus *1/nT* plots. The modified $ln(I_{0f}/T^2)$ versus *1/nT* plot gives $\phi_{Bf}(T = 0K)$ and A* as 1.10 eV and 8.4 A cm^{-2} K^{-2}, respectively. These results show that the value of the Richardson constant is different from the known theoretical value of 146 AK^{-2}cm^{-2} for electrons in the n-type 4H-SiC [129].

The presented results seem to predict current transport mechanisms not following the pure TE theory.

$$y = -12{,}7671\, x - 6{,}5131$$
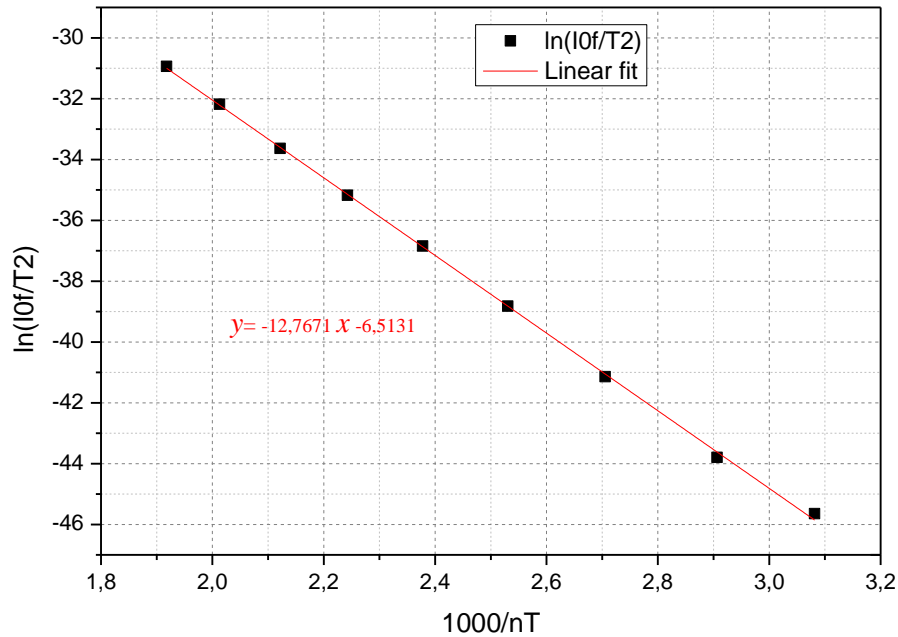
Figure.4. 27. Richardson plots of $ln(I_{0f}/T^2)$ vs. 1000/nT
and their linear fits for the Mo/4H– SiC Schottky diode.

4.3.5. Effect of thermionic field emission

The decrease in barrier height and the increase in ideality factor with a decrease in the temperature are indicative of a deviation from the pure TE theory, and one thus must consider the TFE mechanism. The E_{00} parameter determines the conduction mechanism, whether it is by TE, TFE, or FE [149].

The values of E_{00} have been evaluated as 1.50 and 1.52 meV for T = 303 K and 498 K, respectively. To see the effect of free carriers and to define the dominant current mechanism of the Schottky contact, E_{00} values have been normalized to kT in the investigated temperature region. As seen in figure (4.28), normalized E_{00}/kT values decreases with temperature and $E_{00} << kT$ condition is satisfied for the investigated temperature range. According to the theory, field emission (FE) becomes important when $E_{00} >> kT$ whereas, TFE dominates when $E_{00} \sim kT$ and TE is crucial if $E_{00} << kT$ [136,149, 150]. Therefore, we can postulate that all over the temperature range TE is the dominant current mechanism. According to the equation (4.32) the contribution of TFE results only in an increase of 1.0011 for n at 303 K. This value is low to explain our data value ($n = 1.071$) at 303 K. As a result, the possibility of the FE and TFE can be ruled out. Thus, the higher n values may be related to TE over a Gaussian barrier height distribution and it will be discussed below.
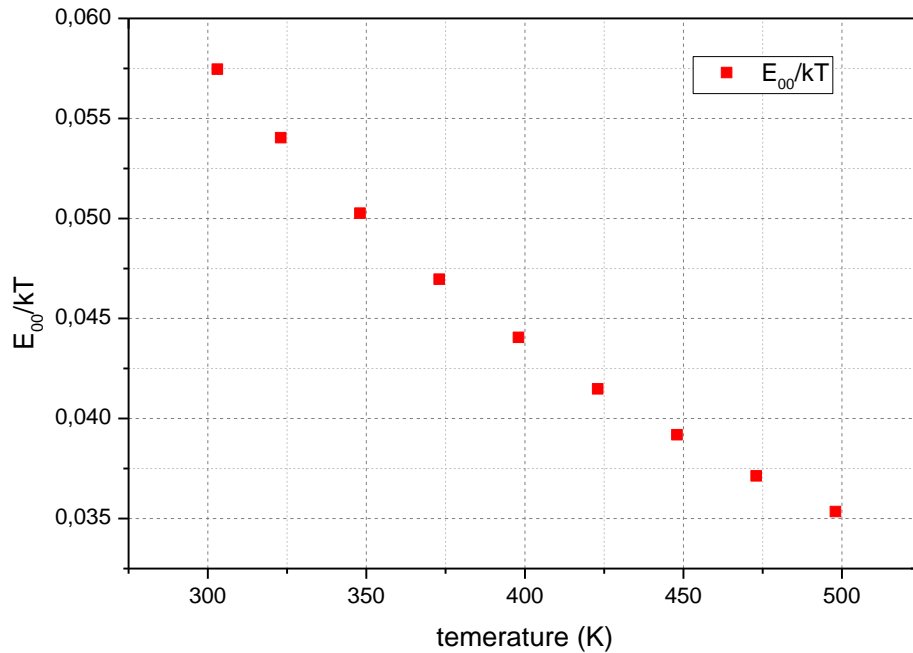
Figure.4. 28. Normalized E_{00}/kT values as a function of temperature.

4.3.6. Inhomogeneous barrier analysis

Werner and Güttler [19] have proposed an analytical potential fluctuation model for the interpretation of I–V measurements on spatially inhomogeneous PtSi/Si Schottky contacts, while Henisch [151] speculated that the fluctuations in BHs are unavoidable as they exist even in the most carefully processed devices. Furthermore, a linear correlation between the zero-bias BH $(\emptyset_B)$ and the ideality factor (n) has been obtained utilizing Tung's pinch-off model [20] by Schmitsdorf et al [141]. Figure (4.29) shows an example of this plot for Mo/4H-SiC SBD.
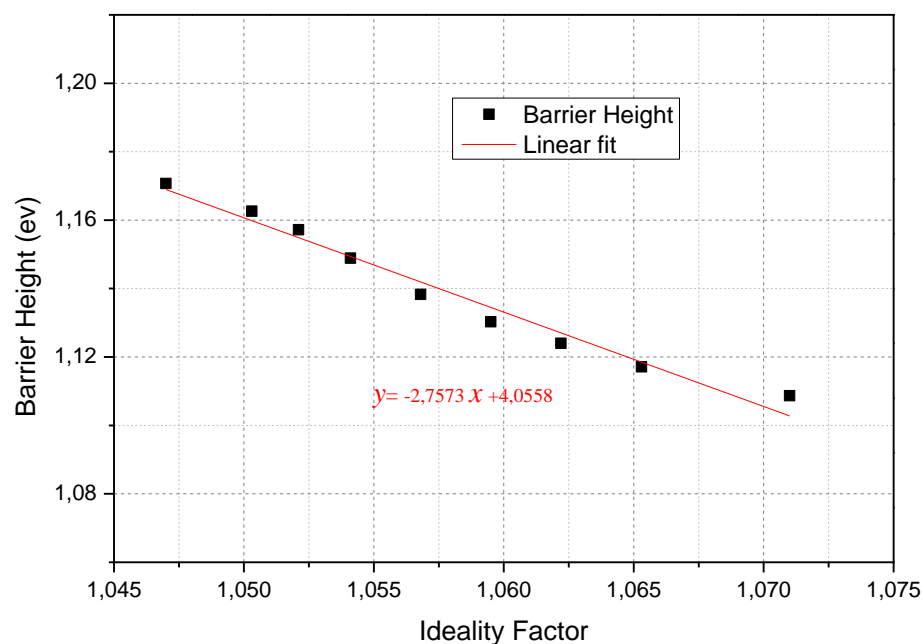
$$y = -2,7573\,x + 4,0558$$

Figure. 4.29. Schmistsdorf's plot showing zero bias barrier height versus ideality factor.

113

A linear relationship between the $\emptyset_B$ and *n* values in figure (4.29) is an indication of the barrier irregularity and can be explained by lateral inhomogeneities of the BHs [141]. A homogeneous BH of approximately 1.298 eV obtained from the extrapolation of the least-square linear fitting to data to *n* = 1 (figure 4.29).

In order to describe the abnormal behaviours mentioned above, an analytical potential fluctuation model using different types of barrier distribution function at the interface on the spatially inhomogeneous SBDs has been proposed by different workers [23,27,122 127, 152–154]. A spatial distribution of the barrier height at the metal-semiconductor interface of Schottky contacts by a Gaussian distribution A($\emptyset_B$) with a standard deviation (σ_0) around a mean SBH ($\overline{\emptyset_B}$) value has been suggested by Werner and Güttler [19]:

The plot of the barrier height and ideality factor as a function of $q/2kT$ aids to characterize the behavior of the inhomogeneous potential barrier as shown in figure (4.30) and figure (4.32), respectively.
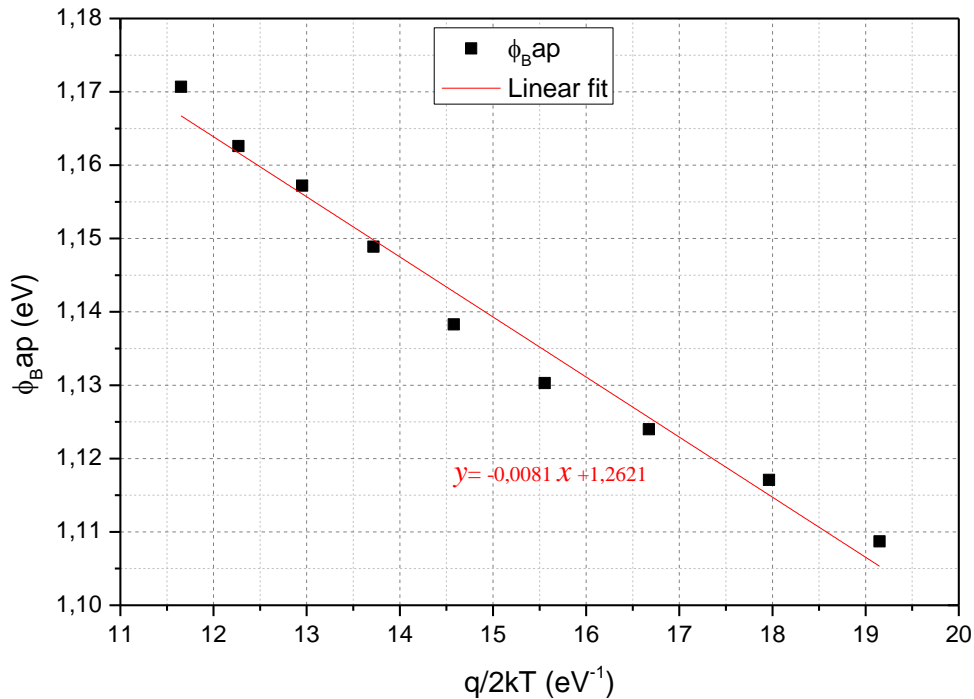
Figure. 4.30. $\emptyset_{Bap}$ vs. $q/2kT$ according to a Gaussian distribution of the SBH.

As can be seen in figure (4.30), The graphical representation of $\emptyset_{Bap}$ versus $q/2kT$ is a straight line of the best linear fit with the intercept on the ordinate determines the zero mean barrier height $\overline{\emptyset}_{B0}$ and the slope gives the zero bias standard deviation σ_0. The values obtained are 1.262 eV and 0.0905 eV for $\overline{\emptyset}_{B0}$ and σ_0 respectively. Compensate of these values in equation (4.15) allows us to get the Gaussian distribution function of SBH as shown in figure (4.31). The standard deviation is a measure of the barrier homogeneity where the lower value of

σ_0 corresponds to a more homogeneous barrier height. However, the value of $\sigma_0 = 90.5$ meV is not small compared to the mean value of $\overline{\emptyset}_{B0} = 1.262$ eV (7%) which indicates the presence of the interface inhomogeneities.
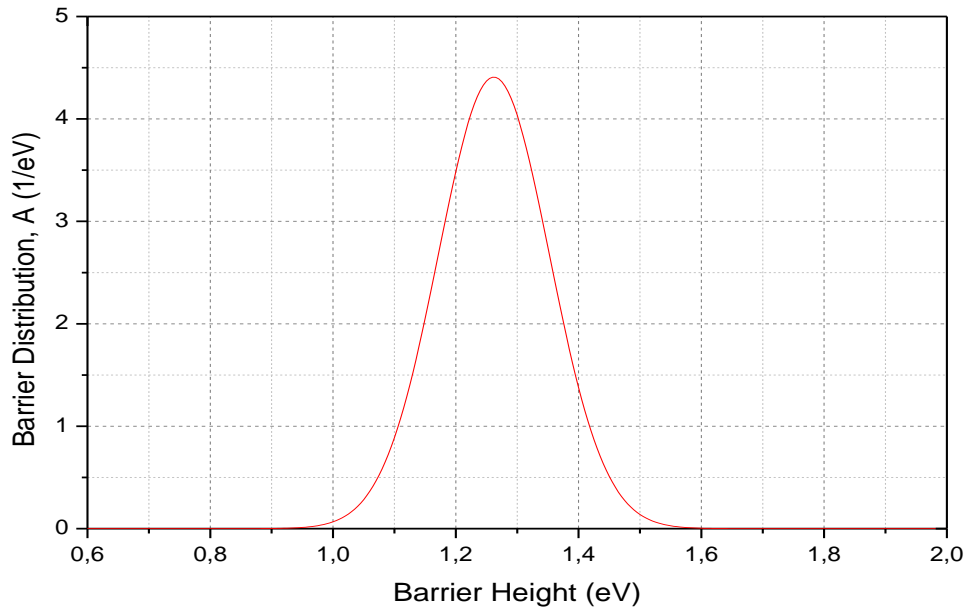
Figure.4. 31. Gaussian distribution function for Mo/4H–SiC junction

Similarly, from the plot of the term $(n_{ap}^{-1} - 1)$ vs. $q/2kT$ in figure (4.32), we calculated the coefficients ρ_2 as the intercept and ρ_3 as the slope of the straight line which fits the diode data for each temperature range.
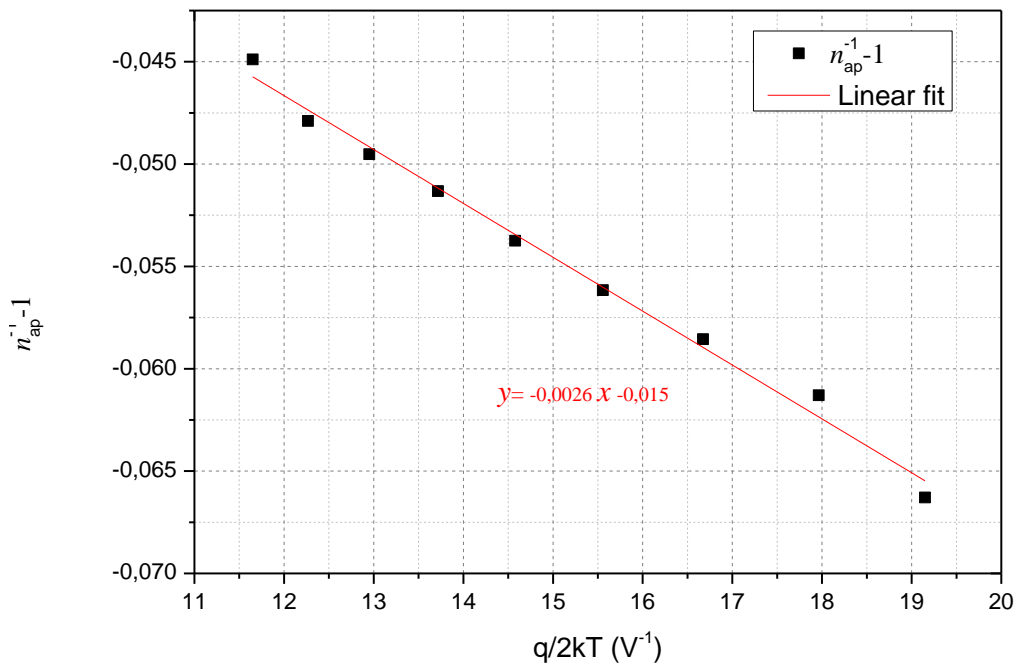
Figure. 4.32. $(n_{ap}^{-1} - 1)$ vs. $q/2kT$ according to a Gaussian distribution of the SBH.

The analysis of this plot gives the values of the following voltage coefficients: $\rho_2 = 0.015$ V and $\rho_3 = -0.0026$ V.

According to Werner and Guttler [19] the ideality factor can be written as

$$n_{ap} \cong 1 + \rho_2 - \frac{\rho_3}{2kT/q} \cong 1 + \frac{T_0}{T} \tag{4.35}$$

which yields to (in most cases the terms ρ_2 is neglected)

$$T_0 \cong -\frac{\rho_3}{2kT/q} \tag{4.36}$$

If we use the calculated value of ρ_3 we obtain a T_0 value of 15.07 K .

According to Saxena [100], such behaviour is typical to a SBD displaying the so-called ''T_0 effect'' which means that the ideality factor can be expressed in the form $n(T)=1+T_0/T$. This implies that a plot of nT vs. T is a straight line with a slope of unity and the intercept T_0 at the ordinate.

Figure (4.33) shows such a plot with the slope equal to 1.013, which is close to unity as predicted by the empirical relation and the intercept T_0 =17.16K. Tung [20] and Sullivan et al [134] have shown that the ''T_0 effect'' is typical to SBD with a distribution of barrier inhomogeneities.
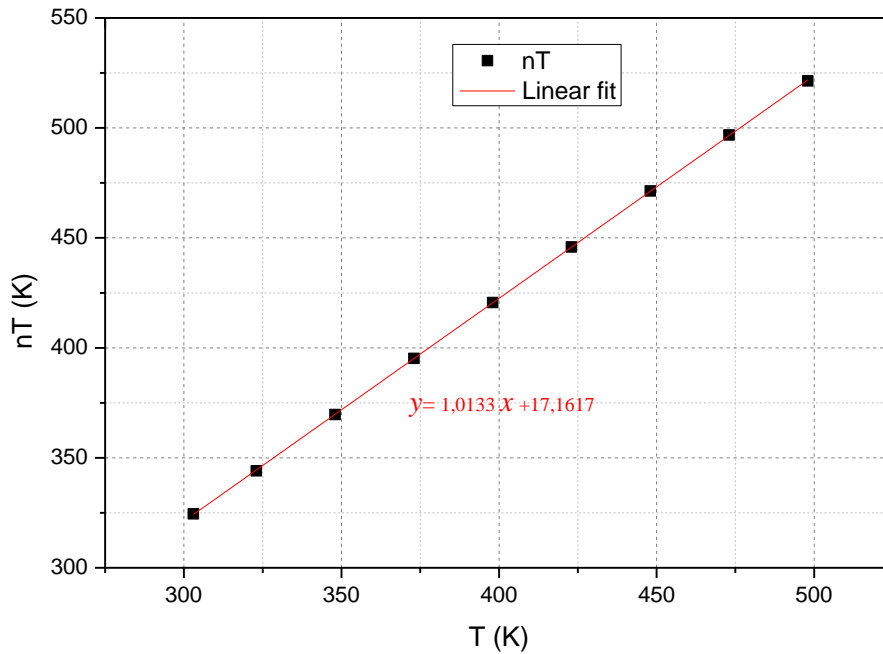
Figure. 4.33. Plot of nT versus T showing the T_0 effect.

Finally, by combining (4.20) and (4.27), we obtain $ln\left(\frac{I_0}{T^2}\right) - \left(\frac{q^2\sigma_0^2}{2k^2T^2}\right) = ln(AA^*) - \left(\frac{q\overline{\phi}_{B0}}{kT}\right)$. The slope and intercept of the linear fitting of the plot $ln(I_0/T^2) - (q^2\sigma_0^2/2k^2T^2)$ vs

q/kT (see figure (4.34)) allow to determine $\overline{\emptyset}_{B0}$ and $A*$ as follows: 1.265 eV and 155.78 A cm^{-2} K^{-2} respectively.
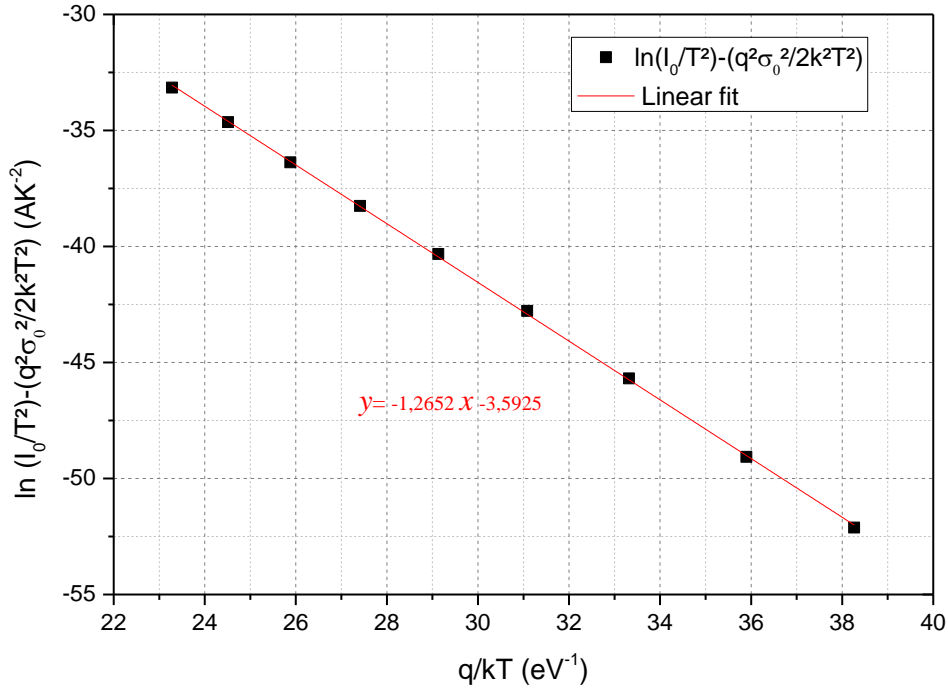
Figure.4.34. $ln(I_0/T^2) - (q^2\sigma_0^2/2k^2T^2)$ vs.q/kT
according to a Gaussian distribution of the SBH.

It is worthwhile noting that $\overline{\emptyset}_{B0}$ is in good agreement with the results in figure (4.30). At the same time, the modified Richardson constants are close around the expected theoretical value (146 AK^{-2}cm^{-2} for n-type 4H-SiC [129]). These results show that the temperature dependence of current transport characteristics can be successfully interpreted by using TE theory with Gaussian distribution of the barrier heights due to the inhomogeneous barrier heights at the Mo/4H–SiC interface.

4.3.7. State of Mo/4H-SiC interface

In spite of the fact that the analysis of the *I–V–T* data gives an indirect proof of barrier inhomogeneities at the Mo/SiC interface, the method does not directly give information on the many issues that might contribute to the degradation of the quality of the interface.

The chemical reactions, during the process of fabrication of the Mo/4H–SiC interface, play an important role in the Schottky barrier formation. It is known that molybdenum can readily react with the SiC. It forms a silicide when reacting with elemental Si and carbide when reacting with elemental C. It shows also a little added reaction when performing an annealing up to 800 ^{0}C [27, 155]. Due to the mixture of these different phases (Mo$_2$C, MoSi$_2$, Mo$_3$Si) at the metal/semiconductor interface, an increase in the barrier height leads to significant

inhomogeneity. Leroy et al [156] have reported that the Mo carbide system suggests that molybdenum carbide Mo_2C is a promising alternative, since the phase shows a lower resistivity, the carbide forms below 900 ^0C, and its formation is less sensitive to oxidation as compared to other system. The sample which we have been studied by simulation is annealed at 500 ^0C, This makes us believe that there will be a reaction between the molybdenum and Si-forming silicides and between the molybdenum and C-making carbides; however, those carbides are stables as demonstrated by Leroy et al [156] and Toumi et al [157]. We believe also, that The Low T_0 value obtained in this work is attributable to technique used to deposit the Mo, which means that the Mo shows a good compatibility, so less inhomogeneity is expected with SiC as evidenced by the results discussed above.

4.3.8. Mo/4H-SiC SBD Sensor Performances

As a temperature sensor[26], the SBD is forward biased at a constant current. In this case, the relationship between the forward voltage drop and the current of the SBD considering the series resistance can be expressed as $V = R_s I + n\emptyset_B + \frac{kTn}{q} ln \left(\frac{I}{AA^*T^2} \right)$. The forward voltage (*V*) as a function of temperature for applied current values in the range from 10 nA to 10 mA for the whole temperature range of 303 K up to 498 K are shown in figure (4.35).
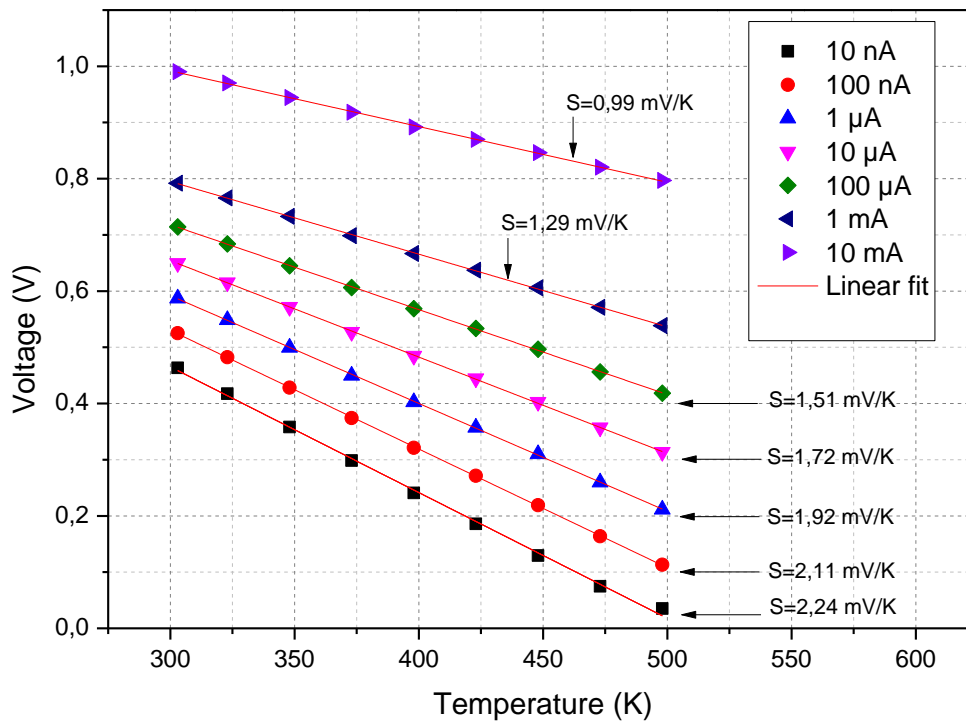
Figure. 4.35. Forward voltages versus temperature at seven
currents *I* (10 nA, 100 nA,1µA, 10µA, 100µA, 1 mA and 10 mA).

Thanks to an almost constant value of the ideality factor, V-T characteristics exhibit a very high degree of linearity in the whole considered temperature range.

The sensor sensitivity (*S*) is defined as the temperature derivative of forward voltage (V) equation and, therefore, it can be obtained from the slope of the V–T characteristics. The calculated sensitivity varies from 2.24 mV/K to 0.99 mV/K in the 303-498 K temperature range.

Moreover, in order to evaluate the agreement between the *V-T* data and the corresponding linear best-fit the coefficient of determination (R^2) and the temperature error (e_T) had been calculated. In figure 4.36 (a) is shown the calculated value of S and R^2 for different bias currents. The *V-T* characteristics show a good degree of linearity. As reported, when *I* is 10 mA the sensitivity is 0.99 mV/K and monotonically increases up to 2.24 mV/K for *I* =10 nA.

The maximum of R^2=0.99974 has been calculated for *I*=4.16 mA corresponding to a sensitivity S=1.14 mV/K. It is worth noting that the coefficient of determination varies by only 0.018% from an average of $R_a^2 \sim 0.9996$ over the considered temperature range for applied current values in the range from 86.9 nA to 7.23 mA where the sensor shows its best performances, leading to a temperature sensor with a highly linear behavior in a wide range of biasing currents. While the values of R^2 decrease for bias currents higher than 7.23 mA due to the influence of the series resistance, and for low currents (‹ 86.9 nA) due to non-exponential behaviour of diodes at low voltages (side-wall leakage and other leakage paths).

The temperature error (e_T) between the *V-T* data and the corresponding linear best-fit, evaluated as [26]:

$$e_T = S^{-1} e_{RMS,V} = S^{-1} \sqrt{n^{-1} \sum_{i=1}^{n} (V_{D,i} - f_{L,i})^2} \ .$$

The calculated plot, e_T versus *I*, for the considered temperature range is reported in figure (4.36(b)). e_T is always lower than 1.6 K for applied current values in the range from 86.9 nA to 7.23 mA while the minimum $e_T = 1.15$ K is obtained for *I* = 4.16 mA.

These results show that Mo/4H-SiC Schottky diodes are good candidates for high temperature sensing applications in a wide range of biasing currents.
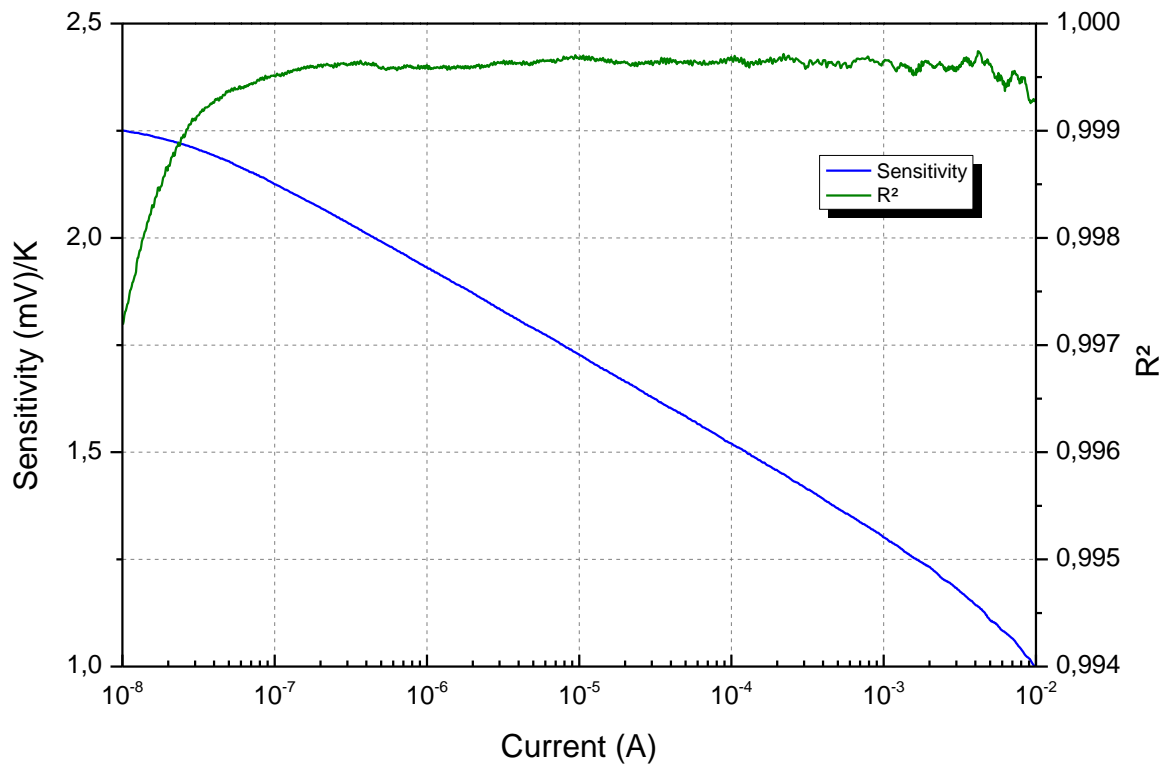
(a)
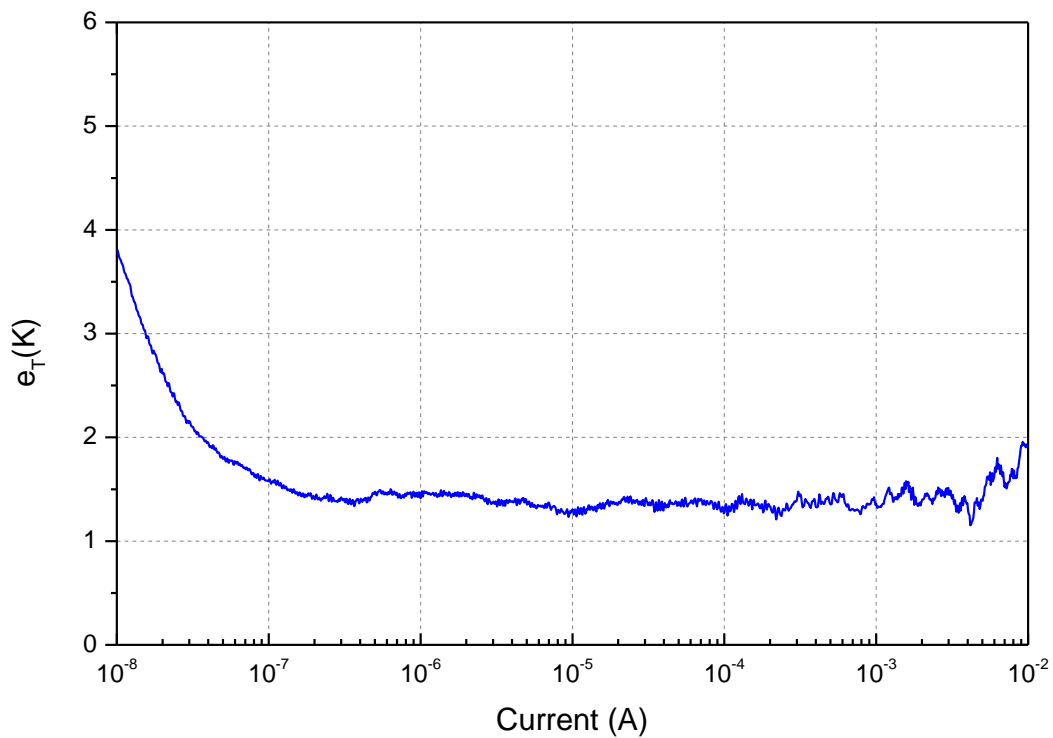
(b)

Figure. 4.36. (a) Coefficient of determination and sensitivity calculated for 1251 values of the bias currents between I= 10 nA and 10 mA. (b) Corresponding RMSE in the temperature range T = 303–498 K.

4.4. Simulation and analysis of the current–voltage–temperature (*I-V-T*) characteristics of W/4H-SiC Schottky diode for high performance temperature sensor

A 4H-SiC Schottky diode fabricated and reported by S. Toumi et al [28] was simulated in the cylindrical coordinate system by using the thermionic emission model in a commercial device simulator Atals-Silvaco [109]. All the physical models described in chapter three were used. Resultant *I-V-T* curves were compared with measured data.

4.4.1. Device structure

A schematic cross sectional view of the 4H-SiC Schottky diodes considered in this work is shown in figure (4.37) (plot not in scale).
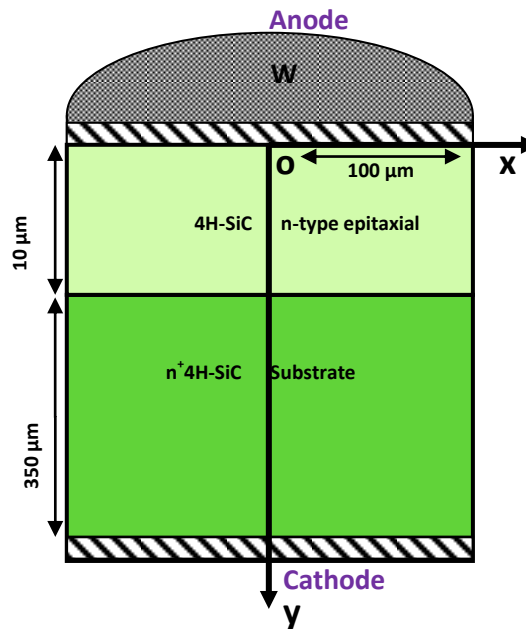
Figure. 4.37. W/4H-SiC Schottky barrier diode schematic cross section.

The substrate material used for the experimental devices was n-type 4H–SiC <0001> from Cree Inc. The epi-layer is 10 μm thick and has a net doping density of about 1.3×10^{16} cm^{-3}. The Schottky diodes had a circular geometry with a diameter of 200 μm.

The Schottky contacts were formed by depositing, through e-beam evaporation, Tungsten on the SiC substrate at a pressure of approximately 1×10^{-5} Pa followed by annealing in an open furnace at 500 °C under a N$_2$ flow of about 1000 sccm. More details about the diode fabrication process are provided in [28].

4.4.2. *I-V -T* characteristics

The measured (as reported in [28]) and simulated forward *I-V-T* curves of the considered W/4H-SiC SBDs for seven different temperatures from 303 K to 448 K are shown in figure (4.38).
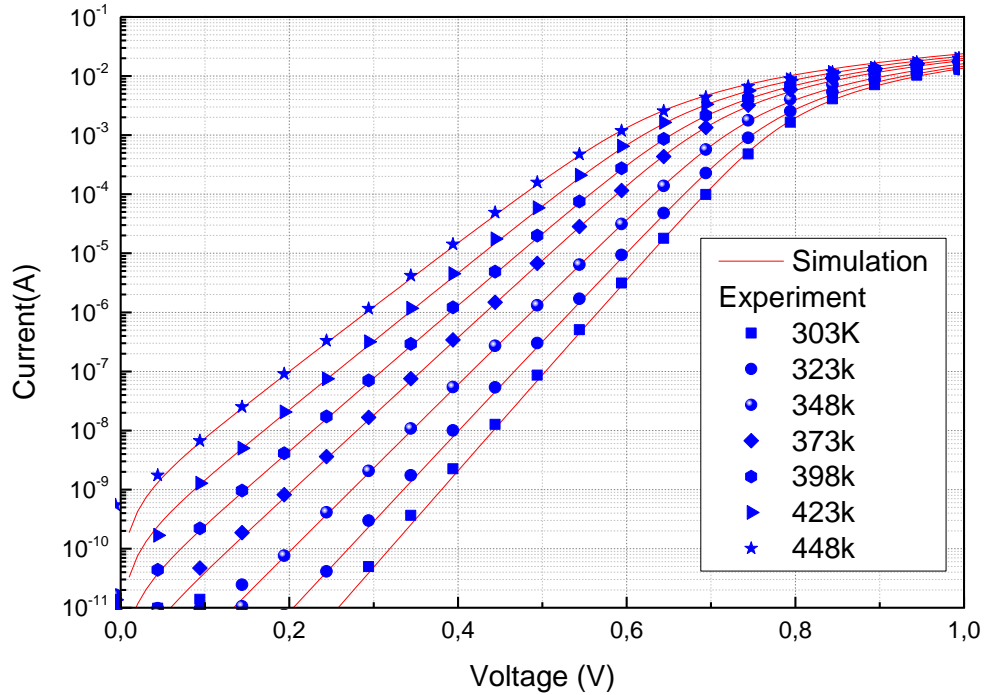
Figure.4.38. Measured (symbols) and simulated (solid lines) current–voltage characteristics of the W/4H-SiC Schottky diode at different temperatures.

It is worth noting that the numerical simulation results are in good agreement with the experimental data.

From the simulation *I-V-T* curves in figure (4.38) we extracted the fundamental diode parameters I_0 ,$\emptyset_B$, and n similarly to [130]. In particular, at each temperature, the saturation current I_0 was determined from the intercept of the plot $ln(I)$ vs V for $V = 0$.

Afterwards, the barrier height $\emptyset_B$ was calculated from equation (4.2) resulting $\emptyset_B = (kT/q)ln(AA^*T^2/I_0)$. Finally, the ideality factor n was extracted determining the slope of the linear region of the curves $ln(I)$ vs V .

The values of the ideality factor and barrier height of the diode at different temperature are plotted as function of temperature in figure (4.39). The barrier height and ideality factor are found to be strong dependence, the plot shows that the ideality factor decrease while the barrier height increase with increasing temperature.
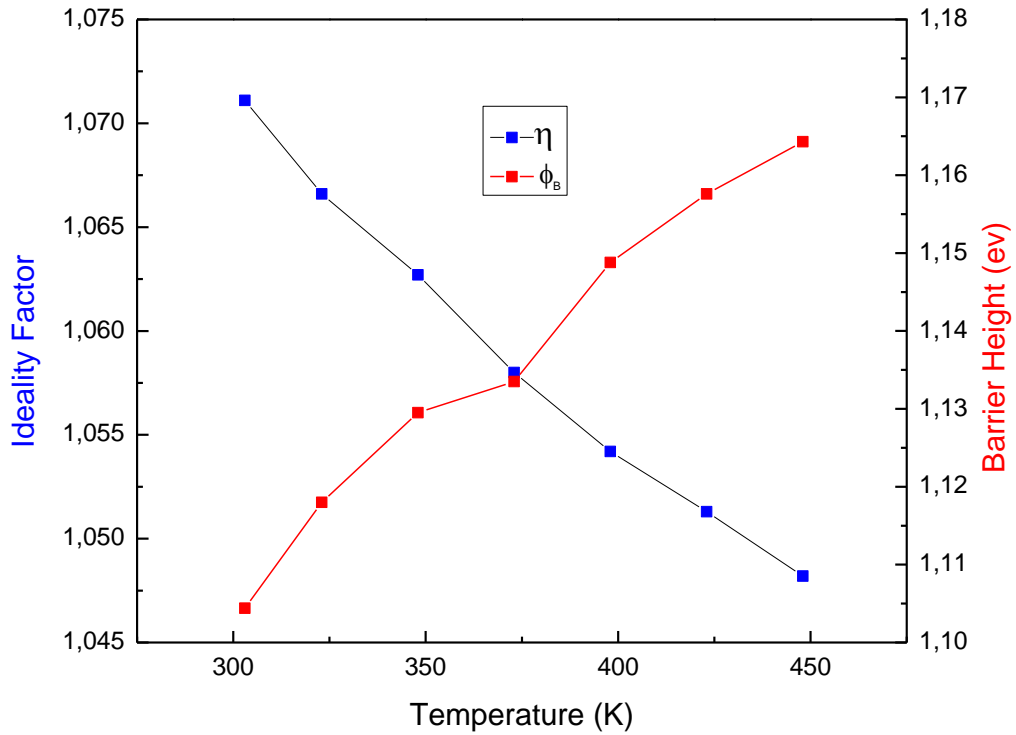
Figure. 4.39. Ideality factor and barrier height behaviors as a function of temper-ature for the device in figure (4.38).

As shown in figure (4.38), the forward bias *I-V* characteristics are linear on a semi-logarithmic at low forward bias voltages, but deviate from linearity due to the effect of series resistance *Rs*. The variation of series resistance values of W/4H-SiC versus temperature extracted from our curves is shown in figure (4.40). As seen in this figure, the values of *Rs* are near constant and equal to 12.6 Ω.
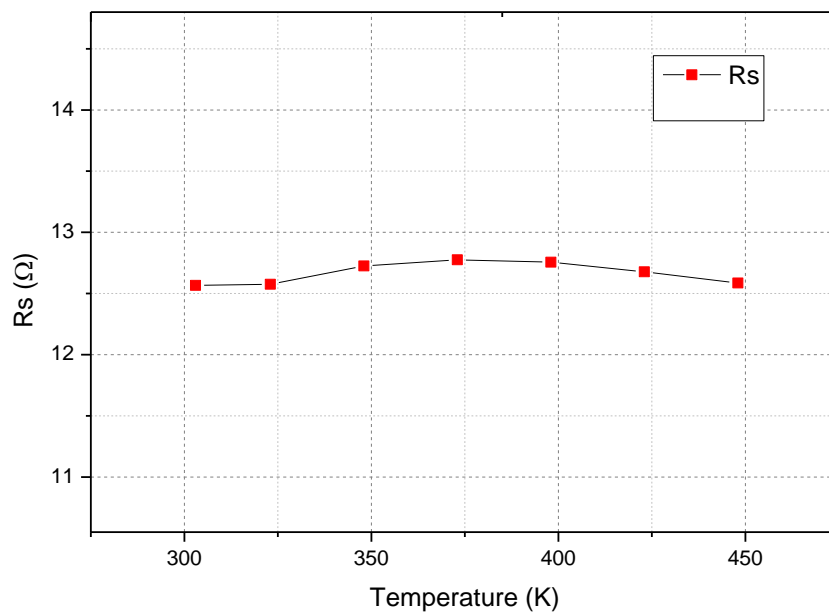
Figure. 4.40. The temperature dependence of the series resistance.

By considering (4.2) in the form of $ln(I_0/T^2) = ln(AA^*) - (q/kT)\emptyset_B$, the Arrhenius plot of term $ln(I_0/T^2)$ against $1000/T$ is shown in figure (4.41).
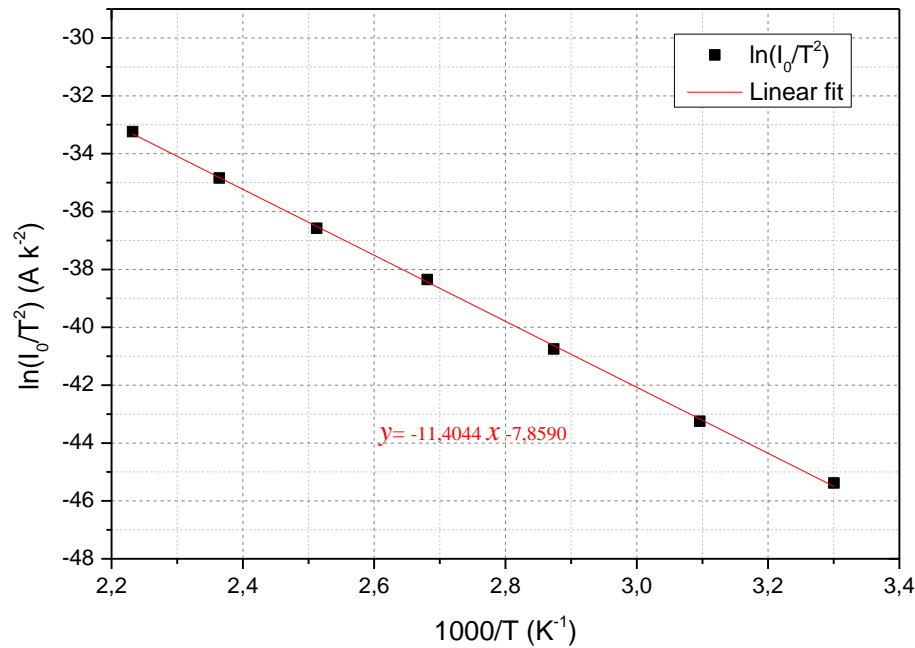
Figure. 4.41.Arrhenius plot of $ln(I_0/T^2)$vs.$1000/T$.

The value of A* obtained from the intercept of the linear portion of the ordinate is $1.23\,\text{A} \cdot \text{cm}^{-2} \cdot \text{K}^2$ that is much lower than the theoretically calculated value, which is $\approx 146\,\text{A} \cdot \text{cm}^{-2} \cdot \text{K}^2$ for n-type 4H-SiC [129]. A barrier height value of $0.983\,eV$ is obtained from the slope of the straight line.

The presented results seem to predict current transport mechanisms not following the pure TE theory and the barrier height and ideality factor are found to be strong dependence.

4.4.3. Effect of image-force lowering

The barrier lowering due to image charge is a possible explanation for the temperature dependence of the barrier height and ideality factor.

The $\Delta\emptyset$ reduction at V = 0.2V due to the image-force lowering effect was calculated as 23.77 meV at 448 K and as 24.26 meV at 303K using equation (4.8). Thus, it may be noted that these values of the $\Delta\emptyset$ are almost constant for 303–448 K temperature range and the image-force lowering effect alone cannot account for the decreasing of the barrier height with decreasing temperature in W/4H-SiC Schottky diode. The ideality factors found by using equation (4.9) are 1.009 and 1.010 at 303 and 448 K, respectively. These values also show that the observed variation in the ideality factor cannot be explained by the image-force lowering.

4.4.4. Flat-band barrier height and modified Richardson plots

The variation of flat-band barrier height ($\emptyset_{Bf}$) of the 4H-SiC Schottky barrier diodes calculated from the current–voltage barrier heights and the corresponding ideality factor at each temperature is shown in the figure (4.42). The barrier height obtained under flat-band condition is considered to be real quantity. Unlike the case of zero-bias barrier height ($\emptyset_B$), the electric field is zero under flat-band condition. This eliminates the effect of the image force lowering that would affect the current–voltage characteristics and removes the influence of lateral inhomogeneity [135-138].

As seen in figure (4.42), $\emptyset_{Bf}$ is always larger than zero-bias barrier height. The temperature dependence of flat-band barrier height can be expressed as $\emptyset_{bf}(T) = \emptyset_{bf}(T = 0) + \alpha T$, where $\emptyset_{Bf}(T = 0K)$ is the zero-temperature flat-band barrier height and is the temperature coefficient of $\emptyset_{Bf}$. where $\emptyset_{Bf}(T = 0K)$ is the flat-band barrier height extrapolated to 0 K and α is the temperature coefficient. From the slope and intercept of the least square fit of the $\emptyset_{Bf}(T)$ data in the temperature range of 303–448 K give the value of the zero-temperature flat-band barrier height and the temperature coefficient. The values obtained are $\emptyset_{Bf}(T = 0K)$ is 1.098 eV and α is 2.43 x10^{-4} eV/K.
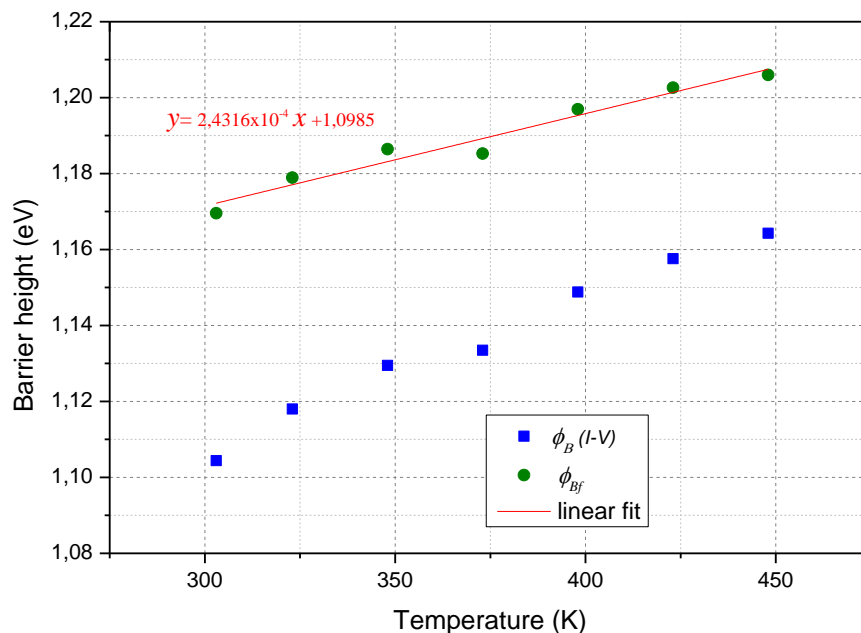
Figure.4. 42. Temperature dependence of the zero-bias BH $\emptyset B$ and flat-band BH $\emptyset Bf$ for the W/4H–SiC Schottky barrier diode in the temperature range of 303–448 K.

Considering the temperature dependence of the ideality factor n, the plot of $ln(I_{0f}/T^2)$ versus $1/nT$ according to equation (4.14) should be a straight line with the slope directly yielding $\emptyset_{Bf}$ (T = 0K) and the intercept at the ordinate determining A* for a given diode area A [136].

Figure (4.43) shows the $ln(I_{0f}/T^2)$ versus $1/nT$ plots. The modified $ln(I_{0f}/T^2)$ versus $1/nT$ plot gives $\emptyset_{Bf}$ (T = 0K) and A* as 1.074 eV and 3.43 A cm^{-2} K^{-2}, respectively.

$$y = -12,4601\, x - 6,83319$$
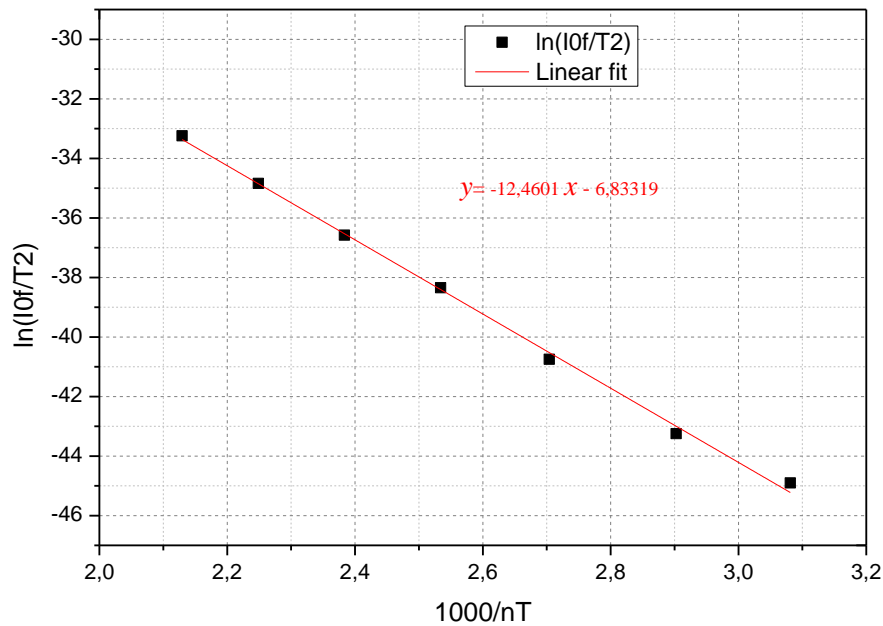
Figure.4. 43. Richardson plots of $ln(I_{0f}/T^2)$ vs. 1000/nT
and their linear fits for the W/4H− SiC Schottky diode.

4.4.5. Effect of thermionic field emission

The contribution of tunnelling (FE or TFE) to the current of a Schottky diode is the most common explanation for the temperature dependence of the barrier height and ideality factor.The E_{00} parameter determines the conduction mechanism, whether it is by TE, TFE, or FE. In general, the current transportation mechanism which dominates the barrier may be determined using E_{00} tunneling parameter expressed in equation (4.31). In Schottky junctions, the dominat mechanism is the thermionic emission mechanism when $E_{00} << kT$, the thermoionic-field emission if $E_{00} = kT$, the field emission when $E_{00} >> kT$ [136,149, 150].

The E_{00} values for W/4H-SiC were calculated to be 1.50 meV and 1.51meV at 303 K and at 448 K, respectively. In addition, according to this consideration, it may be reported that the thermionic emission is the dominant current mechanism because E_{00} values are significantly lower than kT for the whole temperature range. Due to the relation to E_{00} characteristic tunneling parameter of ideality factor in equation (4.32), the ideality factors for tunneling according to

equation (4.32) are obtained as 1.001 and 1.0005 that are too low to explain the temperature dependence of the ideality factor showed in figure (4.39) (n =1.071 and 1.048 at 303 K and 448 K for the device, respectively). Thus, the tunneling current or TFE cannot possibly account for the observed high ideality factor values

4.4.6. Inhomogeneous barrier analysis

According to the earlier studies, the ideality factor of an inhomogeneous Schottky barrier diode with a distribution of low Schottky barrier heights increase with decrease in temperature [23,28,122 127, 152–154]. The Schottky barrier consists of lateral inhomogeneous patches of different barrier heights. Schmitsdorf et al [141] used Tung's theoretical approach and found linear correlation between zero-bias Schottky barrier height and ideality factor.

Figure (4.44) shows the plot of zero-bias barrier height($\emptyset_B$) versus the ideality factor (n). The straight line in figure (4.44) is the least squares fit to the data and indicates a linear relationship between the effective barrier heights and the ideality factors of the Schottky contact. The extrapolation of the zero-bias barrier heights versus ideality factor plot to $n = 1$ gives a homogeneous barrier height of approximately 1.287 eV. Thus, it can be said that the significant decrease of the zero-bias barrier height and increase of the ideality factor especially at low temperature are possibly caused by the barrier inhomogeneities.
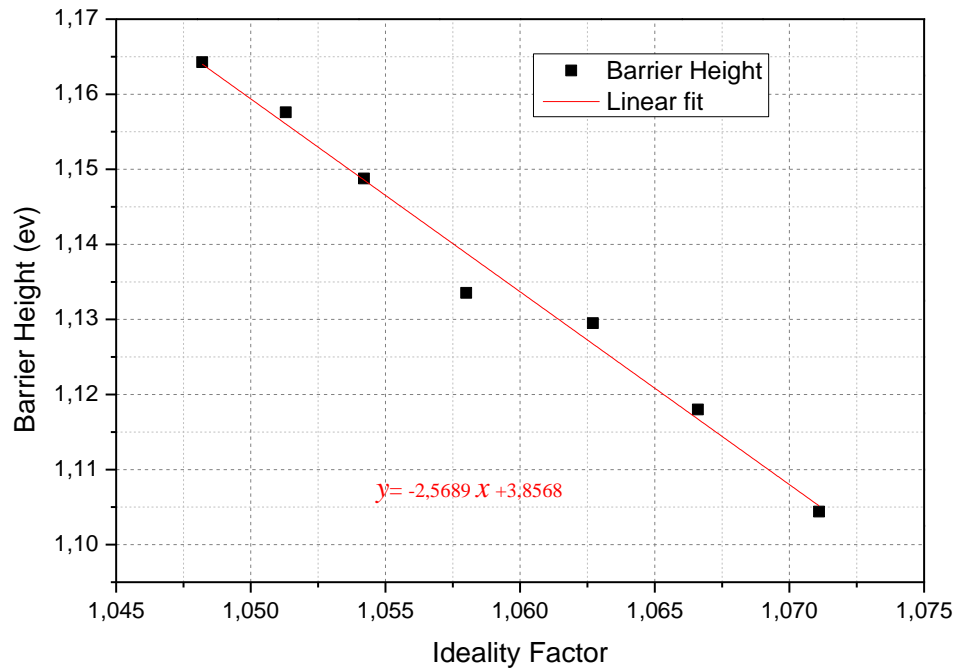
Figure. 4.44. Schmistsdorf's plot showing zero bias barrier height versus ideality factor.

Following Sullivan et al [134], in order to evidence the presence of barrier inhomogeneity, the temperature dependence of the ideality factor can be reported in the form of a plot of *nT vs T*. This plot for W/4H-SiC SBD is reported in figure (4.45), where the dashed line represents the ideal behavior *n=1*. The *n(T)* data of W/4H-SiC SBD show a linear trend, nearly parallel to the straight line of the ideal Schottky contact behavior. This latter means that the ideality factor can be expressed in the form *n=1+T₀ /T* where T_0 is a constant. This behavior, which is commonly referred to as the "*T₀* anomaly" [15], is typical of a real Schottky contact, i.e., a contact with a distribution of barrier inhomogeneities [158]. The fit of the data give a value of T_0=21.47 K
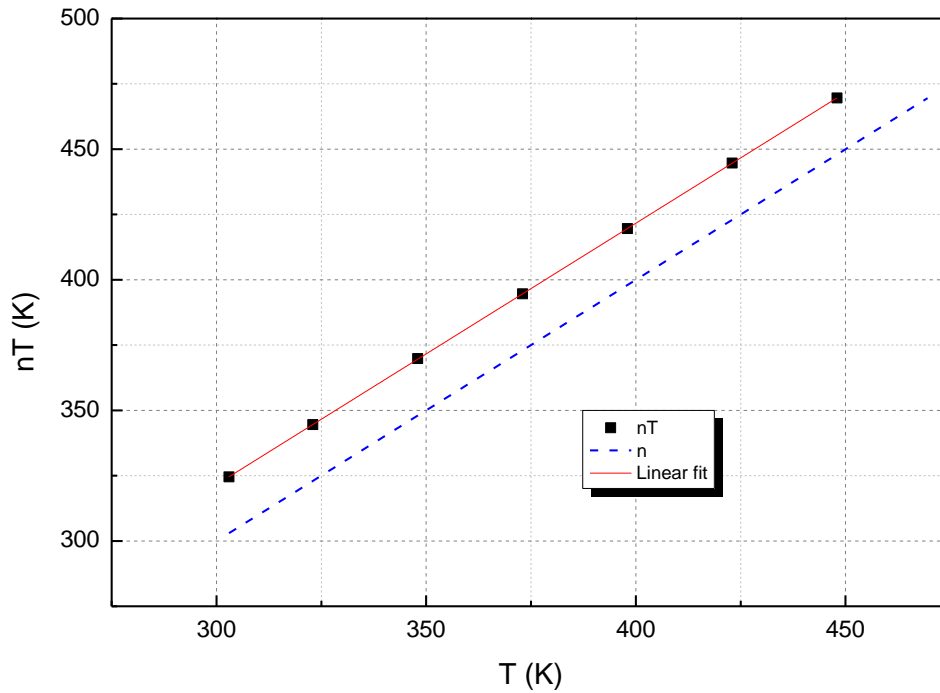
Figure. 4.45. Plot of *nT* versus *T* showing the T_0 effect.

Werner and Güttler [19] have proposed an analytical potential fluctuation model for the interpretation of I–V measurements on spatially inhomogeneous PtSi/Si Schottky contacts, the $\emptyset_B$ and *n* anomalous behaviors reported above are explained by assuming spatially inhomogeneous barrier heights and potential fluctuations at the Schottky interface that consist of low and high barrier areas. It is assumed that $\overline{\emptyset}_B$ and σ are linearly bias-dependent on Gaussian parameters ($\overline{\emptyset}_B = \overline{\emptyset}_{B0} + \rho_2 V$ and $\sigma^2 = \sigma_0{}^2 + \rho_3 V$).

The plot of the barrier height and ideality factor as a function of $q/2kT$ aids to characterize the behavior of the inhomogeneous potential barrier as shown in figure (4.46) and in figure (4.48), respectively.

$y= -0,0094\,x\,-1,2865$
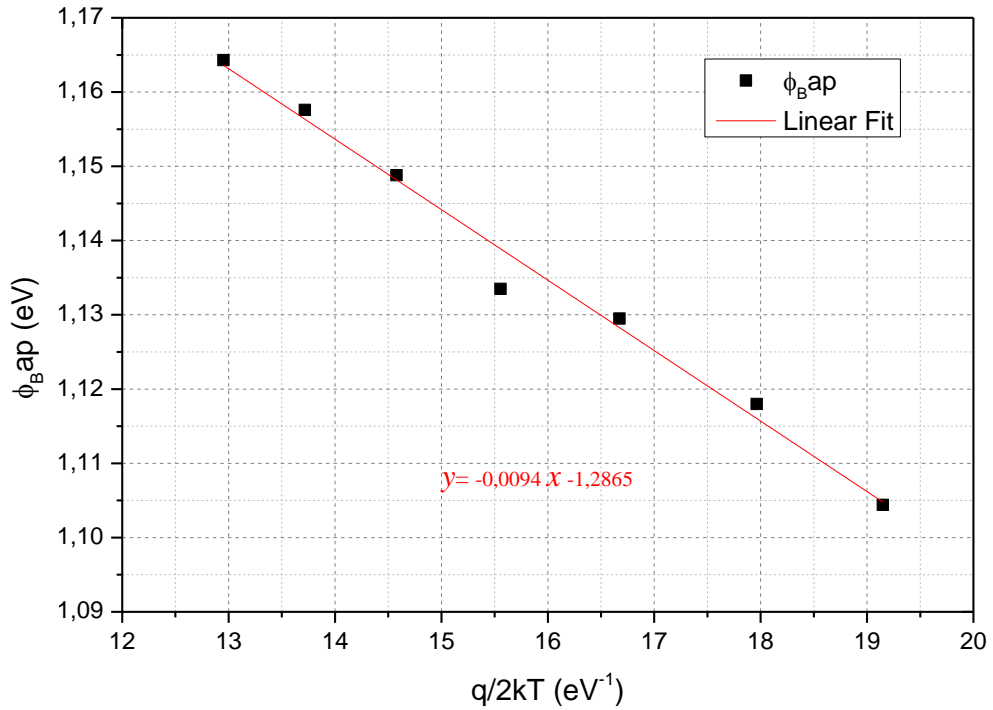
Figure.4.46. $\emptyset_{Bap}$ vs.$q/2kT$ according to a Gaussian distribution of the SBH.
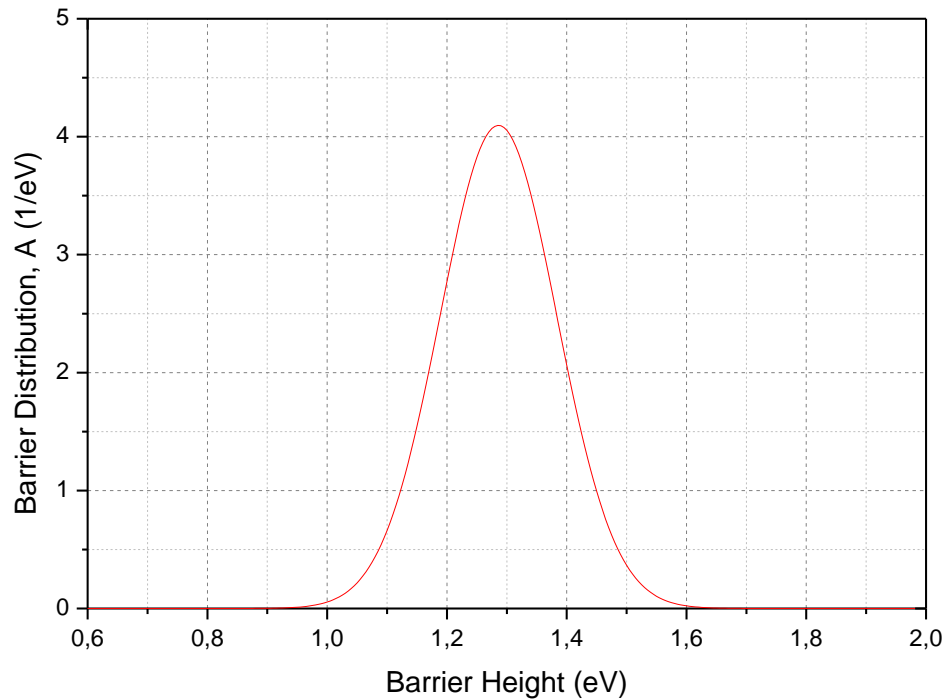
Figure.4. 47. Gaussian distribution function for W/4H–SiC junction

As can be seen in figure (4.46), the graphical representation of $\emptyset_{Bap}$ versus $q/2kT$ is a straight line of the best linear fit with the intercept on the ordinate determines the zero mean barrier height $\overline{\emptyset}_{B0}$ and the slope gives the zero bias standard deviation σ_0.

The values obtained are 1.286 eV and 0.0974 eV for $\overline{\emptyset}_{B0}$ and σ_0 respectively. Compensate of these values in equation (4.15) allows us to get the Gaussian distribution function of SBH as shown in figure (4.47). The standard deviation is a measure of the barrier homogeneity where the lower value of σ_0 corresponds to a more homogeneous barrier height. However, the value of $\sigma_0 = 97.4$ meV is not small compared to the mean value of $\overline{\emptyset}_{B0} = 1.286$ eV (7.58%) which indicates the presence of the interface inhomogeneities.

Similarly, from the plot of the term $(n_{ap}^{-1} - 1)$ vs. $q/2kT$ in figure (4.48), we calculated the coefficients ρ_2 as the intercept and ρ_3 as the slope of the straight line which fits the diode data for each temperature range.

The analysis of this plot gives the values of the following voltage coefficients: $\rho_2 = 0.00365\,V$ and $\rho_3 = -0.00329\,V$.

The linear behaviour of the $(n_{ap}^{-1} - 1)$ vs $q/2kT$ plot confirms that the ideality factor does indeed denote the voltage deformation of the Gaussian distribution of the barrier height.
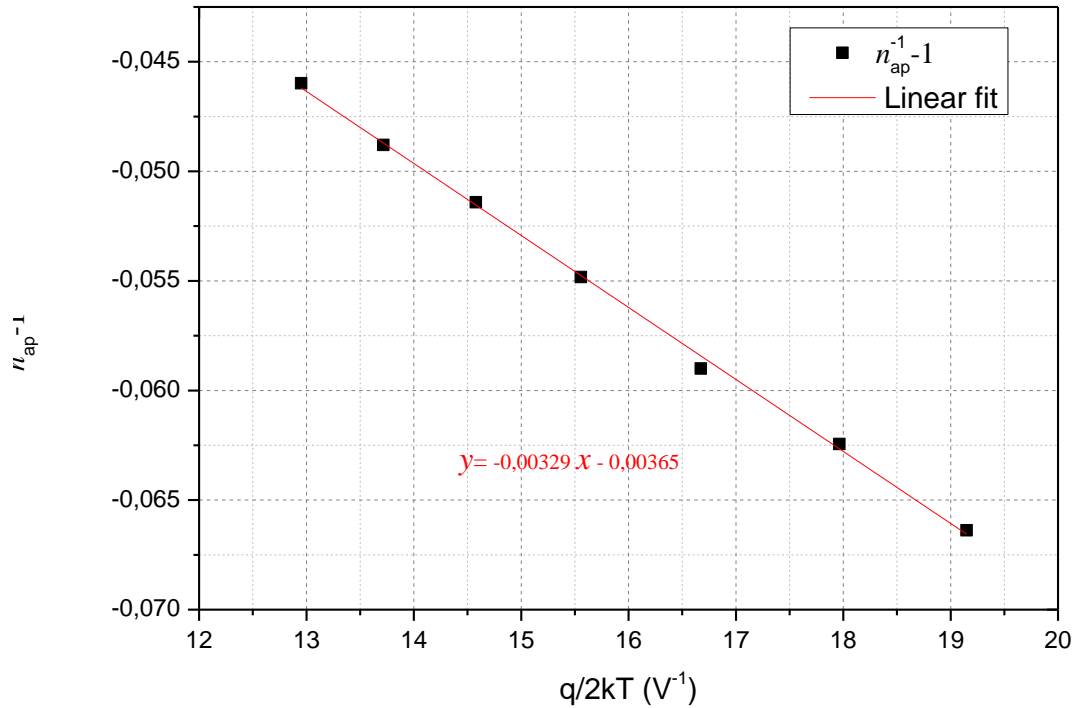
Figure. 4.48. $(n_{ap}^{-1} - 1)$vs.$q/2kT$ according to a Gaussian distribution of the SBH.

Finally, by combining (4.20) and (4.27), we obtain $ln\left(\frac{I_0}{T^2}\right) - \left(\frac{q^2\sigma_0^2}{2k^2T^2}\right) = ln(AA^*) - \left(\frac{q\overline{\emptyset}_{B0}}{kT}\right)$.

The slope and intercept of the linear fitting of the plot $ln(I_0/T^2) - (q^2\sigma_0^2/2k^2T^2)$ vs. q/kT (see figure(4.49)) allow to determine $\overline{\emptyset}_{B0}$ and A^* as follows: 1.287 eV and 148.8 A cm^{-2} K^{-2} respectively.

It is worthwhile noting that $\overline{\emptyset}_{B0}$ is in good agreement with the results in figure (4.46). At the same time, the modified Richardson constants are close around the expected theoretical value.

These results show that the temperature dependence of current transport characteristics can be successfully interpreted by using TE theory with GD of the barrier heights due to the inhomogeneous barrier heights at the W/4H–SiC interface.
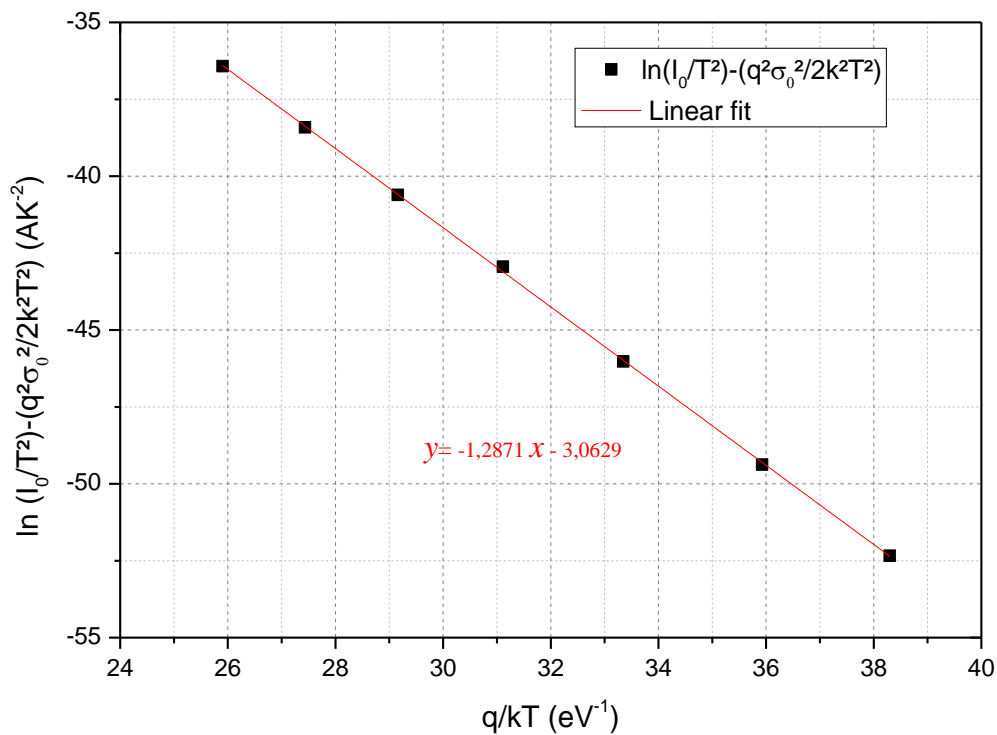
Figure.4.49. $ln(I_0/T^2) - (q^2\sigma_0^2/2k^2T^2)$ vs. q/kT according to a Gaussian distribution of the SBH.

4.4.7. State of W/4H-SiC interface

The solid-state reaction between metal and Si only occurs in those regions of a patterned substrate where the metal is in direct contact with the Si to form (WSi$_2$, W$_5$Si$_3$) when reacted with elemental Si and form a carbide (WC, W$_2$C) when reacted with elemental C [28, 159]. In particular, W reacts with SiC below 970 K by forming WSi$_2$ and WC which are stable with SiC. At temperatures between 970 K and 2140 K. W form the metal rich silicide W$_5$Si$_3$ and WC At

higher temperatures (above 2140 K) the stable carbide changes to (W_2C) [28,160]. Geib et al [159] deposited W on b-SiC via electron beam deposition and identified WSi_2 and WC as the resulting phases formed after annealing at 1123 K.

High temperature thermal stability of $Au/Ti/WSi_x$ Schottky contacts on 4H-SiC have been observed by Kim et al. [161]. The contacts show a maximum Schottky barrier height of 1.15 eV at an annealing temperature of 500 ^{0}C. The barrier height decreased for anneals above 600 ^{0}C. Sputter-deposited WSix Schottky contacts on n-type 4H-SiC were also characterized as a function of annealing and measuremental temperature by Kim et al [162]. The diodes have produced a maximum barrier height of 1.15 eV after a 500 ^{0}C annealing which appears to be the optimum condition to maximizing the barrier Height. The contacts were unstable after annealing above 700 ^{0}C.

According to these studies which show that the final phases formed in the interface depend on the method of metal deposition as well as the temperature of annealing, and on the basis of the results presented in our study, we believe that the reaction mechanism W/4H-SiC Schottky contacts   annealed at 500 ^{0}C as described in Section (4.4.1) lead to a formation of a silicide WSi_2 and WC which are stable with SiC, so less inhomogeneity is expected with SiC as evidenced by the T_0 value and results discussed above.

4.4.8. W/4H-SiC SBD Sensor Performances

As a temperature sensor, the SBD is forward biased at a constant current. In this case, the relationship between the forward voltage drop and the current of the SBD considering the series resistance can be expressed as $V = R_s I + n\emptyset_B + \frac{kTn}{q} ln\left(\frac{I}{AA^*T^2}\right)$.

The forward voltage (V) as a function of temperature for applied current values in the range from 1nA to 10 mA for the whole temperature range of 303 K up to 448 K are shown in figure (4.50).

Thanks to an almost constant value of the ideality factor, V-T characteristics exhibit a very high degree of linearity in the whole considered temperature range. The sensor sensitivity (S) is defined as the temperature derivative of forward voltage (V) equation; therefore, it can be obtained from the slope of the V–T characteristics. The calculated sensitivity varies from 2.41 mV/K to 1.07 mV/K in the 303-448 K temperature range.
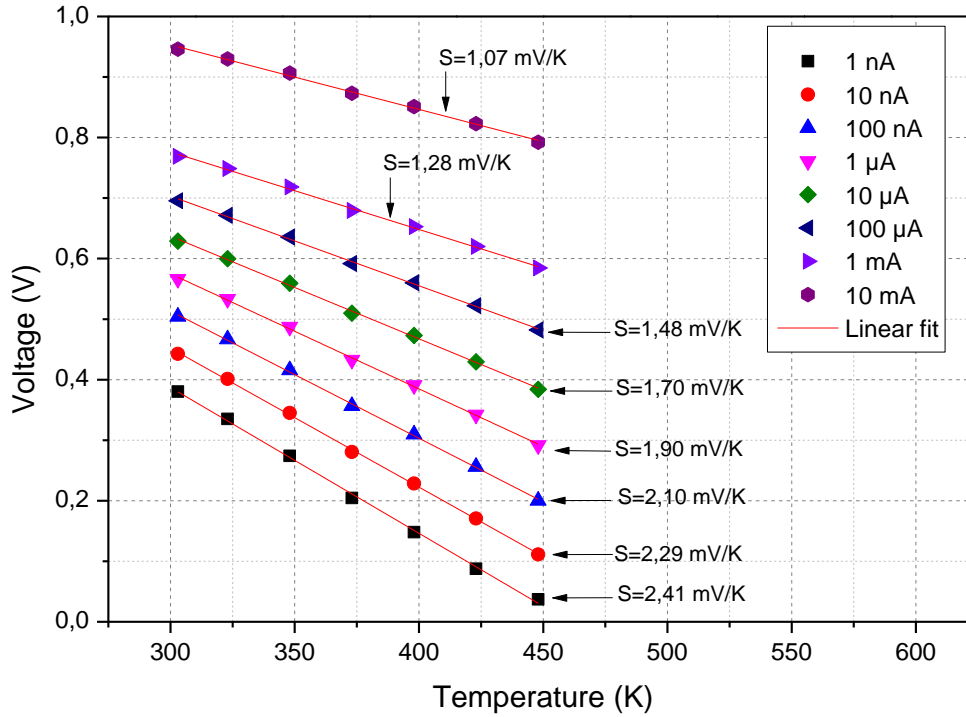
Figure. 4.50. Forward voltages versus temperature at eight
currents *I* (1 nA, 10 nA ,100 nA, 1µA, 10µA, 100µA, 1 mA, and 10 mA). *V-T* data are fitted
with the best-calculated linear model.

Moreover, in order to evaluate the agreement between the *V-T* data and the corresponding linear best-fit the coefficient of determination (R^2) and the temperature error (e_T) had been calculated. In figure (4.51 (a)) is shown the calculated value of *S* and R^2 for different bias currents. The *V-T* characteristics show a good degree of linearity. As reported, when *I* is 10 mA the sensitivity is 1.07mV/K and monotonically increases up to 2.41 mV/K for *I* =1 nA. The maximum of R^2=0.99961 has been calculated for *I*=5.97 nA corresponding to a sensitivity S=2.33 mV/K.

The temperature error e_T between the *V-T* data and the corresponding linear best-fit, evaluated as: $e_T = S^{-1}e_{RMS,V} = S^{-1}\sqrt{n^{-1}\sum_{i=1}^{n}(V_{D,i} - f_{L,i})^2}$. The calculated plot, e_T versus *I*, for the considered temperature range is reported in figure (4.51(b)). e_T is always lower than 3.4 K for applied current values in the range from 1 nA to 10 mA while the minimum e_T = 1.14 K is obtained for *I* = 5.97 nA.

These results show that W/4h-SiC Schottky diodes are good candidates for high temperature sensing applications in a wide range of biasing currents.
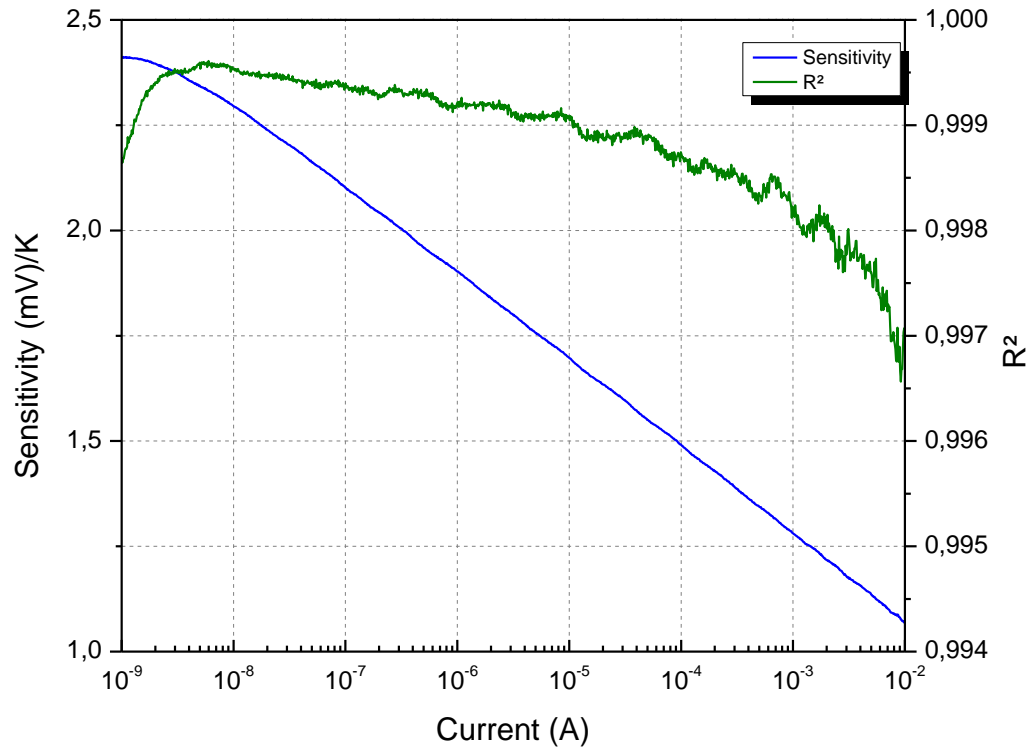
(a)
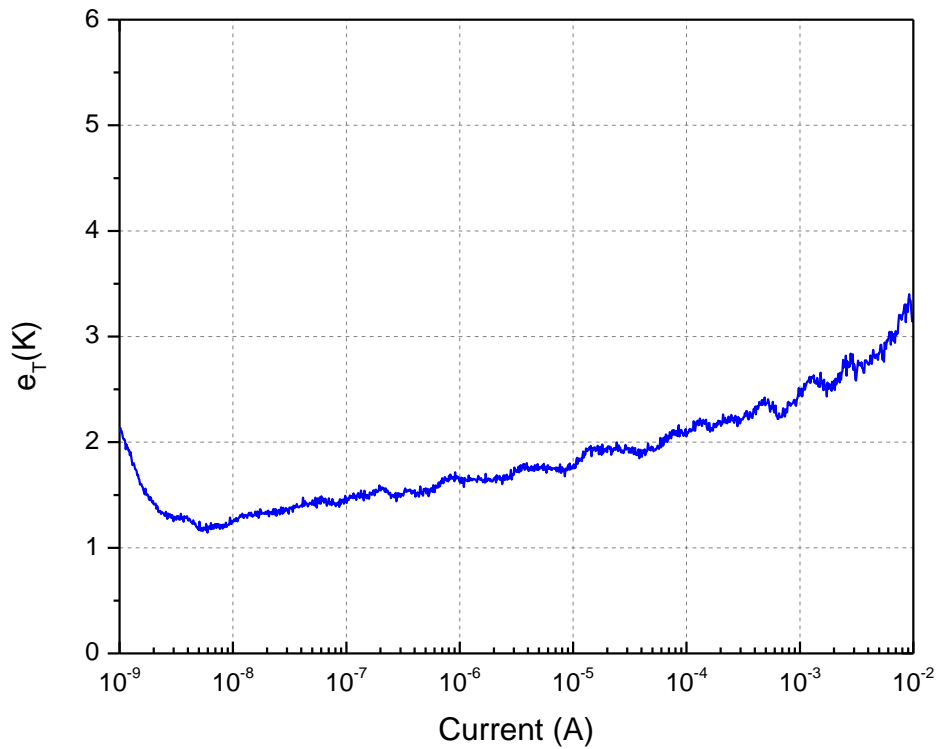
(b)

Figure. 4.51. (a) Coefficient of determination and sensitivity calculated for 1165 values of the bias currents between $I = 1$ nA and 10 mA. (b) Corresponding RMSE in the temperature range T = 303–948 K.

4.5. Analysis of main results

I–V–T characteristics are usually used in order to identify the different conduction mechanisms in current transport. The electronic transport in metal/SiC contacts is of great importance, and the exact description of the forward characteristics is still in issue.

The forward *I-V* characteristics of Ti/Al 4H–SiC, Mo/4H–SiC and W/4H–SiC Schottky barrier diodes devices was investigated by means of a combined numerical and analytical simulation study in wide temperatures range. The simulated characteristics of Ti/Al 4H–SiC obtained by considering a pure thermionic emission (TE) theory with homogeneous Schootky barrier height did not fit the experimental ones due to the strong temperature dependence of barrier height and ideality factor. The model proposed by Padovani and Sumner were adopted in order to precisely fitted the experimental *I-V* characteristics of Ti/Al 4H–SiC SBD, because it has been already stated that no deep level has been proved in the diode annealed at high temperatures by using the DLTS (deep-level transient spectroscopy measurements). While the forward *I-V* characteristics Mo/4H–SiC and W/4H–SiC was simulated in the cylindrical coordinate system only by using the thermionic emission model in a commercial device simulator Atals-Silvaco after calibrating the barrier height as such mentioned in [120] and [121] due to the small values of the ideality factor of these devices and results showed a good agreement with the experimental data.

The simulated characteristics of Ti/Al 4H–SiC showed an intersection in curves I-V, unlike the simulated curves *I-V* of Mo/4H–SiC and W/4H–SiC SBDs, this can be attributed to great degree of inhomogeneity of BH in Ti/Al 4H–SiC compared to Mo/4H–SiC and W/4H–SiC SBDs ones. Subhash Chand [127] have reported that the crossing of *I–V* curves is an inherent property even of homogeneous Schottky diodes of constant BH and is normally hidden due to saturation in current caused by series resistance. While the intersection of *I-V* curves is observable in the normal range due to the apparent temperature-dependent BH in inhomogeneous Schottky diodes.

Analysis of the current–voltage characteristics of Ti/Al 4H–SiC, Mo/4H–SiC and W/4H–SiC Schottky structure based on thermionic emission mechanism showed some anomalies such that the increase in the barrier height Φ_B and decrease of ideality factor n with increasing temperature. In addition to the extracted value of the effective Richardson constant has been found to be several orders of magnitude lower than the theoretically predicted value (146 Acm^{-2}K^{-2}). The most common effects to explain these anomalies were investigated. A flat-band barrier height, image force lowering, and tunnelling effects have all been used to help explain the temperature-dependent barrier heights observed. Furthermore, it was demonstrated that the

abnormal characteristics observed in the barrier height, ideality factor and Richardson plot only cannot be caused by the factors such as image-force lowering barrier, flat-band barrier height and tunneling.

The temperature dependence of ideality factor in Schottky diodes is called the "T_0 effect". The determination of T_0 value allows knowing the degree of SBH inhomogeneity. The values of T_0 obtained varied from 52K to 264K in the 85 – 445 K temperature range for the Ti/Al 4H–SiC, While its value were found to be 15.07K and 21.47K for Mo/4H–SiC and W/4H–SiC Schottky diodes, respectively. The high values of T_0 for the Ti/Al 4H–SiC compared to Mo/4H–SiC and W/4H–SiC SBDs ones indicate a strong deviation from the pure TE model as well as to the high degree of SBH inhomogeneity. According to Saxena [100], the variation of T_0 as a function of temperature Indicates the presence of TFE mechanism.

The abnormal behaviour in the temperature dependent ideality factor and the barrier height in the Mo/4H–SiC and W/4H–SiC SBDs have been successfully cleared up accounting the (TE) theory with a single-Gaussian distribution of the BH having spatial variations due to the less degree of SBH inhomogeneity in these devices. While the observed behaviors in Ti/Al 4H–SiC SBD have been successfully interpreted by using the thermionic emission (TE) theory with a triple-Gaussian distribution of the barrier height (BH) in three different temperature ranges and this is attributable to the high degree of SBH inhomogeneity in Ti/Al 4H–SiC SBD, in addition to the possibility of TFE-dominated current transport. This possibility was further supported by the observed high characteristic energy E_{00} in the current transport below 230K. The possible origin of such high characteristic energies implies that the conduction mechanism is dominated by TFE at low temperatures instead of TE. The origin of high characteristic energies was not predicted by the simple theory, but has been related to several effects. The parameter, E_{00} is related to the transmission probability of the carrier through the barrier. It is affected by the electric field at the semiconductor surface and the density of states at the semiconductor.

Based on information gained from SiC defect investigation and various accomplishments published by other researchers, the more credible causes of these inhomgeneities can be attributed to the different conditions of preparation of the devices, i.e. the quality of the semiconductor, surface preparation, the morphology of the surface, the edge of termination used and also the temperature of annealing.

Proceeding from the results presented in our study, we believe that the reaction mechanism in Al/Ti 4H-SiC Schottky contact which formed by depositing Al/Ti on the SiC substrate and annealed at 1000 ^{0}C lead to a formation of Al spiking. The reactions and the creation of new

phases, which is due to the greater amount of heat used in the annealing treatment, can increase the barrier height and lead to significant inhomogeneity due to a mixture of different phases at the M-S interface and yield a high T_0 value. As we believe that the reaction mechanism Mo/4H–SiC and W/4H–SiC Schottky contacts annealed at 500 ^{0}C lead to a formation of a silicide and carbide which are stable with SiC, so less inhomogeneity is expected with SiC and yield a low value of T_0.

In our study, the Ti/Al 4H–SiC, Mo/4H–SiC and W/4H–SiC Schottky barrier diodes based temperature sensors for high power and high temperature sensing applications, were characterized. Results showed a good degree of linearity (R^2(Ti/Al 4H–SiC)=0.9999, R^2(Mo/4H–SiC)=0.9997, R^2(W/4H–SiC)=0.9996) and a high sensitivity (S(Ti/Al 4H–SiC)=1.7 mV/K, S(Mo/4H–SiC)=1.14 mV/K, S(W/4H–SiC)=2.41 mV/K) in a wide temperature range. It was seen that the good physical characteristics of Mo/4H–SiC (i.e. the barrier height is more stable and ideality factor n~1 remaining almost constant during the thermal variations) allow to obtain a highly linear sensor in a wide range of biasing currents with respect to those based on Ti/Al 4H–SiC and W/4H–SiC Schottky contacts. While the values of R^2 showing a significant decline for higher bias currents in Ti/Al 4H-SiC, because the variation of series resistance versus temperature in Ti/4H-SiC structure is more important compared to the Mo/4H-SiC and W/4H–SiC ones. These higher Rs values could be result from the change to α-TiAl phase at the Al–Ti interface layer because of excessive diffusion of Ti and Al, which is due to the greater amount of heat used in the annealing treatment.

Conclusion

Conclusion

In this thesis, we have investigated the *I-V-T* characteristics of Ti/Al/4H–SiC, Mo/4H–SiC and W/4H–SiC SBDs in order to fix the temperature effect on the main device electrical parameters. In particular, the experimental curves have been fitted over a wide temperatures range by means of a careful simulation analysis achieving an excellent agreement in the whole explored current range.

The current-voltage *(I-V)* characteristics of Ti/Al 4H-SiC Schottky barrier diodes (SBDs) have been investigated in the 85 - 445 K temperature range. Simulation results showed a good agreement with measurements in the whole explored current range from 10 µA to 10 mA. The main device electrical parameters, such as the barrier height and ideality factor, were found strongly temperature-dependent. In particular, the ideality factor decreases while the barrier height increases with increasing temperature. The observed behaviors have been successfully interpreted by using the thermionic emission *(TE)* theory with a triple-Gaussian distribution of the barrier height *(BH)* in three different temperature ranges, namely $85 \leq \Delta T1 \leq 135$ K, $180 \leq \Delta T2 \leq 270$ K, and $315 \leq \Delta T3 \leq 445$ K. The corresponding Richardson constants are $A_1* = 138.59$ $Acm^{-2}K^{-2}$, $A_2* = 275.62$ $Acm^{-2}K^{-2}$, and $A_3* = 141.89$ $Acm^{-2}K^{-2}$, respectively. These values are close to the theoretical result of 146 $Acm^{-2}K^{-2}$ for n-type 4H-SiC. It has been highlighted that the current flowing through the Schottky junction is also determined by the thermionic field emission (TFE) mechanism. The obtained results reveal that the device is well suited for temperature sensing applications, showing a good coefficient of determination, $R^2 = 0.9999$ for I =76.7 µA corresponding to a sensitivity S=1.7 mV/K. The temperature error between the voltage measurements and their linear best-fit is lower than 1.14 K.

The experimental forward current-voltage-temperature *(I-V-T)* characteristics of Mo/4H-SiC Schottky barrier diodes (SBDs) are investigated by means of a careful simulation study. The simulations are in excellent agreement with measurements in the whole explored current range extending over ten orders of magnitude for temperatures from 303 K to 498 K. The diode ideality factor tends to decrease while the Schottky barrier height increases with increasing temperature. These variations are explained on the basis of the thermionic emission *(TE)* theory with a single- Gaussian distribution of the barrier height *(BH)* around the Mo/4H-SiC interface. The calculated Richardson constant is $A* = 155.78$ $Acm^{-2}K^{-2}$, which is very close to the theoretical value of 146 $Acm^{-2}K^{-2}$ expected for n-type 4H-SiC. The device performance as temperature sensor has been evaluated. For a forward bias current that spans from 100 nA to 1 mA, the simulation results showed a good coefficient of determination $R^2 = 0.99974$ (100 nA $\leq I$

≤ 1 mA) and a high sensitivity value S = 1.92 mV/K (I= 1 μA). The temperature error calculated between the voltage measurements and their linear best-fit is in the limit of 1.5 K.

The current-voltage *(I-V)* characteristics of W/4H-SiC Schottky barrier diodes (SBDs) have been investigated in the 303 - 448 K temperature range. Simulation results showed a good agreement with measurements in the whole explored current range from 100 nA to 10 mA. The main device electrical parameters, such as the barrier height and ideality factor, were found strongly temperature-dependent. In particular, the ideality factor decreases while the barrier height increases with increasing temperature. The observed behaviors have been successfully interpreted by using the thermionic emission *(TE)* theory with a single-Gaussian distribution of the barrier height *(BH)*. The corresponding Richardson constants are A^*=148.8 Acm^{-2}K^{-2}. This value is close to the theoretical result of 146 Acm^{-2}K^{-2} for n-type 4H-SiC. The performance of temperature sensor based on W/4H-SiC Schottky diodes is investigated in the range from 1 nA to 10 mA for the whole temperature range of 303 K up to 448 K. The simulation results reveal that at a bias current of 5.97 nA, the diode forward voltage shows a good linear dependence on the temperature R^2=0.99961, with a sensitivity of 2.33 mV/K and a temperature error of 1.14 K.

On the basis of various achievements published by other researchers and according to the results presented in our study, It can be said that the reaction between the metal and SiC may occur at the interface during the annealing treatments, and the interface material, particularly the new phases formed in the interface, plays a key role in the electrical properties of the contact. The performance of SiC Schottky diodes as temperature sensors largely depends on the quality of the metal/SiC contact.

Optimization of 4H-SiC Schottky diodes for temperature Sensing and precise characterization are one of the perspectives for future work. Numerical simulation study of the influence of physical and geometrical parameters of Schottky diodes, such as epilayer, doping concentration and thickness on the sensors performance is an important step towards the optimization of these sensors. Future work should include also investigation of the behavior of Mo/4H-SiC and W/ 4H-SiC Schottky diodes as sensors at temperatures lower than 303 K, to enable their use in harsh environments, such as aerospace as well as terrestrial applications.

References

Bibliography

[1] M. Megherbi, F. Pezzimenti, L. Dehimi, A. Saadoune and F. Della Corte, "Analysis of the Forward I–V Characteristics of Al-Implanted 4H-SiC p-i-n Diodes with Modeling of Recombination and Trapping Effects Due to Intrinsic and Doping-Induced Defect States", Journal of Electronic Materials, vol. 47, no. 2, pp. 1414-1420, 2017.

[2] Y. Hijikata, Physics and technology of silicon carbide devices. Rijeka, Croatia: InTech, 2012.

[3] F. Nava, G. Bertuccio, A. Cavallini and E. Vittone, "Silicon carbide and its use as a radiation detector material", Measurement Science and Technology, vol. 19, no. 10, p. 102001, 2008.

[4] M. Wijesundara and A. Robert, Silicon carbide microsystems for harsh environments. Springer Science & Business Media, 2011.

[5] K. Zekentes and K. Vasilevskiy, Advancing Silicon Carbide Electronics Technology I: Metal Contacts to Silicon Carbide: Physics, Technology, Applications. Materials Research Forum LLC, 2018.

[6] T. Dinh, N. Nguyen and D. Dao, Thermoelectrical Effect in SiC for High-Temperature MEMS Sensors. Springer, 2018.

[7] G. Pristavu, G. Brezeanu, R. Pascu, F. Drăghici and M. Bădilă, "Characterization of non-uniform Ni/4H-SiC Schottky diodes for improved responsivity in high-temperature sensing", Materials Science in Semiconductor Processing, vol. 94, pp. 64-69, 2019.

[8] S. Rao, G. Pangallo, L. Di Benedetto, A. Rubino, G. Licciardo and F. Della Corte, "A V2O5/4H-SiC Schottky diode-based PTAT sensor operating in a wide range of bias currents", Sensors and Actuators A: Physical, vol. 269, pp. 171-174, 2018.

[9] G. Pristavu et al., "Barrier Stability of Pt/4H-SiC Schottky Diodes Used for High Temperature Sensing", Materials Science Forum, vol. 897, pp. 606-609, 2017.

[10] S. Rao, G. Pangallo, F. Pezzimenti and F. Della Corte, "High-Performance Temperature Sensor Based on 4H-SiC Schottky Diodes", IEEE Electron Device Letters, vol. 36, no. 7, pp. 720-722, 2015.

[11] G. Brezeanu et al., "4H-SiC Schottky Diodes for Temperature Sensing Applications in Harsh Environments", Materials Science Forum, vol. 679-680, pp. 575-578, 2011.

[12] M. Alexandru et al., "SiC Integrated Circuit Control Electronics for High-Temperature Operation", IEEE Transactions on Industrial Electronics, vol. 62, no. 5, pp. 3182-3191, 2015.

[13] D. Perrone, M. Naretto, S. Ferrero, L. Scaltrito and C. Pirri, "4H-SiC Schottky Barrier Diodes Using Mo-, Ti- and Ni-Based Contacts", Materials Science Forum, vol. 615-617, pp. 647-650, 2009.

[14] S. Dong et al., "Analysis of the inhomogeneous barrier and phase composition of W/4H-SiC Schottky contacts formed at different annealing temperatures", Chinese Physics B, vol. 27, no. 9, p. 097305, 2018.

[15] F. Padovani and G. Sumner, "Experimental Study of Gold-Gallium Arsenide Schottky Barriers", Journal of Applied Physics, vol. 36, no. 12, pp. 3744-3747, 1965.

[16] K. Ejderha, N. Yıldırm and A. Turut, "Temperature-dependent current-voltage characteristics in thermally annealed ferromagnetic Co/n-GaN Schottky contacts", The European Physical Journal Applied Physics, vol. 68, no. 2, p. 20101, 2014.

[17] M. Mamor, "Interface gap states and Schottky barrier inhomogeneity at metal/n-type GaN Schottky contacts", Journal of Physics: Condensed Matter, vol. 21, no. 33, p. 335802, 2009.

[18] B. Abay, G. ankaya, H. G der, H. Efeoglu and Y. Yogurt u, "Barrier characteristics of Cd/p-GaTe Schottky diodes based onI V Tmeasurements", Semiconductor Science and Technology, vol. 18, no. 2, pp. 75-81, 2002.

[19] J. Werner and H. Güttler, "Barrier inhomogeneities at Schottky contacts", Journal of Applied Physics, vol. 69, no. 3, pp. 1522-1533, 1991.

[20] R. Tung, "Electron transport at metal-semiconductor interfaces: General theory", Physical Review B, vol. 45, no. 23, pp. 13509-13523, 1992.

[21] J. Yu-Long et al., "Schottky Barrier Height Inhomogeneity of Ti/n-GaAs Contact Studied by theI-V-TTechnique", Chinese Physics Letters, vol. 19, no. 4, pp. 553-556, 2002.

[22] M. Gülnahar and H. Efeoğlu, "Double barrier nature of Au/p-GaTe Schottky contact: Linearization of Richardson plot", Solid-State Electronics, vol. 53, no. 9, pp. 972-978, 2009.

[23] M. Gülnahar, "Temperature dependence of current-and capacitance–voltage characteristics of an Au/4H-SiC Schottky diode", Superlattices and Microstructures, vol. 76, pp. 394-412, 2014.

[24] P. Kaushal, S. Chand and J. Osvald, "Current–voltage characteristics of Schottky diode simulated using semiconductor device equations", International Journal of Electronics, vol. 100, no. 5, pp. 686-698, 2013.

[25] P. Kaushal and S. Chand, "Numerical analysis of inhomogeneous Schottky diode with discrete barrier height patches", International Journal of Electronics, vol. 103, no. 6, pp. 937-949, 2015.

[26] S. Rao, L. Di Benedetto, G. Pangallo, A. Rubino, S. Bellone and F. Della Corte, "85–440 K Temperature Sensor Based on a 4H-SiC Schottky Diode", IEEE Sensors Journal, vol. 16, no. 17, pp. 6537-6542, 2016.

[27] L. Boussouar, Z. Ouennoughi, N. Rouag, A. Sellai, R. Weiss and H. Ryssel, "Investigation of barrier inhomogeneities in Mo/4H–SiC Schottky diodes", Microelectronic Engineering, vol. 88, no. 6, pp. 969-975, 2011.

[28] S. Toumi, A. Ferhat-Hamida, L. Boussouar, A. Sellai, Z. Ouennoughi and H. Ryssel, "Gaussian distribution of inhomogeneous barrier height in tungsten/4H-SiC (000-1) Schottky diodes", Microelectronic Engineering, vol. 86, no. 3, pp. 303-309, 2009.

[29] T. Kimoto and J. Cooper, Fundamentals of silicon carbide technology. Singapore: Wiley-IEEE Press, 2014.

[30] S. Saddow and A. Agarwal, Advances in silicon carbide processing and applications. Boston: Artech House, 2004.

[31] J. FAN, SILICON CARBIDE NANOSTRUCTURES. SPRINGER, 2014.

[32] S. Saddow, Silicon carbide biotechnology: a biocompatible semiconductor for advanced biomedical devices and applications. Elsevier Science, 2012.

[33]M. Levinshtein, S. Rumyantsev and M. Shur, Properties of advanced semiconductor materials. New York: John Wiley & Sons, Inc., 2001.

[34]G. Harris, Properties of silicon carbide. London: INSPEC, 1995.

[35]W. Lambrecht, S. Limpijumnong, S. Rashkeev and B. Segall, "Electronic Band Structure of SiC Polytypes: A Discussion of Theory and Experiment", physica status solidi (b), vol. 202, no. 1, pp. 5-33, 1997.

[36]C. Persson and U. Lindefelt, "Relativistic band structure calculation of cubic and hexagonal SiC polytypes", Journal of Applied Physics, vol. 82, no. 11, pp. 5496-5508, 1997.

[37]R. Humphreys, D. Bimberg and W. Choyke, "Wavelength modulated absorption in SiC", Solid State Communications, vol. 39, no. 1, pp. 163-167, 1981.

[38]S. Sridhara, S. Bai, O. Shigiltchoff, R. Devaty and W. Choyke, "Differential Absorption Measurement of Valence Band Splittings in 4H SiC", Materials Science Forum, vol. 338-342, pp. 567-570, 2000.

[39]W. Chen, N. Son, E. Janzén, D. Hofmann and B. Meyer, "Effective Masses in SiC Determined by Cyclotron Resonance Experiments", physica status solidi (a), vol. 162, no. 1, p. 79, 1997.

[40]W. Choyke, H. Matsunami and G. Pensl, Silicon carbide. Berlin: Springer, 2004.

[41]W. Choyke, D. Hamilton and L. Patrick, "Optical Properties of Cubic SiC: Luminescence of Nitrogen-Exciton Complexes, and Interband Absorption", Physical Review, vol. 133, no. 4, pp. A1163-A1166, 1964.

[42]S. Adachi, Properties of semiconductor alloys. Chichester, U.K.: John Wiley & Sons, Ltd, 2009.

[43]C. Persson, U. Lindefelt and B. Sernelius, "Band gap narrowing in n-type and p-type 3C-, 2H-, 4H-, 6H-SiC, and Si", Journal of Applied Physics, vol. 86, no. 8, pp. 4419-4427, 1999.

[44]S. Sridhara, R. Devaty and W. Choyke, "Absorption coefficient of 4H silicon carbide from 3900 to 3250 Å", Journal of Applied Physics, vol. 84, no. 5, pp. 2963-2964, 1998.

[45]P. Yu and M. Cardona, Fundamentals of semiconductors. New York: Springer, 2005.

[46]N. Watanabe, T. Kimoto and J. Suda, "Thermo-Optic Coefficients of 4H-SiC, GaN, and AlN for Ultraviolet to Infrared Regions up to 500 °C", Japanese Journal of Applied Physics, vol. 51, no. 11, p. 112101, 2012.

[47]D. Marple, "Refractive Index of ZnSe, ZnTe, and CdTe", Journal of Applied Physics, vol. 35, no. 3, pp. 539-542, 1964.

[48]S. Ninomiya and S. Adachi, "Optical Constants of 6H–SiC Single Crystals", Japanese Journal of Applied Physics, vol. 33, no. 1, 5, pp. 2479-2482, 1994.

[49]T. Troffer et al., "Doping of SiC by Implantation of Boron and Aluminum", physica status solidi (a), vol. 162, no. 1, pp. 277-298, 1997.

[50]N. Kuznetsov and A. Zubrilov, "Deep centers and electroluminescence in 4H瑈SiC diodes with a p-type base region", Materials Science and Engineering: B, vol. 29, no. 1-3, pp. 181-184, 1995.

[51] Y. Negoro, T. Kimoto, H. Matsunami and G. Pensl, "Abnormal Out-Diffusion of Epitaxially Doped Boron in 4H–SiC Caused by Implantation and Annealing", Japanese Journal of Applied Physics, vol. 46, no. 8, pp. 5053-5056, 2007.

[52] K. Purcell and J. Kotz, Inorganic chemistry. W.B. Saunders, 1977.

[53] W. Götz et al., "Nitrogen Donors, Aluminum Acceptors and Strong Impurity Vibrational Modes in 4H-Silicon Carbide (4H-SiC)", Materials Science Forum, vol. 143-147, pp. 69-74, 1993.

[54] A. Efros, N. Lien and B. Shklovskii, "Impurity band structure in lightly doped semiconductors", Journal of Physics C: Solid State Physics, vol. 12, no. 10, pp. 1869-1881, 1979.

[55] T. Kimoto, A. Itoh and H. Matsunami, "Step-Controlled Epitaxial Growth of High-Quality SiC Layers", physica status solidi (b), vol. 202, no. 1, pp. 247-262, 1997.

[56] S. Sze and K. Ng, Physics of optoelectronic devices. Hoboken: John Wiley & Sons, Inc, 2007.

[57] G. Pensl and W. Choyke, "Electrical and optical characterization of SiC", Physica B: Condensed Matter, vol. 185, no. 1-4, pp. 264-283, 1993.

[58] W. Schaffer, G. Negley, K. Irvine and J. Palmour, "Conductivity Anisotropy in Epitaxial 6H and 4H Sic", MRS Proceedings, vol. 339, 1994.

[59] M. Schadt, G. Pensl, R. Devaty, W. Choyke, R. Stein and D. Stephani, "Anisotropy of the electron Hall mobility in 4H, 6H, and 15R silicon carbide", Applied Physics Letters, vol. 65, no. 24, pp. 3120-3122, 1994.

[60] M. Shinohara et al., "Growth of High-Mobility 3C-SiC Epilayers by Chemical Vapor Deposition", Japanese Journal of Applied Physics, vol. 27, no. 2, 3, pp. L434-L436, 1988.

[61] W. Nelson, F. Halden and A. Rosengreen, "Growth and Properties of β- SiC Single Crystals", Journal of Applied Physics, vol. 37, no. 1, pp. 333-336, 1966.

[62] C. HAMAGUCHI, BASIC SEMICONDUCTOR PHYSICS, 2nd ed. SPRINGER I, 2010.

[63] Khan and J. Cooper, "Measurement of high-field electron transport in silicon carbide", IEEE Transactions on Electron Devices, vol. 47, no. 2, pp. 269-273, 2000.

[64] W. v. Muench and E. Pettenpaul, "Saturated electron drift velocity in 6H silicon carbide", Journal of Applied Physics, vol. 48, no. 11, pp. 4823-4825, 1977.

[65] B. Baliga, Fundamentals of power semiconductor devices. JWS Publishing, 1996.

[66] Chynoweth, "Ionization Rates for Electrons and Holes in Silicon", Physical Review, vol. 109, no. 5, pp. 1537-1540, 1958.

[67] Konstantinov, Q. Wahab, N. Nordell and U. Lindefelt, "Ionization rates and critical fields in 4H silicon carbide", Applied Physics Letters, vol. 71, no. 1, pp. 90-92, 1997.

[68] Dmitriev, A. Konstantinov, D. Litvin and V. Sankin, "Impact ionization and super-lattice in 6H-SiC", Sov. Phys. Semicond, vol. 17, pp. 686-689, 1983.

[69] S. Nakamura, H. Kumagai, T. Kimoto and H. Matsunami, "Anisotropy in breakdown field of 4H–SiC", Applied Physics Letters, vol. 80, no. 18, pp. 3355-3357, 2002.

[70] J. Palmour, J. Edmond, H. Kong and C. Carter, "6H-silicon carbide devices and applications", Physica B: Condensed Matter, vol. 185, no. 1-4, pp. 461-465, 1993.

[71] P. Neudeck, D. Larkin, J. Starr, J. Powell, C. Salupo and L. Matus, "Electrical properties of epitaxial 3C- and 6H-SiC p-n junction diodes produced side-by-side on 6H-SiC substrates", IEEE Transactions on Electron Devices, vol. 41, no. 5, pp. 826-835, 1994.

[72] D. Morelli, J. Heremans and c. Beetz, "Carrier concentration dependence of the thermal conductivity of silicon carbide", Inst. Phys. Conf. Ser, vol. 137, p. 313, 1994

[73] H. McD. Hobgood et al., "Status of Large Diameter SiC Crystal Growth for Electronic and Optical Applications", Materials Science Forum, vol. 338-342, pp. 3-8, 2000.

[74] D. Feldman, J. Parker, W. Choyke and L. Patrick, "Phonon Dispersion Curves by Raman Scattering in SiC, Polytypes3C,4H,6H,15R, and21R", Physical Review, vol. 173, no. 3, pp. 787-793, 1968.

[75] F. Bechstedt et al., "Polytypism and Properties of Silicon Carbide", physica status solidi (b), vol. 202, no. 1, pp. 35-62, 1997.

[76] J. Steeds, W. Sullivan, S. Furkert, G. Evans and P. Wellmann, "Creation and identification of the two spin states of dicarbon antisite defects in4H-SiC", Physical Review B, vol. 77, no. 19, 2008.

[77] C. Zorman and R. Parro, "Micro- and nanomechanical structures for silicon carbide MEMS and NEMS", physica status solidi (b), vol. 245, no. 7, pp. 1404-1424, 2008.

[78] T. Suzuki, I. Yonenaga and H. Kirchner, "Yield Strength of Diamond", Physical Review Letters, vol. 75, no. 19, pp. 3470-3472, 1995.

[79] M. Zaman, Modeling and characterization of metal/SiC interface for power device application. di Torino: PhD thesis, Department of Applied Science and Technology in Politecnico, 2012.

[80] R. Trew, SiC for microwave power applications: present status and future trends. 1998.

[81] R. Clarke and J. Palmour, "SiC microwave power technologies", Proceedings of the IEEE, vol. 90, no. 6, pp. 987-992, 2002.

[82] B. Sharma, Metal-Semiconductor Schottky Barrier Junctions and Their Applications. New York, NY: Springer, 2013.

[83] A. Tesfaye, SiC Semiconductor Devices Technology, Modeling, and Simulation. Austria: Doctor, Technical University of Vienna, 2004.

[84] E. Rhoderick, "Metal-semiconductor contacts." IEE Proceedings I-Solid-State and Electron Devices", IEE Proceedings I-Solid-State and Electron Devices, vol. 129, no. 1, p. 1, 1982.

[85] J. Bardeen, "Surface States and Rectification at a Metal Semi-Conductor Contact", Physical Review, vol. 71, no. 10, pp. 717-727, 1947.

[86] A. Cowley and S. Sze, "Surface States and Barrier Height of Metal-Semiconductor Systems", Journal of Applied Physics, vol. 36, no. 10, pp. 3212-3220, 1965..

[87] V. Heine, "Theory of Surface States", Physical Review, vol. 138, no. 6, pp. A1689-A1696, 1965.

[88] W. Mönch, Semiconductor Surfaces and Interfaces. Berlin, Heidelberg: Springer Science & Business Media, 2013.

[89] W. Spicer, I. Lindau, P. Skeath and C. Su, "Unified defect model and beyond", Journal of Vacuum Science and Technology, vol. 17, no. 5, pp. 1019-1027, 1980.

[90] G. Hughes, "Transition metals on GaAs(110): A case for extrinsic surface states", Journal of Vacuum Science & Technology B: Microelectronics and Nanometer Structures, vol. 4, no. 4, p. 924, 1986.

[91] O. Sankey, "Dangling bonds and Schottky barriers", Journal of Vacuum Science & Technology B: Microelectronics and Nanometer Structures, vol. 3, no. 4, p. 1162, 1985.

[92] C. Crowell and S. Sze, "Current transport in metal-semiconductor barriers", Solid-State Electronics, vol. 9, no. 11-12, pp. 1035-1048, 1966.

[93] S. Lee, "ChemInform Abstract: Electrode Materials and Electrode-Oxide Interfaces in Semiconductor Gas Sensors", ChemInform, vol. 45, no. 40, p. no-no, 2013.

[94] F. Padovani and R. Stratton, "Field and thermionic-field emission in Schottky barriers", Solid-State Electronics, vol. 9, no. 7, pp. 695-707, 1966.

[95] M. Shur, S. Rumyantsev and M. Levinshtein, SiC materials and devices. Hackensack, NJ: World Scientific, 2007.

[96] H. Card and E. Rhoderick, "Studies of tunnel MOS diodes I. Interface effects in silicon Schottky diodes", Journal of Physics D: Applied Physics, vol. 4, no. 10, pp. 1589-1601, 1971.

[97] C. Weitzel, "Comparison of SiC, GaAs, and Si RF MESFET power densities", IEEE Electron Device Letters, vol. 16, no. 10, pp. 451-453, 1995.

[98] J. Casady and R. Johnson, "Status of silicon carbide (SiC) as a wide-bandgap semiconductor for high-temperature applications: A review", Solid-State Electronics, vol. 39, no. 10, pp. 1409-1422, 1996.

[99] Z. Horváth, "Comment on "Analysis of I-V measurements on CrSi2璞Si Schottky structures in a wide temperature range"", Solid-State Electronics, vol. 39, no. 1, pp. 176-178, 1996.

[100] A. Saxena, "Forward current-voltage characteristics of Schottky barriers on n-type silicon", Surface Science, vol. 13, no. 1, pp. 151-171, 1969.

[101] W. Mönch, Semiconductor surfaces and interfaces. Berlin: Heidelberg: Springer Science & Business Media, 2013.

[102] R. Tung, "The physics and chemistry of the Schottky barrier height", Applied Physics Reviews, vol. 1, no. 1, p. 011304, 2014.

[103] G. Vanalme, R. Meirhaeghe, F. Cardon and P. Daele, "A ballistic electron emission microscopy (BEEM) study of the barrier height change of Au/n-GaAs Schottky barriers due to reactive ion etching", Semiconductor Science and Technology, vol. 12, no. 7, pp. 907-912, 1997.

[104] H. Im, B. Kaczer, J. Pelz and W. Choyke, "Ballistic electron emission microscopy study of Schottky contacts on 6H- and 4H-SiC", Applied Physics Letters, vol. 72, no. 7, pp. 839-841, 1998.

[105] G. Vanalme, L. Goubert, R. Meirhaeghe, F. Cardon and P. Daele, "A ballistic electron emission microscopy study of barrier height inhomogeneities introduced in Au/III-V semiconductor Schottky barrier contacts by chemical pretreatments", Semiconductor Science and Technology, vol. 14, no. 9, pp. 871-877, 1999.

[106] J. Luy and P. Russer, Silicon-based millimeter-wave devices. Berlin: Springer-Verlag, 1994.

[107] P. Friedrichs, Silicon carbide, v. 2: power devices and sensors. Weinheim, Germany: Wiley-WCH, 2010.

[108] C. Sarkar, TECHNOLOGY COMPUTER AIDED DESIGN. CRC Press, 2013.

[109] Silvaco Atlas User's Manual. Device Simulator Software, 2013.

[110] X. Li et al., "On the temperature coefficient of 4H-SiC BJT current gain", Solid-State Electronics, vol. 47, no. 2, pp. 233-239, 2003.

[111] U. Lindefelt, "Doping-induced band edge displacements and band gap narrowing in 3C–, 4H–, 6H–SiC, and Si", Journal of Applied Physics, vol. 84, no. 5, pp. 2628-2637, 1998.

[112] M. Ruff, H. Mitlehner and R. Helbig, "SiC devices: physics and numerical simulation", IEEE Transactions on Electron Devices, vol. 41, no. 6, pp. 1040-1054, 1994.

[113] M. Roschke and F. Schwierz, "Electron mobility models for 4H, 6H, and 3C SiC [MESFETs]", IEEE Transactions on Electron Devices, vol. 48, no. 7, pp. 1442-1447, 2001.

[114] T. Troffer et al., "Doping of SiC by Implantation of Boron and Aluminum", physica status solidi (a), vol. 162, no. 1, pp. 277-298, 1997.

[115] S. Selberherr, Analysis and Simulation of Semiconductor Devices. Springer Science & Business Media, 1984.

[116] A. Galeckas, J. Linnros, V. Grivickas, U. Lindefelt and C. Hallin, "Auger recombination in 4H-SiC: Unusual temperature behavior", Applied Physics Letters, vol. 71, no. 22, pp. 3269-3271, 1997.

[117] P. Landsberg and G. Kousik, "The connection between carrier lifetime and doping density in nondegenerate semiconductors", Journal of Applied Physics, vol. 56, no. 6, pp. 1696-1700, 1984.

[118] X. Li et al., "On the temperature coefficient of 4H-SiC BJT current gain", Solid-State Electronics, vol. 47, no. 2, pp. 233-239, 2003.

[119] M. Bakowski, U. Gustafsson and U. Lindefelt, "Simulation of SiC High Power Devices", physica status solidi (a), vol. 162, no. 1, pp. 421-440, 1997.

[120] M. Philip and A. O'Neill, "Conference on Optoelectronic and Microelectronic Materials and Devices.", Materials Science Forum, vol. 717-720, pp. 1101-1104, 2012.

[121] L. Di Benedetto, G. Licciardo, S. Rao, G. Pangallo, F. Della Corte and A. Rubino, "V2O5/4H-SiC Schottky Diode Temperature Sensor: Experiments and Model", IEEE Transactions on Electron Devices, vol. 65, no. 2, pp. 687-694, 2018.

[122] K. Zeghdar and L. Dehimi, "Inhomogeneous barrier height effect on the current-voltage characteristics of a W/4H-Sic Schottky diode", 2017 5th International Conference on Electrical Engineering-Boumerdes (ICEE-B), 2017.

[123] F. Pezzimenti, "Modeling of the Steady State and Switching Characteristics of a Normally Off 4H-SiC Trench Bipolar-Mode FET", IEEE Transactions on Electron Devices, vol. 60, no. 4, pp. 1404-1411, 2013.

[124] G. De Martino, "Design and numerical characterization of a low voltage power MOSFET in 4H-SiC for photovoltaic applications", 13th Conference on Ph. D. Research in Microelectronics and Electronics (PRIME). IEEE, 2017.

[125] F. Pezzimenti and D. Francesco, "Design and modeling of a novel 4H-SiC normally-off BMFET transistor for power applications", Melecon 2010-2010 15th IEEE Mediterranean Electrotechnical Conference. IEEE, 2010

[126] F. Pezzimenti, L. Albanese, S. Bellone and F. Della Corte, "Analytical model for the forward current of Al implanted 4H-SiC pin diodes in a wide range of temperatures", IEEE Bipolar/BiCMOS Circuits and Technology Meeting. IEEE, 2009.

[127] S. Chand, "On the intersecting behaviour of current–voltage characteristics of inhomogeneous Schottky diodes at low temperatures", Semiconductor Science and Technology, vol. 19, no. 1, pp. 82-86, 2003.

[128] F. Bouzid, F. Pezzimenti, L. Dehimi, M. Megherbi and F. Della Corte, "Numerical simulations of the electrical transport characteristics of a Pt/n-GaN Schottky diode", Japanese Journal of Applied Physics, vol. 56, no. 9, p. 094301, 2017.

[129] F. La Via et al., "Schottky–ohmic transition in nickel silicide/SiC-4H system: is it really a solved problem?", Microelectronic Engineering, vol. 70, no. 2-4, pp. 519-523, 2003.

[130] S. Cheung and N. Cheung, "Extraction of Schottky diode parameters from forward current- voltage characteristics", Applied Physics Letters, vol. 49, no. 2, pp. 85-87, 1986.

[131] L. Calcagno, A. Ruggiero, F. Roccaforte and F. La Via, "Effects of annealing temperature on the degree of inhomogeneity of nickel-silicide/SiC Schottky barrier", Journal of Applied Physics, vol. 98, no. 2, p. 023713, 2005.

[132] J. Osvald and Z. Horváth, "Theoretical study of the temperature dependence of electrical characteristics of Schottky diodes with an inverse near-surface layer", Applied Surface Science, vol. 234, no. 1-4, pp. 349-354, 2004.

[133] S. Chand and J. Kumar, "Current-voltage characteristics and barrier parameters of Pd2Si/p-Si(111) Schottky diodes in a wide temperature range", Semiconductor Science and Technology, vol. 10, no. 12, pp. 1680-1688, 1995.

[134] J. Sullivan, R. Tung, M. Pinto and W. Graham, "Electron transport of inhomogeneous Schottky barriers: A numerical study", Journal of Applied Physics, vol. 70, no. 12, pp. 7403-7424, 1991.

[135] S. Shankar Naik and V. Rajagopal Reddy, "Analysis of current–voltage–temperature and capacitance–voltage–temperature characteristics of Ni/Au Schottky contacts on n-type InP", Superlattices and Microstructures, vol. 48, no. 3, pp. 330-342, 2010.

[136] M. Soylu and B. Abay, "Barrier characteristics of gold Schottky contacts on moderately doped n-InP based on temperature dependent I–V and C–V measurements", Microelectronic Engineering, vol. 86, no. 1, pp. 88-95, 2009.

[137] M. Bhaskar Reddy, A. Ashok Kumar, V. Janardhanam, V. Rajagopal Reddy and P. Narasimha Reddy, "Current–voltage–temperature (I–V–T) characteristics of Pd/Au Schottky contacts on n-InP (111)", Current Applied Physics, vol. 9, no. 5, pp. 972-977, 2009.

[138] S. Hardikar, M. Hudait, P. Modak, S. Krupanidhi and N. Padha, "Anomalous current transport in Au/low-doped n-GaAs Schottky barrier diodes at low temperatures", Applied Physics A: Materials Science & Processing, vol. 68, no. 1, pp. 49-55, 1999.

[139] L. Wagner, R. Young and A. Sugerman, "A note on the correlation between the Schottky-diode barrier height and the ideality factor as determined from I-V measurements", IEEE Electron Device Letters, vol. 4, no. 9, pp. 320-322, 1983.

[140] J. Yu-Long et al., "Schottky Barrier Height Inhomogeneity of Ti/n-GaAs Contact Studied by theI-V-TTechnique", Chinese Physics Letters, vol. 19, no. 4, pp. 553-556, 2002.

[141] R. Schmitsdorf, T. Kampen and W. Mönch, "Correlation between barrier height and interface structure of Schottky diodes", Surface Science, vol. 324, no. 2-3, pp. 249-256, 1995.

[142] H. Cetin and E. Ayyildiz, "Temperature dependence of electrical parameters of the Au/n-InP Schottky barrier diodes", Semiconductor Science and Technology, vol. 20, no. 6, pp. 625-631, 2005.

[143] E. Özavcı, S. Demirezen, U. Aydemir and Ş. Altındal, "A detailed study on current–voltage characteristics of Au/n-GaAs in wide temperature range", Sensors and Actuators A: Physical, vol. 194, pp. 259-268, 2013.

[144] E. Ayyildiz, H. Cetin and Z. Horváth, "Temperature dependent electrical characteristics of Sn/p-Si Schottky diodes", Applied Surface Science, vol. 252, no. 4, pp. 1153-1158, 2005.

[145] S. Kyoung, E. Jung and M. Sung, "Post-annealing processes to improve inhomogeneity of Schottky barrier height in Ti/Al 4H-SiC Schottky barrier diode", Microelectronic Engineering, vol. 154, pp. 69-73, 2016.

[146] F. La Via, F. Roccaforte, A. Makhtari, V. Raineri, P. Musumeci and L. Calcagno, "Structural and electrical characterisation of titanium and nickel silicide contacts on silicon carbide", Microelectronic Engineering, vol. 60, no. 1-2, pp. 269-282, 2002.

[147] C. Fisher, "On the Schottky Barrier Height Lowering Effect of Ti3SiC2 in Ohmic Contacts to P-Type 4H-SiC", International Journal of Fundamental Physical Sciences, vol. 4, no. 3, pp. 95-100, 2014.

[148] Q. Song, Y. Zhang, Y. Zhang, F. Chen and X. Tang, "Investigation of current transport parameters of Ti/4H-SiC MPS diode with inhomogeneous barrier", Chinese Physics B, vol. 20, no. 5, p. 057301, 2011.

[149] M. Hudait and S. Krupanidhi, "Doping dependence of the barrier height and ideality factor of Au/n-GaAs Schottky diodes at low temperatures", Physica B: Condensed Matter, vol. 307, no. 1-4, pp. 125-137, 2001.

[150] Ş. Karataş, Ş. Altındal, A. Türüt and A. Özmen, "Temperature dependence of characteristic parameters of the H-terminated Sn/p-Si(1 0 0) Schottky contacts", Applied Surface Science, vol. 217, no. 1-4, pp. 250-260, 2003.

[151] H. Henisch, Semiconductor contacts. Oxford: Clarendon Press, 1985.

[152] T. Zhang, C. Raynaud and D. Planson, "Measure and analysis of 4H-SiC Schottky barrier height with Mo contacts", The European Physical Journal Applied Physics, vol. 85, no. 1, p. 10102, 2019.

[153] L. Huang, R. Geiod and D. Wang, "Barrier inhomogeneities and interface states of metal/4H-SiC Schottky contacts", Japanese Journal of Applied Physics, vol. 55, no. 12, p. 124101, 2016.

[154] Z. Ouennoughi, S. Toumi and R. Weiss, "Study of barrier inhomogeneities using I–V–T characteristics of Mo/4H–SiC Schottky diode", Physica B: Condensed Matter, vol. 456, pp. 176-181, 2015.

[155] K. Geib, C. Wilson, R. Long and C. Wilmsen, "Reaction between SiC and W, Mo, and Ta at elevated temperatures", Journal of Applied Physics, vol. 68, no. 6, pp. 2796-2800, 1990.

[156] W. Leroy, C. Detavernier, R. Van Meirhaeghe, A. Kellock and C. Lavoie, "Solid-state formation of titanium carbide and molybdenum carbide as contacts for carbon-containing semiconductors", Journal of Applied Physics, vol. 99, no. 6, p. 063704, 2006.

[157] S. Toumi and Z. Ouennoughi, "A vertical optimization method for a simultaneous extraction of the five parameters characterizing the barrier height in the Mo/4H–SiC Schottky contact", Indian Journal of Physics, 2019.

[158] S. Duman, "Temperature dependence of current–voltage characteristics of an In/p-GaSe:Gd/Au–Sb Schottky barrier diode", Semiconductor Science and Technology, vol. 23, no. 7, p. 075042, 2008.

[159] K. Geib, C. Wilson, R. Long and C. Wilmsen, "Reaction between SiC and W, Mo, and Ta at elevated temperatures", Journal of Applied Physics, vol. 68, no. 6, pp. 2796-2800, 1990.

[160] W. Seng and P. Barnes, "Calculations of tungsten silicide and carbide formation on SiC using the Gibbs free energy", Materials Science and Engineering: B, vol. 72, no. 1, pp. 13-18, 2000.

[161] J. Kim, F. Ren, A. Baca, R. Briggs and S. Pearton, "High temperature thermal stability of Au/Ti/WSix Schottky contacts on n-type 4H-SiC", Solid-State Electronics, vol. 47, no. 8, pp. 1345-1350, 2003.

[162] J. Kim, F. Ren, A. Baca, G. Chung and S. Pearton, "Thermal stability of WSiX Schottky contacts on n-type 4H-SiC", Solid-State Electronics, vol. 48, no. 1, pp. 175-178, 2004.

Publication and conferences

Publication and conferences

- Kamal Zeghdar, Lakhdar Dehimi, Fortunato Pezzimenti, Sandro Rao and Francesco G. Della Corte«*Simulation and analysis of the current–voltage–temperature characteristics of Al/Ti/4H-SiC Schottky barrier diodes*» 2019 Jpn. J. Appl. Phys. 58 014002.

- Kamal Zeghdar and Lakhdar Dehimi «*Inhomogeneous barrier height effect on the current–voltage characteristics of a Mo/4H-SiC Schottky diode*» ICEPA Djelfa 2017 /16-17 September 2017 Algeria

- K.Zeghdar and L.Dehimi «*Inhomogenous barrier height effect on the current voltage characteristics of W/4H-SiC Shottky diode*» ICEE Boumerdes, 29-31 October *2017*, Algeria

- K.Zeghdar, L.Dehimi «*Investigation on the non-ideal behavior of Tungsten/4H_SiC Shottky diodes by simulation of I-V-T*» ICENT Msila 2017/14-15 November 2017 Algeria

- K.Zeghdar, L.Dehimi « *Numerical simulation study of current–voltage characteristics of a Molybdenum/4H-SiC Schottky diode containing barrier inhomogeneities using SILVACO-TCAD software* ICMS setif 2018/12-14 September 2018 Algeria